Reconstruction et analyse des gerbes électromagnétiques dans l'expérience OPERA et étude des oscillations neutrino avec détection d'électrons

Florian Brunet

UNIVERSITÉ DE GRENOBLE

PhD Thesis

Submitted in fulfillment of the requirements for the degree of

DOCTEUR DE L'UNIVERSITÉ DE GRENOBLE

Specialty : **Particle Physics**

Prepared by

Florian Brunet

Thesis supervised by **Amina Zghiche**

Prepared at the **Laboratoire d'Annecy-le-Vieux de Phyisque des Particules**

Electromagnetic showers reconstruction and analysis in the OPERA experiment and neutrino oscillation study by electron detection.

Thesis publicly defended the 12th **December 2012**,
In front of the comity :

M. Lounis Abdenour
LAL - Paris XI Orsay, Examinateur
M. Marcos Dracos
IPHC - Strasbourg, Rapporteur
M. Yannis Karyotakis
LAPP - Annecy-le-Vieux, Examinateur
M. Georges Vasseur
CEA - Saclay, Rapporteur
Mme. Amina Zghiche
LAPP - Annecy-le-Vieux, Directeur de thèse

To my grandmother,

Remerciements

Avant d'entrer dans le vif du sujet, je souhaiterais remercier toutes les personnes qui ont rendu possible la réalisation de ce travail de thèse représenté par ce manuscrit.

Je voudrais tout d'abord exprimer ma profonde reconnaissance à Amina Zghiche, directrice de cette thèse qui m'a encadré pendant 3 ans et demi et qui a su me guider pas à pas du "petit" étudiant diplômé d'un master de physique subatomique au docteur en physique des particules que je suis à présent. Ce chemin n'a pas été de tout repos et elle a su anticiper toutes les étapes importantes afin que j'y sois préparé au mieux. Merci de ton soutien pendant ces 3 ans et particulièrement pendant les périodes de rédaction et de soutenance en me faisant part de ta confiance en la qualité de ce travail plus que je n'en avais moi-même.

Je tiens à remercier Yannis Karyotakis de m'avoir accueilli au LAPP et assuré la présidence de mon jury. Merci à Marcos Dracos et Georges Vasseur pour la lecture approfondie de mon manuscrit, les discussions téléphoniques qui ont suivies et l'évaluation qu'ils ont fait de mon travail en tant que rapporteurs. Merci à Lounis Abdenour de l'intérêt qu'il a porté à ce travail, de sa présence à ma soutenance et des questions intéressantes qu'il a posées.

De plus, je voudrais aussi remercier le groupe Neutrinos du LAPP pour leur investissement dans mon travail de thèse par la tenue deux fois par semaine de réunion ayant entre autres objectifs celui de la présentation de l'avancement de mon travail. Ces réunions ont toujours été pour moi une source de remise en question ainsi que de nouvelles pistes à poursuivre. Plus particulièrement, je tiens à remercier Dominique Duchesneau pour sa grande connaissance de la physique du neutrino ainsi que pour les lectures assidues de mon manuscrit pendant la rédaction. Un grand merci va aussi à Henri Pessard l'historien des neutrinos ainsi qu'à Jean Favier pour son sens aïgu de la physique expérimentale et plus spécifiquement des efficacités des émulsions.

Enfin, un grand merci à Pablo Del Amo Sanchez, collègue de bureau et surtout aguerri aux techniques d'analyse en physique des particules qui m'a permis d'apprendre et de lui confronter toute sorte de problèmes qui ont pu se poser à moi pendant ma thèse.

Un immense merci à Frédéric Juget pour m'avoir accueilli à Berne lors de mes débuts dans OPERA et de m'avoir initié à la physique des gerbes électromagnétiques.

Ich möchte vielen Dank auch an Frank W. Meisel sagen für haben mich wie funktioniert den Algorithmus auf elektromagnetisch Blumengebinde Wiederaufbau gelernt und für haben sein Wissen auf das Subjekt mit meinen Resultate gegenübergestellt.

I wish to thank Akitaka Ariga to welcome me in his laboratory in Bern for sessions of hard work for the analysis of electrons in OPERA and Tomoko as well to teach me the science of emulsion scanning.

Je souhaiterais remercier Isabelle De Bonis pour l'encadrement de mes enseignements à l'Université de Savoie et d'avoir été une tutrice pédagogique qui m'ait initié à l'enseignement supérieur. J'aimerais remercier également Didier Verkindt pour avoir supervisé mon projet de diffusion scientifique en lycée.

Merci tout particulièrement à Sandrine Ferrari de l'Ecole Doctorale de physique à Grenoble qui a tellement bien géré le parcours administratif de nos doctorats, avec bonne humeur de surcroît.

J'aimerais saluer tous les membres du LAPP et les remercier pour leur accueil. Merci notamment à Françoise Sublet pour ses petites visites de courtoisie et d'encouragement régulières dans mon bureau ainsi que pour sa présence à ma soutenance et à mon pot de thèse. Merci aussi à Nicole Berger pour sa bonne humeur, Myriam Froger et Chantal Vallée pour leur aide perpétuelle avec l'aspect administratif et leur sympathie, Brigitte Putanier (ou madame Missions) pour sa bonne humeur, Cécile Jacob et Jean-Marc Dubois pour leur sympathie et Laurent Brunetti, entre badminton et café toujours une petite discussion pour se détendre. Merci enfin à tous ceux que j'aurai oublié de mentionner ici et avec lesquels j'ai passé de bons moments au laboratoire.

Pour continuer, j'aimerais remercier mes collègues thésards qui ont animés la vie du laboratoire de même que la vie annécienne : Guillaume pour les sortie nocturnes, Maud comme partenaire de badminton, Ludovica comme partenaire de badminton et de restaurant, Dimitra pour sa science des alcools, Michael et Loïc pour les soirées jeux de société, Jonathan pour ses blagues jamais drôles, Vincent pour sa bonne humeur même si je n'en ai pas profité longtemps, Timur et enfin Céline, la doctorante de sciences humaines, pour sa constante envie de discuter de tout et de n'importe quoi. Une mention spéciale pour Timothée, sans qui, l'aventure de la thèse n'aurait pas été la même : cafés, badminton, restaurants, sandwiches, ski, sorties, rédaction, soutenance, déménagement, discussions sans fin et tous ces bons moments passés ensemble.

Pour finir, je souhaiterais remercier tous ceux qui m'ont soutenu pendant ces 3 années : mes parents qui m'ont toujours aidé peu importe ce que je leur demandais, Lucie qui lors de ces périples à Annecy ou lors des miens à Paris a toujours été prête à me changer les idées, mes collègues du Master de Physique Subatomique de Lyon croisés ici et là Benoît, Nicolas, Elisabeth, Laura qui s'est lancée dans la même aventure que moi, et toutes les personnes que j'ai rencontrées pendant 3 ans avec lesquelles j'ai passé un agréable moment lors un dîner, d'une conférence ou d'une école d'été. Many thanks also to the CS scanning shifters friends from Moscow, Dubna, Ankara and Hambourg.

Pour conclure, merci à celle qui est derrière chaque mot de ce manuscrit qu'elle a lu et lu encore et qui m'a soutenu constamment avant et pendant ces 3 années et pour de nombreuses autres encore.

Contents

Introduction

At the end of the 19th century radioactivity was discovered by H. Becquerel in 1897. From that discovery, scientists knew that radiation was emitted from specific nuclei. J. Chadwick in 1914 measured the energy spectrum of the β-decay of tritium nuclei according to the reaction $^3H \longrightarrow {}^3He + e^- + \overline{\nu_e}$ and showed that it was continuous. In order to recover the β-decay theory, one has to assume that another neutral particle of spin $\frac{1}{2}$ was emitted with the electron : W. Pauli did postulate the existence of the "neutronen" as he called it to save the energy conservation principle. J. Chadwick in 1932 observed a neutral particle as heavy as the proton that he called "neutron". When E. Fermi developed his theory of weak interaction [1] including the β-decay as a 3-body process, he decided to call the famous Pauli neutral particle "neutrino" ; it was in 1934. On the same year, H. Bethe and R. Peierls showed the peculiar nature of the neutrino because they calculated its cross section [2] and predicted the neutrinos were not easy to be detected. The observation of this particle has been actually waiting for 22 years. F. Reines and C.L. Cowan built a detector in South Carolina (USA) and through the inverse β-decay reaction $\nu + p \rightarrow n + e^+$, they captured three neutrinos per hour produced by the nuclear power plant of Savannah River [3]. By measuring this low rate with respect to the huge number of neutrinos produced in a reactor core, they confirmed the elusive character of the neutrino. In addition, precise measurements of the energy spectrum of the β-decay process [4] gave hints of the smallness of the neutrino mass implying a massless neutrino in most of theoretical calculations including the Standard Model (SM).

Later, in 1962, L. Lederman *et al.* [5] observed neutrinos in the pion decay which mainly produced muons when interacting. With the two known leptons, electron and muon, the association of each to a corresponding neutrino could be made. A third lepton τ was discovered at Stanford Linear Accelerator Center (SLAC) [6]. The assumption was thus to expect a third neutrino. It was finally observed, in year 2000 by Direct Observation of NU Tau (DONUT) experiment [7]. Three families of leptons have been observed and, experimentally, LEP experiments evaluated the decay width of Z boson [8] showing that three families of leptons are expected and confirmed that there are three different active light neutrinos : ν_e, ν_μ and ν_τ at the Z boson energy scale.

An additional unusual property of this particle is the helicity which has been investigated in 1958. M. Goldhaber *et al.* [9] by studying the conservation of the angular momentum in the inverse β-decay process on Europium nuclei demonstrated that neutrinos can only have a left-handed helicity and right-handed for antineutrinos, respectively.

Another important brick of the neutrino picture is the oscillation phenomenon formalized by B. Pontecorvo in 1957 [10] then by Z. Maki *et al.* in 1962 [11]. Starting in 1964 and data analysis having finished 20 years ago, the Homestake chlorine experiment detected ν_e produced by the Sun and captured by chlorine nuclei in the detector by inverse β-decay process. The neutrino rate measured was much lower than the one expected from the Standard Solar Model (SSM) computation [12] suggesting that some of ν_e changed into another flavour travelling from the Sun to the Homestake mine. In the following years, this result has been confirmed by Soviet-American Gallium Experiment (SAGE) in Russia [13] and GALLium EXperiment (GALLEX)/Gallium Neutrino Observatory (GNO) in the Laboratori Nazionali del Gran Sasso (LNGS) [14]. The oscillation was a possible explanation of these measurements but all these experiments were designed to measure only one specific neutrino flavor contribution to the total solar neutrino spectrum.

One of the most exciting oscillation result was given by SuperKamiokande in 1998 on atmospheric neutrinos when the experiment measured an unexpected ratio between the upward and the downward going muon neutrinos [15]. This effect is the first experimental proof of neutrino oscillation and of the existence of a non-zero neutrino mass as well. Indeed, downward going muon neutrinos produced in the terrestrial atmosphere traveled a longer distance inside the Earth before entering in the detector. Assuming oscillation depends on the baseline length, there should be a dependance of atmospheric neutrino rate on zenith angle. From this result, neutrino oscillation seemed to be a valid theory and an experimental quest started to characterize this phenomenon by measuring the different associated parameters : two squared masses differences and three mixing angles. Later on, water Cerenkov detectors came up to perform estimations of the total solar neutrino flux and, as the Sudbury Neutrino Observatory (SNO) experiment did in 2000 in Canada, validate the neutrino oscillation hypothesis in the solar sector [16]. These important results were completed with other sources of neutrinos, for instance the nuclear power plant experiment KamLAND in Japan observed the oscillations in 2005 ; furthermore, experiments like K2K in Japan with neutrinos produced in accelerators also confirmed the neutrino oscillation. All these experiments allow physicists to build a global picture of the neutrino oscillation and in 2009, when I started this work, four out of the five above-named parameters were determined. The mixing angle called θ_{13} remained not measured and the sign of Δm_{23}^2 unknown. Moreover the Charge conjugation Parity (CP) violation phase, possibly existing if θ_{13} has a non-zero value, was also undetermined. The knowledge of θ_{13} is thus crucial and in 2009 the best limit was the result of the Chooz experiment [17] published in 1999 : $sin^2(2\theta_{13}) < 0.14$ at 90% Confidence Level (C.L.) with $\Delta m_{13}^2 = 2.5 \times 10^{-3} \text{eV}^2$. In this context, several experiments were being built in order to push down this limit and possibly to measure the actual value of θ_{13} : some of them with nuclear power plant neutrinos as Daya Bay, Reactor Experiment for Neutrino Oscillations (RENO) and Double Chooz, some others with accelerator neutrinos as Main Injector Neutrino Oscillation Search (MINOS) or Tokai to Kamioka (T2K). The first ones are reactor $\overline{\nu_e}$ disappearance experiments and measure a difference between the neutrino rate in a near detector close to the nuclear power plant (a few hundred meters) and another placed at a far position ($\approx$ 1 km). MINOS and T2K are in the other hand ν_e appearance experiments in a ν_μ beam and have a double goal : measure θ_{13} and validate the oscillation phenomenon by observing an appearance of a new flavour instead of measuring a deficit of a certain flavour.

Oscillation Project with Emulsion-tRacking Apparatus (OPERA) is also an experiment designed to measure oscillations in the atmospheric sector in the appearance mode $\nu_\mu \to \nu_\tau$. Although the ν_μ beam is optimized for ν_τ appearance, OPERA remains sensitive to the $\nu_\mu \to \nu_e$ oscillation. This thesis work aims to evaluate the potential sensitivity of OPERA to this oscillation and to θ_{13} measurement. First a brief theoretical and experimental review of neutrino oscillation will be done. Then a description of the OPERA experiment, of the DAQ system and the analysis framework will be given. I will then come to the work I have done on the the reconstruction and the analysis of electromagnetic showers in OPERA bricks using MC studies of both $\tau \to e$ appearance channel and the $\nu_\mu \to \nu_e$ oscillation.

Chapter 1

Neutrino Physics

From the theoretical point of view [18], in an extension of the SM, the neutrino can acquire a mass through coupling with a Higgs doublet which is rather natural for what is expected from particle mass generation. In addition, different kind of experiments can put a limit on the neutrino mass and some future ones are dedicated to the measurement of the actual value of this mass. In this uncertain context, the best proof of the existence of a massive neutrino is definitely the neutrino oscillation phenomenon. In this chapter, the formalism of neutrino oscillations will be described and a review of the present experimental picture of neutrino oscillation will be drawn.

1.1 Neutrino Oscillation

1.1.1 Mixing and oscillation

The idea that a particle can oscillate between different states goes back to 1950's and to the studies of kaons, particles that were discovered in cosmic rays interaction in the late 1940's [19]. In 1953, in a scheme for classifying the newly found particles, theorist M. Gell-Mann represented the neutral kaon K^0 and its antiparticle $\overline{K^0}$ as two distinct particles. Both of them should be decaying into two or three charged pions with different lifetimes. So the problem was to determine which particle, K^0 or $\overline{K^0}$, has originated a final state with two or three charged pions. The key to this problem is in realising that what we observe must be an admixture of the two states K^0 and $\overline{K^0}$. M. Gell-Mann made the link with quantum mechanics and the superposition principle : the neutral kaons are two quantum states with finite and distinct lifetime, short and long, thus different ways to decay into two or three pions[1], as shown in equation 1.1.

B. Pontecorvo used the same principle for another neutral particle : the neutrino. In 1957, he discussed the idea of neutrino-antineutrino mixing but 10 years later he turned to the idea, that through the mixing, a ν_e could oscillate into a ν_μ and vice & versa [10]. Z. Maki *et al.* also made that same hypothesis in 1962 [11].

---

[1] Note that in case of a small CP violating effect, $K^0_L \to \pi^+\pi^-$ is allowed with a branching ratio of order 10^{-3}.

$$|K_S^0\rangle = \frac{|K^0\rangle + |\overline{K^0}\rangle}{\sqrt{2}} \ [\text{CP} = +1] \qquad K_S^0 \to 2\pi \tag{1.1}$$

$$|K_L^0\rangle = \frac{|K^0\rangle - |\overline{K^0}\rangle}{\sqrt{2}} \ [\text{CP} = -1] \qquad K_L^0 \to 3\pi$$

1.1.2   Oscillation principle

The basic idea behind neutrino mixing is that the states that participate in weak interactions are not exactly the same as the states of specific mass ; instead the weak interaction states are mixtures of states of specific mass. For instance, when electron-neutrinos are emitted at a certain energy, the different mass states propagate through space at different velocities, i.e. the mass states become out of phase with each other so that mixture will evolve with time. In this way, the mixture corresponding to electron-neutrino will change into another mixture corresponding to a muon-neutrino or a tau-neutrino. The matrices used to diagonalize the Yukawa coupling matrices of charged leptons and neutrinos are mixed in the charged current Lagrangian to yield the Maki Nakagawa Sakata Pontecorvo (MNSP) neutrino mixing matrix $U_{\text{MNSP}} = U$ [20]. The neutrino lepton flavour states $|\nu_\alpha\rangle$ are thereby related to the mass states $|\nu_k\rangle$ by U through :

$$|\nu_\alpha\rangle = \sum_{k=1}^{n} U_{\alpha k}^* \, |\nu_k\rangle \tag{1.2}$$

The lepton flavour state of a neutrino with an energy E_k and a momentum p_k travelling for a time t is given by :

$$|\nu_\alpha(t)\rangle = \sum_{k=1}^{n} U_{\alpha k}^* \, e^{-iE_k t} \, |\nu_k\rangle \tag{1.3}$$

By inverting relation 1.2, we obtain the following relation showing that after its production, a neutrino is a linear superposition of the existing flavour states :

$$|\nu_\alpha(t)\rangle = \sum_{\beta = e,\mu,\tau} \left(\sum_{k=1}^{n} U_{\alpha k}^* \, e^{-iE_k t} \, U_{\beta k} \right) |\nu_\beta\rangle \tag{1.4}$$

Neutrinos produced in a flavour state α have a probability to be in a flavour state β as a function of time t written below :

$$P_{\nu_\alpha \to \nu_\beta}(t) = |\langle \nu_\beta | \nu_\alpha(t, L)\rangle|^2 = \left| \sum_{k=1}^{n} U_{\alpha k}^* \, e^{-iE_k t} \, U_{\beta k} \right|^2 \tag{1.5}$$

From the De Broglie dispersion relation $E^2 = p^2 + m^2$ and the fact that neutrinos are ultrarelativistic, the dispersion relation can be approximated by :

$$E_k \approx E + \frac{m_k}{2E} \Rightarrow E_k - E_j \approx \frac{\Delta m_{kj}^2}{2E} \tag{1.6}$$

Hence, in neutrino experiments, the propagation time t is not measured and as far as ultrarelativistic neutrinos travel at the speed of light : $t = L$, with L the propagation distance.

The oscillation probability is finally given by :

$$P_{\nu_\alpha \to \nu_\beta}(L, E) = \delta_{\alpha\beta} + 2\Re \sum_{k>j} U_{\alpha k}^* U_{\beta k} U_{\alpha j} U_{\beta j}^* e^{-i\frac{\Delta m_{jk}^2 L}{2E}} \tag{1.7}$$

with the squared mass states difference $\Delta m_{jk}^2 = m_k^2 - m_j^2$.

and where $\delta_{\alpha\beta} = 1$ if $\alpha = \beta, 0$ otherwise.

As it is presented in section 1.2.2.4, the upper bound on the neutrino mass is within the eV and, in experimental particle physics, the neutrinos have an energy above the MeV. Therefore, they are considered as relativistic. In addition, in the oscillation formalism, neutrinos have been described by plane waves for simplicity while it should have been wave packets. The treatment with wave packets leads to the same formula but adds the possibility of decoherence due to different group velocities. The latter can happen only for very large travel distances what is not the case in the current neutrino oscillation experiments.

Only the second term in expression 1.7 describes the oscillation as a function of the distance L between the source and the detector and the neutrino energy E. Furthermore, the dependence on the mass difference between the mass states allows to establish that an observation of the oscillation phenomenon implies that neutrinos are massive. It is important to notice that, in absence of CP violation, the oscillation probabilities $P_{\nu_\alpha \to \nu_\beta}$ do not depend on possible phases of the U_{MNSP} matrix. Moreover, in the case of invariance under Charge conjugation Parity Time (CPT), we obtain:

$$P_{\nu_\alpha \to \nu_\beta} = P_{\overline{\nu_\alpha} \to \overline{\nu_\beta}} \tag{1.8}$$

1.1.3 Two flavours oscillation in vacuum

For the establishment of the neutrino oscillation probability in vacuum used in the past experiments, let us consider the simplest case where only two neutrino flavours are involved : ν_α and ν_β linked by a rotation matrix depending only on a mixing angle θ :

$$\begin{pmatrix} \nu_\alpha \\ \nu_\beta \end{pmatrix} = \begin{pmatrix} cos\theta & sin\theta \\ -sin\theta & cos\theta \end{pmatrix} \begin{pmatrix} \nu_1 \\ \nu_2 \end{pmatrix} \tag{1.9}$$

From equation 1.7 the resulting oscillation probability is :

$$P_{\nu_\alpha \to \nu_\beta}(L) = sin^2 2\theta \, sin^2 \left(\frac{\Delta m^2 L}{4E} \right) \tag{1.10}$$

where Δm^2 is the squared masses difference between the mass states ν_1 and ν_2, and $sin^2 2\theta$ controls the amplitude of the oscillations whereas $sin^2 \left(\frac{\Delta m^2 L}{4E} \right)$ is the oscillating term with the phase $\frac{\Delta m^2 L}{4E}$.

To obtain appreciable oscillation, there should be a large mixing angle θ but also a phase so that :

$$\frac{\Delta m^2 L}{4E} \approx 1 \tag{1.11}$$

When the phase is very large compared to one, the finite energy resolution and/or the finite detector size lead to an averaged oscillation probability of about half the amplitude factor. Past oscillation experiments have largely used the following formula where the h and c constants have been restored :

$$P_{\nu_\alpha \to \nu_\beta}(L) = sin^2 2\theta \, sin^2 \left(1.27 \frac{\Delta m^2 [\text{eV}^2] \, L[\text{km}]}{E[\text{GeV}]} \right) \tag{1.12}$$

1.1.4   Three neutrino flavours oscillations

In the case of three involved neutrino flavours in the oscillation, the U_{PMNS} matrix depends on three mixing angles: θ_{12} , θ_{23} and θ_{13} and a CP violation phase δ. This phase introduces a possible asymmetry between the oscillation probabilities of neutrinos $P_{\nu_\alpha \to \nu_\beta}$ and antineutrinos $P_{\overline{\nu_\alpha} \to \overline{\nu_\beta}}$. If the neutrino is a Majorana particle, see section 1.2.2.2, there are two additional phases α_2 and α_3 that have no impact on the neutrino oscillation probabilities. U can be parametrized by the product of three rotation matrices and a diagonal matrix carrying the two Majorana phases :

$$
\begin{aligned}
U &= \begin{pmatrix} 1 & 0 & 0 \\ 0 & c_{23} & s_{23} \\ 0 & -s_{23} & c_{23} \end{pmatrix} \times \begin{pmatrix} c_{13} & 0 & s_{13}e^{-i\delta} \\ 0 & 1 & 0 \\ -s_{13}e^{-i\delta} & 0 & c_{13} \end{pmatrix} \times \begin{pmatrix} c_{12} & s_{12} & 0 \\ -s_{12} & c_{12} & 0 \\ 0 & 0 & 1 \end{pmatrix} \times \begin{pmatrix} 1 & 0 & 0 \\ 0 & e^{i\alpha_2} & 0 \\ 0 & 0 & e^{i\alpha_3} \end{pmatrix} \\
&= \begin{pmatrix} c_{12}c_{13} & s_{12}c_{13} & s_{13}e^{-i\delta} \\ -s_{12}c_{23} - c_{12}s_{23}s_{13}e^{+i\delta} & c_{12}c_{23} - s_{12}s_{23}s_{13}e^{-i\delta} & s_{23}c_{13} \\ s_{12}s_{23} - c_{12}c_{23}s_{13}e^{+i\delta} & -c_{12}s_{23} - s_{12}c_{23}s_{13}e^{+i\delta} & c_{23}c_{13} \end{pmatrix} \times \begin{pmatrix} 1 & 0 & 0 \\ 0 & e^{i\alpha_2} & 0 \\ 0 & 0 & e^{i\alpha_3} \end{pmatrix}
\end{aligned} \tag{1.13}
$$

with $c_{ij} = cos(\theta_{ij})$ and $s_{ij} = sin(\theta_{ij})$, $i, j = 1, 2, 3$.

When considering oscillation probabilities, there are three additional parameters coming from the squared masses differences between the mass states (m_1, m_2, m_3): Δm_{12}^2, Δm_{23}^2 and Δm_{31}^2. However, only two of these parameters are independent since :

$$\Delta m_{12}^2 + \Delta m_{23}^2 + \Delta m_{31}^2 = 0 \tag{1.14}$$

and consequently neutrino oscillations depends on six parameters. As it is described in section 1.3, (θ_{12}, Δm_{12}^2) were first determined in the solar neutrino experiments and called (θ_{sol}, $\Delta m_{\mathrm{sol}}^2$) while ($\theta_{32}$, Δm_{32}^2) were determined in atmospheric neutrino experiments and so-called (θ_{atm}, $\Delta m_{\mathrm{atm}}^2$).

Given the fact that this thesis is about the study of neutrino oscillation in the $\nu_\mu \rightarrow \nu_e$ channel with the OPERA experiment, the computation of the related probability of oscillation in this channel can be obtained from the equation 1.7 and using the parametrization of U_{PMNS} in equation 1.13 and the result is :

$$P(\nu_\mu \rightarrow \nu_e) = 4c_{13}^2 s_{13}^2 s_{23}^2 sin^2\frac{\Delta m_{13}^2 L}{4E} \times \left[1 \pm \frac{2a}{\Delta m_{13}^2}(1 - 2s_{13}^2)\right] \tag{1.15}$$

$$+ 8c_{13}^2 s_{12} s_{13} s_{23}(c_{12}c_{23}cos\delta - s_{12}s_{13}s_{23})cos\frac{\Delta m_{23}^2 L}{4E}sin\frac{\Delta m_{13}^2 L}{4E}sin\frac{\Delta m_{12}^2 L}{4E}$$

$$\pm 8c_{13}^2 c_{12}c_{23}s_{12}s_{13}s_{23}sin\delta sin\frac{\Delta m_{23}^2 L}{4E}sin\frac{\Delta m_{13}^2 L}{4E}sin\frac{\Delta m_{12}^2 L}{4E}$$

$$+ 4s_{12}^2 c_{13}^2(c_{13}^2 c_{23}^2 + s_{12}^2 s_{23}^2 s_{13}^2 - 2c_{12}c_{23}s_{12}s_{23}s_{13}cos\delta)sin^2\frac{\Delta m_{12}^2 L}{4E}$$

$$\mp 8c_{12}^2 s_{13}^2 s_{23}^2 cos\frac{\Delta m_{23}^2 L}{4E}sin\frac{\Delta m_{13}^2 L}{4E}\frac{aL}{4E}(1 - 2s_{13}^2)$$

1.1.5 Oscillations in matter

Neutrinos travelling through matter may be coherently forward scattered by interacting with electrons and nucleons composing the medium. This modifies the mixing between flavour states and propagation states and the eigenvalues of the Hamiltonian, leading to a different oscillation probability with respect to vacuum. To simplify the formalism, only the 2-flavour oscillation will be considered in this section.

1.1.5.1 Matter with constant density

In the SM, fermions can interact with matter through different types of processes : absorption, inelastic and elastic scatterings. For practical purposes and because neutrino interactions are weak, absorption processes are negligible. Inelastic scattering going as G_{F}^2, with G_{F} the Fermi coupling constant[2], is typically negligible as well with respect to coherent scattering going as G_{F}. Neutrinos undergo thus forward elastic scattering, in which they do not change momentum.

---

[2]The most precise experimental determination of the Fermi constant comes from measurements of the muon lifetime, which is inversely proportional to the square of G_{F}, $G_{\mathrm{F}} = 1.16637 \times 10^{-5}\,\mathrm{GeV}^{-2}$ [21].

Neutrinos interact with matter via Neutral Current (NC) interactions, regardless of their flavour. This interaction creates an overall phase factor which has no physical effect on oscillations [22]. However, because of the natural presence of electrons in matter, we must include the Charged Current (CC) scattering of ν_e's which do affect the oscillation by adding a phase shift. This interaction is at the origin of the addition of a potential to the free Hamiltonian called matter potential :

$$V_{\text{CC}} = \sqrt{2}\, G_{\text{F}} N_e \tag{1.16}$$

where N_e the electron density in the medium. V_{CC} is the potential induced by the CC.

In the two flavours case, which is a good theoretical exercise to understand the principle of oscillation in matter with constant density, the diagonal basis and the flavour basis are related by a unitary matrix with angle in matter [23] :

$$\tan(2\theta_{\text{M}}) = \frac{\frac{\Delta m^2}{2E} sin(2\theta)}{\frac{\Delta m^2}{2E} cos(2\theta) - \sqrt{2}\, G_{\text{F}} N_e} \tag{1.17}$$

Here, three interesting limits are arising :

$\sqrt{2}\, G_{\text{F}} N_e \ll \frac{\Delta m^2}{2E} cos(2\theta)$: the vacuum case is recovered and $\theta_{\text{M}} = \theta$.

$\sqrt{2}\, G_{\text{F}} N_e \gg \frac{\Delta m^2}{2E} cos(2\theta)$: matter effects dominate and oscillations are suppressed.

$\sqrt{2}\, G_{\text{F}} N_e = \frac{\Delta m^2}{2E} cos(2\theta)$: there is a resonance implying a maximal mixing $\theta_{\text{M}} = \frac{\pi}{4}$

for the resonance density $N_{\text{R}} = N_e$.

The resonance condition can be satisfied for neutrinos, if $\Delta m^2 > 0$, and antineutrinos, if $\Delta m^2 < 0$. If there is an enhancement in one of the two channels, it is possible to deduce the sign of Δm^2 as will be described in section 1.2.2.4.

1.1.5.2   Varying density and Mikheyev-Smirnov-Wolfenstein (MSW) effect

Neutrino oscillations in the matter were investigated by Mikheyev and Smirnov who pointed out the appearance of a resonance region : at a given neutrino energy, the probability for oscillation will be enhanced to large values, even when the mixing angles in vacuum are small. This mechanism is called the MSW effect [24]. Let us consider the case in which N_e is not uniform. This happens in the Sun where neutrinos are produced and then propagate through a medium of varying density. In this case the evolution of flavour eigenstates are not decoupled and in general, it is very difficult to find analytical solution to this problem. However some assumptions can be made : if density is not varying too fast, adiabatic transformation can be considered. This adiabacity condition is available in the Sun for a certain energy range.

Below this energy range, about a few MeV, the vacuum oscillations are recovered. If energy and density conditions are fulfilled, an interesting case of the adiabatic matter resonance appears. A neutrino produced in the center of the Sun in the flavour eigenstate ν_e will be guided to the surface by that resonant adiabicity condition which modifies the oscillation to a propagation eigenstate ν_1, or ν_2, with the probability $cos^2\theta_{\rm M}$, or $sin^2\theta_{\rm M}$. The oscillation wavelength has to be small with respect to the propagation length i.e. the Sun radius. Detailed calculation can be found in reference [25]. In the extreme case of a matter effect dominance $sin^2\theta_{\rm M} \approx 1$, ν_e's will leave the Sun in the ν_2 eigenstate which is composed by the 3 flavours of neutrinos approximately in equal fractions as shown in the figure 1.1 : the ν_e quantity on Earth is suppressed without considering the oscillation in vacuum between the Sun and the Earth. In a realistic case, solar neutrinos will reach the Earth in the propagation states ν_1 and ν_2. The measured ν_e flux on Earth could be affected by this MSW effect and both solar neutrino experiments sensitive to all flavours and accelerator experiments producing high energy neutrinos could investigate this phenomenon.

1.2 Other Properties

1.2.1 Helicity

First, if one assumes a fermion, i.e. a neutrino, it can be described by the Dirac equation :

$$H\psi = (\overrightarrow{\alpha} \cdot \overrightarrow{p} + \beta m)\psi \tag{1.18}$$

Considering neutrino has a zero mass, it gives two decoupled equations for two-component spinors $\chi(p)$ and $\Phi(p)$:

$$E\chi = -\overrightarrow{\sigma} \cdot \overrightarrow{p}\chi$$
$$E\Phi = +\overrightarrow{\sigma} \cdot \overrightarrow{p}\Phi \tag{1.19}$$

where σ are 2×2 Pauli matrices. Each of these equations has respectively a solution which describe a particle with a positive energy and a negative helicity $\lambda = -\frac{1}{2}$ for the first one : a left-handed neutrino $\nu_{\rm L}$ and an antiparticle with a negative energy and a positive helicity $\lambda = +\frac{1}{2}$ for the second one : a right-handed antineutrino $\overline{\nu_{\rm R}}$. As far as neutrino interacts only by weak current exchange and that current is of the Vector - Axial vector (V-A) form, only left-handed neutrino and right-handed antineutrino respectively can exist. If neutrino mass is not strictly zero, a Lorentz transformation would turn a $\nu_{\rm L}$ into a $\nu_{\rm R}$ and the assertion that only $\nu_{\rm L}$ exists in nature cannot be made.

1.2.2 Neutrino mass

Previous section showed that the neutrino oscillation are a well-established phenomenon and proves experimentally that neutrinos are massive. It becomes interesting to look how theory will give a mass to the neutrino. The oscillation formalism described in section 1.1.2 and the helicity considerations presented in section 1.2.1 showed that left-handed flavour eigenstates can be expressed as left-handed mass eigenstates :

$$|\nu_\alpha^{\mathrm{L}}\rangle = \sum_{k=1}^{n} U_{\alpha k}^* \, |\nu_k^{\mathrm{L}}\rangle \tag{1.20}$$

Different mass generation mechanisms can be considered [18] as shown in the following sections.

1.2.2.1 Dirac mass term

As it has been already discussed, the SM does not predict the neutrino mass. Expressing the Lagrangian, the mass generation of the neutrino has to be formulated by introducing a new term called the Dirac mass term :

$$\mathcal{L}_{\mathrm{Dirac}} = -m_{\mathrm{D}}\overline{\nu_{\mathrm{L}}}\nu_{\mathrm{R}} + \mathrm{h.c.} \tag{1.21}$$

where ν_{L} and ν_{R} are triplets of left-handed and right-handed neutrino mass eigenstates respectively.

Note that this term connects right and left parts then it is invariant under $U(1)$ symmetry : $\nu_{\mathrm{L}} \to e^{i\alpha}\nu_{\mathrm{L}}$ which implies that the total lepton number is conserved.

1.2.2.2 Majorana mass term

As neutrino is a neutral particle, it could be a Majorana particle i.e. neutrino could be its own antiparticle. According to that assumption, the SM Lagrangian should be modified by adding :

$$\mathcal{L}_{\mathrm{Majorana}}^{\mathrm{L}} = -\frac{1}{2}m_{\mathrm{L}}\nu_{\mathrm{L}}^{\mathrm{T}}C\nu_{\mathrm{L}} + \mathrm{h.c.} \tag{1.22}$$

where C is the charge conjugation operator.

Considering this Majorana mass term, it is not anymore invariant under $U(1)$ symmetry and the total lepton number is consequently violated by $|\Delta L| = 2$. Processes like double-β decay are therefore allowed.

If the neutrino is a truly Majorana particle which means $\nu_{\mathrm{M}}^{\mathrm{C}} = \nu_{\mathrm{M}}$, where ν_{M} stands for Majorana neutrino, and in general $\nu_{\mathrm{M}}^{\mathrm{C}} = e^{i\alpha}\nu_{\mathrm{M}}$, one can express in terms of chiral components :

$$\nu_{\mathrm{M}} = \nu_{\mathrm{L}} + e^{-i\alpha}\nu_{\mathrm{L}}^{\mathrm{C}} \tag{1.23}$$

From equation 1.22 the Majorana Lagrangian term becomes :

$$\mathcal{L}_{\mathrm{Majorana}}^{\mathrm{L}} = -\frac{1}{2}m_{\mathrm{M}}\overline{\nu_{\mathrm{M}}}\nu_{\mathrm{M}} \tag{1.24}$$

where the Majorana phase has just been attached to the mass.

The previous section explained that a right component can exist through the Dirac mass term, one can introduce Majorana mass terms acting on the right-handed neutrino :

$$\mathcal{L}_{\mathrm{Majorana}}^{\mathrm{R}} = -\frac{1}{2}M_{\mathrm{R}}\nu_{\mathrm{R}}^{\mathrm{T}}C\nu_{\mathrm{R}} + \mathrm{h.c.} \tag{1.25}$$

It is interesting to notice that electroweak symmetry is not broken since this mass term links two right-handed neutrinos. Same as for the Majorana mass term for left-handed neutrinos, the lepton flavour symmetry is broken $|\Delta L| = 2$ with the same consequences of the previous case.

1.2.2.3 Dirac + Majorana

Considering all these different Lagrangians and that both right and left helicities exist for the neutrino, one can write a general mass Lagrangian with the mass term expressed in the $(\nu_{\mathrm{L}}, \nu_{\mathrm{R}}^{\mathrm{C}})$ basis :

$$\begin{aligned}\mathcal{L}_{\mathrm{mass}} &= \mathcal{L}_{\mathrm{Dirac}} + \mathcal{L}_{\mathrm{Majorana}}^{\mathrm{L}} + \mathcal{L}_{\mathrm{Majorana}}^{\mathrm{R}} \\ &= -\frac{1}{2}\overline{\nu}\begin{pmatrix} m_{\mathrm{L}} & m_{\mathrm{D}} \\ m_{\mathrm{D}}^{\mathrm{T}} & M_{\mathrm{R}} \end{pmatrix}\nu^{\mathrm{C}} + \mathrm{h.c.}\end{aligned} \tag{1.26}$$

In conclusion, the neutrino mass is hereby generally expressed. However the neutrino nature, Majorana or Dirac, is not yet determined. Observation of a double-β decay with neutrinos emission could stand for the Dirac nature. On the contrary, double-β decay without neutrinos emission could stand for the Majorana nature. Moreover this would be also the first proof of lepton flavour symmetry breaking. Apart from these considerations, the form of the mass term matrix is not yet known, several limits can however be scrutinized :

- $m_{\mathrm{L}} = M_{\mathrm{R}} = 0$ corresponds to a Dirac neutrino which is strangely comparable to two Majorana neutrinos with equal masses of opposite sign.
- $(m_{\mathrm{L}} = M_{\mathrm{R}}) \ll m_{\mathrm{D}}$ corresponds to a pseudo-Dirac neutrino.
- $M_{\mathrm{R}} \gg m_{\mathrm{D}}$ corresponds to the see-saw mechanism describes in appendix C.2

1.2.2.4 Experimental constraints on the neutrino mass

There are different sources of experimental constraints on the neutrino mass : from cosmology, from astrophysics, from accelerator physics and from neutrino physics.

– Cosmology constraints

In the early universe, neutrinos were in equilibrium with the primordial plasma. As the universe expanded, the rate of interactions decreased leading to the decoupling, first, of neutrinos followed by photons. The temperature of neutrinos at that time can be inferred from the photon temperature determined precisely thanks to the Cosmological Microwave Background (CMB). From their temperature, one can derive the present contribution to the universe energy density that is constrained by astronomical data. This constraint is transformed into a bound on the sum of the neutrino masses. Furthermore, since neutrinos were relativistic at the time of decoupling, they must have suppressed the formation of small scale structures but participated to clustering on large scales resulting in changes in the matter power spectrum. The heavier the neutrino masses, the more pronounced the effect. Consequently, a constraint on the neutrinos masses can be derived from the survey of the angular matter power distribution and particularly of large scale structures, i.e. the galaxy distribution. The combination of WMAP, CBI, ACBAR (CMB experiments) and 2dFGRS (galaxy survey) yields at 95% C.L. [26] :

$$\sum m_\nu < 0.24 \text{ eV for a single massive neutrino.} \qquad (1.27)$$

$$\sum m_\nu < 0.71 \text{ eV for 3 degenerate massive neutrinos.}$$

This limit is definitely low with respect to the others but the early universe description is strongly model dependant.

– Astrophysics constraint

The famous supernova SN1987A offered the opportunity to detect supernova neutrinos and given the tremendous baseline and measuring the time of flight from :

$$\Delta t[\text{ms}] = 5.15 \left(\frac{m_\nu}{1\text{eV}}\right)^2 \left(\frac{10\text{MeV}}{E^2}\right) \frac{D}{10\,\text{kpc}} \qquad (1.28)$$

it allows to put a constraint on the neutrino mass at 95% C.L. :

$$m_\nu < 5.8\,\text{eV} \qquad (1.29)$$

– Accelerator physics constraints

One can evaluate an upper limit on the neutrino mass for each flavour by knowing the kinematics of different particle decays :

$$
\begin{aligned}
m_{\nu_e} &< 2 \times 10^{-6} \text{ MeV} && \text{from the tritium decay} && (1.30)\\
m_{\nu_\mu} &< 0.19 \text{ MeV} && \text{from the pion decay} \\
m_{\nu_\tau} &< 18.2 \text{ MeV} && \text{from the tau decay}
\end{aligned}
$$

– Neutrino physics

Finally, neutrino physics experiments probing the oscillation parameters measure the squared masses differences and one of the lastest fit [27] gives :

$$|\Delta m^2| = 2.43^{+0.23}_{-0.28} \times 10^{-3} \text{ eV}^2 \qquad (1.31)$$
$$\delta m^2 = 7.54^{+0.64}_{-0.55} \times 10^{-5} \text{ eV}^2$$

A simple observation on this experimental result is that only the solar mass difference $\delta m^2 = m_1^2 - m_2^2 = \Delta m_{\text{sol}}^2$ is fully known, the sign has been determined thanks to MSW effect on solar neutrinos.

The atmospheric mass difference, defined by $\Delta m^2 = m_1^2 - m_3^2 = \Delta m_{\text{atm}}^2$, has been measured without a hint about the sign. So the ordering of mass eigenstates on an absolute mass scale is not yet defined : this is the problem of mass hierarchy. Nevertheless, the situation can be summarized by stating on the lightest neutrino which lets only 2 possibilities summarized on figure 1.1 the Normal Hierarchy (NH) or the Inverse Hierarchy (IH) :
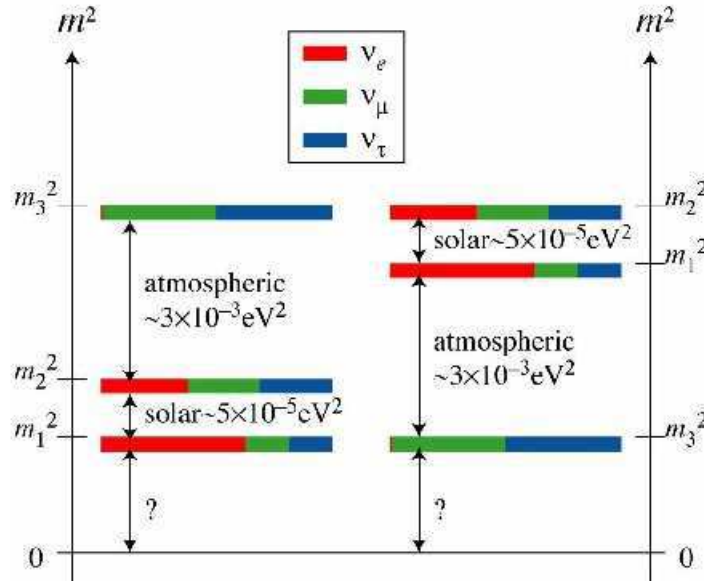
Figure 1.1: Mass splitting in the neutrino sector. Left : NH. Right : IH. [28]

In the future, several experiments will try to lower this limit on the neutrino mass and may find the actual value of this mass. Among these experiments, one can distinguish the β-decay experiments like KATRIN [29] and the neutrinoless double β-decay experiments like SuperNemo [30]. Their principles are described in appendices C.3 and C.4.

1.3   Experimental Status Of Neutrino Oscillation

An important part of the neutrino physics, in which the OPERA experiment takes part, consists in measuring all parameters driving the oscillation phenomenon described in section 1.1.4. We quickly determined the mixing angles, and consequently squared masses differences, in the solar and in the atmospheric sectors because of the abundance of neutrino sources and because of the relatively large value of these parameters. In 2009, θ_{13} which is the coupling between the two oscillation regimes, was not measured and the limit put by nuclear reactor experiments described in the following was compatible with a zero value meaning that a two flavours oscillation scheme was a possibility. In addition, the measurement of CP phase and the other parameters would be significantly affected depending on the large, small or zero value of θ_{13}.

The best limit was put by the CHOOZ experiment at 90% C.L. [17] :

$$sin^2 2\theta_{13} < 0.1 \tag{1.32}$$

CHOOZ measured the $\overline{\nu_e}$ flux produced by the nuclear power plant with a liquid scintillator detector at 1km from the reactor trying to observe a deficit in this neutrino rate with respect to the expected flux produced by the nuclear reactor.

Meanwhile, the other mixing angles and squared masses differences were quite well fitted. According to the global analysis [31], the solar and reactor parameters, θ_{12} and δm^2 were fitted with data from GALLEX, SNO, KamLAND and Borexino :

$$\delta m^2 = 7.67^{+0.52}_{-0.53} \times 10^{-5} \text{ eV}^2 \tag{1.33}$$
$$sin^2 \theta_{12} = 0.312^{+0.063}_{-0.049}$$

GALLEX was a Homestake-like experiment but using gallium instead of chlorine in the LNGS from 1991 to 1997. SNO was a water Cerenkov detector filled with heavy water instead of normal water and was sensitive to all flavours of solar neutrinos and to neutral current interactions as well ; data acquisition started in 1999 and ended in 2006. KamLAND is an experiment which was detecting $\overline{\nu_e}$ from several nuclear reactors but since the baseline was long, for neutrinos at higher energies, the solar sector was also probed by KamLAND using a liquid scintillator detector. Note these data are compatible with neutrino oscillation predictions corrected by the MSW effect mentioned in section 1.1.5.2. Finally, Borexino is a liquid scintillator detector located in the LNGS and measuring sub-MeV solar neutrinos ; it started to acquire data since 2007 and is still on going.

Similarly the atmospheric sector is driven by Δm^2 and $sin^2\theta_{23}$ and these parameters were determined in 2009 [31] within 1σ :

$$\Delta m^2 = 2.39^{+0.11}_{-0.08} \times 10^{-3} \text{ eV}^2 \tag{1.34}$$
$$sin^2\theta_{23} = 0.466^{+0.073}_{-0.058}$$

with data from atmospheric neutrinos experiments like SuperKamiokande (SK) and from Long BaseLine (LBL) experiments like KEK To Kamioka (K2K) and MINOS. Note that the squared masses difference is much larger than in the solar sector which indicates two different oscillation regimes.

This picture being incomplete, several experiments dedicated to measure the undetermined mixing angle θ_{13} were to be built in 2009. On the one hand, LBL experiments like T2K in Japan which aims to measure the appearance of ν_e into a beam of ν_μ with the SuperKamiokande detector placed 295km away from the neutrino source. On the other hand, nuclear power plant experiments like Double Chooz in France, Daya Bay in China and Reno in Korea based on the same principle of the CHOOZ experiment but adding a detector to compare fluxes at near position and far position to reduce the neutrino flux prediction uncertainties.

At the beginning of summer 2012, these experiments published their results and completed the oscillation picture by measuring the value of θ_{13} :

$$\begin{aligned} sin^2 2\theta_{13} &= 0.092 \pm 0.016(\text{stat}) \pm 0.005(\text{syst}) & \text{Daya Bay [32]} & \quad (1.35) \\ sin^2 2\theta_{13} &= 0.113 \pm 0.013(\text{stat}) \pm 0.019(\text{syst}) & \text{RENO [33]} \\ sin^2 2\theta_{13} &= 0.086 \pm 0.041(\text{stat}) \pm 0.030(\text{syst}) & \text{Double Chooz [34]} \\ sin^2 2\theta_{13} &= 0.104^{+0.060}_{-0.045} & \text{T2K [35]} \end{aligned}$$

First, Daya Bay and RENO exclude the zero value of θ_{13} with a large significance. The different results of these experiments are compatible with each others. But these experiments are only sensitive to the reactor sector whereas some others will be sensitive to the solar or atmospheric ones. A global analysis [27] is required to combine all experimental results to probe the full parameters space drawn by (δm^2, $\pm\Delta m^2$, θ_{12}, θ_{13}, θ_{23}, δ). However, experiments have to be grouped with respect to their impact on the parameters of the U_{MNSP} matrix.

First group corresponds to LBL plus solar plus KamLAND data. LBL experiments are dominantly driven by Δm^2 with an amplitude $cos^2\theta_{13}sin^2\theta_{23}(1 - cos^2\theta_{13}sin^2\theta_{23})$ for the $\nu_\mu \rightarrow \nu_\mu$ disappearance channel and with an amplitude $cos^2\theta_{13}sin^2\theta_{13}sin^2\theta_{23}$ for the $\nu_\mu \rightarrow \nu_e$ appearance channel. LBL data used come from experiments already described earlier in the previous global analysis and adding new results of MINOS in ν_μ (and $\overline{\nu_\mu}$) disappearance as well as updates in appearance mode. Recent T2K results disappearance and appearance in its ν_e beam are also added. These channels will be analyzed in the same time in a 3ν oscillation framework with solar and KamLAND data in addition to constrain independantly (δm^2, θ_{12}, θ_{13}).

The second group adds to the first one the Short BaseLine (SBL) data of CHOOZ, Double Chooz, Daya Bay and RENO described earlier in this section which are dominantly driven by Δm^2 with an amplitude $sin^2\theta_{13}cos^2\theta_{13}$.

The third group adds to the second one atmospheric neutrino data from SK which are dominantly driven by Δm^2 and θ_{23}.

The mixing parameters thus fitted by this global analysis are summarized below with their 1σ error in table 1.1.

Parameter	Best fit $\pm 1\sigma$ error
$\delta m^2/10^{-5}\,\text{eV}^2$ (NH or IH)	$7.54^{+0.26}_{-0.22}$
$sin^2\theta_{12}$ (NH or IH)	$0.307^{+0.018}_{-0.016}$
$\Delta m^2/10^{-3}\,\text{eV}^2$ (NH) $\Delta m^2/10^{-3}\,\text{eV}^2$ (IH)	$2.43^{+0.06}_{-0.10}$ $2.42^{+0.07}_{-0.11}$
$sin^2\theta_{13}/10^{-2}$ (NH) $sin^2\theta_{13}/10^{-2}$ (IH)	2.41 ± 0.25 $2.44^{+0.23}_{-0.25}$
$sin^2\theta_{23}$ (NH) $sin^2\theta_{23}$ (IH)	$0.386^{+0.024}_{-0.021}$ $0.392^{+0.039}_{-0.022}$
δ/π (NH) δ/π (IH)	$1.08^{+0.28}_{-0.31}$ $1.09^{+0.38}_{-0.26}$

Table 1.1: Result of the global 3ν oscillation analysis for the 3ν mass-mixing parameters in the NH or IH picture.

It is now clear that the picture is a 3-flavours oscillation since θ_{13} is not compatible with zero anymore. Actually its value is large and allows to put a limit on the CP violation phase which seems more likely about π as shown on figure 1.2. The LBL+solar+KamLAND data fit allows large range of θ_{13} value, SBL experiments results strongly narrow the allowed region and finally the addition of atmospheric data makes the δ value π emerge within 1σ error. In the 2σ contour, all δ values are allowed. The situation is approximately similar in IH as in NH.
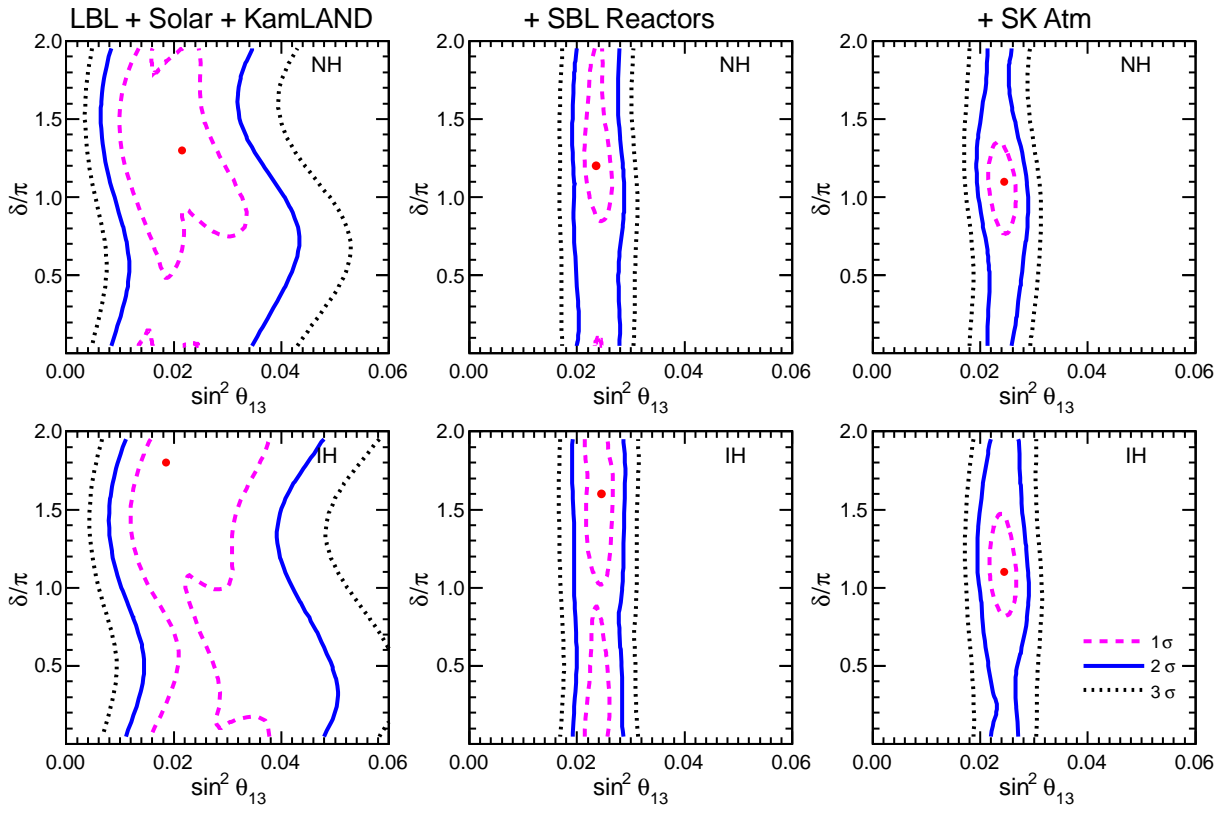
Figure 1.2: Results of the global analysis of neutrino masses, mixings and phases in the plane charted by ($sin^2\theta_{13}$, δ), all other parameters being marginalized away. From left to right, the regions allowed at 1, 2 and 3σ refer to increasingly rich datasets: LBL+solar+KamLAND data (left panels), plus SBL reactor data (middle panels), plus SK atmospheric data (right panels). A preference emerges for δ values around π in both normal hierarchy (NH, upper panels) and inverted hierarchy (IH, lower panels)[27].

In figure 1.3, the first group of data shows a degeneracy for θ_{23} between the first ($0 \leq \theta \leq \frac{\pi}{4}$) or the second octant ($\frac{\pi}{4} \leq \theta \leq \frac{\pi}{2}$) value. The SBL data lift the degeneracy, at least within 1σ, by constraining θ_{13}. In IH, T2K and MINOS allow larger values of θ_{13} and so the degeneracy is not lifted. SK data validate the preference to the first octant for θ_{23}.

The value of θ_{23} within 1σ which was $43.1°\,^{+4.2°}_{-3.4°}$ in the former global analysis and is now down to $38.4°\,^{+1.4°}_{-1.2°}$. This modification between the previous and present value of θ_{23} is important since it affects the oscillation probability and the expected neutrino rates by about 20% in the $\nu_\mu \rightarrow \nu_e$ oscillation study in OPERA.

cs
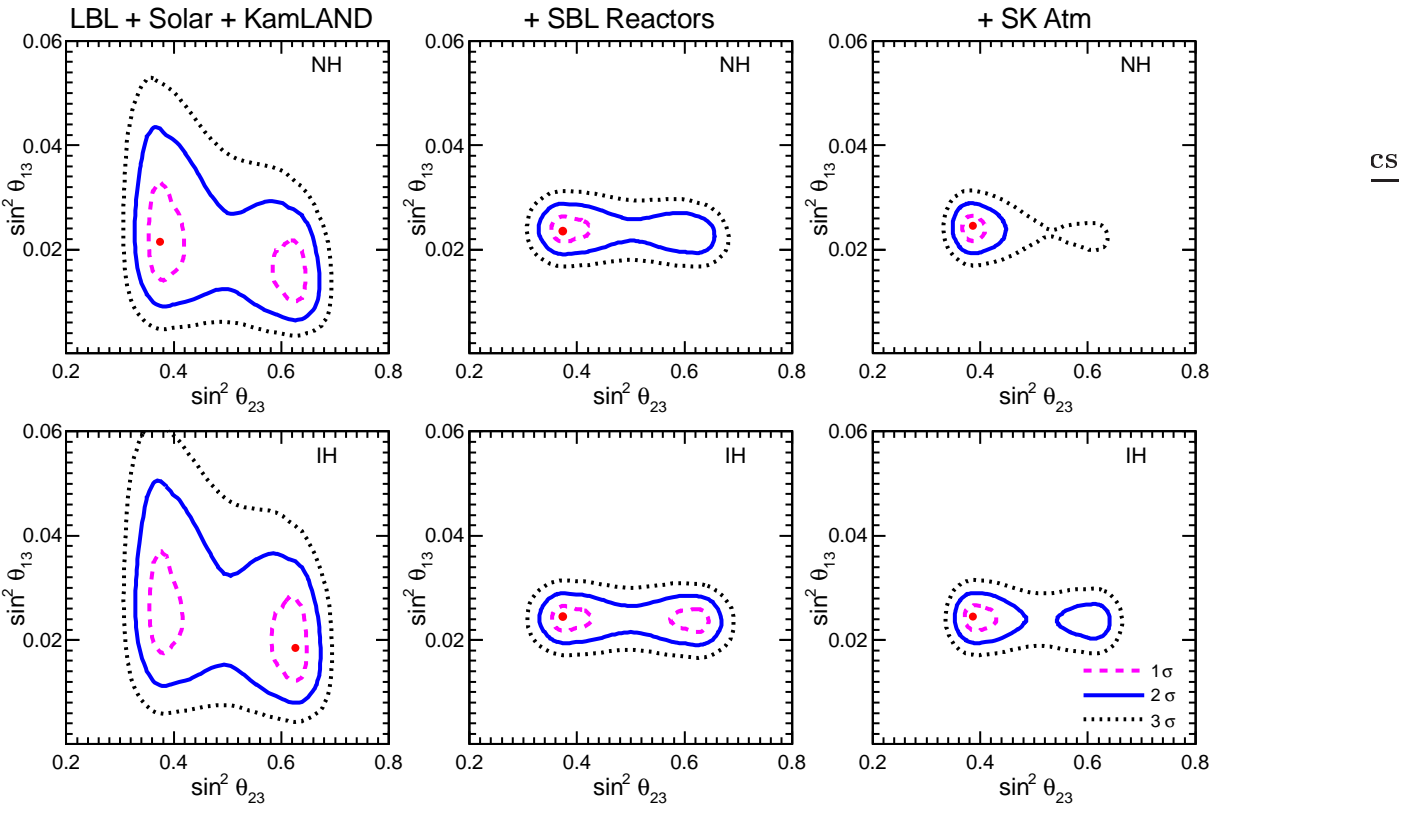
Figure 1.3: Results of the global analysis of neutrino masses, mixings and phases in the plane charted by ($sin^2\theta_{13}$, $sin^2\theta_{23}$), all other parameters being marginalized away. From left to right, the regions allowed at 1, 2 and 3σ refer to increasingly rich datasets: LBL+solar+KamLAND data (left panels), plus SBL reactor data (middle panels), plus SK atmospheric data (right panels). Best fits are marked by dots. A preference emerges for θ_{23} in the first octant $[0, \frac{\pi}{4}]$ in both normal hierarchy (NH, upper panels) and inverted hierarchy (IH, lower panels)[27].

Finally, there is a summary of all mixing parameters determined by this new global analysis illustrated by the figure 1.4. The distributions of squared masses differences, $sin^2\theta_{12}$ and $sin^2\theta_{13}$ are linear and symmetrical which means their distributions are Gaussian, moreover there is none or small variations between NH and IH. $sin^2\theta_{23}$ is skewed towards the first octant and δ is highly non Gaussian and gives no constrain above 2σ.
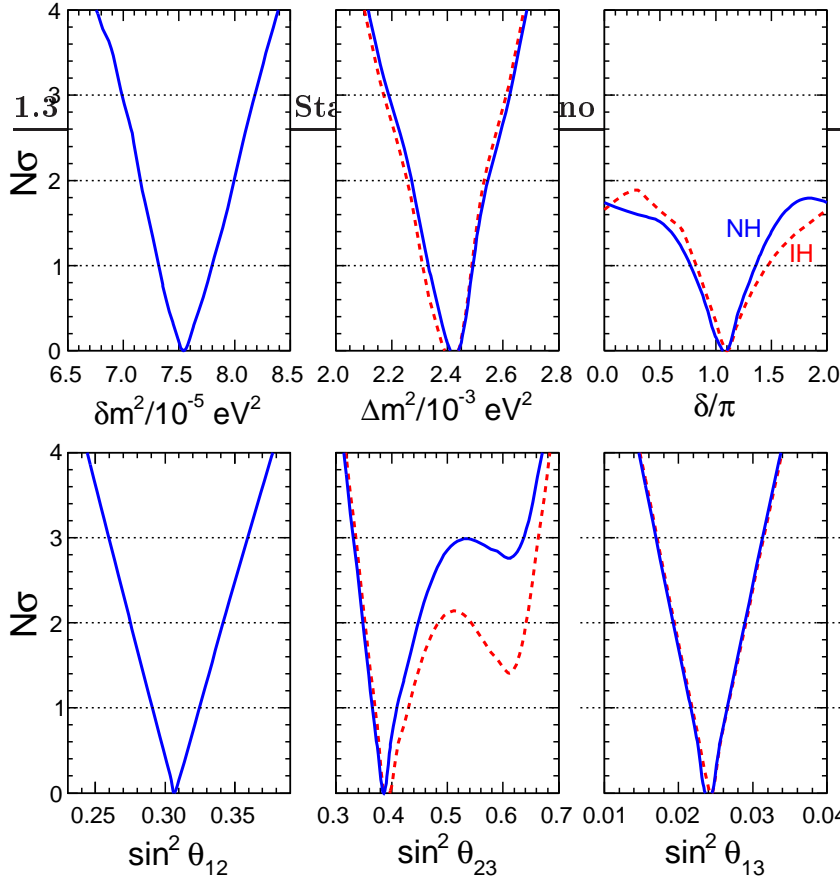
Figure 1.4: Data used are the same as in 2009 adding T2K, Daya Bay, Reno and Double Chooz results [27].

In this chapter, the theoretical and experimental neutrino physics pictures have been drawn. The oscillation principle, its formalism in the 2ν and 3ν framework in the vacuum as well as in matter have been described. Other properties, i.e. helicity and mass, have been also studied ; a brief experimental status reported about the different constraints on the neutrino mass. Finally an experimental status of neutrino oscillation has been given and more specifically the recent evolution in the oscillation results between 2009 and nowadays. Indeed, the 2ν framework has been significantly excluded by reactor experiments in 2012 as well as they have measured the mixing angle θ_{13}. A global analysis of the mixing parameters emphasize the ambiguity for $sin^2(\theta_{23})$ to be in the first octant or in the second one and a preference for the CP phase δ for π.

In this present context, the contribution of OPERA is still to validate the oscillation in the atmospheric sector in the appearance mode and provide result in order to confirm the first-octant value of θ_{23}. About θ_{13}, by measuring $\nu_\mu \rightarrow \nu_e$ oscillation, OPERA can also confirm the above mentioned results.

Chapter 2

The OPERA Experiment

OPERA [36] is a long-baseline neutrino experiment located at the Gran Sasso Laboratory in Italy, 730 km from Centre Européen pour la Recherche Nucléaire (CERN), downstream in the CERN Neutrinos to Gran Sasso (CNGS) neutrino beam. The OPERA experiment is designed and optimised for a direct appearance search of $\nu_\mu \rightarrow \nu_\tau$ oscillations in the parameter region indicated by Super-Kamiokande [15] to explain the zenithal angle dependence of the atmospheric neutrino deficit. It detects the ν_τ Charged Current (CC) interactions in an almost pure muon neutrino beam produced at the CNGS. In addition to $\nu_\mu \rightarrow \nu_\tau$ oscillations, the OPERA detector will also be searching for $\nu_\mu \rightarrow \nu_e$ oscillations thanks to its electron identification capability. OPERA is a large detector made of a VETO plane followed by two identical Super-Module (SMod) each consisting of a target section and a muon spectrometer. The Emulsion Cloud Chamber (ECC), a part of the target section, is made of a modular structure called the "brick" : a sandwich of passive material plates of lead interspaced with emulsion layers. By assembling a large quantity of such modules, it has been possible to conceive and realize 1.25 kt fine-grained vertex detector optimized for the study of ν_τ appearance. The walls of bricks are alternated with scintillator detectors called Target Tracker (TT) for event location. The target part is completed with magnetised iron spectrometers for muon charge and momentum measurements. Finally, two automated systems called Brick Manipulating System (BMS) have been built in order to insert bricks during the construction phase of the detector and extract them once a neutrino interaction is located during the physics runs. Each part described above will be detailed in the following sections starting with the CNGS beam. In addition, the description of the neutrino interaction and the expected rates in the OPERA target will be given. The detection of the interactions in a brick, the scanning and the analysis process will be described and the efficiency of each step will be assessed.

2.1   The CNGS Beamline Description

The CNGS [37] neutrino beam was optimized for ν_τ appearance in the parameter region indicated by the atmospheric neutrino experiments. A topological description of the OPERA experiment including the CNGS beam is given in the figure 2.1.
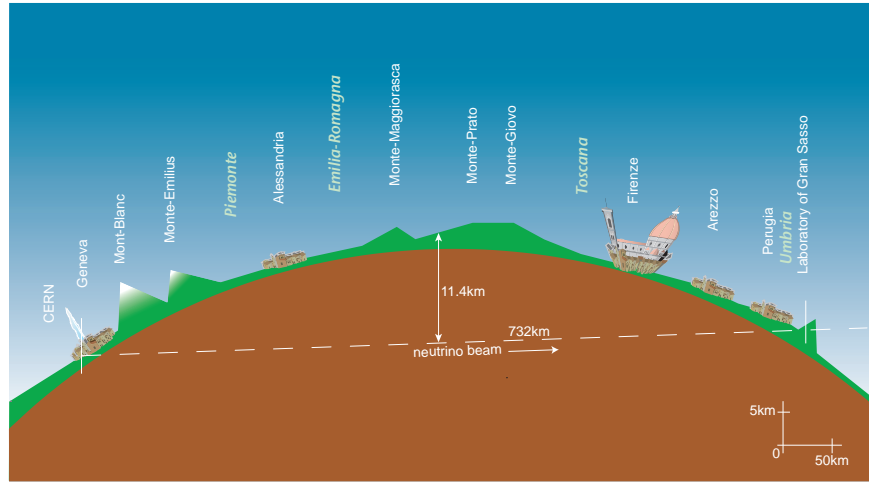
Figure 2.1: The OPERA baseline [38].

The CNGS beamline starts with the Linac which accelerates protons to an energy of 50 MeV. These protons are injected to the Booster acquiring an energy of 1.5 GeV. Then, they are sent to the Proton Synchrotron (PS) where they reach an energy of 14 GeV before they are transferred to the Super Proton Synchrotron (SPS). Finally, the protons reach their final energy of 400 GeV. The schematic view of the accelerator complex of CERN is shown in figure 2.2.
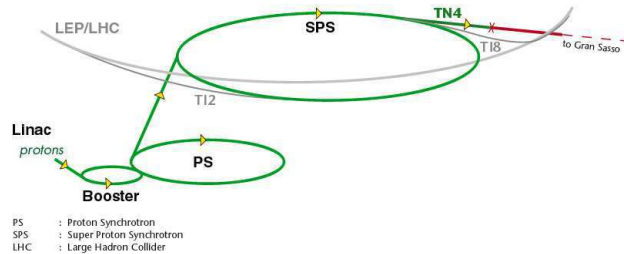
Figure 2.2: The CERN proton accelerators used for the CNGS [38].

Two bunches of 400 GeV protons are extracted from the CERN SPS in a 6 s cycle. Each bunch is obtained in a $10.5\,\mu$s short pulse with nominal intensity of 2.4×10^{13} protons on target (p.o.t.) per pulse. The proton beam is transported through the transfer line TT41 to the CNGS target T40 [38]. The target consists of series of thin graphite rods cooled with helium. Secondary pions and kaons of positive charge produced in the target are focused into a parallel beam by a system of two magnetic lenses, called horn and reflector. A 1000 m long decay tunnel allows the pions and kaons to decay into muon-neutrinos and muons. The remaining hadrons are absorbed by an iron beamdump. The muons are monitored by two sets of detectors downstream of the dump, where the muon intensity, the beam profile and its centre are measured. Further downstream, the muons are absorbed in the rock while neutrinos continue to travel towards the LNGS.

Regarding to the beam parameters, the average neutrino energy at the LNGS location is about 17 GeV. The $\overline{\nu_\mu}$ contamination is about 2.1%. The ν_e and $\overline{\nu_e}$ contaminations are lower than 1% while the number of prompt ν_τ from D_S decay is negligible. The average $\frac{L}{E_\nu}$ ratio is $43\,\mathrm{km.GeV^{-1}}$. Due to the Earth's curvature, neutrinos from CERN enter the LNGS halls with an angle of 0.0585 rad with respect to the vertical plane.

The diameter of the beam in the LNGS is about 2 km [39] and the beam intensity is uniform along X and Y axis of the detector.
The CNGS beamline setup is shown in figure 2.3 and the main features of the beam are summarized in table 2.1.
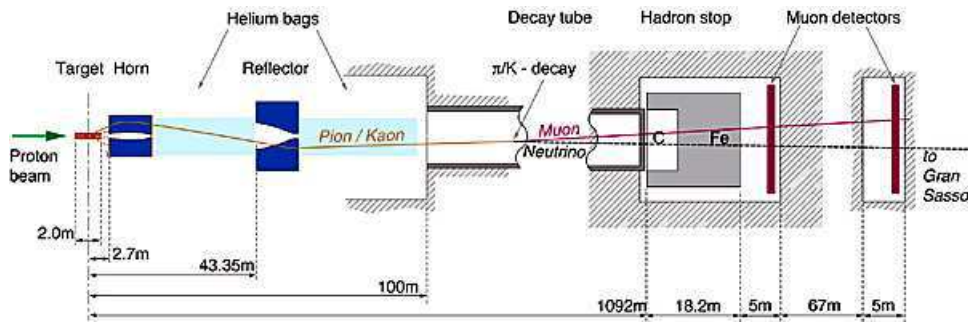
Figure 2.3: Main components of the CNGS beamline [38].

L	730 km
$\langle E \rangle$	17 GeV
$L / \langle E_\nu \rangle$	43 GeV/km
$\nu_e + \overline{\nu_e} / \nu_\mu$	0.87%
$\overline{\nu_\mu} / \nu_\mu$	2.1%
ν_τ prompt	negligible

Table 2.1: The CNGS neutrino beam features [36].

2.2 The Experimental Setup

The OPERA detector located in hall C of the LNGS in Italy, beneath 1400 m of rock which reduces the muon flux by a factor 10^{-7} to $1\,\mu/\mathrm{m^2/h}$ [36], combines Emulsion Cloud Chambers (ECC) with electronic detectors. This combination is also called the "hybrid" structure. VETO planes are located at the upstream part of the detector and aim to identify muons incoming the detector. The target part is composed of 31 walls per SMod, because of emulsion shortage only 27 walls are filled. Each wall contains one layer of ECC bricks and a second layer of TT scintillators. Each brick wall is composed of 64 rows and 52 columns and only 56 rows are filled with 52 bricks.

These bricks are composed of a stack of 56 layers of lead with a thickness of 1 mm, interleaved with $43\,\mu$m thick emulsion layers on both sides of a $205\,\mu$m thick plastic base. These bricks are inserted into brick walls with the help of the BMS robots. A Changeable Sheet doublet (CSd) [40] is independently packed and placed downstream of each brick. In addition, SMod is equipped with a spectrometer to measure the charge and momentum of charged particles. Detailed description of these parts is given in the following sections and can be seen in figure 2.4.
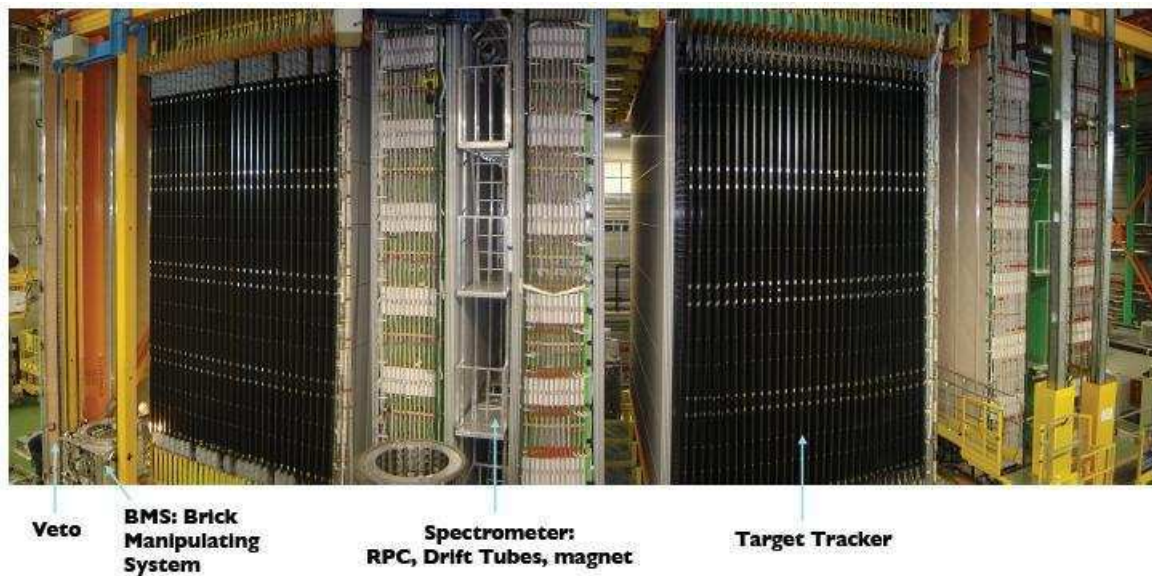
Figure 2.4: A picture of the OPERA detector. The Super-Module (SMod)s are composed of a lead target combined with a scintillator target tracker and an electronic muon spectrometer.

2.2.1   The OPERA films

In order to produce emulsion plates in large-scale applications, an R&D project was carried out between the Fuji-Film company and Nagoya University in Japan [41]. A target mass of 1 kt requires an area of emulsion sheets having the order of $100\,000\,\mathrm{m}^2$. Because the production of this amount of films by hand is not possible, Fuji Film company has used some commercial machines in order to avoid time consuming production. The cross section view of the OPERA emulsion film is shown in figure 2.5.
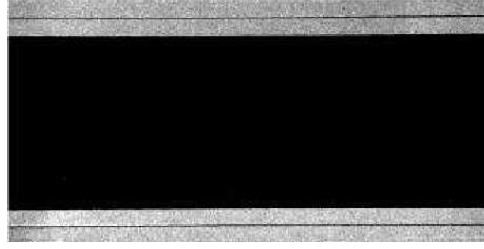
Figure 2.5: A cross section view of the machine-coated OPERA film [41].

The emulsion sheet has been processed by pouring emulsion gel, containing embedded silver halide crystals, on plastic plates and drying them in climate-controlled room. The thickness of the plastic base is $205\,\mu$m. Emulsion gel has been spread out on both sides of the base material. The black lines, displayed in figure 2.5 in the middle of the emulsion layers, are protection coats with thickness of $1\,\mu$m. The OPERA emulsion layers are $43\,\mu$m thick.

With the usage of the machine coating system, a layer was generated automatically on the emulsion film surface. The aim of that layer is to protect the active layer of the coated gel from any kind of mechanical effects. It also allows to avoid extra cleaning procedure for the emulsion films being exposed to lead radioactivity inside ECC. The emulsion films get some spots after being in contact with lead. More detailed information about the lead induced effects inside the ECC brick is given by reference [42]. These spots are called fog. They can be erased with a refreshing procedure. The OPERA emulsions are refreshed by applying high humidity and high temperature for 6 days. The remaining fog level for the films after refreshing process is 5 grains/$1000\,\mu$m^3.

2.2.2 The Emulsion Cloud Chamber

The main components of the ECC are lead, 1mm thick, and emulsion films. The choice of lead has been driven by its high density and its short radiation length allowing an optimization of the neutrino interaction rates and the momentum measurement by Multiple Coulomb Scattering (MCS) respectively. The ECC brick has been made by the Brick Assembling Machine (BAM). The BAM assembled and produced the ECC bricks, weighting $8.3\,$kg, as a stack of 56 lead plates interleaved with 57 nuclear emulsion films. The transverse dimension of an ECC brick is $10.2\,$cm $\times$ $12.7\,$cm ; the thickness is $7.5\,$cm. This dimension corresponds to about $10X_0$ radiation lengths, enough to allow electron identification and to estimate the energy with a resolution of about 30% reported in section 4.3.2 via electromagnetic shower reconstruction in ECC and momentum measurements by Multiple Coulomb Scattering (MCS) with a resolution of about 30% reported in reference [43]. After the BAM produces the ECC brick, two additional emulsion films called Changeable Sheet doublet (CSd) are assembled and attached to the downstream face of each ECC brick. The CSd provides information when developed to confirm the finding of the ECC brick which contains the neutrino interaction vertex. The aim is to avoid wasted film handling and processing of the misidentified bricks. It is important because of the scanning overload of the ECC bricks [40].

2.2.3   The Changeable Sheet

Since the connection criteria between Target Tracker (TT) and the ECC bricks with respect to providing vertex localization inside the ECC is an important subject for the $\nu_\mu \to \nu_\tau$ oscillations, the CSd is used as an interface between TT detectors and the ECC bricks. The Changeable Sheet (CS) is composed of two nuclear emulsions packed in polyethylene-aluminium laminated envelope and installed inside a plastic box. The CSd are taped to the downstream side of the ECC brick. A sketch of the CSd localized between TT and the ECC brick is shown in figure 2.6.
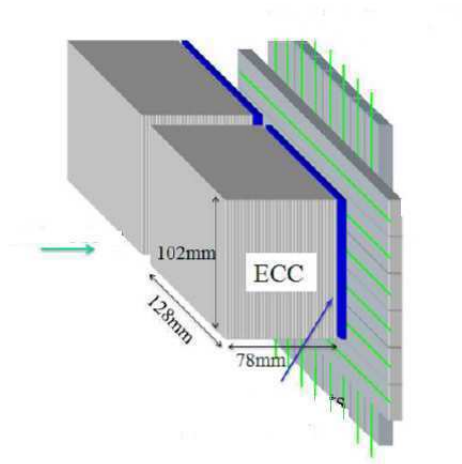
Figure 2.6: Sketch of ECC bricks associated with TT plane. The CSd in the blue box is attached to the downstream side of the ECC brick, so placed between the TT wall and the brick.

There are two goals of the CSd attached to the ECC bricks. The first one is to confirm the neutrino interaction signals obtained from TT detector, the other one is to find neutrino-related interactions for the ECC brick ScanBack (SB) analysis : CSd improve the location efficiency by 50%, in the 2009 data sample, 1.5 bricks are extracted per event.

2.2.4   The Target Tracker

The electronic TT following the brick walls are composed of two planes oriented along the X and Y axis respectively. These two planes are constituted by 4 modules of $6.7 \times 6.7\,\mathrm{m}^2$ sensitive edge-to-edge surface. A sketch of a target tracker plane is shown on the Left Hand Side (LHS) of figure 2.7.
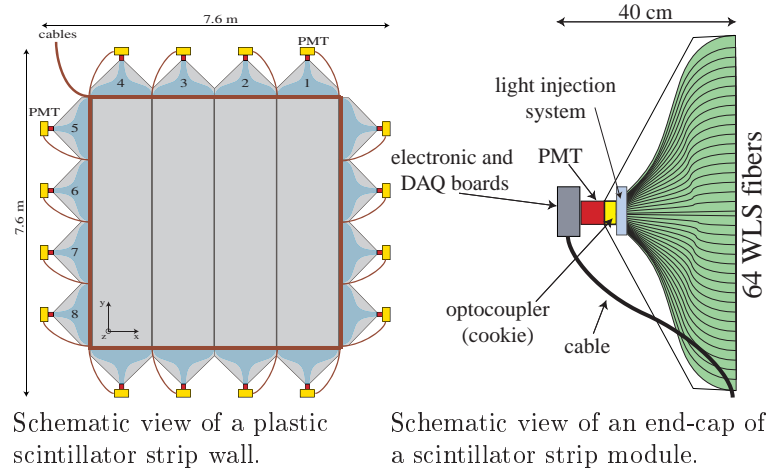
Figure 2.7: Main components of a TT wall of the OPERA detector [44].

A basic unit of the module consists of 64 strips, 26.3 mm wide and 10.6 mm thick, readout by Wave-Length Shifting (WLS) fibres coupled to two 64-pixels photodetectors. The two end-caps of each target tracker module play an important role ; they protect the WLS fibres emerging from the scintillating strips that are guided towards the input window of the multi-anode photomultipliers. In addition, they host the PhotoMultiplier (PM) tubes as well as the monitoring light injection system, the front-end electronic cards and the High Voltage (HV) power supplies. They also provide the mechanical structure by which the modules will be suspended on the OPERA detector. A sketch of the end-cap of a scintillator strip module can be seen on the Right Hand Side (RHS) of figure 2.7.

2.2.5   The Brick Manipulating System and brick handling

As already mentioned, the OPERA detector is located underground at the LNGS. Composed of about 150 000 ECC bricks, handling these bricks to different analysis sites needs several infrastructures : the Brick Manipulating System (BMS) to insert and extract the ECC from the detector, an X-ray marking machine to align the CSd with the ECC films, one underground film development laboratory for the CS to avoid their contamination with cosmic ray tracks, another film development laboratory on the surface level of the lab for the bricks. To handle the about 150 000 ECC bricks needed to reach an initial target mass of 1.25 kt two dedicated manipulators were developed and built to automatize the insertion and extraction of bricks to and from the detector : the BMS [45]. They are installed on each side of the detector, one BMS automaton takes care of the insertion and extraction in both SMod. It consists of the carousel part and the loading station. To keep track of the various activities of the insertion during the target filling, and the later extraction and reinsertion during the run of the experiment, a database is associated to track every brick and its history from the assembly until it is disassembled and scanned.

On the BMS platform where brick insertion and extraction take place, a carousel serves as an intermediate storage for 26 bricks, corresponding to the amount of bricks needed to fill one half-row of the OPERA target. It pushes the bricks inside the detector and to extract them, a small suction-vehicle can drive inside the target rows to catch the bricks. There is one loading station at each side of the detector. On this station a brick drum can be placed, hosting up to 234 bricks in nine rows. The brick drum can be quickly replaced to allow a continuous operation during the target filling and extraction of bricks with a possible neutrino interaction. The use of that drum avoids too many manipulations of the bricks to keep good alignment between plates, so that submicron resolution can be achieved. Each above mentioned part of the BMS can be seen on figure 2.8.
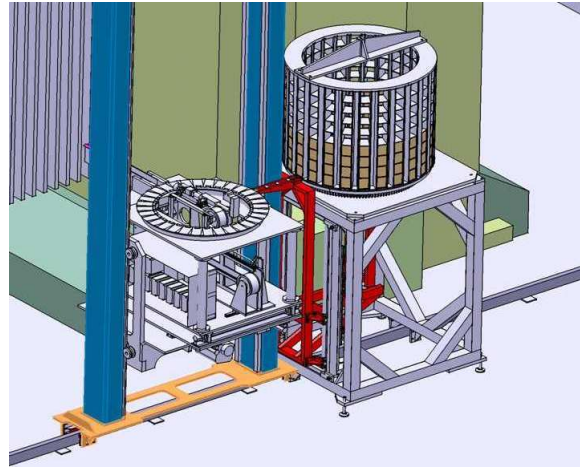
Figure 2.8: Overview over the BMS. On the left, the carousel is shown. On the right, the loading station with a half filled drum.

2.2.6 The Spectrometer

The two OPERA SMod are both equipped with a spectrometer. Each of those is composed of :

– A dipolar magnet : 2 iron layers with a gap of 1.0m in between. They are composed of 12 iron slabs each and 2 coils delivering a magnetic field of 1.55 T.

– A High Precision Tracker (HPT) : 3 groups of 4 planes of 8m-long vertical drift tubes ($\times 2$ SMod) placed in front, behind and in between the iron layers of the magnet. They measure the curvature of the charged particle trajectories from which the momentum is inferred. The spatial resolution of 0.5 mm of the HPT allows a momentum measurement with a resolution of about 20% for momenta < 50 GeV/c for charged particles coming from the CNGS direction [46].

– 22 Resistive Plate Chambers (RPC) planes per SMod are embedded in the magnet iron slabs : one RPC plane is made of 21 RPC units, arranged in a 3×7 matrix. Each RPC unit is sandwiched between two polypropilene layers with pickup copper strips with horizontal (35 mm pitch) and vertical orientation (26 mm pitch) [36]. RPC planes allow to generate the prompt signal to trigger the HPT. Apart of that,

another RPC plane is located between the target and the spectrometer just before the first drift tube plane. It is tilted by 45° to improve the resolution along the Y axis and resolve ambiguities in the track spatial reconstruction : this RPC plane is called XPC.

High energy charged particles produced in neutrino interactions can reach the spectrometers. The RPC planes inside the magnets will provide the spatial resolution necessary to use MCS together with the bending of the track in the magnetic field to measure the momentum with high precision. The deviation of the charged particles in the magnetic field will also define their charge. Figure 2.9 shows the cross section of a spectrometer.
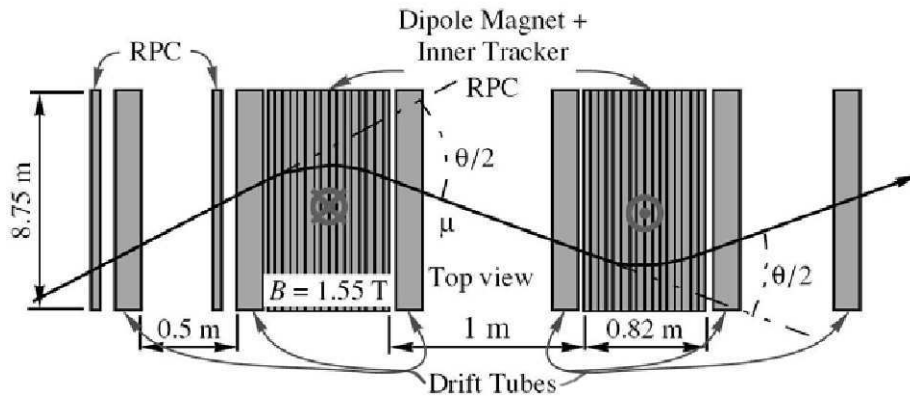
Figure 2.9: The OPERA spectrometer showing the HPT and the dipole magnet equipped with RPC layers. The HPT planes are aligned in 3 parts per magnet arm. The two additional RPC planes shown on the left are the XPC [47].

2.3 The Scanning System

Once an event is triggered by Electronic Detectors (EDs) and the interaction point is found using the TT, a candidate brick is extracted and, if validated by CSd, is scanned. The emulsion scanning load in the OPERA experiment is shared equally between Europe and Japan. The scan area required to locate a neutrino interaction in the OPERA experiment ranges from $5 \times 5 \, \text{cm}^2$ to $12.5 \times 10 \, \text{cm}^2$ i.e. the entire emulsion surface. In order to scan these large areas, new scanning systems of high speed automatization were developed, both in Japan and in Europe. To increase the image acquisition rate, two different designs were followed : in Japan the speed of the previouly used in CERN Hybrid Oscillation Research apparatUS (CHORUS) system was increased into a Super-Ultra Track Selector (S-UTS) [48, 49], while in Europe a large number of high-speed microscopes with standard components, European Scanning System (ESS), was chosen.

2.3.1   The European Scanning System

The design goal of the European laboratories was to develop an automatic microscope stage with a scanning speed of $20 \, \text{cm}^2/\text{hour}$, shown in figure 2.10, and described in detail in [50, 51, 52, 53].
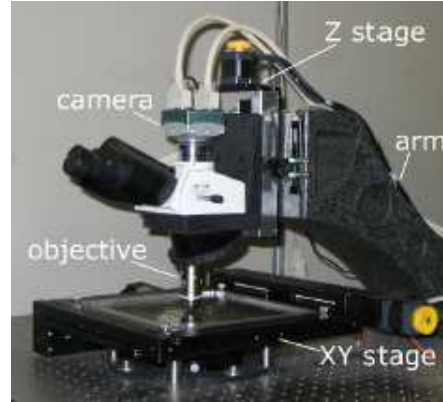
Figure 2.10: ESS microscope setup [53].

To achieve the scanning speed required by the OPERA experiment, many microscopes are used. The main design idea is the software-based approach for data processing. Thus, new algorithms can be easily tested and by the integration of commercially available components to build the microscope, upgrades due to technological improvements are possible. The ESS microscope consists of a mechanical stage moving along X and Y axis where the emulsion is set for the scanning and an optical part mounted on a vertical stage moving along Z axis including an objective immerged in oil or in dry condition. The images are taken in 16 views along the Z axis of each emulsion layer, with a continuous movement along Z. The depth of field in one view is about $3 \, \mu\text{m}$. These tomographic images are captured with a Complementary Metal Oxide Semiconductor (CMOS) camera.

2.3.2   The CS scanning

Everyday about 30 single Changeable Sheet (CS) emulsion sheets are scanned at the LNGS scanning laboratory equipped with 12 microscopes where the CSd attributed to Europe are analysed ; the other CS scanning lab is located in Japan. To confirm the result of the Brick Finding (BF) of the EDs, the CS is detached from the predicted brick and developed underground and scanned, the ECC is taken outside the underground area only in the case of a CS confirmation. With the CS scanning the muon angle of a CC interaction can be reconstructed with an error of about $10 \, \text{mrad}$, constraining the track candidate predictions from the CS for the ScanBack (SB) procedure of the ECC [40]. Both SB and BF processes will be described later in section 2.4.

2.3.3   The ECC scanning in Europe

In the various scanning laboratories in Europe, Russia, Turkey and Japan up to 57 emulsion films per brick have to be scanned. Bern, Bari, Bologna, Napoli, Padova and Salerno have automatized the changing of emulsion plates working for dry objectives as well as with oil. For instance, about one day is needed to scan and locate a neutrino interaction with one microscope of the Bern scanning laboratory equipped with automatic plate changers.

The Data AcQuisition (DAQ) of the emulsion is divided into many steps, the first is the online processing of tomographic images acquired from the emulsion films to convert grains, created by charged particles, into groups of dark pixels called clusters. Afterwards, the clusters are converted into reconstructed tracks, MicroTracks (MTs) for each emulsion layer and BaseTracks (BTs) connecting two MicroTracks as shown in figure 2.11. After the reconstruction of the MicroTracks and BaseTracks, other software packages are used to do an offline reconstruction, first to align the emulsion plates, and then to reconstruct the tracks and vertices. The software for these steps will be described later in section 3.1.4.
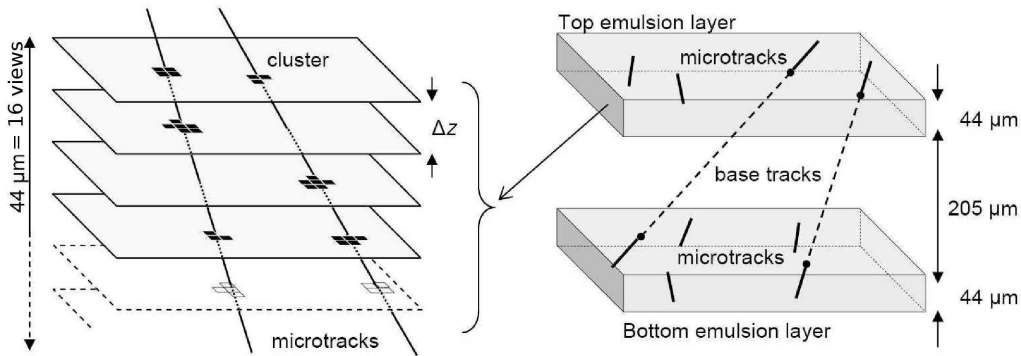
Figure 2.11: On the Left Hand Side (LHS), the MicroTracks reconstruction in one emulsion layer by combining clusters belonging to images at different levels [53]. On the Right Hand Side (RHS), MicroTrack connections across the plastic base to form BaseTracks [53].

The scanning software used to reconstruct MicroTracks and BaseTracks from the acquired images is called Systema di Salerno (SySal) and is described in [51]. The images are transferred into a computer, where an algorithm is executed to find the clusters. About $1\,000 - 2\,000$ clusters are found per view, mostly due to random background. Using quality cuts on the shape and size, their number can be reduced by 60%, before tracking. A MicroTrack consists of a straight line, along which the clusters are placed in the different tomographic views, about $20\,000$ clusters have to be checked.

To avoid that every combination is used, thus increasing the time required, two checks are used for filtering good hints for a MicroTrack (MT) :

– Only physically interesting track slopes are accepted, with an angular acceptance of $tan\theta < 1$ with $tan\theta_{x,y} = \frac{dx,dy}{dz} = TX, TY$ and the dx,dy on the distances in X,Y directions between top and bottom X,Y position of the MT in the emulsion layer and dz : thickness of the emulsion layer. The track coordinates system is described on figure 2.12.

– The emulsion sensitivity for Minimum Ionizing Particle (mip) is 31 grains/100 μm, thus the average number of grains per emulsion is 13. For each grain-pair internal trigger layers are defined, only when another grain is found in one of these layers, the MT search for this combination continues. The minimum number of clusters for a MT is 6.
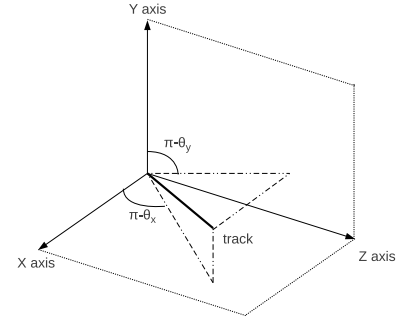
Figure 2.12: Track coordinates system

If after the MicroTrack (MT) search a cluster belongs to more than one MT, only the MT with the highest number of clusters is kept. The final tracking step is the combination of MTs to BaseTracks (BTs)s, where each MT's stopping Z position is extrapolated towards the corresponding Z level of the plastic support, and if two MTs agree within certain position and slope tolerances, they are considered as correlated, i.e. a BT is reconstructed. The angular resolution of a BT is related to the accuracy in the measurement of the microtrack intercept positions in the plastic base $\Delta X, \Delta Y \sim 0.3\mu$m and $\Delta Z \sim 3\mu$m [52]. Both MTs and BTs will be saved in the database, the clusters, i.e. the raw data will not be stored, reducing the need of the data storage. A description of clusters, MTs and BTs in the OPERA films is shown in figure 2.11.

2.3.4 The Scanning efficiency

Scanning efficiencies depending on hardware and software parameters of the microscopes have been assessed with a global survey compiling bricks scanned and analysed by different laboratories. These bricks have been exposed to cosmic rays and then the efficiencies are computed with the number of missing MTs or BTs in each layer or emulsion expected to contain a MT or a BT. Of course these efficiencies will depend strongly on the track angle and are shown in figure 2.13. Note that BT efficiencies derive from the MT ones since a BT is the combination of two MTs : $\epsilon_{BT} = \epsilon_{MT}^2$.
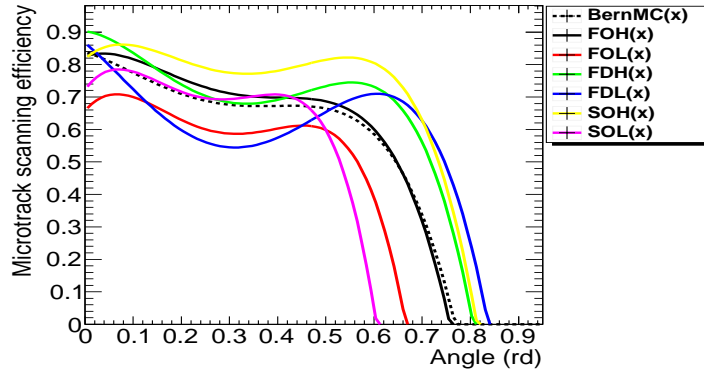
Figure 2.13: MT scanning efficiency as a function of the MT angle. Acronyms in the legend mean : F for Fedra and S for SySal telling which reconstruction software has been used, D for Dry and O for Oil showing the microscope objective type used, L for Low and H for High distinguishing variability in the scanning efficiencies among different laboratories. BernMC is a scanning efficiency evaluated in the Bern scanning laboratory. Fedra and SySal softwares are described in section 3.1.4.

The *BernMC* efficiency is the one implemented and used to train the Artificial Neural Network (ANN) to identify and estimate the energy of electromagnetic showers described in sections 4.3 and 4.4. The others have been implemented in the analysis framework OpEmuRec and are usually used by the collaboration to apply on MC samples. In the performance study of the electromagnetic shower tools detailed in chapter 4, I chose the closest official efficiency to the *BernMC* one. The difference is taken as the systematic uncertainty on the efficiency as shown in table 2.2.

MicroTrack angle (rad)	0.0	0.1	0.2	0.3	0.4	0.5
Scanning efficiency (%)	82.5 ± 1.4	81.6 ± 4.2	75.6 ± 4.7	71.1 ± 3.5	69.8 ± 2.6	68.7 ± 2.2

Table 2.2: MicroTrack scanning efficiency (OpEmuRec_FOH) applied to the MC samples described in section 3.1.5.1 and used for this thesis work.

2.4 The Analysis Chain

The trigger signal indicating the vertex location is obtained by Electronic Detectors (EDs), i.e. the hit TT planes and the hit RPC planes in the spectrometer, and is used to extract the candidate brick where a neutrino interaction has taken place : this process is called Brick Finding (BF).

An event recorded by the EDs has to be on time with the CNGS : the proton extraction is tagged in CERN with a clock synchronized with the OPERA clock with a time window of $20\,\mu$s [54].

In addition, the considered event must not be tagged by the VETO as external event.

The Brick Finding

The TT provides information to find secondary particles obtained from the neutrino interaction and determines the related brick to be extracted for reconstruction and analysis. It is not easy to find in which brick exactly the interaction happened. Sophisticated Brick Finding (BF) algorithms are applied to extract the right brick from the wall. Only, when the neutrino interaction left enough visible energy in the EDs, the event can be reconstructed.

The detection of a muon with the EDs, correctly reconstructed with an energy of at least 1 GeV, allows the classification of such events as 1μ, which are mainly CC interactions. Otherwise, if no muons are reconstructed, the events are identified as 0μ, which are mainly NC interactions [55]. Note that CC and NC interactions are different because of the charge of the boson exchanged during the process : $W^{\pm}$ for CC and Z^0 for NC as explained in section 2.5.1.

The BF procedure is based on the track reconstruction in the EDs to detect the most probable brick ; the track reconstruction in EDs will be explained in section 3.1.3. The hits inside the TT are filtered, to increase the efficiency and to reduce cross talk of the PhotoMultiplier Tube (PMT) channels, degrading the resolution. The most probable bricks are then extracted with the BMS. The BF performance has been studied with MC samples simulating neutrino interactions and the various ED response [56, 57]. A display of the BF result on a MC neutrino interaction in the OPERA detector is shown in figure 2.14.
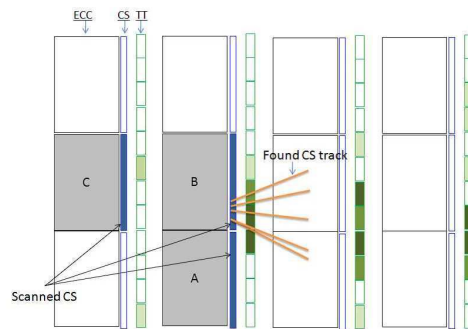
Figure 2.14: MC event in the OPERA detector. BF gives probabilities and the candidate which has the highest probability is the one which is extracted first and its CSd developed - here the brick B. The brick C is probably indicated by backscattering tracks. Brick A has been selected because there is a strong activity in the TT close to the interface of bricks A and B [56].

The efficiency performance of the BF algorithm evaluated on 2008-2009 data are summarized in table 2.3. A MC sample simulating 3000 ν_μ CC interactions and 3000 ν_μ NC interactions in the entire OPERA detector has been processed through the same electronic reconstruction software as data. The efficiency is calculated looking for the number of events found by the BF algorithm out of the number of generated events. The BF efficiency on data has been estimated by dividing the number of events where an actual neutrino interaction has been found in one of the extracted brick by the number of events triggered by the Electronic Detectors.

	0mu	1mu
2008-2009 data	35.2%	61.9%
MC	49.4%	76.3%

Table 2.3: BF efficiencies evaluated on the 2008-2009 data sample [58] and on 2 MC samples : *MC_ numuCC_ 1k_ march2011* and *MC_ numuNC_ 1k_ march2011* described in section 3.1.5.1.

The positive effect of the existence of a long fitted electronic track of the ν_μ CC interactions on the result of the BF prediction is clear.

The MC/data discrepancy can be explained by two arguments. First, the presence of external background (interaction in the rock and structures surrounding the detector) in the data and not in the official MC simulation which represents an effect of about 1% for CC and 23% for NC events evaluated with a dedicated MC study [59]. Then the OPERA simulation is not describing exactly the numerous procedures of the data analysis, especially the reclassification of CC events as NC and NC events as CC. In fact, if data are an admixture of CC and NC events, MC samples are made of pure CC or NC interactions. The effect of the external background will be enlightened in section 3.1.3 and the one of the reclassification of events will be assessed properly in section 3.2.2. In addition, in 2009, the classification (0μ, 1μ) algorithm described later in section 3.1.3 has been improved by tuning the selections with MC simulation in order to reject the external background. 2008-2009 data sample should be reprocessed with this new version of the classification algorithm to better control this background.

The localised brick with the highest probability is extracted. Its CSd is developed and scanned to confirm the connection between TT and the ECC brick or to reject the candidate and extract the second brick selected by the BF.

The Changeable Sheet in the BF process

Before detaching the CS box from the brick for scanning, the X-ray marking of the ECC done underground [40] is used to give a first reference frame for the scanning. The X-ray machine prints four calibration marks in the corner of the CSd and the first emulsion plate, before the X-rays are absorbed by the first lead plate, as shown in figure 2.15. This alignment allows already a resolution of a few microns between the CSd and the last ECC plate.
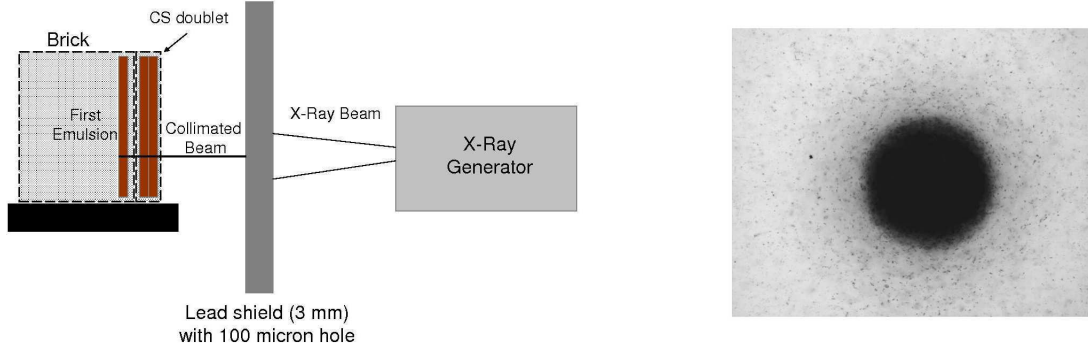
Figure 2.15: On the LHS, a schematic view of the X-ray marking system [60]. On the RHS, one X-ray spot of about $100\,\mu$m of diameter in an emulsion [60].

Then, CSd is developed underground and is moved to the surface to the CS scanning lab while the brick is stored in a shielded area next to the detector. The CS scanning process has been already explained in section 2.3.2. Once the CSd are scanned and tracks are connected with TT result, these tracks have to be followed down to the ECC brick and this process will require a few μm alignment between CSd and the most downstream film in the brick, i.e. the first to be scanned.

Other lateral X-ray marks are printed on the brick to allow an ordering of the emulsion films, and a first coarse alignment of about 5 μm from one ECC plate to another in case the cosmic ray exposure of the ECC is not done, for instance the black CS case, where the CS cannot be analysed due to failure of CS development or a too high fog level.

As already mentioned, in order to reproduce the alignment of the films of one brick once it is disassembled, the bricks are exposed to cosmic rays before development. There is a cosmic pit in the basement of the OPERA building of the LNGS surface site. The bricks are exposed for about 8 to 12 hours to accumulate high energetic straight cosmic ray tracks with a density of about few muon per mm^2 [61], which are needed for the emulsion plate to plate alignment with a precision of a few μm. Above the cellar room, a shaft with a 40 cm thick iron shielding was put to filter low energetic cosmic ray electrons. To shield the ECC bricks from ambient radioactivity, they are stored in lead containers. Then, ECC bricks are moved to the development laboratory next door and finally are sent to one of the scanning laboratories where the reconstruction and analysis processes will be done and the result uploaded into the database.

2.5   Physics Performance

After having described the OPERA experimental setup and the analysis chain of the EDs as well as the emulsion films, this section will assess the physics performance of the OPERA detector in the search for ν_μ oscillations. The neutrino interactions and cross sections used to compute the neutrino fluxes and rates expected in the detector are described. Then, a summary of signal and background event rates is given.

2.5.1 Neutrino interactions and neutrino cross sections

In the neutrino interaction with matter, one can list : lepton and nucleus, Charged Current (CC) and Neutral Current (NC), and according to the depth of the interaction with respect to the energy involved : Deep Inelastic Scattering (DIS), Quasi-Elastic (QE) and Resonant (RES).

CC and NC interactions are different because of the charge of the weak interaction boson exchanged during the process : $W^\pm$ for CC and Z^0 for NC. All these interactions are summarized in figure 2.16.
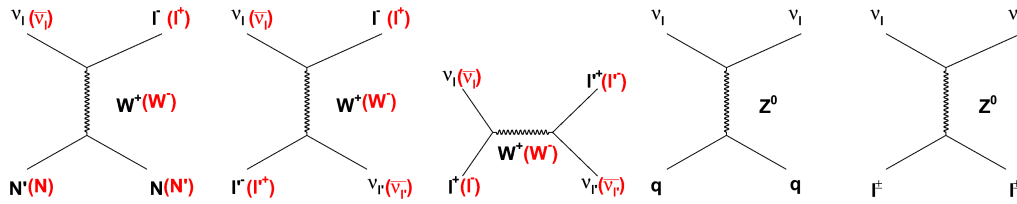
Figure 2.16: Feynman diagrams of the possible interactions of a neutrino with matter. From the left to the right, CC interaction with a nucleus then with a lepton and then with a lepton in s-channel and NC interaction with a nucleus and with a lepton at the most right of the figure.

DIS, QE and RES interactions could happen through CC with a charged lepton outcoming or through NC without the emission of a charged lepton or any flavour change for the neutrino.

In QE-CC interaction , a neutrino interacts with a nucleon (neutron n or proton p) and changes its nature as described by equation 2.1 :

$$\nu_l + n \to l^- + p$$
$$\overline{\nu_l} + p \to l^+ + n \tag{2.1}$$

A QE process is also possible through NC interaction with a neutrino escaping with the same flavour as the incoming one. These processes depend on the nuclear form factor and the typical transfer energy is about 10 MeV.

The RES process is characterized by the presence of pions in the final state. The incoming neutrino turns the nucleon in an excited state and, if the excitation energy is sufficient, one can create a Δ resonance. The energy transfer for such process to occur should be greater than 300 MeV, corresponding to the mass difference between a Δ resonance and a nucleon.

This type of interaction is described in the CC case by equation 2.2 :

$$\nu_l + p \to l^- + \Delta^{++} \text{ followed by } \Delta^{++} \to \pi^+ + p \tag{2.2}$$

The NC case gives :

$$\nu_l + p \to \nu_l + \Delta^+ \to \pi^0 + p + \nu_l$$

or according to another de-excitation mode of the Δ^+

$$\nu_l + p \to \nu_l + \Delta^+ \to \pi^+ + n + \nu_l$$

The DIS process is characterized by the presence of hadronic showers in the final state as shown by equation 2.3 :

$$\nu_l + \text{nucleon} \to l^- + \text{hadrons} \quad\quad (\text{CC}) \tag{2.3}$$
$$\nu_l + \text{nucleon} \to \nu_l + \text{hadrons} \quad\quad (\text{NC})$$

The energy transfer for the DIS process is much greater than the QE or RES processes. The nucleon goes through the fragmentation process, its components, the quarks and gluons, recombine to give hadrons and mostly pions in the final state.

Inclusive cross sections of CC interaction have been measured by several experiments and are compiled by the Particle Data Group (PDG) into the plot of figure 2.17. NC processes are much less measured especially at energies higher than 1 GeV. Note also that the number of experimental measurements is quite small even at low energy. In the Glashow Weinberg Salam (GWS) theory well described in the review [62], the $\frac{\sigma_\nu^{CC}}{\sigma_\nu^{NC}}$ ratio is near 3 because of electroweak coupling ; its ratio is also inferred from experimental data and confirm this value :

$$\frac{\sigma_\nu^{CC}}{\sigma_\nu^{NC}} \approx 3 \tag{2.4}$$

This means for OPERA that CC interactions will represent 75% of the total number of interactions while NC will represent 25%.
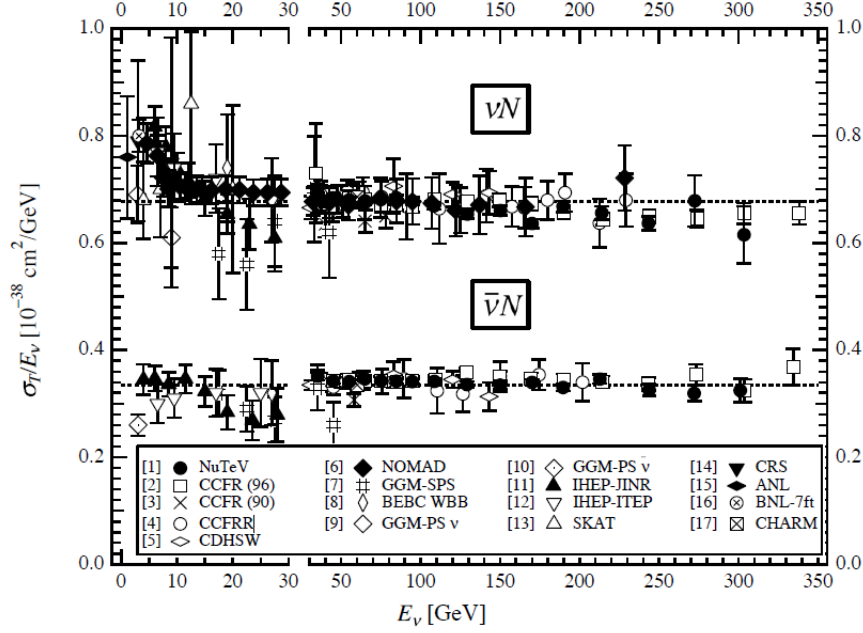
Figure 2.17: σ_ν/E_ν are represented for the muon neutrino and anti-neutrino-nucleon charged-current interaction total cross section as a function of the neutrino energy. The error bars include both statistical and systematic errors. The straight lines are the isoscalar-corrected total cross-section values averaged over $30 - 200\,GeV$: $\sigma_\nu^{Iso}/E_\nu = (0.677 \pm 0.014) \times 10^{-38}\mathrm{cm}^2.\mathrm{GeV}^{-1}$; $\sigma_{\overline{\nu}}^{Iso}/E_{\overline{\nu}} = (0.334 \pm 0.008) \times 10^{-38}\mathrm{cm}^2.\mathrm{GeV}^{-1}$. The average ratio of the anti-neutrino to neutrino cross section in the energy range 30-200 GeV is $\sigma_{\overline{\nu}}^{Iso}/\sigma_\nu^{Iso} = 0.504 \pm 0.003$. Note that there is a change in the energy scale at 30 GeV [63].

As explained above, the CC interactions are dominant and the following consideration about neutrino fluxes and rates in the OPERA experiment will be restrained to this type of neutrino interaction. Nevertheless, the NC interactions are important for the study of $\nu_\mu \to \nu_e$ oscillation since a significant background to the electron search will be neutral pions in the ν_μ NC interactions. NC event location efficiency, presented in section 3.2, is about 50%, implying an expected rate about 50 events per 10^{19} p.o.t. with respect to 500 ν_μ CC per 10^{19} p.o.t.. Despite this non negligible rate of ν_μ NC interactions, it will be shown in chapter 5 that this background is well rejected by a lower cut on the electron energy. Moreover, there is no experimental absolute measurement of the NC interaction cross section ; only the $\frac{\sigma_\nu^{CC}}{\sigma_\nu^{NC}}$ is determined.

On the other hand, the different contributions of DIS, QE and RES processes to the total neutrino cross section are shown on figure 2.18.
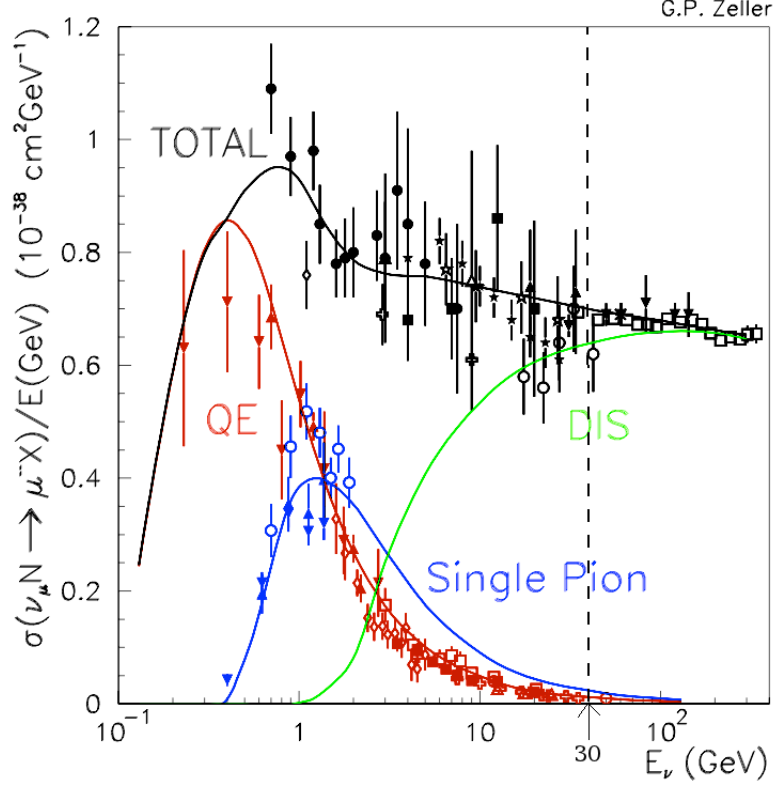
Figure 2.18: Neutrino CC interaction on nucleon cross sections divided by the neutrino energy of the DIS, QE and RES processes as a function of the neutrino energy [64].

Looking at the figure 2.18, below 30 GeV QE and RES processes contributes significantly to the total cross-section. Above, they are negligible and only DIS processes dominate. Hence looking at figure 2.17, the parametrization computed by the PDG between 30 and 200 GeV is describing well the neutrino CC interaction through DIS process and will be used in the calculation of neutrino rates.

For QE and RES processes, cross sections are given for neutron and proton targets and are assumed constant as a function of the energy [65] :

$$
\begin{array}{llll}
\nu_\mu + n \longrightarrow \mu^- + p & : \sigma_{\nu_\mu n \to \mu^- p} = 0.891 \times 10^{-38}\,\mathrm{cm}^2 & \mathrm{QE} & \\
\nu_\mu + n \longrightarrow \mu^- + p + \pi^0 & : \sigma_{\nu_\mu n \to \mu^- p \pi^0} = 0.537 \times 10^{-38}\,\mathrm{cm}^2 & \mathrm{RES} & \\
\nu_\mu + n \longrightarrow \mu^- + n + \pi^+ & : \sigma_{\nu_\mu n \to \mu^- n \pi^+} = 0.276 \times 10^{-38}\,\mathrm{cm}^2 & \mathrm{RES} & (2.5) \\
\nu_\mu + p \longrightarrow \mu^- + p + \pi^+ & : \sigma_{\nu_\mu p \to \mu^- p \pi^+} = 0.330 \times 10^{-38}\,\mathrm{cm}^2 & \mathrm{RES} &
\end{array}
$$

The last issue in the cross section contribution to the neutrino rates is the non-isoscalarity of the target. Indeed, all cross section measurements have been done on isoscalar targets. In the OPERA case, the fiducial mass is represented by the lead $^{208}_{82}Pb$. The rate calculation with the QE and RES processes is straight forward, but DIS process is occurring on protons as well as on neutrons. However, several experiments compiled by the Kuzmin, LyubushkIn and Naumov (KLiN) project [66] have determined that total cross sections on neutron and on proton are different. Compiling these data, the $R = \sigma_n/\sigma_p$ ratio and one parametrization are shown on figure 2.19. Note this ratio concerns the total cross section and it is applied only to DIS processes assuming that QE and RES interactions are negligible in the energy region where DIS processes are significant according to figure 2.18.
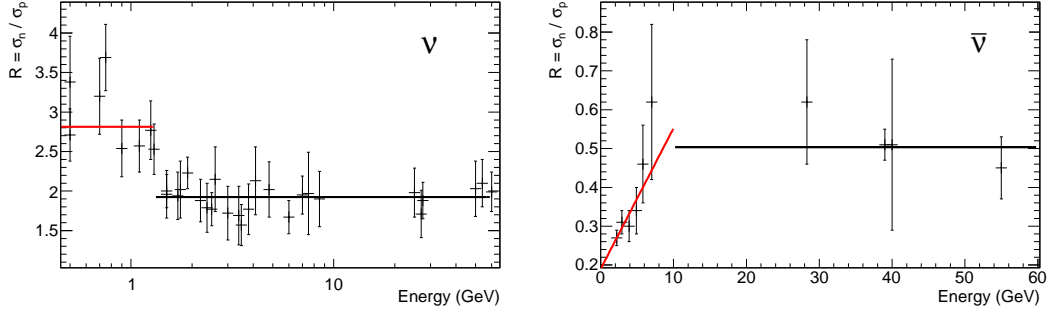
Figure 2.19: On the LHS, the ratio of neutrino interaction cross section on neutron divided by the proton one. The parametrization gives $R = 2.81 \pm 0.13$ for $E_\nu \leq 1.3\,\text{GeV}$ and $R = 1.92 \pm 0.06$ for $E_\nu > 1.3\,\text{GeV}$. On the RHS, is shown the same ratio for antineutrino interaction cross section. The parametrisation gives $R = (0.036 \pm 0.015) \times E + (0.19 \pm 0.05)$ for $E_{\overline{\nu}} \leq 10\,\text{GeV}$ and $R = 0.50 \pm 0.03$ for $E_{\overline{\nu}} > 10\,\text{GeV}$.

Finally, we can calculate the total neutrino CC interaction on nuclei non-isoscalar cross section with the equation :

$$\sigma_\nu^{\text{non-iso}}(E) = \sigma_\nu^{\text{RES, QE}} + \sigma_\nu^{\text{DIS, non-iso}}(E) \tag{2.6}$$

where $\sigma_\nu^{\text{RES, QE}} = \dfrac{Z}{A} \times \sigma_{\nu_\mu p \to \mu^- p\pi^+}^{\text{RES}} + \dfrac{N}{A}(\sigma_{\nu_\mu n \to \mu^- p}^{\text{QE}} + \sigma_{\nu_\mu n \to \mu^- p\pi^0}^{\text{RES}} + \sigma_{\nu_\mu n \to \mu^- n\pi^+}^{\text{RES}})$

and $\sigma_\nu^{\text{DIS,non-iso}}(E) = \sigma_\nu^{\text{DIS, iso}}(E) \times f_{\text{non-iso}} = 0.677 \times E \times 2\,\dfrac{R(E) \times (A - Z) + Z}{(1 + R(E)) \times A}$

with N, Z and A numbers of neutrons, protons and nucleons of the target nucleus, and $R(E)$ given in figure 2.19.

Considering antineutrino rates, DIS cross section are shown in figure 2.17. Note that for neutrino rates, QE and RES contribute 10% with the mean neutrino energy of the CNGS 17 GeV and note also that antineutrino interaction cross section is twice less than neutrino interaction cross section for DIS processes. Moreover, the $\overline{\nu_\mu}$ and $\overline{\nu_e}$ fluxes delivered by the CNGS and quoted in table 2.1 correspond to 2% of the ν_μ flux and 10% of the ν_e flux, respectively. All these considerations imply that I will neglect the contribution of the QE and RES processes in the antineutrino rates calculation.

2.5.2   CNGS performance

The CNGS beam started in 2006 by two years of commissioning. The physics run started in 2008 and is still on going. The status of the CNGS in terms of number of protons on target (p.o.t.) is summarized in table 2.4.

Year	Number of p.o.t.	Integrated p.o.t. / Expected p.o.t. over 5 years
2006	0.076×10^{19}	-
2007	0.082×10^{19}	-
2008	1.74×10^{19}	7.7%
2009	3.53×10^{19}	23.4%
2010	4.09×10^{19}	41.6%
2011	4.75×10^{19}	62.7%
2012	3.86×10^{19}	79.9%

Table 2.4: The CNGS neutrino beam status in 2012 [67, 68, 36].

The muon-neutrino and electron-neutrino fluxes Φ, delivered by the CNGS are given in reference [38]. Two more pieces of information are needed, the OPERA target mass and the neutrino interaction cross-section, in order to compute the expected neutrino rates in the OPERA detector for the different flavours composing the CNGS beam : ν_μ, $\overline{\nu_\mu}$, ν_e and $\overline{\nu_e}$ which all can be seen in figure 2.20. The 3 last components are of a small fraction and constitute to what is commonly considered as "ν_μ beam contamination" as shown in table 2.1.

The event rate N_ν is the convolution of the ν flux $\Phi_\nu(E)$, the neutrino interaction cross section $\sigma_\nu^{CC}(E)$ and the $\nu_\mu \rightarrow \nu_e$ oscillation probability $P_{\nu_\mu \rightarrow \nu_e}(E)$. Figure 2.21 shows the superimposition of the oscillation probability convolved with the ν_τ DIS CC interaction cross section on the ν_μ flux delivered by the CNGS.
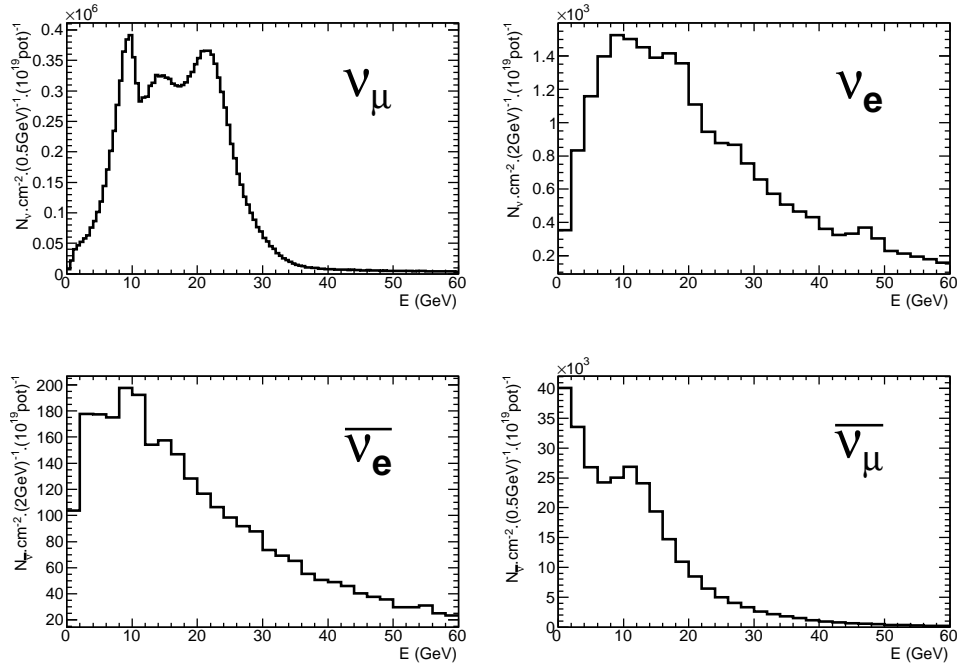
Figure 2.20: Neutrino fluxes delivered by the CNGS beam. On the top LHS, the ν_μ flux. On the top RHS, the ν_e from the beam contamination. On the bottom LHS, the $\overline{\nu_e}$ from the beam contamination. On the bottom RHS, the $\overline{\nu_\mu}$ from the beam contamination.
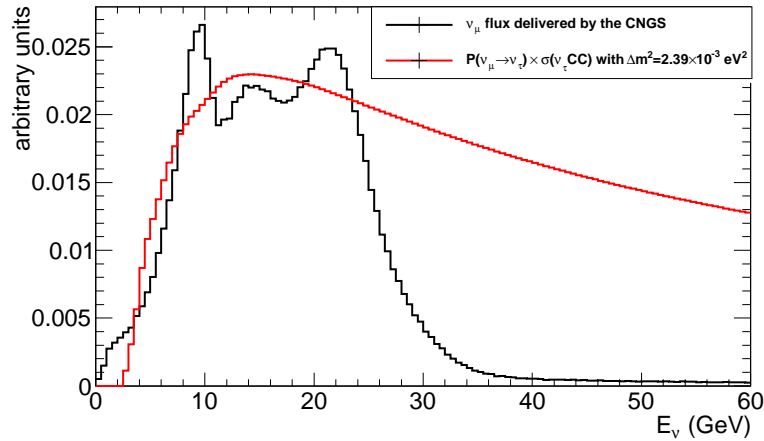
Figure 2.21: Muon neutrino flux delivered by the CNGS beam superimposed to the $\nu_\mu \rightarrow \nu_\tau$ oscillation probability convolved to the ν_τ(DIS-CC) cross section, with $\Delta m^2 = 2.39 \times 10^{-3}\,\mathrm{eV}^2$.

From the CNGS fluxes, the cross sections, the non-isoscalarity correction and the oscillation probability quoted in section 1.1.4 if it is needed, neutrino rates per 10^{19} p.o.t. can be computed and are shown in figure 2.22 and summarized for different configurations in table 2.5.
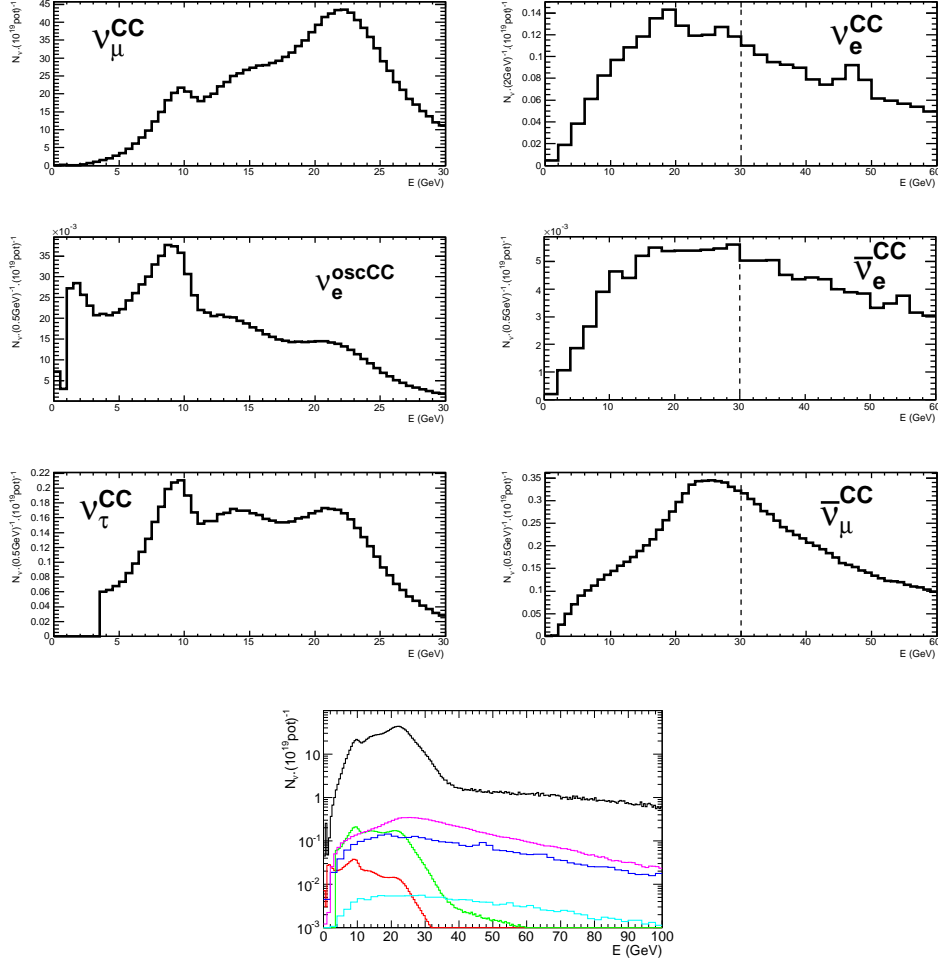
Figure 2.22: Expected neutrino CC interaction rates in the LNGS. On the top LHS, the ν_μ CC of the beam. On the top RHS, the prompt ν_e CC from the beam contamination. On the middle LHS, the ν_e CC which result from the oscillation. On the middle RHS, the prompt $\overline{\nu_e}$ CC from the beam contamination. On the bottom LHS, the ν_τ CC which result from the oscillation from the ν_μ. On the bottom RHS, the $\overline{\nu_\mu}$ CC from the beam contamination. The dashed lines on the RHS plots indicate the upper limit of the integration to compute the rates ; on the LHS plots, the integration will be done on the whole energy range. The bottom plot presents each contribution superimposed to each others with a logarithmic scale : ν_μ CC in black, oscillated ν_e CC in red, ν_e CC in dark blue, ν_τ CC in green, $\overline{\nu_\mu}$ CC in pink and $\overline{\nu_e}$ CC in light blue. The mixing parameters used for this calculation resulting from the oscillation are listed in table 5.1.

From the plots in figure 2.22, expected neutrino rates, integrated up to 30 GeV, for these different contributions are summarized in table 2.5.

Channel	Expected rate by 10^{19} p.o.t.		Expected rate for 2008-2009 runs		Expected rates for 5 nominal years (22.5×10^{19}p.o.t.)	
Integration range (GeV)	[0,30]	[0,100]	[0,30]	[0,100]	[0,30]	[0,100]
ν_μ CC	567 ± 58	667 ± 68	3010 ± 310	3540 ± 360	12800 ± 1300	16300 ± 1700
ν_μ CC QE+RES	56 ± 6	59 ± 10	297 ± 32	313 ± 53	1260 ± 135	1330 ± 225
Prompt ν_e CC	2.56 ± 0.18	5.95 ± 0.45	13.6 ± 1.0	31.5 ± 2.4	57.6 ± 4.1	134 ± 10
Prompt ν_e CC QE+RES	0.28 ± 0.02	0.39 ± 0.10	1.5 ± 0.1	2.1 ± 0.5	6.3 ± 0.5	8.8 ± 2.2
ν_τ CC	2.96 ± 0.30	3.10 ± 0.32	15.7 ± 1.6	16.4 ± 1.7	67 ± 7	70 ± 7
ν_τ CC QE+RES	0.52 ± 0.05	0.52 ± 0.05	2.76 ± 0.27	2.76 ± 0.27	11.7 ± 1.1	11.7 ± 1.1
Oscillated ν_e CC	0.86 ± 0.06	0.87 ± 0.07	4.56 ± 0.32	4.61 ± 0.37	19.4 ± 1.4	19.6 ± 1.6
Oscillated ν_e CC QE+RES	0.18 ± 0.01	0.18 ± 0.01	0.95 ± 0.05	0.95 ± 0.05	4.1 ± 0.2	4.1 ± 0.2
$\overline{\nu_\mu}$ CC	6.04 ± 1.80	13.6 ± 3.0	32.0 ± 9.5	71.9 ± 11.0	136 ± 41	306 ± 47
$\overline{\nu_e}$ CC	0.12 ± 0.04	0.32 ± 0.07	0.66 ± 0.23	1.7 ± 0.4	2.8 ± 1.0	7.3 ± 1.7

Table 2.5: The expected neutrino rates in the OPERA detector with a target mass of 1.21 kt integrated up to 30 GeV and up to 100 GeV.

Note that the target mass of 1.21 kt is the mean value obtained by integrating the number of bricks in the detector as a function of the CNGS beam intensity from 2008 up to 2010. This kind of computation is necessary because the OPERA target was not yet filled in 2008 and because the CNGS integrated luminosity summarized in table 2.4 varied between 2008 and 2010. In addition, the OPERA target mass decreases as a function of time since bricks are constantly extracted from the detector.

The uncertainties have been derived from the uncertainty on the cross section (about 10%) given by the parametrisation in figure 2.17 and by the non-isoscalarity correction, the uncertainty of about 4% on the CNGS fluxes reported by the work [69] and the uncertainty on oscillation probability summarized in table 2.6 and estimated by varying mixing parameters in the fit uncertainty of the global analysis [27]. Each oscillation probability is mainly driven by a set of parameters which are used to define the uncertainty on the considered probability. The oscillation probability is computed with each parameter which is given by the outcome in a Gaussian function (mean value is the best fit parameter value and the standard deviation is the 1σ error on the fit). This process is applied iteratively 10 000 times and gives the uncertainty for each oscillation probability type summarized in table 2.6.

	ΔP/P at 6 GeV (%)	ΔP/P at 17 GeV (%)
$\nu_\mu \to \nu_e$	12.3	12.8
$\nu_\mu \to \nu_\tau$	6.2	6.8
$\nu_e \to \nu_e$	0.14	0.012 @ 21 GeV

Table 2.6: Oscillation probabilities uncertainty used in the neutrino event rates calculation. 17 GeV and 21 GeV are mean value of the energy spectrum of the ν_μ flux and the ν_e flux respectively. 6 GeV is the mean value of the neutrino energy spectrum for the $\nu_\tau(\tau \to e)$ channel.

This method overestimates the uncertainties since it considers that all parameters are uncorrelated, but this first order is a good approximation.

2.5.3 Physics performance in τ detection in the OPERA experiment

ν_τ CC interaction are identified by detecting the τ-lepton. This detection made in the brick part will show the occurrence of $\nu_\mu \to \nu_\tau$ oscillation.

The τ decay channels searched in ECC bricks are the electron, muon, single charged hadron and multiple charged hadrons channels. The τ-lepton decay channels and the respective Branching Ratio (BR) are [70] :

$$
\begin{aligned}
\tau^- &\to e^- \nu_\tau \overline{\nu_e} & (17.83 \pm 0.04)\% \\
\tau^- &\to \mu^- \nu_\tau \overline{\nu_\mu} & (17.41 \pm 0.04)\% \\
\tau^- &\to h^- \nu_\tau (+n\pi^0) & (49.16 \pm 0.12)\% \\
\tau^- &\to h^- h^+ h^- \nu_\tau (+n\pi^0) & (15.2 \pm 0.08)\%
\end{aligned}
\tag{2.7}
$$

There are two types of decays, short and long decays, depending on the location of the decay vertex. In the short decay condition, the daughter is produced by the neutrino interaction in the lead plate inside the brick, and then the decay occurs in the same lead plate. In the long decay condition, the τ decay is in a lead plate different from the one where it has been produced. The selection of the long decay events are based on the existence of a kink angle between the parent and the daughter tracks : $\theta_{\mathrm{kink}} > 20\,\mathrm{mrad}$. A sketch of the long decay topology in a brick and the emulsion film design is shown in figure 2.23.
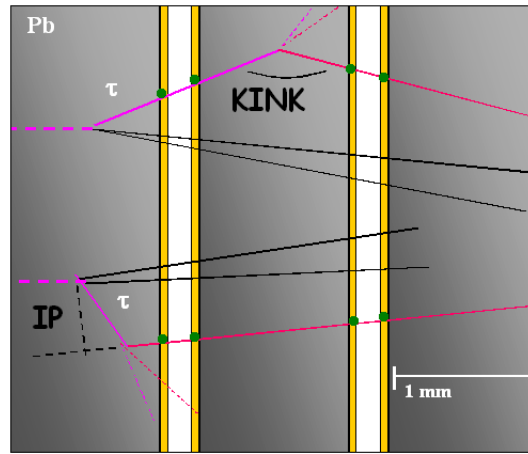
Figure 2.23: Schematic picture of the τ detection technique in the ECC brick for long on the top and short on the bottom decays [50].

The selection of the short decay events are based on the Impact Parameter (IP) of the daughter track with respect to the interaction vertex : IP $> 5 - 20\,\mu\mathrm{m}$. The IP is defined as the minimal distance of approach in 3D as described in the work of E. Barbuto *et al.* [71]. The main background sources to the different channels consist of charm decays for 54% of background events, then hadron interactions correspond to 30% and finally large angle muon scattering represents 16%. The main background for the $\tau \to \mu$ channel comes from charm production in the ν_μ CC interactions. The topological cuts on the kink angle and on the transverse momentum of the muon help to reduce that background. The $\tau \to e$ channel is also affected by the charm background in the electronic mode as far as the decay topology is detected. The search of the τ decay channel into hadrons is favoured due to its high branching ratio. But the hadronic reinteractions affect this hadronic decay mode negatively as a high background. The summary of the OPERA detector performance after 5 years of running is illustrated in table 2.7 [59].

Decay channel	Number of signal events expected		Number of background events expected	
	22.5×10^{19}p.o.t.	4.88×10^{19} p.o.t.	22.5×10^{19}p.o.t.	4.88×10^{19} p.o.t.
$\tau \to \mu$	1.79	0.39	0.09±0.04	0.02±0.01
$\tau \to e$	2.89	0.63	0.22±0.05	0.05±0.01
$\tau \to h$	2.25	0.49	0.24±0.06	0.05±0.01
$\tau \to 3h$	0.71	0.15	0.18±0.04	0.04±0.01
Total	7.63	1.65	0.73±0.15	0.16±0.03

Table 2.7: Expected numbers of observed signal events for the design intensity of 22.5×10^{19}p.o.t. and for the 2008 and 2009 analysed data sample corresponding to 4.88×10^{19}p.o.t. The fourth and the last columns show the expected numbers of observed background events from sources described above for the design intensity and for the 2008-2009 analysed data sample. Errors quoted are systematic : 25% on charm background and 50% on hadron and muon backgrounds are assumed, these errors are combined linearly if they arise from the same source, in quadrature otherwise [59].

2.6 $\nu_\mu \to \nu_e$ Oscillation Channel : detection of electrons and photons in the OPERA experiment

This important subject will be the aim of this thesis showing the performance and the contribution of OPERA to the neutrino physics in the investigation of the $\nu_\mu \to \nu_e$ neutrino oscillation. Such study needs a dedicated tool to detect electrons : a reconstruction tool for electromagnetic showers completed by an identification algorithm and an energy estimation tool in order to perform kinematical analysis. As an example, an electron shower generated in an OPERA brick is shown in figure 2.24.
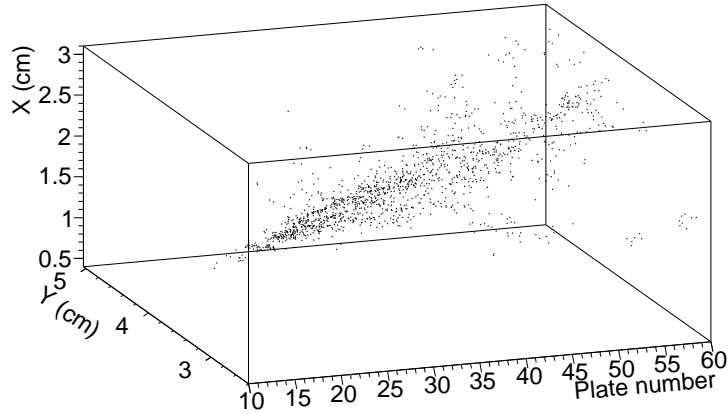
Figure 2.24: A 6.5 GeV electron shower spreading into an OPERA brick.

This electron reconstruction and its analysis will be a crucial point in order to perform the $\nu_\mu \to \nu_e$ oscillation study as well as the $\tau \to e$ mode in the $\nu_\mu \to \nu_\tau$ channel : they will be detailed in chapter 4.

Looking for oscillated ν_e from the ν_μ produced by the CNGS beam is a challenging task since only a few events are expected. Any channel having an electron in the final state will be a source of background. In addition, channels with photon and no other hint identifying clearly the interaction type, e.g. a muon track in a ν_μ CC interaction, will be also a background to the oscillated ν_e search. The different sources of background are thus :

– ν_e from the contamination of the beam, this background is the most statistically significant, moreover the two energy spectra are overlapping within [0,30] GeV which means this background is irreducible in this range. An excess of ν_e events will be thus looked for.
– The $\tau \to e$ decay channel, which becomes a background in this context.
– NC neutrino interactions, are producing hadrons and photons in the final state.
– CC neutrino interactions where the muon track is missed.

The summary of the number of expected signal and background rates for the ν_e detection in the OPERA detector is illustrated in table 2.8. Chapter 5 of this thesis shows the results of this oscillation study.

	Signal	Background channels				
	Oscillated ν_e	$\tau \to e$	ν_μ^{NC}	prompt ν_e	prompt ν_e QE+RES	$\nu_\mu^{CC} \xrightarrow{\text{mis}} \nu_\mu^{NC}$
N_{evt} exp. in 2008-2009	4.61 ± 0.37	2.92 ± 0.30	1180 ± 120 (*)	31.5 ± 2.4	2.1 ± 0.5	138 ± 14 (**)
N_{evt} @ 22.5×10^{19}p.o.t.	19.6 ± 1.6	12.4 ± 1.3	5010 ± 510 (*)	134 ± 10	8.9 ± 2.1	586 ± 59 (**)

Table 2.8: Expected numbers of ν_e signal events in OPERA for the design intensity of 22.5×10^{19}p.o.t. and for the 2008 and 2009 analysed data sample corresponding to 5.3×10^{19}p.o.t. (*) and (**) channels will be drastically reduced by putting a lower cut on the energy of the electron shower as described in section 5.1.3.

This chapter has presented the OPERA experiment which is running from 2008. The CNGS beam has been described and its performance in terms of neutrino fluxes has been assessed. Apart from that, a description of the OPERA detector has been given and the analysis chain has been explained. The expected neutrino rates in the detector taking into account the features of the CNGS beam and the phenomenology of neutrino interactions have been computed and the performance of OPERA in τ detection as well as in ν_e detection have been reported.

Chapter 3

Analysis Framework And Efficiency Assessment

In this chapter, the analysis software of the OPERA experiment, as well as the Monte Carlo (MC) simulation framework will be presented. The reconstruction and analysis software OpRelease using CERN ROOT 5.24 is installed on a 64-bit cluster at the Lyon computing center. Associated with the OpEmuRec package, the software allows a full detector reconstruction for the first time in OPERA, from the electronic neutrino event trigger up to the vertex reconstruction in the ECC. Previously, the electronic reconstruction and the ECC reconstruction were dissociated. In addition, procedures to make the link between these two detections, i.e. the Brick Finding (BF), the Changeable Sheet (CS) scanning and the ScanBack (SB), were not simulated, and the data scanning and the MC scanning simulation were not performed with the same software. The implementation of the shower reconstruction algorithm, developed before in the work of Y. Caffari *et al.* [72, 73], into the reconstruction package OpEmuRec is a part of this thesis work. Event location efficiencies will be assessed in the described analysis framework using MC simulations. The statistical methods used in the next chapters will be also described here.

3.1 Analysis Framework

To test the detector response and the data analysis software thoroughly, MC simulations are used in particle physics. For the OPERA experiment, there are several steps that are detailed in the following.

- The neutrino event generation by OpNEGN described in section 3.1.1.
- The particle track propagation inside the detector is performed with OpRelease, described in section 3.1.2, and is composed of the electronic detector simulation, called OpRec, and the ECC simulation, called OpEmuRec. To analyse the MC samples, the combination OpRelease/OpEmuRec provides a complete simulation of the detector.

3.1.1 MC event generation

The neutrino event generation is the first step of MC studies. In the OPERA experiment, it has been performed using the OpNEGN neutrino generator [74, 56, 39]. The OpNEGN generator is derived from the Neutrino Oscillation MAgnetic Detector (NOMAD) experiment and is needed to generate a large sample of neutrino interactions. The modifications necessary to the OPERA experiment included the CNGS target and the beam fluxes. The Deep Inelastic Scattering (DIS) neutrino interactions are based on a modified version of the LEPTO 6.1 generator, while the fragmentation process is described with a modified version of JETSET 7.4 . Occurring nuclear re-interactions from hadrons produced in the fragmentation process are described with the Formation Zone Intra-nuclear Cascade (FZIC) code (extracted from the DPMJET II.4 generator) and reinserted in the JETSET simulation. The Quasi-Elastic (QE) and Resonant (RES) neutrino interactions as well as the Fermi momenta generation of the target nucleons are described in more detail in [39]. Several thousands of neutrino events were generated, grouped in beamfiles with pure CC or NC neutrino interactions.

3.1.2 Particle propagation in the detector

The software framework OpRelease is the main software of the OPERA experiment, used for the data analysis as well as for the MC simulations. It is designed to allow the running of different MC programs as Geant3 or Geant4 [75] and Fluka [76] for particle propagation. OpRelease is a software architecture composed of different packages to simulate specific processes of particle propagation in the OPERA detector. Each package of the OpRelease is a single shared library libOp*.so ; thus, it can be dynamically loaded by the software. It is managed by the Concurrent Version System (CVS) and stored on the OPERA CVS repository at a 64-bit cluster, the Computing Centre of IN2P3 (CCIN2P3) in Lyon. This allows to keep track of changes in the software. The internal organization and the external interaction with other OpRelease packages is performed through the Configuration Management Tool (CMT). Apart from the packages, the OpRelease needs external kits distributed freely on the web : CERNLIB 2006 release [77], Class Library for High Energy Physics (CLHEP) 2.0.3.2 release [78], ROOT 5.24.00 release [79], Pythia 6 [80], ROOT Virtual Monte Carlo (VMC) [81], Geant3 1.11 release [75] and ORACLE, the oracle library and client to access the database [82]. The coordinate system used for the experiment is defined in figure 3.1. The current version of the OpRelease is 4.1, however that one has been released recently and thus has not been used in this work. The OpRelease 4.0 was the up-to-date version at the beginning of this study.

In order to run, the MC simulation uses the different packages of the OpRelease mentioned above. The geometry of the detector is described in the OpGeom package. It takes into account the fact that the geometry of the OPERA target is changing over the time of the experiment due to the insertion and extraction of the ECC bricks. The geometry used for the simulation includes the full layout of the hall B and surrounding rock to simulate also "rock muons" coming from upstream interactions. Those are not related to the neutrino interactions in OPERA but are registered in the detector.
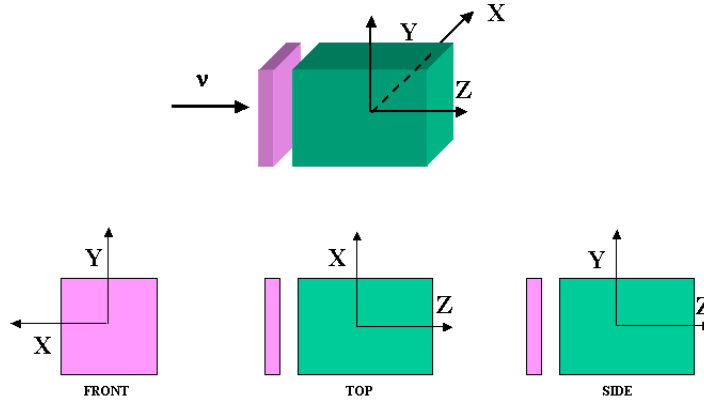
Figure 3.1: OpRelease coordinates system [83].

The full detector MC simulation in the OPERA experiment is based on the OpSim package of the OpRelease framework. OpSim is based on the ROOT VMC kit [81]. By defining the geometry in accordance with ROOT classes, the VMC allows a free choice of the transport engine to propagate the particles.

The output of OpSim is handled with another package called OpDigit, to convert physical hits, i.e. the energy deposits, into the final data format also called "digit" by applying the detector response. Before it can be analysed, one can choose to either ignore the ECC hits and use the electronic detector only, or to propagate the tracks in a 3×3 matrix of bricks surrounding the neutrino interaction. In this case, it is possible to simulate the full processing chain of Electronic Detector (ED) track reconstruction and BF (OpRec), CS scanning and vertex localization with the OpEmuRec package. An overview of the relevant packages of the OpRelease framework is shown in figure 3.2.
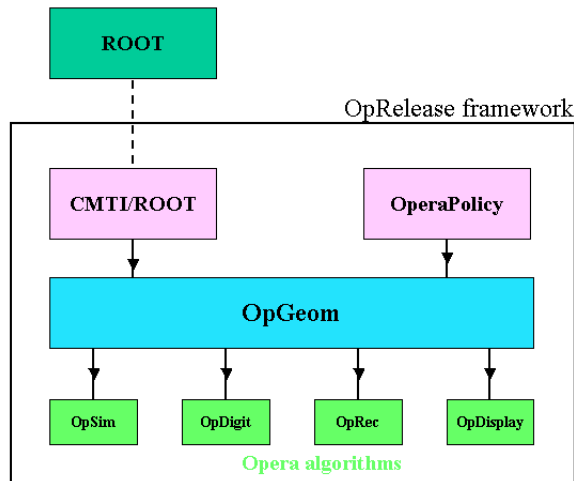
Figure 3.2: Overview of the OpRelease framework and its packages [83].

3.1.3   Analysis of the Electronic Detectors

The OpRec reconstruction package performs many tasks, each one issued by a subpackage : for instance a subpackage to take into account crosstalk in the PMT, another subpackage to check the time coincidence between CNGS and the OPERA event, a third one to reconstruct 3D tracks and so on. Important tasks with respect to the electron neutrino analysis are :

– *Event classification* : OpCarac is the package which classifies whether events are "CONTAINED" in the OPERA detector. If they are not, and depending on the presence of hits in the VETO plane or in the TT on the edge of the detector, events can be classified as "FRONT MUON" or "SIDE MUON", which compose the major part of the external background. The other contribution to the external background comes from another classification which is "BORDER SOFT NC" and which represents NC events without 3D tracks occurring in the regions where the external background is more important. However, these events are analysed to increase the NC event location efficiency since some of them are actual NC neutrino interactions coming from the CNGS beam. Neutrino interactions can eventually occur in the iron of a spectrometer due to its high density and present a low activity in the TT planes. Finally, the class "NO DECISION" is an option if none of the properties of classification described above is fulfilled by the current event. To conclude, only "CONTAINED" and "BORDERSOFTNC" events will be analysed and compose the selected OPERA data. Studies about the OpCarac algorithm including a detailed description of these classes can be found in the work of A. Bertolin *et al.* [84, 85].

– *MuonID package* : does the identification of the muon according to two pieces of information. The number of TT and RPC wall containing hits has to be greater or equal to 14, and the electronic 3D track to be reconstructed in the two longitudinal planes by a pattern recognition algorithm. The two longitudinal tracks thus reconstructed are combined to give a 3D track in order to reject hits which are not present in the two planes and are probably instrumental background. This 3D track is processed by a Kalman Filter (KF) in order to calculate the momentum taking into account the MCS. The product length $\times$ density is computed and used to identify the track : it is taken as a muon if its value is greater than $660 \, \mathrm{g.cm}^{-2}$. A complete description of the muon identification procedure is given in the OPERA collaboration paper [86].

– *Energy package* : estimates the visible energy left in the TT and computes the reconstructed neutrino energy. The energy deposited in the TT is calculated strip by strip using the result of the PMT gain measurement and the calibration parameters : the TT visible energy is defined as the sum of all strips energy. An energy calibration has been made with cosmic ray tracks as a function of the number of photoelectrons measured on the left and the right side of the fibres and of four free parameters. The visible energy deposited in the TT will be used later in the analysis of chapter 5. The reconstructed neutrino energy has been parametrised with MC simulation as a function of the MC true hadronic energy and the visible energy in the TT. The work of C. Jollet *et al.* [87] details these features.

– *BF package* : the OpRec package calls the OpBrickFinder package routines used to find the brick where the neutrino interaction occurred. The principle of this algorithm has been already described in section 2.4.

3.1.4   Analysis of the nuclear emulsions

3.1.4.1   Emulsion reconstruction software

At the level of the ECC, several packages exist to analyse data obtained from the scanning of the emulsions and simulate neutrino interactions in the brick. The scanned data in the OPERA experiment are stored in a central database, from which the reconstruction of events is performed. The OpEmuRec analysis package has been designed to handle scanned events extracted from the database as well as MC simulation samples. Before processing with OpEmuRec, it is necessary to convert the data or the MC simulation to the relevant input format. This is accomplished with the OpEmuIO package. The latter is thus the convergence package for data and MC, it allows to :

– download and extract an event from the database, copying it into a ROOT file. The structure of such a file is named the "emulsion data model" and is defined by the OpRData class.
– read a MC file containing digits and convert it to the emulsion data model format, producing a new ROOT file for each MC event.

The architecture of the ECC reconstruction software is summarized in figure 3.3a.

While data go through the CS finding and the ScanBack (SB) procedure before looking for a vertex in the ECC brick, the MC samples at the OpEmuIO level do not include yet these two processes (CS and SB). It appeared necessary to add the simulation of the CS and the SB in the MC OpEmuRec framework. Each process in the OpEmuRec framework is coded into an algorithm, as a routine called by OpEmuRec if chosen by the user. These routines are interfaced with the external kits Framework for Emulsion Data Reconstruction and Analysis (FEDRA) or SySal. These are needed for their set of classes and methods related to the track reconstruction in the ECC brick. Both of the external kits FEDRA and SySal have been developed in parallel in order to reconstruct tracks and vertices. SySal has already been mentioned in section 2.3.3 because of its use in the scanning process to reconstruct clusters, MicroTracks and BaseTracks. Its developer decided to extend its abilities up to the track reconstruction inside the entire ECC in addition of the BaseTrack reconstruction ; FEDRA, is aimed from the start to perform the track reconstruction inside the brick. In general, SySal follows a MicroTrack-based reconstruction which aims to enhance the track reconstruction efficiency whereas FEDRA uses a BaseTrack-based reconstruction. Details about the two external kits can be found in [51] for SySal and in [88] for FEDRA. Other OpEmuRec algorithms have been developed to perform analysis on reconstructed data as the Decay Search Procedure (DSP) described later in section 5.5.1 or the shower reconstruction algorithm which is thoroughly described in chapter 4. All these algorithms are listed in figure 3.3b.

Scanning labs use either FEDRA or SySal in their standalone versions to reconstruct events in the scanning process. OpEmuRec is not used systematically on data,

nevertheless a sub-dataset has been reconstructed with OpEmuRec and released in the collaboration as a test of this framework. The different steps of the event reconstruction will be described in the following. From the BaseTrack reconstruction during the scanning procedure up to the vertex reconstruction.
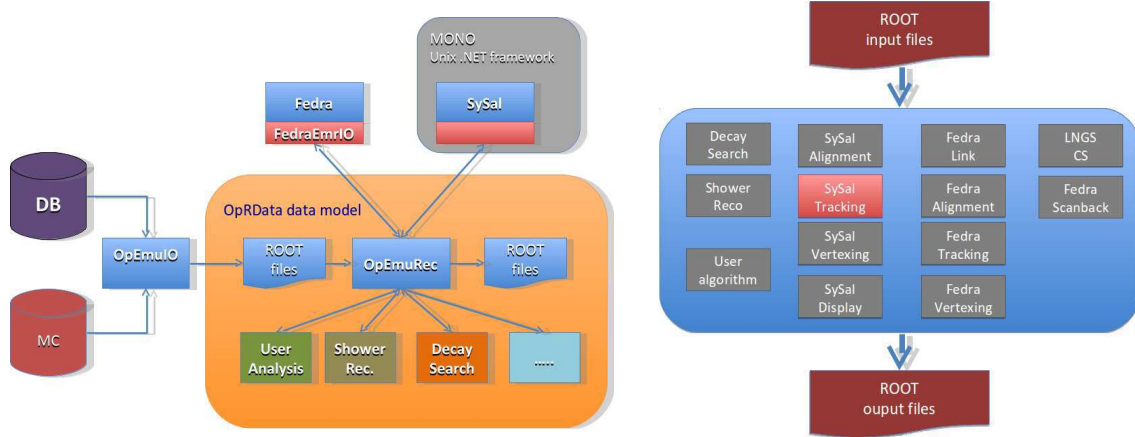
Overview of the OpEmuRec framework.   Algorithms of the OpEmuRec package.

Figure 3.3: OpEmuRec architecture and its algorithms [89].

3.1.4.2   Emulsion scanning and event reconstruction

Different scanning steps are defined for the OPERA experiment, four automatic steps and the visual inspection. In order to assess the total efficiency of the event reconstruction in OPERA, these steps are reproduced in the OpEmuRec framework with different algorithms :

- *CS scanning algorithm* : is the first scanning step. A large area of several cm^2 of the two CS emulsion layers attached to the brick are scanned in Nagoya or in the LNGS to look for the predictions from the ED.
- *SB track scanning algorithm* : is used to follow the tracks predicted in the CS upstream inside the ECC to find the neutrino vertex. This is performed in the various scanning laboratories in Europe or in Japan. The scanning area is small for the prediction scan, when the X-Ray grid is used for alignment. For higher precision, an area of about 1 cm^2 has to be scanned to allow an alignment with cosmic ray tracks.
- *Total volume scanning* : After the confirmation of the stopping point of the SB track, an area of 1 cm^2 of emulsion film is scanned for five plates up, and ten plates downstream the stopping point defining the analysed volume in the ECC. The stopping point will be defined in the following. During this total scan, several algorithms are sequentially processed in the volume : *a) Linking algorithm* which

reconstructs the BaseTracks as described in section 2.3.3 ; *b) Alignment algorithm* which defines an affine transformation from one plate to another by aligning cosmic ray tracks ; *c) Tracking algorithm* which associates BaseTracks plate by plate to reconstruct tracks through the volume and *d) Vertexing algorithm* which combines reconstructed tracks into a vertex.

– *ScanForth track scanning* : When the vertex is found, the tracks are followed downstream to search for possible hadronic re-interactions or decays and to measure the momentum of the tracks with the MCS method [43].

– *Manual check* : Visual inspection of the tracks, including the stopping points confirmation and electron-pair checks.

CS scanning

When a possible neutrino interaction is localized by the BF algorithm in one ECC, the brick is extracted and the X-ray marking is performed. The CS is then detached and developed to be scanned, while the ECC remains underground awaiting for the CS scanning result. In the CS scanning, an area of $4 \times 6\,\mathrm{cm}^2$ per emulsion is scanned around the muon prediction in case of CC interactions while for NC events, a larger area is scanned ; this scanning is called general scan. Inside the scanning area of $24\,\mathrm{cm}^2$ only a few tracks related to the event are expected, and will be confirmed by visual inspection afterwards. A pair of CS tracks inside the emulsion is shown in figure 3.4 ; only tracks with four visually confirmed MicroTracks are selected as CS tracks. The MicroTrack object is described in section 2.3.3.
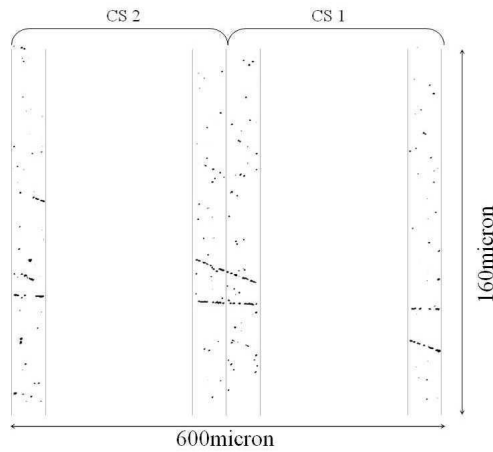
Figure 3.4: A schematic view of two tracks in a CSd [56, 57].

To match the two CS sheets, the position marks of the X-ray grid are used. An even better matching can be achieved by the alignment of the Compton electron tracks found in both CS.This second alignment is done if no CS track candidate was found after the first scanning, and since it is only a computational task, no additional general scanning of the CS is needed. Afterwards a "3-out-of-4" search can be performed i.e. the visual inspection for a fourth MicroTrack in the case of a probable CS track with only three

automatically found MicroTracks. If after the Compton alignment and the "3-out-of-4" procedure, no CS track candidate was found, the CS will be re-scanned at least once, with an improved prediction of the Electronic Detectors. If the scanning result stays negative, a new CSd is attached to the extracted brick which is reinserted in the OPERA target. The next probable brick is extracted and its CS scanned. This procedure improves the location efficiency by 50% ; in the 2009 data sample, 1.5 bricks are extracted per event. This procedure, up to the "3-out-of-4" search is reconstituted with an algorithm which runs as an OpEmuRec package.

SB procedure

After a positive result of the CS scanning, the ECC is disassembled and the emulsions are developed and sent to one of the various scanning laboratories in Europe or in Japan. During the ScanBack (SB) procedure the extrapolations of the CS tracks back into the brick are followed upstream, until no track can be found anymore during 5 plates, which defines the "stopping point". To find the CS track prediction in the first emulsion plate, an area of $3 \times 3\,\mathrm{mm}^2$ is scanned, as the precision of the mechanical alignment between brick and CS is about $1\,\mathrm{mm}$. During the SB procedure, two scans are performed : an inter-calibration area scan to align the emulsion plates with cosmic ray tracks over an area of a typical size of 0.25 up to $1\,\mathrm{cm}^2$, and the prediction scan with an area of one view of $390 \times 310\,\mu\mathrm{m}^2$, which is defined by the prediction from the previous plate. The extrapolation from the previous plate has an accuracy of 10-20 μm, due to the inter-calibration. The absence of a MicroTrack in the predicted area defines the stopping point, which is confirmed by a visual inspection of the predicted position in the four consecutive planes upstream. If more than one CS prediction exists, as shown in figure 3.5, a vertex can be defined.
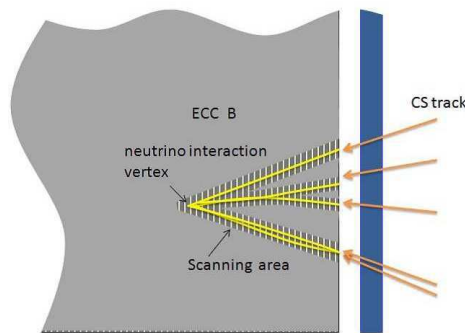
Figure 3.5: If a CS track was found in the CS, the prediction is followed upstream in the brick until a stopping point or vertex is found. The following up inside the brick is performed by point-like scanning [56, 57].

The neutrino interactions are randomly distributed inside the brick, so on average about 30 plates per event have to be scanned for the localization of the interaction. This procedure is reproduced by the SB OpEmuRec algorithm, with the exception that the total surface of each plate is used instead of restricting to the area where the prediction is searched.

The Total Scan volume

After the CS tracks were confirmed as a stopping point, the Total Scan (TS) is performed. The scan volume consists of 15 consecutive plates scanned over an area of about $1\,cm^2$ each, 10 downstream of the stopping point and 5 upstream. If the inter-calibration volume, scanned during the SB, was large enough, it can be used as the TS volume. Inside this volume the track reconstruction is performed after the BaseTrack reconstruction and the plate alignment on possible tracks not followed by the SB.

The Linking and alignment packages : The linking as a part of the scanning procedure, has been already described in section 2.3.3. The linking and alignment processes are simulated as OpEmuRec packages. Nevertheless the alignment process is skipped in MC simulations since plate misalignment is not taken into account.

The Tracking package : The track reconstruction procedure forms chains of BaseTracks without missing films. These chains serve as a trigger to start the Kalman Filter (KF) [90] procedure for track fitting and following. Tracks are reconstructed with a minimum of two BaseTracks and a maximum of three consecutive missing ones. The final result are long tracks consisting of an array of BaseTracks accompanied by the fit function provided by the KF procedure. To improve the tracking accuracy smoothing is used. In addition, apparatus resolution, provided as an input parameter, and multiple scattering effects are taken into account for the probability and fit calculation. The main criteria for tracks BaseTracks acceptance is the probability given by the KF.
This procedure is reconstituted with an OpEmuRec algorithm called "Tracking".

The vertexing package : The vertexing reconstruction tries to find a convergence of tracks into the interaction point. Two methods are used in OPERA. The FEDRA one computes the minimum distance between a couple of tracks ; this is a pair-based approach and it is explained in more detail in the work of V. Tioukov [88]. The other one is implemented in the SySal software and is based on a global vertexing approach. It looks for an intercept of a group of tracks by extrapolating them in the transverse plane with a certain resolution. This process is described in the work of E. Barbuto [71].
This procedure is reconstituted with an OpEmuRec algorithm called "Vertexing".

The Decay Search Procedure (DSP) : In addition, the DSP is performed to reconstruct the neutrino interaction, either as a vertex or a single track. To find possible interesting events, such as τ or charm decays and/or ν_e interactions, a topological search of decay daughters or parent tracks is done, including an electron/gamma separation search for showers. The topological analysis of the event is finalized with the momentum measurement of the tracks found, thus a reconstruction of the neutrino interaction, the event energy and the type of the interaction can be performed.

The Scanforth scanning

During the ScanForth (SF) scanning, tracks that were found at the vertex and do not have a match in the CS track predictions, are followed downstream the brick to find their stopping point or a possible re-interaction. Thus, the SF methods allow to distinguish muons (isolated stop) from hadronic tracks (re-interaction).

3.1.5   Monte Carlo simulation and testbeam data

The analyses in particle physics are carried out on MC samples to test the detector performance and the analysis framework and then, is applied on physics data ; it is important to check if MC samples are compatible with data to validate such study. This section describes various MC and data samples used in this work.

3.1.5.1   Monte Carlo simulation samples

Numerous analyses in this thesis use extensively MC samples to estimate event location efficiency, electron identification efficiency and electromagnetic showers tool performance. All these samples are defined in table 3.2 and have been processed through the entire OpRelease 4.0 reconstruction. They contain interactions that have occurred randomly in an ECC brick chosen randomly in the whole detector except if the "Observation column" mentions something else.

3.1.5.2   OPERA data

OPERA datasets used in this work are called *data_ electron_ TB_ 4GeV* and *data_ electron_ TB_ 2GeV*. To calibrate the energy and identification of electromagnetic showers as well as to compare to MC performance of these tools, two ECC bricks have been exposed to an electron enriched pion beam (2 and 4 GeV) at CERN on summer 2011. The T9 beamline, described in the work of L. Durieu *et al.* [91], is composed of two Čerenkov detectors to measure electron density in the beam, two wire chambers, for the beam profile monitoring, alternated with two scintillator planes for trigger and finally the ECC bricks placed downstream of all these detectors.

The Čerenkov counters will be used to separate electrons from pions. First, the electron ratio has been measured with Čerenkov detectors. But unfortunately, the efficiency of the Čerenkov detectors is about 10%. So it has been decided to rely on the scintillator counts. Then, the number of needed scintillator counts has been computed to obtained the aimed density. Knowing that the scintillator is the same transverse area size as the ECC and the beam profile is almost flat on the entire ECC transverse area, the expected number of electrons in an exposed ECC can be inferred. All these results are summarized in table 3.1.

	Electron density (# of electron per cm^2)	Electron ratio (%)	Expected number of electrons in each ECC
2 GeV	2.5	23	80
4 GeV	1.4	5.2	50

Table 3.1: The pion contamination and electron density measurements. The expected number of electrons in each ECC brick is given and computed according the method described hereafter.

Name	Channel	Stat.	Observation
MC_ nue_ 1k	ν_e from the beam contamination	1000	-
MC_ nueqe_ 1k	ν_e from the beam contamination	1000	Contains only QE and RES processes
MC_ oscillated_ nue_ 1k	Oscillated ν_e	1000	Mixing parameters are taken from the analysis [31] and $sin^2 2\theta_{13} = 0.11$ is given by the T2K collaboration [92].
MC_ oscillated_ nue_ 3k	Oscillated ν_e generated with ν_μ energy spectrum	3000	The oscillation probability has to be applied a posteriori. The low energy component will not be highly populated.
MC_ taue_ 3k	Oscillated ν_τ with τ decay in electronic mode	3000	The oscillation probability has to be applied a posteriori.
MC_ numunc_ 3k	ν_μ NC interactions	3000	-
MC_ numucc_ 3k	ν_μ CC interactions	3000	-
MC_ electronPion_ 4GeV_ 1k	Mixture of electrons and pions	1000	Monochromatic (4 GeV) particles generated in the first lead plate of a random ECC in the detector.
MC_ electronPion_ 2GeV_ 1k	Mixture of electrons and pions	1000	Monochromatic (2 GeV) particles generated in the first lead plate of a random ECC in the detector.
MC_ electron_ 10k	Electrons	10000	Energies in the range [0,30] GeV and incoming angles in the range [-0.6,+0.6] rad. Particles generated randomly in an ECC of the detector.

Table 3.2: Description of all MC samples used in the analyses of this work.

3.2   Event Location Efficiency Assessment

3.2.1   Efficiency assessment on Monte Carlo

The analysis framework and MC samples available have been defined in section 3.1. Thus, it is now possible to compute event location efficiency in the OPERA experiment for all relevant channels for this work and listed in section 2.6 : oscillated ν_e, $\tau \to e$, ν_μ^{NC}, prompt ν_e, prompt ν_e QE+RES and ($\nu_\mu^{\mathrm{CC}} \xrightarrow{\mathrm{mis}} \nu_\mu^{\mathrm{NC}}$). The strategy to assess these efficiencies is to reproduce as closely as possible the data analysis described in sections 3.1.3 and 3.1.4. The MC samples have been processed with the OpRelease combined to the OpEmuRec package in order to reproduce the event location procedure by applying the criteria listed below :

- *OpCarac and muon track rejection* : the event classification by OpCarac as "CONTAINED" in the OPERA detector or "BORDER SOFT NC" is required. As described in section 3.1.3, the muon identification is based on two criteria but the number of hit TT planes causes a significant contamination of the CC sample with energetic NC events. This wrong classification would reject these NC events which represents an important contribution for a ν_e search study. Moreover, these energetic NC events can be manually reclassified as NC in data during the analysis of the CSd. This peculiar process is not simulated and would cause an additional systematic uncertainty to this study. That is why only the rejection of events with a reconstructed track identified as a muon one is used. This selection will be called "$\overline{\mathrm{Muon\ Id}}$" in the following.
- *BF* : the standard Brick Finding (BF) algorithm is applied on our MC samples and the result of a positive BF with one and two bricks is used, positive meaning that the brick where the MC true neutrino interaction occurred is the one indicated by the BF algorithm as the most probable and the second most probable ones. However, the OpRelease 4.0 does not allow the process of the second most probable brick through the reconstruction.
- *CS* : a Changeable Sheet (CS) tracking algorithm similar to the one applied on data has been implemented in the software. A positive result in this step is the presence of at least two tracks which would point out a convergence to a vertex in the brick.
- *SB* : the success of this process is validated by a stopping point found within 5 plates with respect to the true position of the simulated vertex and at least further upstream to plate 55. Indeed, the TS volume is opened 5 plates upstream as described in section 3.1.4.2, which is the limit to find the real vertex position.

Applying these criteria on MC samples related to this study, will give the event location efficiency once the ScanBack (SB) procedure has confirmed the presence of a neutrino interaction in the analysed brick.

These event location efficiencies will depend on the neutrino energy and the vertex depth in the brick. An illustration of these variations is shown in figure 3.6 for the oscillated ν_e sample, in figure 3.7 for the prompt ν_e sample, in figure 3.8 for the prompt ν_e QE+RES sample, in figure 3.9 for the $\nu_\mu \to \nu_\tau(\tau \to e)$ sample and in figure 3.10 for the ν_μ NC sample.
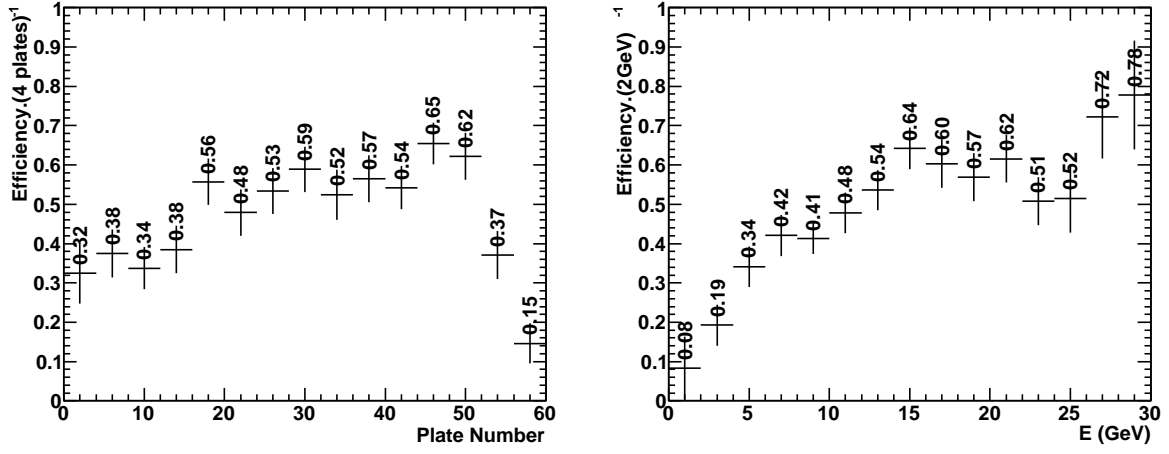
Figure 3.6: On the LHS, location efficiency as a function of the MC true vertex depth in the brick. On the RHS, location efficiency as a function of the MC true neutrino energy. Both of these plots have been obtained with MC simulation of the $\nu_\mu \to \nu_e$ oscillation channel.
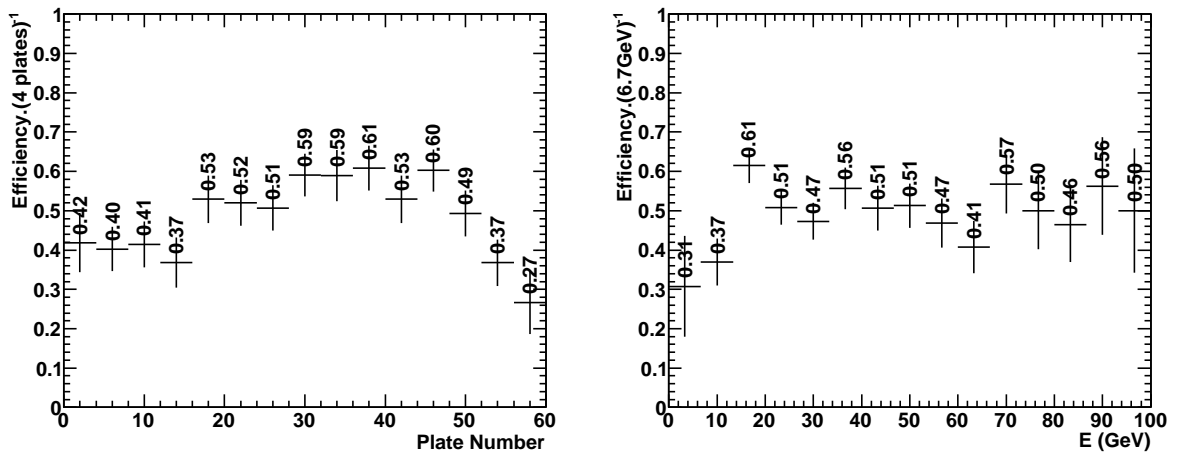
Figure 3.7: On the LHS, location efficiency as a function of the MC true vertex depth in the brick. On the RHS, location efficiency as a function of the MC true neutrino energy. Both of these plots have been obtained with MC simulation of the prompt ν_e channel.
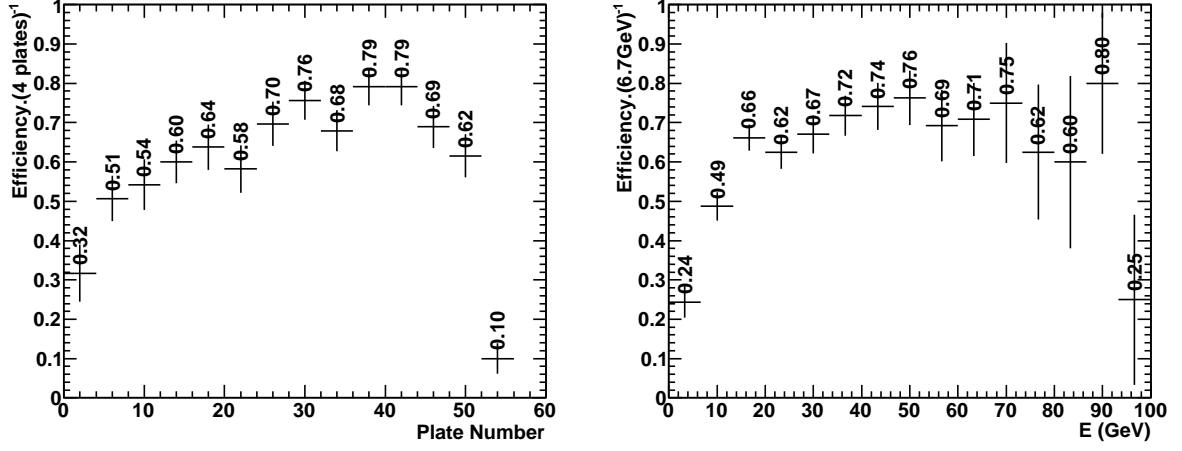
Figure 3.8: On the LHS, location efficiency as a function of the MC true vertex depth in the brick. On the RHS, location efficiency as a function of the MC true neutrino energy. Both of these plots have been obtained with MC simulation of the prompt ν_e QE+RES channel.
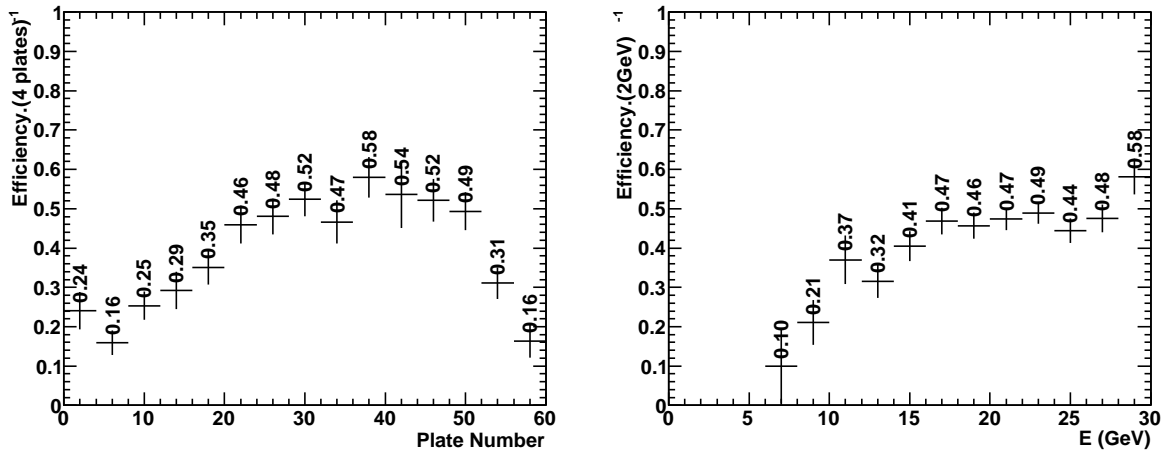
Figure 3.9: On the LHS, location efficiency as a function of the MC true vertex depth in the brick. On the RHS, location efficiency as a function of the MC true neutrino energy. Both of these plots have been obtained with MC simulation of the $\nu_\mu \to \nu_\tau$ with the τ lepton into its electron decay channel.
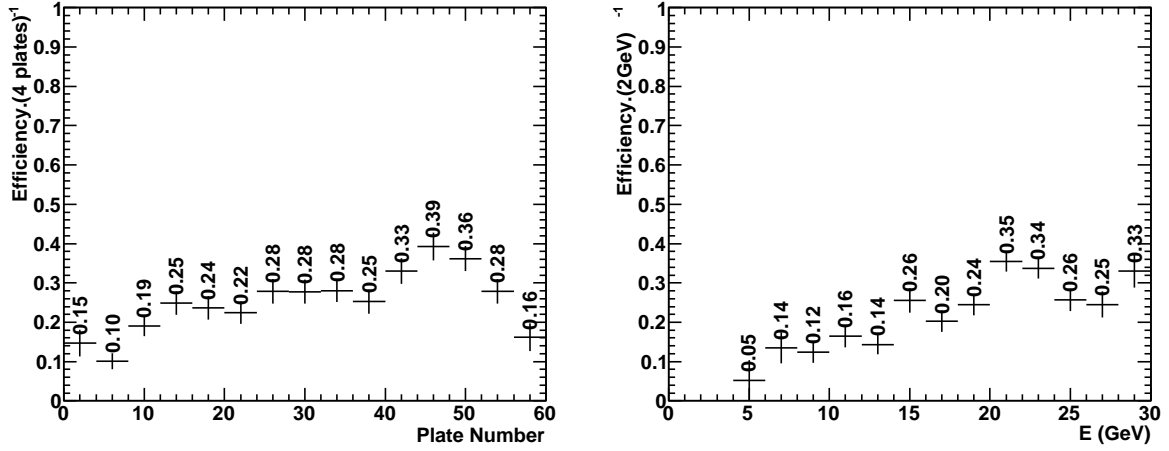
Figure 3.10: On the LHS, location efficiency as a function of the MC true vertex depth in the brick. On the RHS, location efficiency as a function of the MC true neutrino energy. Both of these plots have been obtained with MC simulation of the ν_μ NC channel.
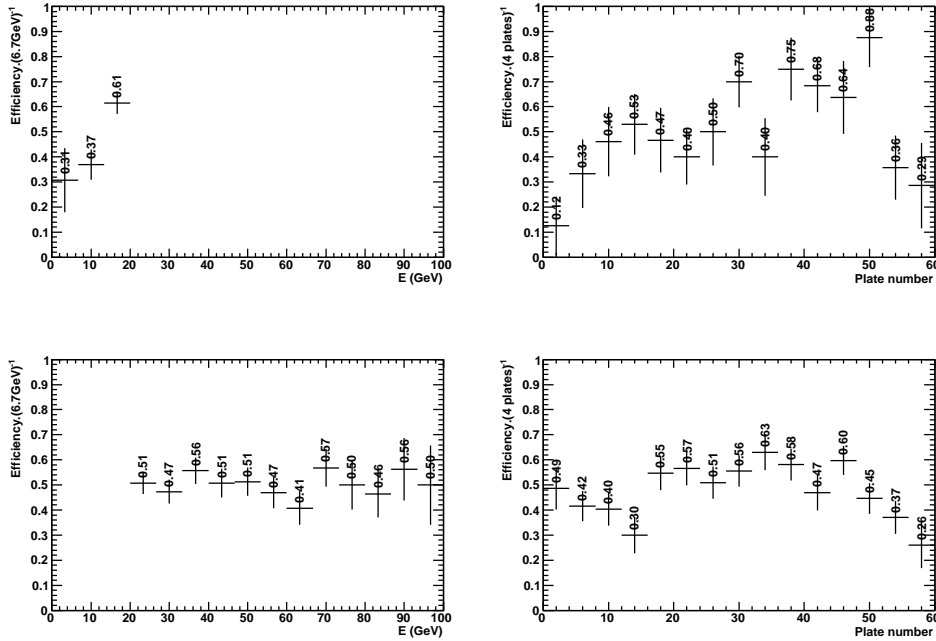
Figure 3.11: Location efficiency as a function of the MC true vertex depth in the brick on the RHS and as a function of the MC true neutrino energy on the LHS. The neutrino events with energy less or equal to 20 GeV on the top panels and the neutrino events with energy greater than 20 GeV on the bottom panels. All these plots have been obtained with MC simulation of the prompt ν_e channel.

The first observation on these plots, looking at the error bars, is that the statistics is not sufficient due to the MC production process of OPERA. The vertex depth decreases significantly in the last 5 plates for all channels because of the small multiplicity in the CSd and in the TT wall downstream of the brick. The event location in the first half-brick is lower, about 40%, than in the second half-brick, about 60%. This effect is due to the low energy neutrino event as we can see for instance with the prompt ν_e MC sample in figure 3.11 where the population has been split in two bins : neutrino energy less or equal to 20 GeV and neutrino energy greater than 20 GeV. Note that these "splitting" methods have been applied to all channels and corresponding plots can be found in appendix F.

Finally the event location efficiency increases with the energy up to 20 GeV. Events with neutrino energies above 30 GeV are not included in this study since an upper energy cut of 20 GeV will be applied.

A summary of the event location efficiency step-by-step for each channel is given in table 3.3 except for the $\nu_\mu^{\mathrm{CC}} \xrightarrow{\mathrm{mis}} \nu_\mu^{\mathrm{NC}}$ channel which is given in table 3.4.

	oscillated ν_e	$\tau \to e$	ν_μ^{NC}	prompt ν_e	prompt ν_e QE+RES
Muon Id	0.897±0.010	0.852±0.009	0.731±0.008	0.752±0.014	0.943±0.007
BF	0.784±0.011	0.727±0.015	0.537±0.009	0.669±0.015	0.841±0.010
CS	0.715±0.026	0.612±0.036	0.376±0.016	0.660±0.024	0.807±0.022
SB	0.642±0.033	0.524±0.054	0.340±0.018	0.636±0.028	0.730±0.029

Table 3.3: Summary of event location efficiency for each reconstruction step up to the location of the neutrino interaction by the SB procedure. The efficiency of each step is cumulative with respect to previous steps. The uncertainties quoted are statistical. It is important to note that numbers from the BF up to the location are extrapolated from the 1-brick BF, CS and SB efficiencies since the OpRelease 4.0 cannot process the second brick ; that is also why the uncertainties are higher than for other numbers.

	$\nu_\mu^{\mathrm{CC}} \xrightarrow{\mathrm{mis}} \nu_\mu^{\mathrm{NC}}$
Muon Id	0.073 ± 0.005
BF	0.060 ± 0.025
CS	0.053 ± 0.007
SB	0.052 ± 0.007

Table 3.4: Event location efficiency for the $\nu_\mu^{\mathrm{CC}} \xrightarrow{\mathrm{mis}} \nu_\mu^{\mathrm{NC}}$ channel. It includes the misidentification of the muon track. The efficiency of each step is cumulative with respect to previous steps. The uncertainties quoted are statistical. It is important to note that numbers from the BF up to the location are extrapolated from the 1-brick BF, CS and SB efficiencies since the OpRelease 4.0 cannot process the second brick ; that is also why the uncertainties are higher than for other numbers.

Table 3.3 shows that channels with an electron in the final state have a location efficiency higher than 50%. The ν_μ NC channel is significantly lower and the difference is in the muon identification. Indeed, energetic NC events present long hadronic tracks which can be misidentified by the ED and the muon identification algorithm as muons. This effect means a reduction of this background for the oscillation studies in chapter 5. Table 3.4 shows that the $\nu_\mu^{\mathrm{CC}} \xrightarrow{\mathrm{mis}} \nu_\mu^{\mathrm{NC}}$ location efficiency is small thanks to the muon identification which is fortunate since the ν_μ CC rate quoted in table 2.8 is high.

These location efficiencies have to be checked with the OPERA data, especially as the data reconstruction is not exactly the same as the MC reconstruction process. This is performed in the next section.

3.2.2 Comparison of the Monte Carlo simulation with data and systematic uncertainty

It will be explained in section 5.3.1 that analysed data in this thesis will be the 2008 and 2009 data samples. At that time, the muon identification was not as efficient as it is now. Muon identification has to be reprocessed with the last developments of this algorithm. Meanwhile, the present knowledge of the classification of the events in 2008 and 2009 data is summarized in table 3.5.

	2008		2009	
	0μ	1μ	0μ	1μ
Events found with the ED	406	1292	1097	2460
Events located in ECC	169	834	360	1490
DATA location efficiency	0.416 ± 0.024	0.646 ± 0.013	0.328 ± 0.014	0.605 ± 0.010
MC location efficiency with two CS tracks	0.340 ± 0.018	0.579 ± 0.029	0.340 ± 0.018	0.579 ± 0.029
MC location efficiency with one CS track	-	0.775 ± 0.026	-	0.775 ± 0.026
Systematic uncertainty	0.038	0.065	0.006	0.085

Table 3.5: Summary of event location in 2008 and 2009 data. 1μ numbers are quoted as a reference sample. 0μ represents the sample in which we look for electrons [58]. The MC location efficiency computed in section 3.2.1 is added for 0μ (ν_μ NC) and the event location efficiency for the 1μ events is computed as for the ν_μ CC events in section 3.2.1 but accepting events with a reconstructed muon track in the EDs instead of rejecting them. The last line presents the systematic uncertainty inferred from the MC/data comparison.

On the one hand, two types of MC event location efficiency are quoted, one using the CS selection of two tracks as described in section 3.1.4.2 and the other one with only one CS track. For 0μ events, the 2 CS tracks are well suited to determine roughly whether the vertex is in the brick. For 1μ events, if only one CS track is found and is connected with the ED 3D track identified as muon, the decision process can come up to validate the event as located in the considered brick according to the information of TT hits and possibly a neighbour brick. The true CS selection efficiency of 1μ events is most probably between the two values quoted in table 3.5. There is room for improvements by implementing the state-of-the-art of the decision process in the CS scanning in the MC simulation. The systematic uncertainty for 1μ events kept in this study will be the larger one in order to be conservative. Taking the event location efficiency difference between MC and data is motivated by the fact that the main error on this process is the classification of the events as 0μ or 1μ. In data, after the systematic classification, the sample are purified by reclassifying misidentified 0μ events as 1μ ($\sim 15\%$ of located 0μ events) or misidentified 1μ events as 0μ ($\sim 1\%$ of located 1μ events). The difference between event location in data and in a pure sample of NC events assesses the systematic uncertainty on the remaining muon misidentification after reclassification. Finally, to take into account this discrepancy between the MC and data, the half of the difference will be considered as the systematic uncertainty of the location efficiency within 2σ. The systematic uncertainties quoted in table 3.5 are different between 2008 and 2009. Because of the presence of external background in 2008 data sample, the event location efficiency are larger. Given the relatively large variability of the location efficiency with the number of CS tracks, it seems reasonable to take as the systematic uncertainty on the event location efficiency the average value, weighted by the beam luminosity in 2008 and 2009, inferred from the comparison of 2008 and 2009 data with MC simulations : 0.340 ± 0.017 for NC events and 0.775 ± 0.078 for CC events.
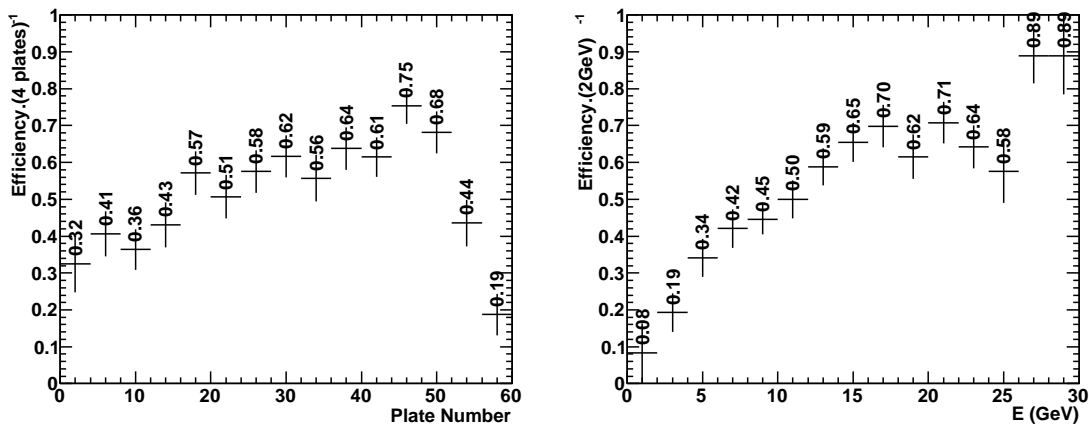
Figure 3.12: On the LHS, the location efficiency as a function of the MC true vertex depth in the brick. On the RHS, the location efficiency as a function of the MC true neutrino energy. Both of these plots have been obtained with MC simulation of the $\nu_\mu \to \nu_e$ oscillation channel by using only the OpCarac "CONTAINED" or "BORDERSOFTNC" classification.

To estimate the impact of the muon misidentification on the different channels used in this work, the event location efficiency by using the ED tags "CONTAINED" and "BORDERSOFTNC" associated to the absence of a muon track (defined as the standard procedure) is compared at the same sample using only the ED tags, for instance on the oscillated ν_e MC sample. The standard procedure has been already shown in figure 3.6 and the simplified selection is shown in figure 3.12. The same plots for the other channels can be found in appendix F.

The event location efficiency is globally enhanced of about 10%. Indeed, some 0μ events, misclassified as 1μ because of the misidentification of an energetic hadron track as a muon one, are recovered and in addition are easy to localize since those are energetic. In fact, figure 3.12 shows a more important enhancement at high energy than figure 3.6.

Table 3.6 summarizes the difference between the two types of event classification for each channel studied in this thesis work.

	oscillated ν_e	$\tau \to e$	ν_μ^{NC}	prompt ν_e	prompt ν_e QE+RES
Standard event location	0.642±0.033	0.524±0.054	0.340 ± 0.018	0.636±0.028	0.730±0.029
Simplified event location	0.695±0.031	0.585±0.054	0.430 ± 0.019	0.805±0.024	0.732±0.029
Efficiency loss	0.053	0.061	0.09	0.169	0.002

Table 3.6: Summary of event location efficiency for each event classification procedure. The possible misidentification of the muon track is irrelevant for the $\nu_\mu^{\mathrm{CC}} \xrightarrow{\mathrm{mis}} \nu_\mu^{\mathrm{NC}}$ channel.

The muon misidentification implies a drop of 5% of the event location efficiency for the signal. However, the drop for the prompt ν_e events is much more important. The irreducible background represented by this channel is thus reduced.

3.3   Statistical Methods

Statistical methods in the analysis tools are used for several purposes in this thesis : electron/pion separation, electromagnetic shower energy estimation and background rejection for an oscillation study. In all these studies, there is a large number of discriminating variables and correlations among them. Hence a combination of independent cuts on each variable would not be suitable. Moreover, in the oscillation study, the number of signal events expected is about one order of magnitude below the number of background events. We chose to use multivariate analysis to optimize the separation power of each variable. Two methods have been used : Fisher discriminant and ANN.

These two methods are naturally different and achieve also different performances. Differences include robustness, linear or non-linear correlations, overtraining and so on. For the shower analysis purpose, independent C++ programs based on a ROOT class TMultilayerPerceptron have been used. For the oscillation study, the method has been implemented in an analysis software called Toolkit for MultiVariate Analysis with ROOT (TMVA) [93]. For a classification study, typically signal and background, distributions of discriminating variables fed the analysis tool which gives a unique classification output variable. This method has to be previously trained on a specific sample to determine the coefficients used afterwards to optimize the background rejection on another sample. The two methods are described in detail in appendix E.

Chapter 4

Electromagnetic Shower Reconstruction In Nuclear Emulsions

Electron detection in the OPERA experiment is a crucial goal to the neutrino oscillation physics in the $\nu_\mu \rightarrow \nu_\tau$ ($\tau \rightarrow e$) as well as in the $\nu_\mu \rightarrow \nu_e$ ($\nu_e \rightarrow e +$ hadronic shower) channels. To this end, the geometrical reconstruction of the electromagnetic showers which spread in the OPERA brick, the identification of the showers as electrons (or pions) and the estimation of the energy are performed. In this section, I will describe the shower reconstruction algorithm in the OPERA framework followed by the identification and energy estimation performance. A comparison with test beam data to calibrate these analysis tools will be also shown. Finally, I will report on the systematic uncertainties and the new features of the electromagnetic shower reconstruction tool.

4.1   Phenomenology Of Electromagnetic Shower

Passage of charged particles through matter has been extensively studied in the 1950's. A good summary is given in the reference [21]. However, a brief reminder of what is important for our purpose is given hereafter. From the Bethe-Bloch formula, it is assumed that the energy loss by the incident particle in a single interaction is negligible with respect to its total kinetic energy. This hypothesis is true only if the mass of the incident particle is much greater than the electron mass. Since electrons and positrons do not satisfy this hypothesis, the formula that describes their energy losses is different. As we shall see, in the energy range of our interest [1-20 GeV] electromagnetic processes, which are responsible for the electron-positron shower development, dominate. The integrated energy losses of an electron of energy E traversing a material of thickness t decrease exponentially with t and are proportional to the incident energy E_0 as $\delta E_{\mathrm{e}}(t) = E_0\, e^{-\frac{t}{X_0}}$ where X_0 is the radiation length of the material. For a pion, $\delta E_{\mathrm{e}}(t) = \mathrm{constant}$. This difference will be used to distinguish electrons from pions detected in the OPERA bricks.

High energy electrons predominantly loose energy in matter by bremsstrahlung and high energy photons by e^+e^- pair production ; the ionization is negligible at high energy. The characteristic amount of matter which is significant for these interactions is called the radiation length X_0. According to the previous statement about the integrated average energy losses, the radiation length is the mean distance over which a high energy electron looses $\frac{1}{e}$ of its energy by bremsstrahlung and also $\frac{7}{9}$ of the mean free path for pair production by a high energy photon. Consequently, X_0 corresponds also to an appropriate scale to describe electromagnetic shower and can be parametrized as in equation 4.1 [94, 21].

$$X_0 = \frac{716.4\,[\text{g/cm}^2]\,A}{Z(Z+1)\,ln(287/\sqrt{Z})} \tag{4.1}$$

with Z and A the atomic number and the atomic mass of the absorber, respectively.

The critical energy E_c can be defined as the energy at which the electron energy loss rate by bremsstrahlung is equal to ionization loss rate :

$$(\frac{dE}{dx})_\text{brem} = (\frac{dE}{dx})_\text{ionization} \tag{4.2}$$

A fit of experimental measurements of the critical energy for different chemical compounds gives two computations [21] :

$$E_c(\text{liquids, solids}) = \frac{610\text{MeV}}{Z+1.24} \tag{4.3}$$

$$E_c(\text{gases}) = \frac{710\text{MeV}}{Z+0.96} \tag{4.4}$$

When secondary particles in the electromagnetic shower reach this critical energy, the development of the shower is considered as stopped. In OPERA, the fiducial mass is composed of lead which means : $E_c \approx 7\,\text{MeV}$ and $X_0 = 5.6$mm.

A possible parametrization of an electromagnetic shower is given by the work of C.W. Fabjan *et al.* [95]. The longitudinal profile can be described by a gamma distribution :

$$\frac{dE}{dt} = E_0\,b\,\frac{(bt)^{a-1}e^{-bt}}{\Gamma(a)} \tag{4.5}$$

with the scale variable $t = \frac{x}{X_0}$ and where a and b are free parameters. "x axis" is defined by the direction of the incoming electron which generates the shower.

The various possibilities to use such information in the algorithms for the particle identification and energy estimation will be discussed in the following. The transverse development of the shower has been extensively studied e.g. in the work of W.R. Nelson *et al.* [96] and the work of G. Bathow *et al.* [97]. These examples use the sum of exponential functions or Gaussian functions calibrated according to the detector response for each case. On the average, only 10% (1%) of the energy lies outside the

cylinder with radius R_M (3.5 R_M) called Moliere radius and is used as the scale variable to describe the transverse profile :

$$R_M = X_0 \, \frac{E_s}{E_c} \quad \text{where } E_s \approx 21 \text{ MeV.} \tag{4.6}$$

$$R_M = 1.7 \, \text{cm} \quad \text{in the OPERA case.}$$

4.2 Electromagnetic Shower Reconstruction Algorithm

4.2.1 Principle

In order to reconstruct an electromagnetic shower as it develops in an OPERA brick, an algorithm has been elaborated in 1998 [72]. The mechanism of electron and photon interactions in matter has been previously described in section 4.1 and has shown that many tracks are expected in the emulsions. A simplified representation of those showers stands in two steps :

1. *The shower initiation with reconstructed tracks* : a shower needs to be initiated with a seed. A reconstructed track corresponds more likely to a physical object instead of a single BaseTrack (BT) which could be background.

2. *The shower reconstruction* connecting BTs from a film to the next one is based on geometrical criteria and describes the development inside the material.

4.2.2 Shower initiation with reconstructed tracks

First, the algorithm is going to reconstruct tracks. A complete description and the parameter set used for that process is given in section 3.1.4.2. BTs are selected according to the angular and position acceptances to build tracks. From many possible connections, the tracks are selected based on a χ^2 cut. These collections of BTs serve as a trigger for starting the track fitting with the Kalman Filter (KF) [47] in order to get a complete object. Finally, the reconstructed tracks are propagated to check whether they are fragments of tracks or they correspond to a real physical track. Once more the KF is used a posteriori for smoothing.

Each track reconstructed by this procedure is considered as a candidate for the shower reconstruction.

4.2.3 Shower reconstruction

Shower propagation is applied film by film starting with the most upstream one.

For each candidate track, the most upstream BT is considered as an initiator. Then, this BT is projected in the next film downstream where the algorithm will look for a BT to attach to that initiator with geometrical considerations summarized in table 4.1.
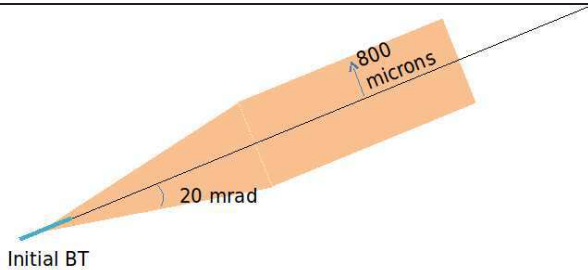
Variables used for the selections	Values of the selections
Basetrack in a transverse area of 2500x2500 μm^2 around the initiator	$abs(x_{\mathrm{BT}} - x_{\mathrm{initiator}}) \leq 1250$ AND $abs(y_{\mathrm{BT}} - y_{\mathrm{initiator}}) \leq 1250$
Cut on the angle of the BT	$abs(\theta_{\mathrm{X}}) < 0.5\,\mathrm{rad}$ AND $abs(\theta_{\mathrm{Y}}) < 0.5\,\mathrm{rad}$
Angle difference between the BT and the projection of the initiator	$abs(\theta_{\mathrm{BT}}^{\mathrm{3D}} - \theta_{\mathrm{init}}^{\mathrm{3D}}) < 0.150\,\mathrm{rad}$
Position difference between the BT and the projection of the initiator	$abs(r_{\mathrm{BT}} - r_{\mathrm{init}}) < 0.150\,\mathrm{mm}$
The BT has to be inside a cone+cylinder shown on the right	

Table 4.1: Summary of the selections in the BT collection process.

The algorithm will proceed iteratively from a film to another up to the last film of the volume used in the analysis and defined in section 3.1.4.2. Usually, only showers which spread over at least four films are kept as physical electromagnetic showers.

Once a shower is reconstructed, it has to be identified and its energy has to be estimated. As we note in section 4.1, the identification which is mainly a separation between electrons and pions can be performed by using Multiple Coulomb Scattering (MCS) of tracks ; it was also shown that it can be used to estimate the energy. Both analyses will use ANN which has been used extensively in many high energy physics experiments for the same goals. A description of the ANNs analysis tool is given in appendix E.2.

4.3 Electron Identification

MCS implies a behaviour that is not the same between electron and pion tracks, especially in terms of angular difference between several fragments of the track. Moreover, this scattering behaviour associated with a different phenomenology of hadronic

showers [98][1] and electromagnetic showers infers a discrepancy between pion and electron shower shapes. These two pieces of information will be used to feed an ANN in order to separate electrons from pions. MC samples used for this purpose will be *MC_electronPion_4GeV_1k* and *MC_electronPion_2GeV_1k*, while data samples will be *data_electron_TB_4GeV* and *data_electron_TB_2GeV* ; all these samples are described in section 3.1.5. Note that the electron-pion proportion is the same for MC as for data. First the principle of the algorithm will be described. Then, the performance of that tool will be presented ; the efficiency of the electron identification for the ν_e and ν_τ ($\tau \to e$) channels have been checked in section 4.3.3 ; simulation samples dedicated to this study are *MC_oscillated_nue_1k* and *MC_taue_3k*.

4.3.1   Principle of the algorithm

As it is shown in figure 4.1, the longitudinal profile of electrons and pions is very different as well as the number of BTs in the reconstructed shower. These pieces of information are used as input values to feed the ANN.
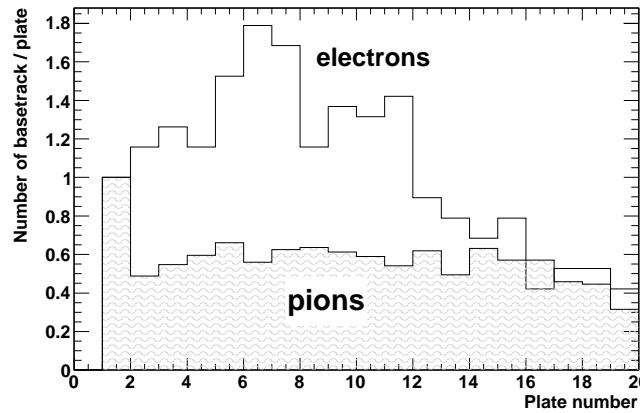
Figure 4.1: Mean longitudinal profiles for electrons and pions, both with an energy of 4 GeV.

Table 4.2 shows all the variables given as inputs for the ANN.

The ANN structure is composed by two hidden layers with 63 and 21 neurons, appendix E.2 describes in more detail the ANN structure. The training is stopped after 120 epochs when the predefined sampling error, computed on the validation sample, reaches a plateau before starting to increase.

---

[1]This reference gives a description of the phenomenology of hadronic showers and compares the characteristic properties of hadronic and electromagnetic showers.

Description of the variables	Physical meaning of the variables	Typical value for electrons at 4 GeV	Typical value for pions at 4 GeV
Multiplicity of BTs in the shower	This observable is expected approximately proportional to the energy	21.3 ± 1.8	12.8 ± 0.2
The mean value of the angular difference between an initiator and one BT in the shower distribution	An effective method to take into account the scattering of particles in the shower	35.9 ± 0.2 mrad	3.97 ± 0.01 mrad
The Root Mean Square (RMS) value of the angular difference between an initiator and one BT in the shower distribution		24.9 ± 0.1 mrad	2.87 ± 0.01 mrad
The mean value of the position difference between an initiator and one BT in the shower distribution		$40.1 \pm 0.2 \, \mu$m	$10.64 \pm 0.03 \, \mu$m
The RMS value of the position difference between an initiator and one BT in the shower distribution		$27.1 \pm 0.1 \, \mu$m	$7.93 \pm 0.03 \, \mu$m
The content of each bin of the shower longitudinal profile i.e. the number of BTs per film.	This profile is physically parametrized with the energy	see figure 4.1	see figure 4.1

Table 4.2: Summary of the ANN inputs of the electron identification algorithm. The typical values are actually the mean value of the distributions of these variables calculated with the MC sample *MC_ electronPion_ 4GeV_ 1k* described in section 3.1.5.1.

The ANN gives an output variable close to 1 for electrons and to 0 for pions. An appropriate cut on this variable depending on the number of films used to identify the shower can give an efficiency-based approach, for which the probability of the shower to be electron-induced is higher than 90% or a purity-based approach, where the probability of the shower to be pion-induced is less than 1%.

data_ electron_ TB_ 4GeV and *data_ electron_ TB_ 2GeV* are the data samples used to calibrate the energy and the identification of electromagnetic showers as well as to compare to MC performance of these tools. Two ECC bricks have been exposed to an electron enriched pion beam (2 and 4 GeV) at CERN on summer 2011.

Figure 4.2 displays a classical identification result of pion-electron separation in a 4 GeV pion beam enriched with electrons. Figure 4.3 displays the same for the 2 GeV case.
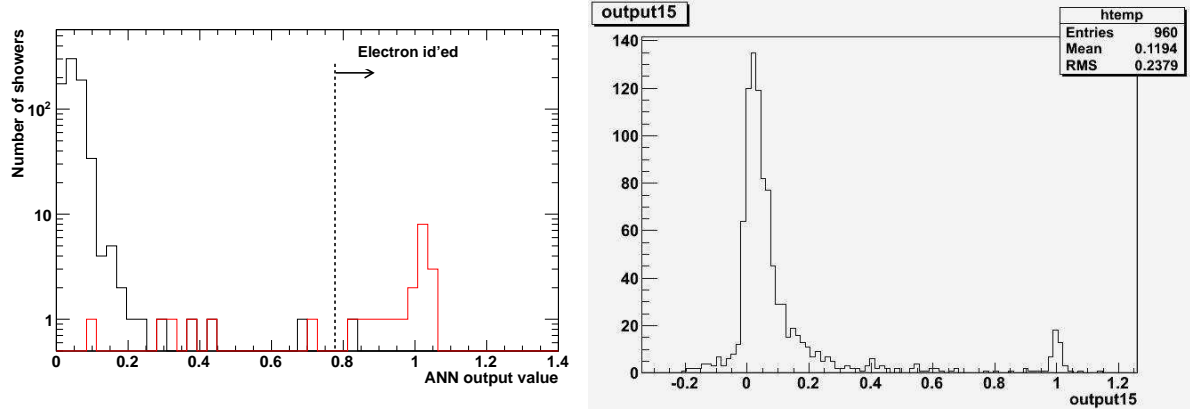
Figure 4.2: Output variable of the identification ANN for testbeam data at 4 GeV on the RHS [99] and for a MC sample testbeam-like on the LHS showing the ANN output value for MC true electrons in red and for MC true pions in black.
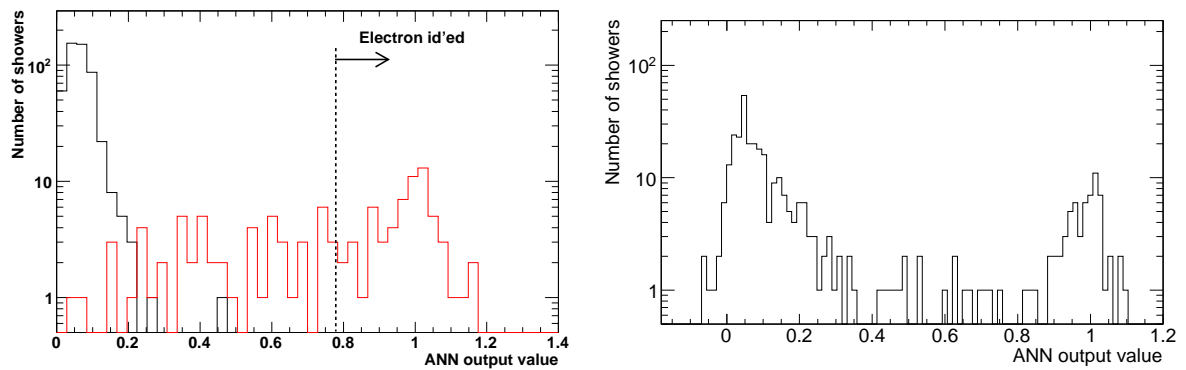
Figure 4.3: Output variable of the identification ANN for testbeam data at 2 GeV on the RHS [99] and for a MC sample testbeam-like on the LHS showing the ANN output value for MC true electrons in red and for MC true pions in black.

Figure 4.2 shows the good separation capability of the identification tool with the MC simulations : only one pion is identified as an electron and almost all electrons are well identified. On the plot corresponding to data, the ANN gives for some showers an output value below 0. This can be explained by the fact that the Neural Network (NN) has been trained with MC simulations where the instrumental background is missing. In data, due to the presence of background tracks, unexpected inputs feed the NN and the output can be out of the "normal" range [0,1]. However the proportion of identified electrons and pions in data are in agreement with the MC results.

Figure 4.3 shows the same behaviour but none pion is identified as electron. There are more misidentified electrons because of a smaller development of showers at low energy which reduces the performance of the identification algorithm.

4.3.2   Performance

As stated earlier, the ANN output values vary from 0 to 1, around 0 for pions and 1 for electrons. An appropriate cut on this value to ensure an electron identification efficiency of more than 90% is determined. However, it varies depending on the number of films used for the shower reconstruction. In this case, less than 1% of the selected showers are from pion contamination. Figure 4.4 shows the performance of the algorithm with a MC simulation of pure electrons within the entire brick. This allows to define a cut on the output variable distribution at a value of 0.78 beyond which the shower is identified as an electron. Figure 4.5 displays the performance of the algorithm with a MC simulation of oscillated $\nu_\mu \to \nu_e$. On the LHS of this figure, the distribution shows the result when the full brick available volume is considered whilst on the RHS, the distribution is computed for showers reconstructed in the OPERA standard volume for which 10 emulsion films are considered for the scanning. Figure 4.6 shows the performance of the algorithm when the $\nu_\mu \to \nu_\tau$ sample is used in the MC simulation with the τ lepton reconstructed into its electron decay channel. Evenly, the left distribution corresponds to the ANN output using the full brick available volume whilst the right one considers the standard 10 emulsion films volume.
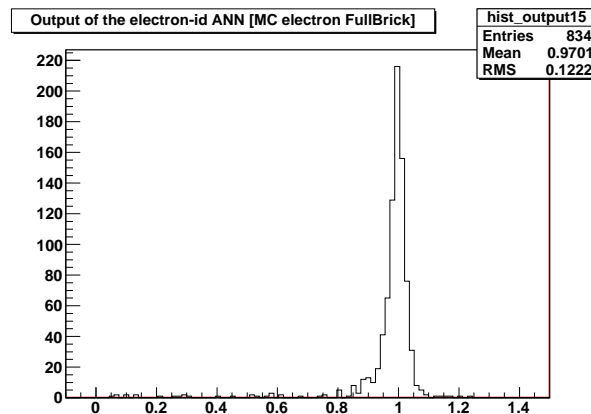
Figure 4.4: MC simulation Neural Network output distribution for the pure electron sample using the full brick information thus defining the cut at 0.78 for the ANN output.
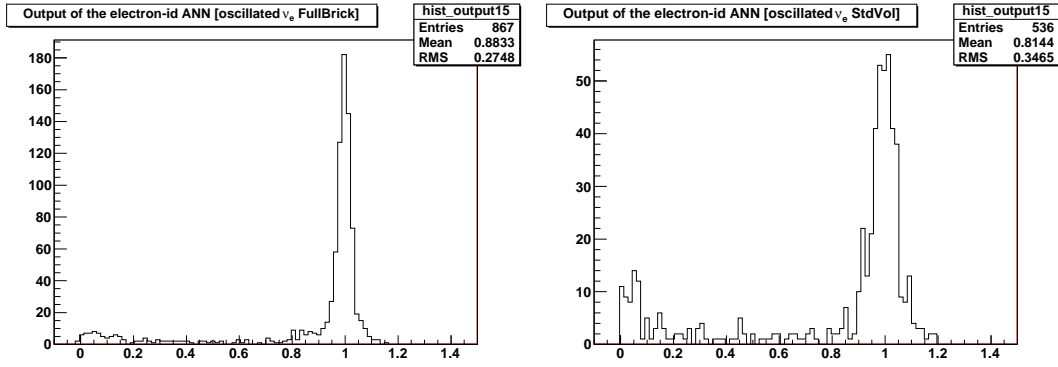
Figure 4.5: MC simulation Neural Network output distribution for the $\nu_\mu \to \nu_e$ oscillation channel. The left distribution corresponds to the ANN output using the full brick available volume whilst the right one considers the standard 10 emulsion films volume.
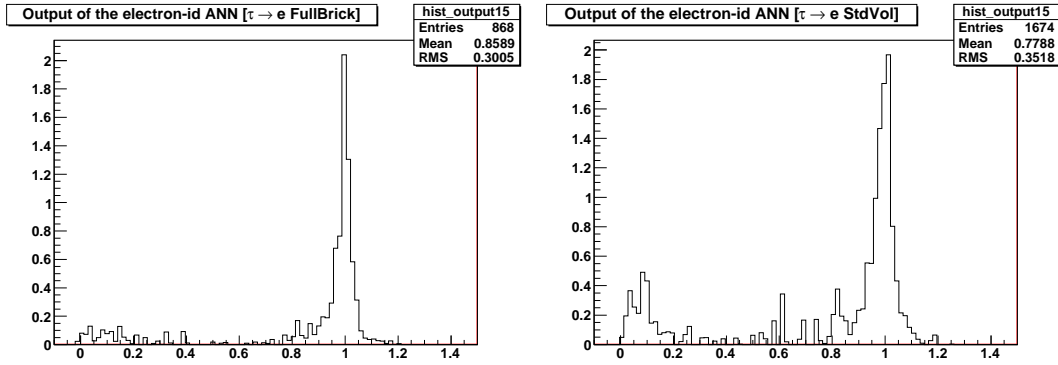
Figure 4.6: MC simulation Neural Network output distribution for the $\nu_\mu \to \nu_\tau$ oscillation channel with the τ lepton reconstructed into its electron decay channel. The left distribution corresponds to the ANN output using the full brick available volume whilst the right one considers the OPERA standard 10 emulsion films volume.

The identification performance can be estimated both on the MC samples testbeam-like and on the data of the above mentioned testbeam campaign. In the MC sample, each track is systematically processed through the shower reconstruction and the identification algorithm. In the data, the first approach has been to process the shower reconstruction as in the MC sample, on all tracks called "beam" tracks. The brick exposure implies that particles, electrons and pions, are incoming the brick by the upstream side and then loose energy by showering for the electrons and ionization for the pions. "Beam" tracks correspond to all reconstructed tracks with three fragments of tracks in the three first emulsion films. Those will be used as what we called initiator track in the shower algorithm.

The result of this process gives 260 tracks identified as showers out of 960 "beam" tracks in the 4 GeV brick ; the number of expected electrons quoted in table 3.1 is 50 and is inferred from the analysis of the Čerenkov counters placed in the beam upstream of the

ECC as explained in section 3.1.5.2. Pions have been reconstructed as electron showers because of the presence of a large amount of background tracks (instrumental) along the pion track. This effect is not reproducible in MC simulations since the instrumental background is not yet included. In the data processing, a specific quality cut on BTs has been applied in order to reject this background and avoid the misidentification of pions as electrons to purify the sample before reprocessing shower identification. The identified electrons are then visually inspected to determine if they looks like electron showers or pions associated to background tracks. The result of this processing is summarized in table 4.3.

E (GeV)	"Beam" tracks	Expected electrons	Selected tracks	Electron tracks confirmed
2	350	80	69	49
4	960	50	52	43

Table 4.3: Result of the electron testbeam data reprocessing according to the selections described above.

The identification efficiencies with the testbeam data and with the MC simulations are summarized in table 4.4. Note that I estimated these identification efficiencies up to 4 GeV because of the existence of the testbeam data up to that energy. Identification performance for electromagnetic showers up to 16 GeV can be found in the work of F. Juget and F.Meisel [73] as well as in the work of L. Arrabito *et al.* [100].

E (GeV)	MC		DATA		
	$\epsilon_{e \to e}$ (%)	$\epsilon_{\pi \to e}$ (%)	$\frac{\text{selected}}{\text{expected}}$ (%)	$\frac{\text{confirmed}}{\text{selected}}$ (%)	$\frac{\text{confirmed}}{\text{expected}}$ (%)
2	60.2±4.5	0.14±0.14	86 ± 4	71 ± 5	61 ± 5
4	76±8	0.14±0.14	100±3	83 ± 5	86 ± 5

Table 4.4: Summary of the electron identification algorithm performance with $\epsilon_{\alpha \to \beta} = \frac{\text{Number of MC true } \beta \text{ identified as } \alpha}{\text{Total number of MC true } \beta}$ and $\eta_\alpha = \frac{\text{Number of particle identified as } \alpha}{\text{Number of expected } \alpha \text{ particles}}$.

Comparing the results with the MC simulations and with the testbeam data obtained with a systematic identification algorithm use shows that identification efficiencies are different for MC and for data mainly due to a different analysis process described above. The pion contamination in data is not reproducible in the MC simulation since the instrumental background is not included in the latter. However, if we consider the visual inspection as a process which makes the pion contamination in data going to 0, the first and the last column of table 4.4 become comparable and could show an agreement between MC and data.

An on-going development with the same algorithm consist in a separation of electron showers from gamma showers based on the principle that shower development is slightly different due to the first process which initiates the interaction, i.e. bremsstrahlung or pair production.

4.3.3   Identification efficiency results

4.3.3.1 $\nu_\mu \to \nu_e \, (e)$ channel

Shower reconstruction and electron identification processes thus established are applied to MC simulation of OPERA electron neutrino events, both from beam and from the oscillation process $\nu_\mu \to \nu_e$. The identification efficiency has been evaluated as a function of a variable number of films. The results are shown in figure 4.7 and summarized in table 4.5.
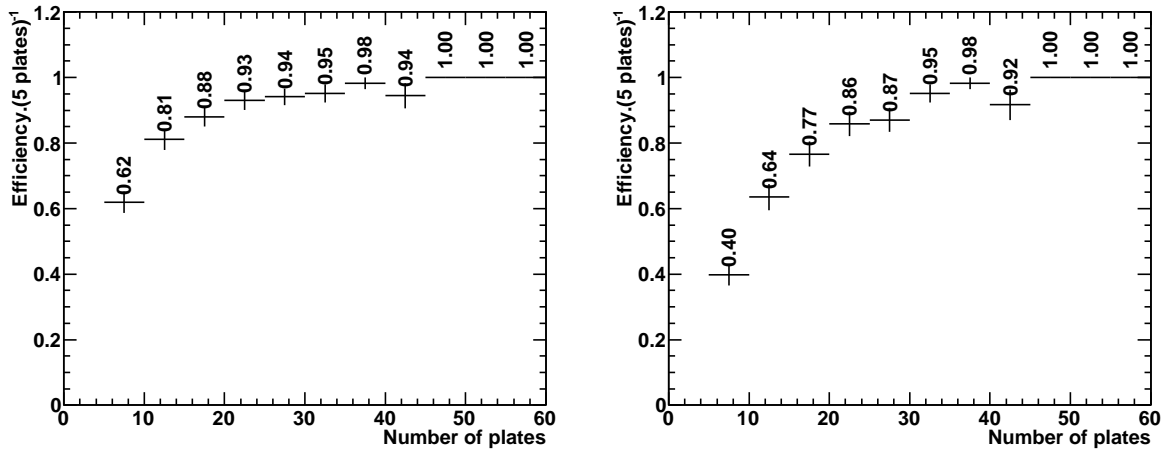
Figure 4.7: Electron identification efficiency as a function of the shower extension in terms of number of films obtained with MC simulation of the $\nu_\mu \to \nu_e$ oscillation channel on the LHS. The same efficiency but only for MC true electron showers on the RHS. The difference gives the systematic uncertainty on identification of showers.

On the LHS of figure 4.7, the plot shows the result given by the identification tool. The right plot shows the efficiency only for the true electrons. The difference between the two plots comes from the gamma contamination produced by neutral pions. These two cases correspond to the limits of the effect of the gamma contamination on the electron identification. The mean value of the difference between the two histograms is taken as the systematic uncertainty of the identification process. If the difference is zero, the statistical error corresponding to 1 event out of the bin population is taken as the systematic uncertainty. The purity of the electron identification process is given by dividing the left histogram by the right one.

The MC true identification of reconstructed showers is done by computing the ratio of BaseTracks linked to a hit of the primary electron divided by the total number of BaseTracks in the shower. This ratio is illustrated by figure 4.8. The 0-value of that ratio is mostly composed by π^0 and stress the importance of a gamma-electron separation tool.
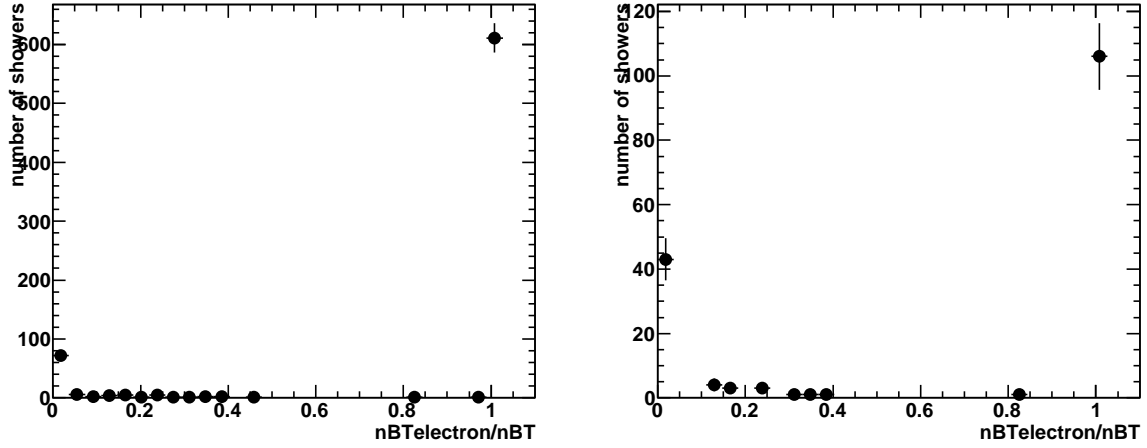
Figure 4.8: Ratio of BaseTracks linked to a hit of the primary electron divided by the total number of BaseTracks in the shower with all events on the LHS and with only showers which have an extension of 10 plates at maximum on the RHS. Both of these plots are obtained with MC simulation of the $\nu_\mu \to \nu_e$ oscillation channel. A cut to 0.5 is used to evaluate the misidentification of electron showers.

Number of films	Identification efficiency	Identification efficiency systematic uncertainty	Identification purity
7.5	0.62	0.11	0.65
12.5	0.81	0.09	0.79
17.5	0.88	0.06	0.88
22.5	0.93	0.04	0.92
27.5	0.94	0.04	0.93
32.5	0.95	0.02	1.00
37.5	0.98	0.01	1.00
42.5	0.94	0.01	0.98
47.5	1.00	0.01	1.00
52.5	1.00	0.03	1.00
57.5	1.00	0.03	1.00

Table 4.5: Electron identification efficiency and purity for the $\nu_\mu \to \nu_e$ oscillation channel.

It is shown with the values of table 4.5 that showers reconstructed with an extension of 10 films have an electron identification efficiency value of $(81 \pm 9)\%$. If more films are used, the mean electron identification efficiency is about $(95 \pm 4)\%$. Thus, to search for and identify an electron and therefore a ν_e candidate event in the OPERA ECC,

within the OPERA nominal scanning procedure, a minimal number of 10 scanned films is required. In which case, the final shower reconstruction and identification mean efficiency combined to the location one is $(47 \pm 10)\%$ for the oscillation channel $\nu_\mu \to \nu_e$ using the efficiencies and their systematic error mentioned above for the electron identification and quoted in table 3.6 for the event location.

However, once the event is identified as an electron event, the volume scanned is extended to the entire brick. Since the systematic uncertainty depends on the number of films as illustrated in table 4.5, one can improve the systematic uncertainty by using all emulsions available in the event and thus give a more realistic uncertainty on the identification procedure. In our 2008-2009 data sample, the ν_e candidate events span over 20 plates in average. The final shower reconstruction and identification mean efficiency combined to the location one is therefore $(47 \pm 8)\%$.

4.3.3.2 $\nu_\mu \to \nu_\tau \, (\tau \to e)$ channel

The same shower reconstruction and electron identification procedures are applied to MC simulation of OPERA tau neutrino events, from the oscillation process $\nu_\mu \to \nu_\tau$ with the τ lepton into its electron decay channel. The identification efficiency has been evaluated for a different number of films. The results are shown in figure 4.9 and summarized in table 4.6. The ratio used to assess the identification systematic uncertainty is illustrated by figure 4.10.
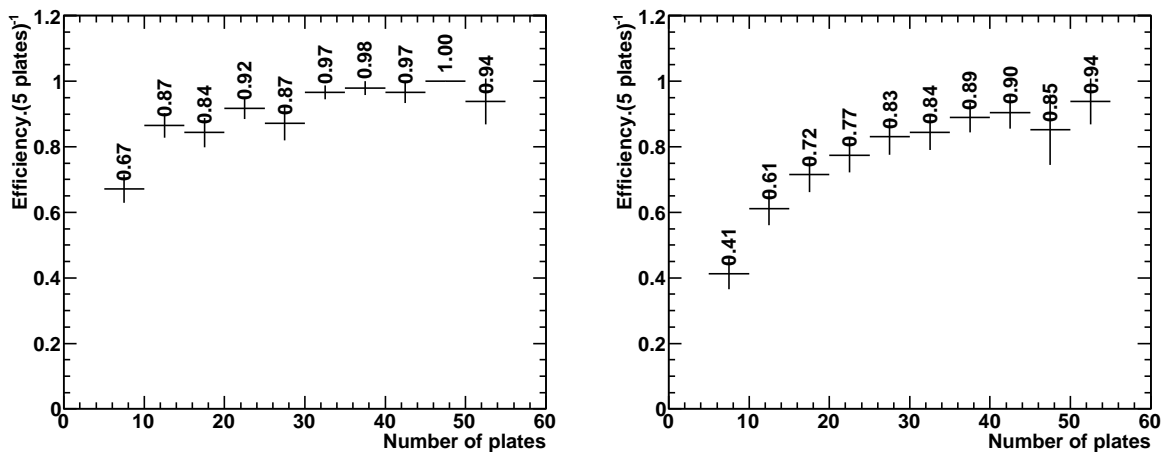
Figure 4.9: Electron Identification efficiency as a function of the shower extension in terms of number of films obtained with MC simulation of the $\nu_\mu \to \nu_\tau$ with the τ lepton into its electron decay channel on the LHS. The same efficiency but only for MC true electron showers on the RHS. The difference gives the systematic uncertainty on identification of showers.
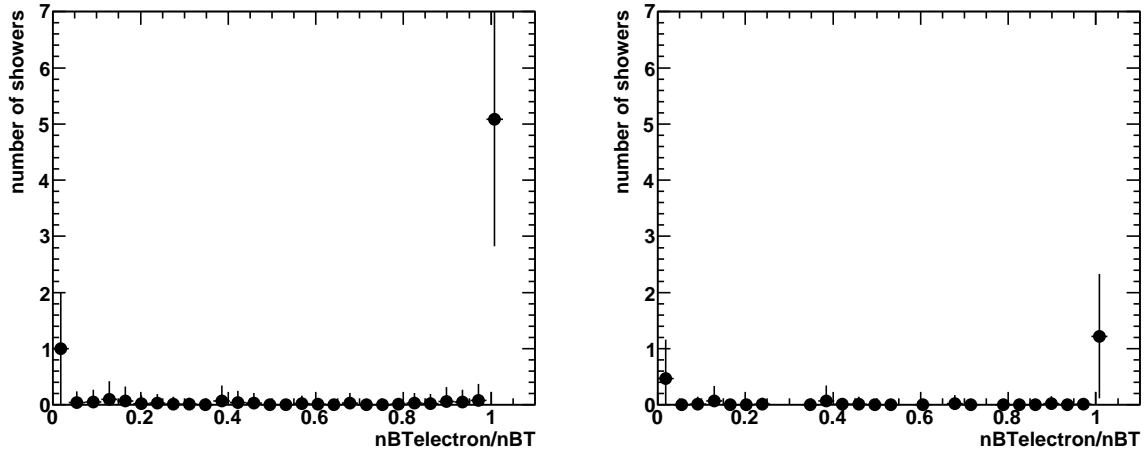
Figure 4.10: Ratio of BaseTracks linked to a hit of the primary electron divided by the total number of BaseTracks in the shower with all events on the LHS and with only showers which have an extension of 10 plates at maximum on the RHS. Both of these plots are obtained with MC simulation of the $\nu_\mu \to \nu_\tau$ with the τ lepton into its electron decay channel.

Number of films	Identification efficiency	Identification efficiency systematic uncertainty	Identification purity
7.5	0.67	0.13	0.61
12.5	0.87	0.13	0.70
17.5	0.84	0.06	0.86
22.5	0.92	0.08	0.84
27.5	0.87	0.02	0.95
32.5	0.97	0.07	0.87
37.5	0.98	0.05	0.91
42.5	0.97	0.04	0.93
47.5	1.00	0.08	0.85
52.5	0.94	0.02	1.00

Table 4.6: Electron identification efficiency and purity for the $\nu_\mu \to \nu_\tau$ with the τ lepton reconstructed into its electron decay channel.

It is shown with the values of table 4.6 that showers reconstructed with an extension of 10 films have an electron identification efficiency value of $(87 \pm 13)\%$. If more films are used, the mean electron identification efficiency is about $(92 \pm 7)\%$.

Thus, to search for and identify an electron and therefore a τ lepton candidate event in the OPERA ECC, within the OPERA nominal scanning procedure, a minimal number of 10 scanned films is required. In which case, the final shower reconstruction and

identification mean efficiency combined to the location one is $(28 \pm 6)\%$ for the oscillation channel $\nu_\mu \to \nu_\tau$ with the τ lepton reconstructed into its electron decay channel using the efficiencies and their systematic error mentioned above for the electron identification and quoted in table 3.6 for the event location. By using the maximum number of plates available in the event once it has been located and identified as an electron event, the final shower reconstruction and identification mean efficiency combined to the location one is $(28 \pm 5)\%$.

4.3.3.3 Energy and vertex depth dependencies

The performance of the electron identification procedure is also studied as a function of electron energy as well as of the vertex position (the position of the occurrence of the neutrino interaction) in the ECC brick. Figure 4.11 shows the variation of the electron identification efficiency as a function of the electron energy obtained with the MC simulation when the $\nu_\mu \to \nu_e$ oscillation channel is considered. Figure 4.12 shows the corresponding results for the $\nu_\mu \to \nu_\tau$ oscillation with the τ lepton into its electron decay channel. The efficiencies are given for both figures as a function of the MC true value of the energy (the shower energy estimation will be described in the next section). The electron identification is computed considering the full available volume in the brick. For both oscillation channels, the electron identification is quite high, around 80% at energies below 20 GeV. At low energy, below 5 GeV, the identification efficiency drops because of the small track multiplicity which do not allow to reconstruct showers. If now, we consider the realistic case where the event location efficiency is considered as well as a shower reconstruction over the OPERA standard volume of 10 films extension, the final computed efficiency of the electron identification is displayed in figure 4.13 and figure 4.14 and shows a value around 65% for energies below 20 GeV.
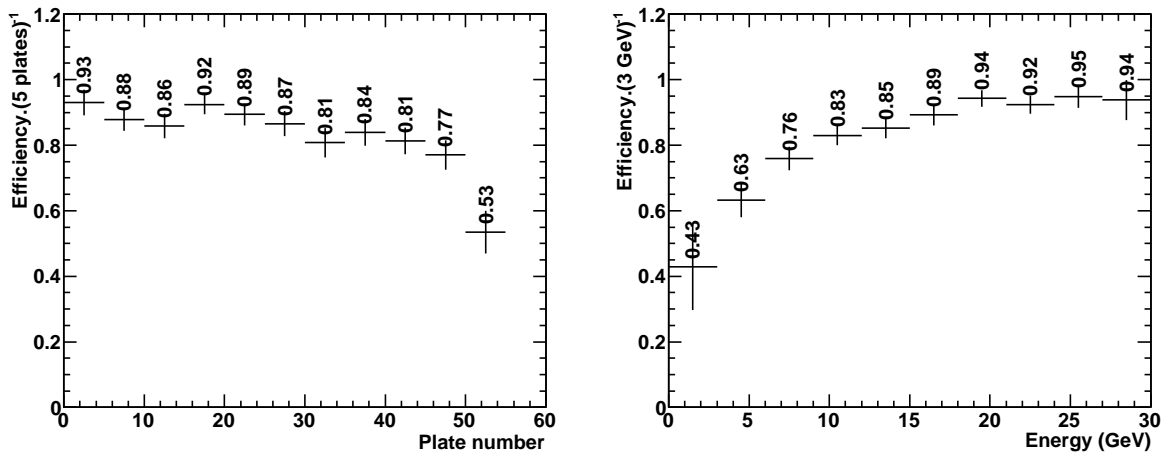
Figure 4.11: Electron identification efficiency as a function of the electron MC true energy on the RHS and electron identification efficiency as a function of the MC true vertex depth on the LHS, both obtained with MC simulation of the $\nu_\mu \to \nu_e$ oscillation channel.
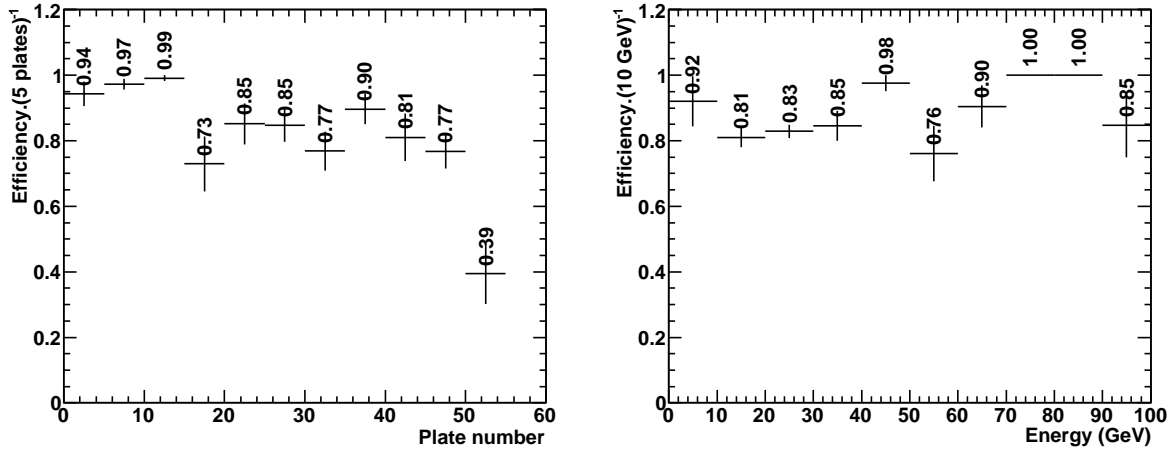
Figure 4.12: Electron identification efficiency as a function of the electron MC true energy on the RHS and electron identification efficiency as a function of the MC true vertex depth on the LHS, both obtained with the MC simulation for $\nu_\mu \to \nu_\tau$ oscillation channel with the τ lepton into its electron decay channel.
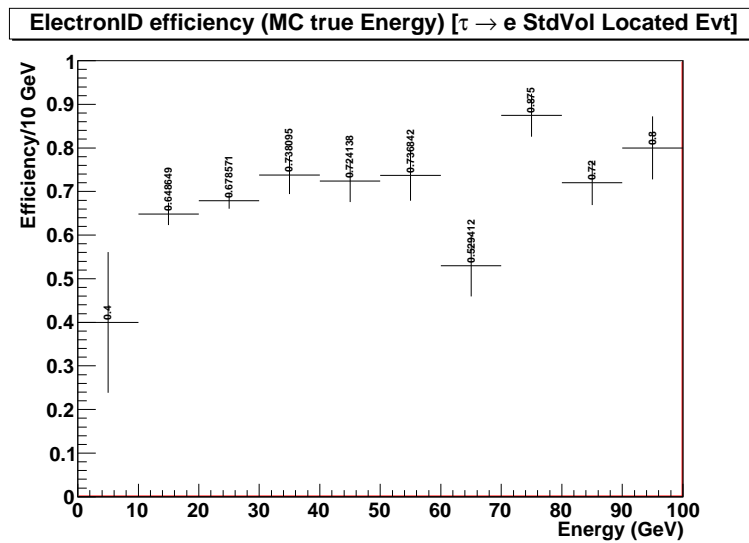
Figure 4.13: Located electron identification efficiency using the OPERA standard volume as a function of the electron MC true energy obtained with the MC simulation for $\nu_\mu \to \nu_\tau$ oscillation channel with the τ lepton into its electron decay channel.
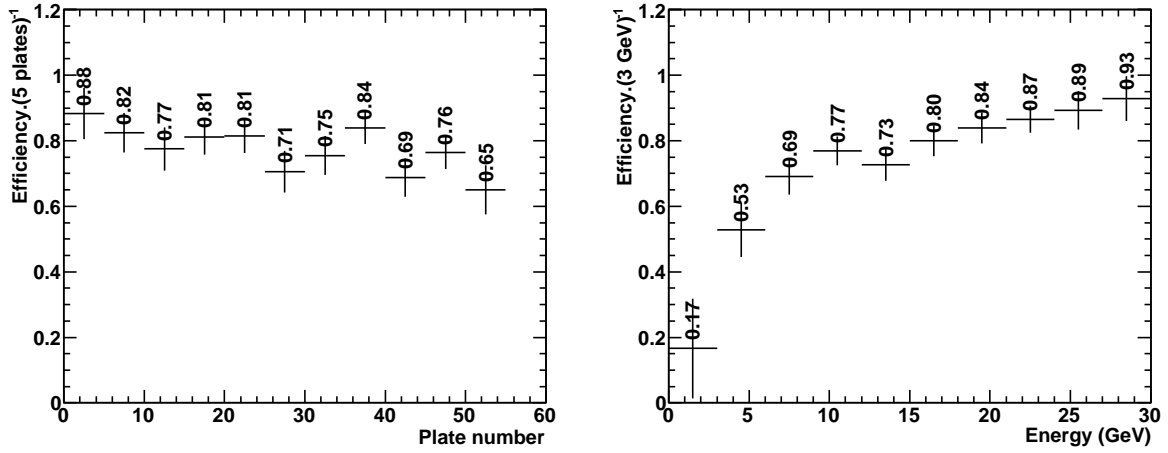
Figure 4.14: Located electron identification efficiency using the OPERA standard volume as a function of the electron MC true energy on the RHS and electron identification efficiency as a function of the MC true vertex depth on the LHS, both obtained with MC simulation of the $\nu_\mu \to \nu_e$ oscillation channel.

As mentioned above, the performance of the electron identification procedure is also studied as a function of the vertex position (the position of the occurrence of the neutrino interaction) in the ECC brick. This vertex position is expressed as the plate (film) number. Figure 4.11 shows the variation of the electron identification efficiency as a function of the film number obtained with the MC simulation when the $\nu_\mu \to \nu_e$ oscillation channel is considered. Figure 4.12 shows the corresponding results for the $\nu_\mu \to \nu_\tau$ oscillation with the τ lepton into its electron decay channel. The efficiencies are given for both figures as a function of the MC reconstructed vertex position. The electron identification is computed considering the full available volume in the brick. For both oscillation channels, the electron identification is quite high, around 90%. There is, nevertheless, a significant drop of the identification efficiency in the last 7 plates because of the too small number of plates available for the proper work of the ANN analysis.

4.4 Energy Estimation

The energy estimation is one of crucial issues for OPERA physics. This algorithm has been developed using the same ANN as for the identification but for that different purpose. From the same input variables described above, this analysis will give in this case, the energy of the shower as the output. The principle of the algorithm will be first presented. Then the performance will be evaluated both on MC samples and on data. Finally, a systematic error study will be shown. MC samples used to calibrate this tool will be *MC_ electronPion_ 4GeV_ 1k*, *MC_ electronPion_ 2GeV_ 1k* and *MC_ electron_ 10k* while data samples will be *data_ electron_ TB_ 4GeV* and *data_ electron_ TB_ 2GeV*. Simulation samples used to test the energy estimation tool are *MC_ oscillated_ nue_ 1k* and *MC_ taue_ 3k*. All these samples are described in section 3.1.5.1.

4.4.1 Principle of the algorithm

The algorithm is based on the same Artificial Neural Network (ANN) as for the identification algorithm. However, an important discrepancy is on the parameters of the BaseTrack (BT) selection. The identification algorithm has been developed before the energy estimation and has shown good performance. Later on, the energy estimation was being revealed more sensitive to background than the identification algorithm. So it has been decided to use more restrictive cuts in order to suppress most of background tracks. The modified parameters can be found in table 4.7.
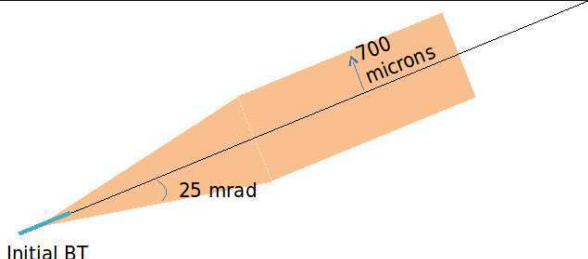
Variables used for the selections	Values of the selections
Angle difference between the BT and the projection of the initiator	$abs(\theta_{\mathrm{BT}}^{\mathrm{3D}} - \theta_{\mathrm{init}}^{\mathrm{3D}}) < 0.130\,\mathrm{rad}$
The BT has to be inside a cone+cylinder shown on the right	

Table 4.7: Summary of the selections specific to the energy estimation algorithm in the BT collection process.

These parameters are handed over as input variables for different types of ANN. For the training of the ANN, two sets of MC sample events have been used ; one of electrons with continuous energies in the range of 0 GeV to 30 GeV and with continuous incoming angles θ_{x} and θ_{y} in the range $[0, 0.4]$ rad and another one with continuous

energies in the range of 0 GeV to 100 GeV and with continuous incoming angles θ_x and θ_y in the range $[0, 0.6]$ rad. Both sets have an energy spectrum close to the one from the $\tau \to e$ channel. The output of the ANN is taken as energy value to be observed. The ANN has been trained for 200 epochs, using the stochastic learning method and consisting of a structure with N input neurons, N+1 and N neurons in the two hidden layers. Different parametrizations for characteristics of an electromagnetic shower in the ECC have been systematically studied. The meaning of the ANN parameters mentioned above is described in appendix E.2.

4.4.2 Performance

Performance of this energy estimation algorithm has been evaluated on the MC sample of 10 000 electrons produced in an energy continuum from 0 to 30 GeV with a flat spectrum and with incoming angles θ_x and θ_y in the range 0 to 0.6 rad. The first step of the analysis has been to define a pure sample of electrons to assess the best performance in energy estimation of this tool. The pure sample has been defined according to the following selections summarized in table 4.8.

Variables used for the selections	Values of the selections
Incoming angle of the electron	$abs(\theta^{3D}) < 0.1 \, \text{rad}$
Contained shower : multiplicity of MicroTracks (MTs)	At least 50% of MTs inside one brick

Table 4.8: Summary of selections defining a pure electron sample.

Showers have been reconstructed over the full volume available for the event. Figure 4.15 shows a scatter plot of the MC true energy as a function of the reconstructed energy and its associated profile.

The reconstructed energy is linear up to 20 GeV with the MC true energy as we can see on the RHS of figure 4.15. For our purpose, 20 GeV is good enough since an upper cut on the neutrino energy at 20 GeV will be used in the analysis reported in chapter 5.

The effect of the "contained" showers selection is illustrated by figure 4.16 where this selection has been removed : the spread of the reconstructed energy values in the high energy region is enhanced as well as the error of the fit which increases above 10%.
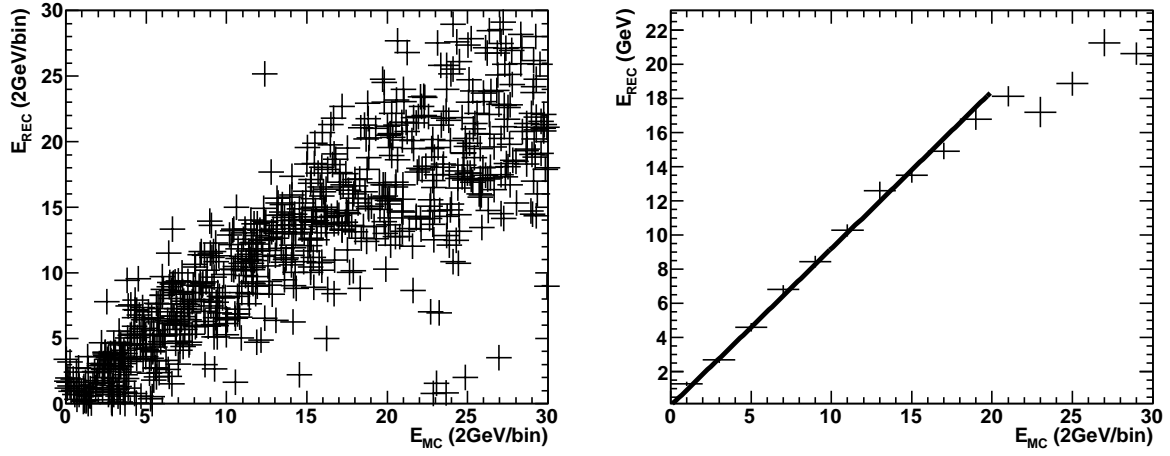
Figure 4.15: On the LHS, a scatter plot of the reconstructed energy as a function of the MC true energy. On the RHS, the fitted profile of the scatter plot shown on the left. The parametrization showed on the profile gives : $E_{\mathrm{REC}} = (0.92 \pm 0.01) * E_{\mathrm{MC}}$. The error quoted here is the error on the fit.
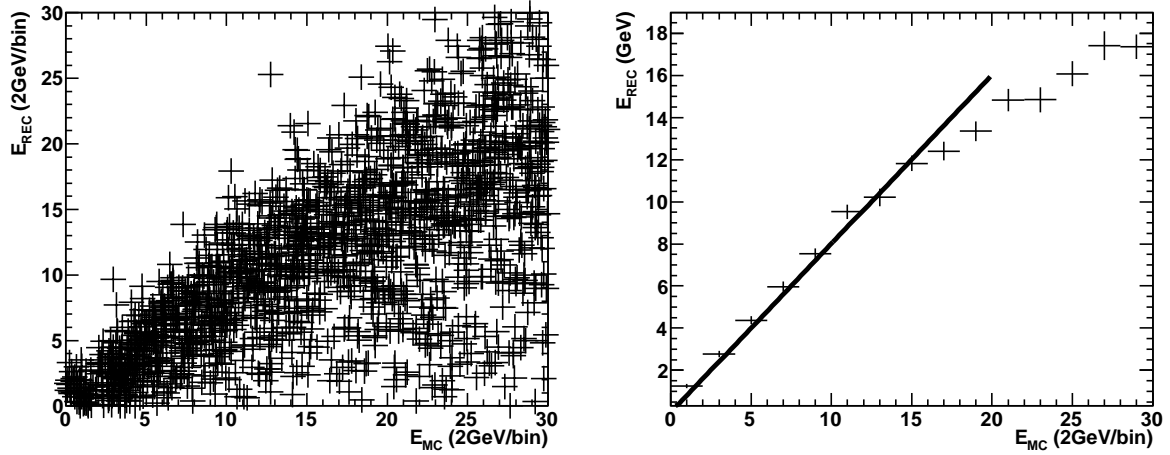
Figure 4.16: On the LHS, a scatter plot of the reconstructed energy as a function of the MC true energy. On the RHS, the fitted profile of the scatter plot shown on the left. The parametrization showed on the profile gives : $E_{\mathrm{REC}} = (0.80 \pm 0.01) * E_{\mathrm{MC}}$.

The correction to the reconstructed energy thus defined above is :

$$E_{\mathrm{REC}} = (0.92 \pm 0.01) * E_{\mathrm{MC}} \qquad (4.7)$$

The parametrization of the reconstructed energy is defined in the linear region [0,20] GeV. Figure 4.17 shows plots of the Reconstructed-MC true energy ratio and residuals of the reconstructed energy below 20 GeV and for "contained" showers. Residuals are defined as :

$$\text{residual} = \frac{E_{\text{REC}} - E_{\text{MC}}}{E_{\text{MC}}} = \frac{\Delta E}{E} \qquad (4.8)$$
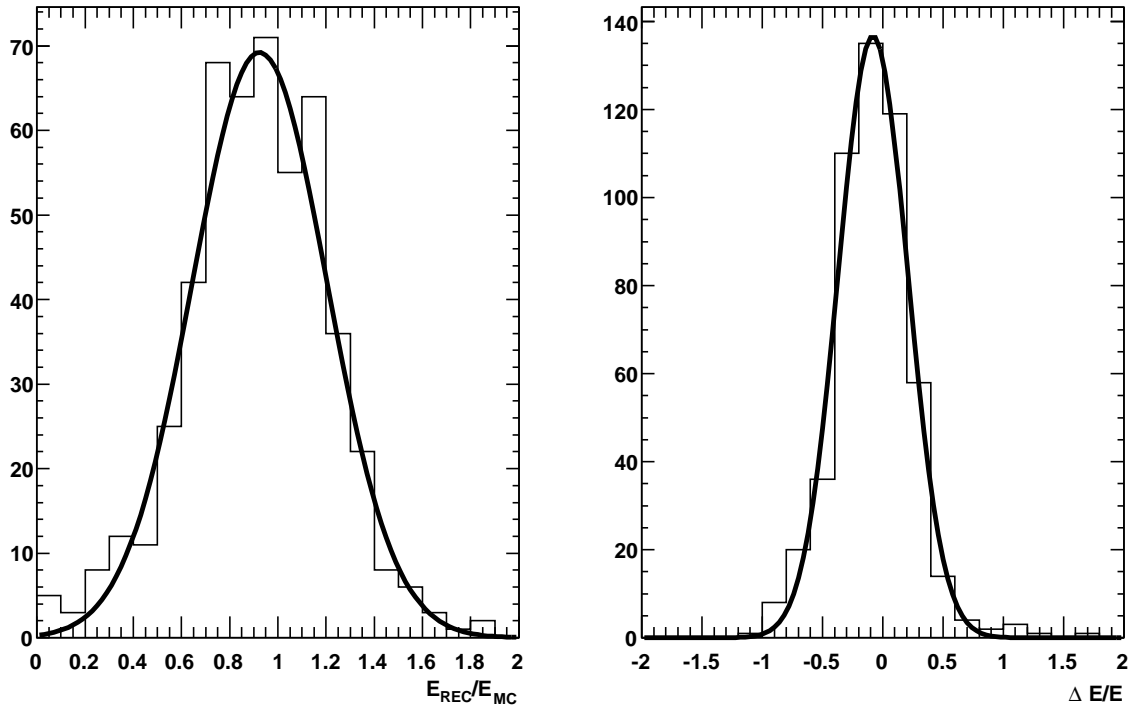
Figure 4.17: On the LHS, the ratio distribution of the reconstructed energy over MC true energy and on the RHS, the distribution of the reconstructed energy residuals are presented for the MC simulation of single electrons. Here, the showers are reconstructed over the full volume available for the event and selected according to table 4.8. The gaussian fit of the energy ratio gives $\sigma(E_{\text{REC}}/E_{\text{MC}}) = 0.28 \pm 0.01$; for the residuals, $\sigma(\Delta E/E) = 0.29 \pm 0.01$ and the mean gaussian value is -0.08 ± 0.01.

The shower reconstruction tool on the pure sample can achieve a mean resolution of 29% with a bias of 8%. Computing the resolution of the reconstructed energy divided by the MC true energy as a function of the latter gives figure 4.18.
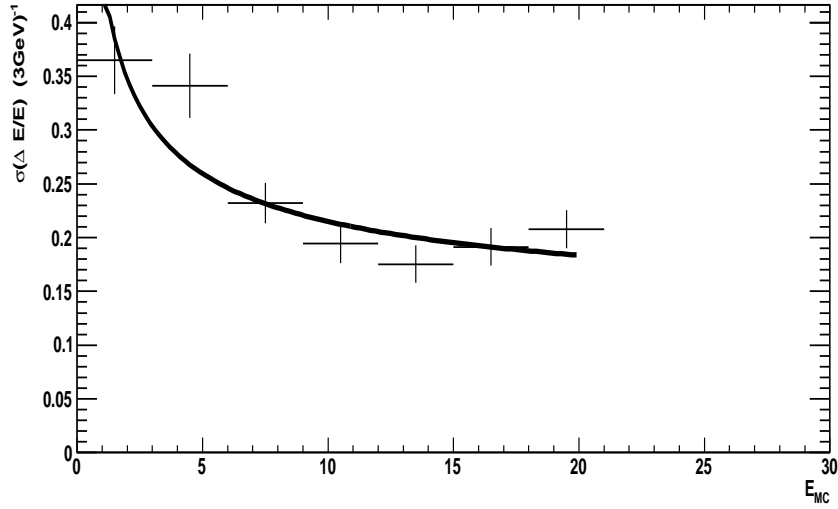
Figure 4.18: Resolution on the shower energy as a function of the MC true energy. The fit of the energy resolution gives $\frac{\sigma(E)}{E} = \frac{0.34\pm0.05}{\sqrt{E}} + 11\%$ with E in GeV.

The resolution parametrization of the OPERA calorimeter is therefore :

$$\frac{\sigma_E}{E} = \frac{(34 \pm 5)\%}{\sqrt{E}} + (11 \pm 2)\% \quad \text{with E in GeV} \tag{4.9}$$

However these performances have been assessed in an "idealistic" case on the pure MC sample because of the variation of the energy estimation with the incoming angle of the electron and with the vertex depth in the brick. These dependencies are studied in the following. Moreover, the existence of electron testbeam data described in section 3.1.5.2 allows to compare data with MC simulations.

4.4.3   Energy calibration and comparison of the MC simulation with data

4.4.3.1   Energy calibration

The variations of the shower energy estimation with the electron incoming angle and with the vertex depth are illustrated in figure 4.19 where the total MC sample of single electrons is analysed. The latter represents the information leakage outside one brick constrained in the pure sample with the "contained" selection.
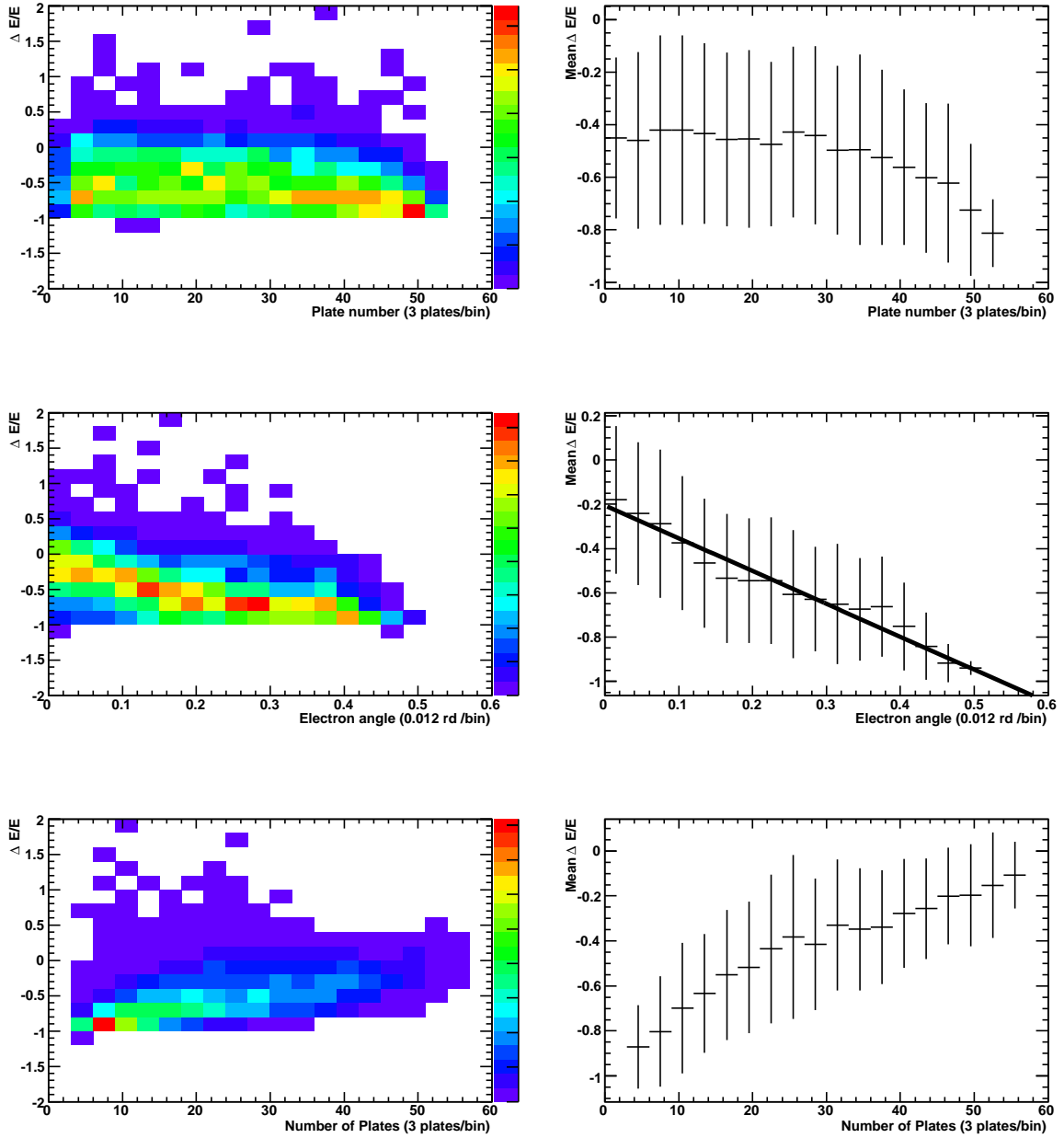
Figure 4.19: In the top panels, the scatter plot of the residuals as a function of the vertex depth and its associated profile. In the middle panel, the energy residuals as a function of the shower axis angle. The parametrization of this dependency gives : $\frac{\Delta E}{E} = -0.206 - 1.48\,\theta_{3D}$(electron). In the bottom panel, the energy residuals as a function of the shower extension in number of plates. All plots presented are obtained with the MC simulation of single electrons.

The energy residuals are stable with the vertex depth up to the plate 40 ; the deviation above this value is visible but not so important up to plate 47. This plate is the last one to consider if the electron is to be identified within one brick procedure. Otherwise, the energy residuals vary strongly with the shower axis angle which degrades the resolution and implies a bias in the energy estimation which could be corrected according to the parametrization. Therefore, the resolution in energy is investigated including this correction. The shower extension has to be 20 plates at least to reach the stability region in shower extension.

Figure 4.20 shows a scatter plot of the MC true energy as a function of the reconstructed energy and its associated profile taking into account the correction of the energy as a function of the shower axis angle. Only showers "contained" are considered. Figure 4.21 shows plots of the Reconstructed-MC true energy ratio and residuals of the reconstructed energy below 20 GeV and for "contained" showers.

In this more realistic approach, the correction has improved the reconstructed/MC energy ratio and the bias on the energy is also improved. The Gaussian fit of the residuals in figure 4.21 shows a bias of 12%, but given the asymmetric shape of this distribution, the fitted mean value is not significant. However, the resolution on the energy has been enhanced. A multivariate correction (shower axis angle, shower extension and vertex depth) would be suited to improve that resolution.
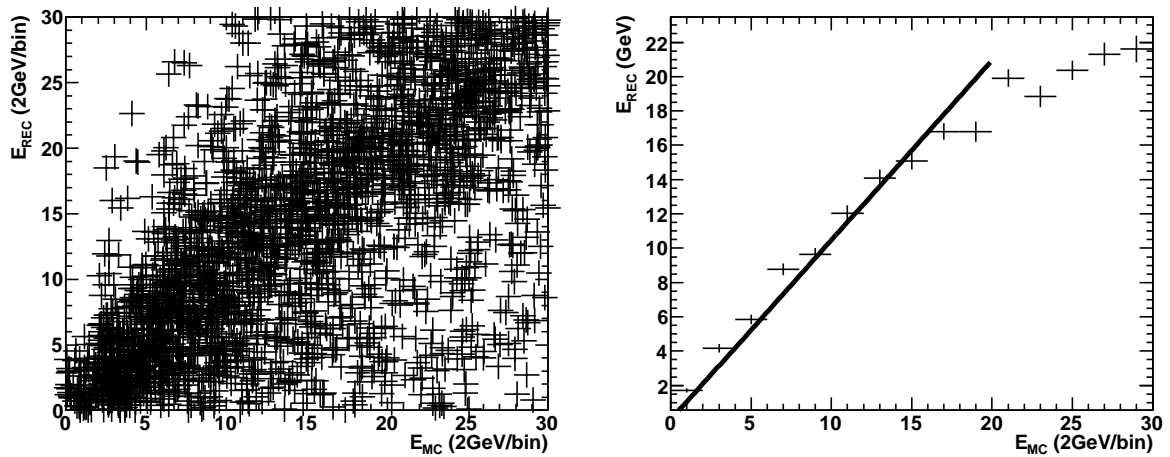
Figure 4.20: On the LHS, a scatter plot of the reconstructed **corrected energy** as a function of the MC true energy. On the RHS, the fitted profile of the scatter plot shown on the left. The parametrization showed on the profile gives : $E_{\mathrm{REC}} = (1.05 \pm 0.01) * E_{\mathrm{MC}}$. The error quoted here is the error on the fit.
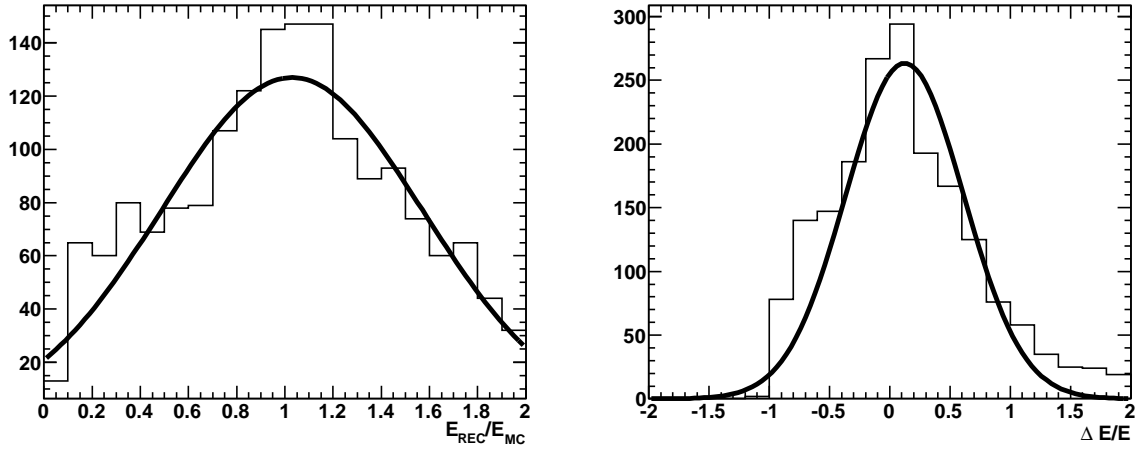
Figure 4.21: On the LHS, the ratio distribution of the reconstructed corrected energy over MC true energy and on the RHS, the distribution of the reconstructed **corrected energy** residuals are presented for the MC simulation of single electrons. Here, the showers are reconstructed over the full volume available for the event and are contained in the brick. The Gaussian fit of the residuals, $\sigma(\Delta E/E) = 0.49 \pm 0.01$ and the mean Gaussian value is 0.12 ± 0.02.

The final resolution of the OPERA calorimeter is therefore constant with the energy and is about 50%. It does not fit with the usual stochastic behaviour in $1/\sqrt{E}$ because of a too low sampling with 10 X_0 in one brick.
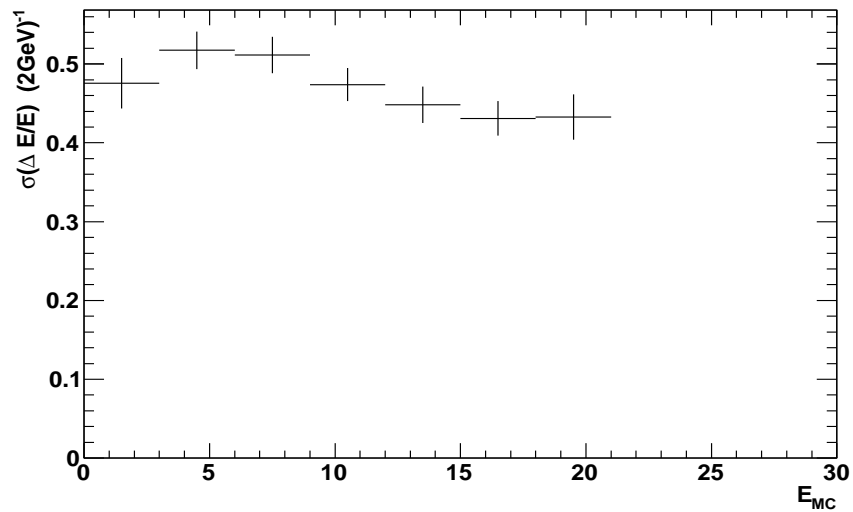
Figure 4.22: Resolution on the shower **energy corrected** as a function of the MC true energy.

4.4.3.2   Test beam data analysis and comparison with the MC simulation

The production of these data are described in section 3.1.5.2. The analysis procedure and the identification of electrons inside this dataset has been detailed in section 4.3.2.

The result in terms of energy estimation of the electron testbeam data at 2 and 4 GeV are presented in figure 4.23.
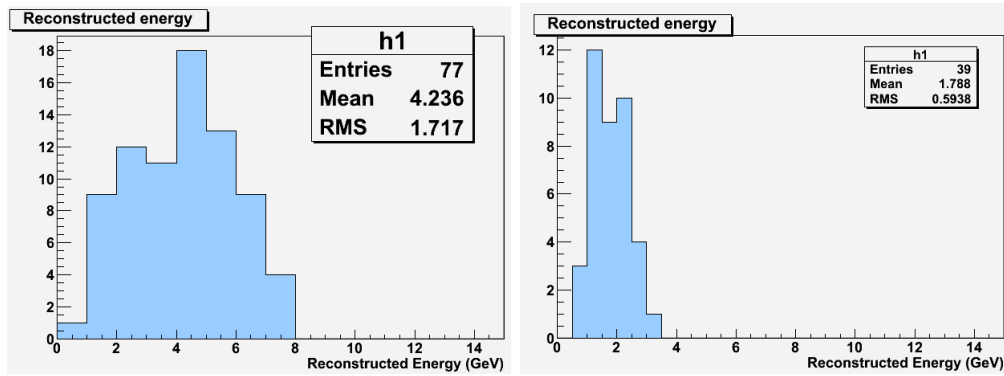
Figure 4.23: Reconstructed energy on the selected electrons in testbeam data for 4 GeV on the LHS and 2 GeV on the RHS.

From the parametrization defined in figure 4.20 with MC simulations, MC energies at 2 and 4 GeV can be computed with their associated statistical uncertainty. The MC/data comparison is shown in table 4.9 and estimate the compatibility between MC and data.

MC Energy (GeV)	2.10±0.03	4.20±0.05
Data Energy (GeV)	1.8±0.1	4.2±0.2
ΔE/E (%)	14	0

Table 4.9:   Summary of the electron energy estimation with testbeam data and MC simulation. The uncertainties on the MC values derive from the errors on the parametrization. The uncertainties on the data values are statistical.

The difference on the energy estimation between the MC simulation and data have to be compared to the resolution shown in figure 4.18 of 34%. The value obtained in data are compatible with the energy given by the MC simulation.

Furthermore, if the shower energy estimation is limited on the low energy electrons because of a small track multiplicity, it would be interesting to perform other testbeams with electrons from 4 up to 20 GeV to be compared at the MC simulations performance.

4.4.4   Energy estimation results

The performance of the energy estimation algorithm has also been studied with the MC samples from the simulation of OPERA electron neutrino events, both from beam and from the oscillation process $\nu_\mu \to \nu_e$ as well as from the simulation of OPERA tau neutrino events, from the oscillation process $\nu_\mu \to \nu_\tau$ with the τ lepton reconstructed into its electron decay channel.

Figures 4.24, 4.25, 4.26 and 4.27 show a scatter plot of the MC true energy as a function of the reconstructed energy and its associated profile - the error bars represent the spread of the E_{REC} values - below which the distributions of Reconstructed Energy over MC true energy ratio and of the reconstructed energy residuals (residual $= \frac{E_{\mathrm{REC}} - E_{\mathrm{MC}}}{E_{\mathrm{MC}}}$) are presented. In figures 4.24 and 4.27, the showers are reconstructed over the OPERA standard volume of 10 plates while in figures 4.25 and 4.26, the full available volume is used. For figures 4.26 and 4.27 the reconstructed shower energy after applying the correction on the energy defined in section 4.4.3 is used. All figures 4.24, 4.25, 4.26 and 4.27 are obtained from the MC simulation of the oscillation process $\nu_\mu \to \nu_e$.
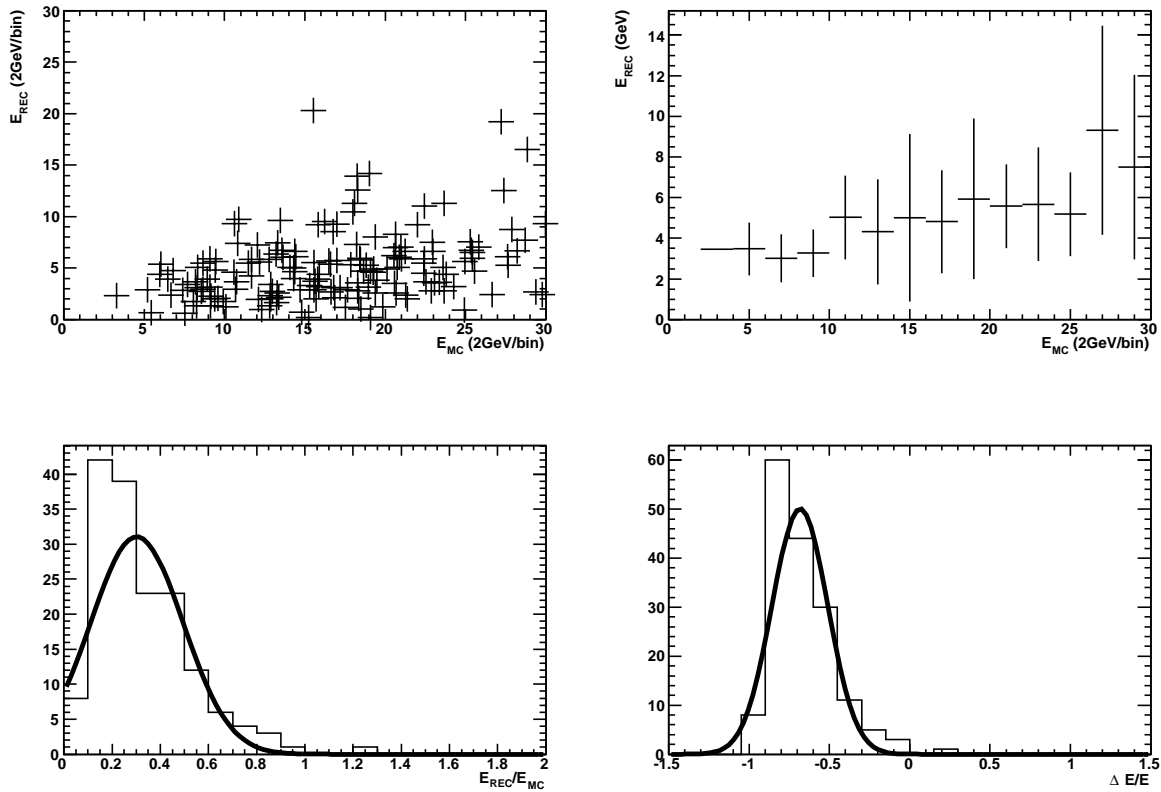
Figure 4.24: A scatter plot of the MC true energy as a function of the reconstructed energy and its associated profile are shown in the top plot, below which the ratio distribution of the reconstructed energy over MC true energy and on the bottom, the distribution of the reconstructed energy residuals are presented for the MC simulation of the oscillation process $\nu_\mu \to \nu_e$. Here the showers are reconstructed over the OPERA standard volume.
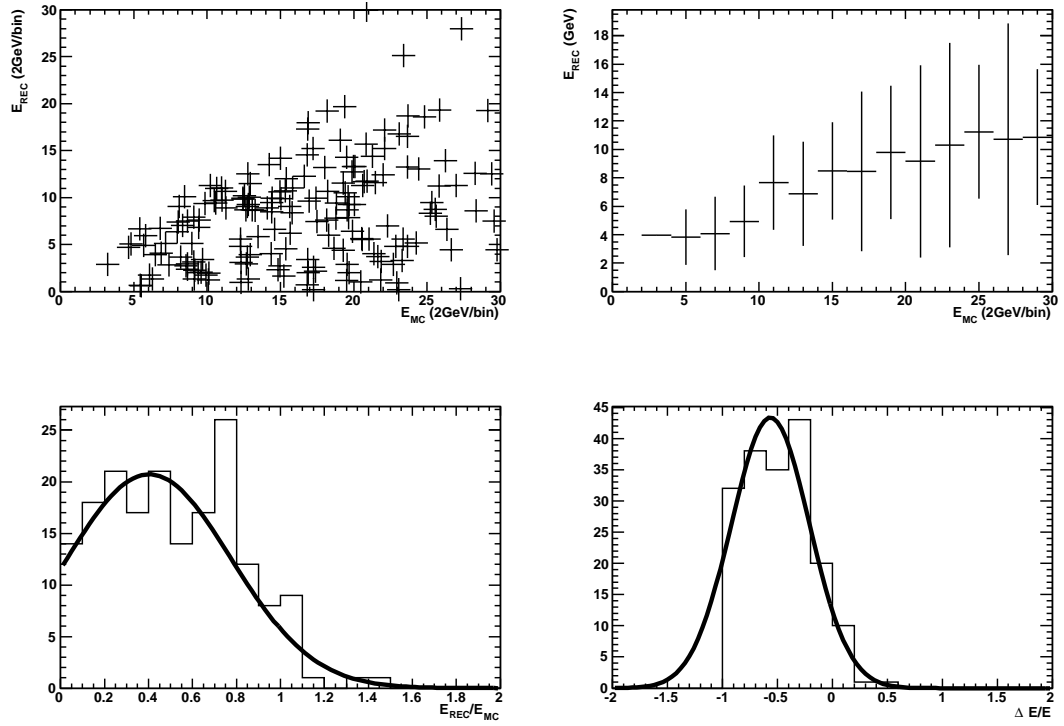
Figure 4.25: *Idem* with showers reconstructed over the full volume.
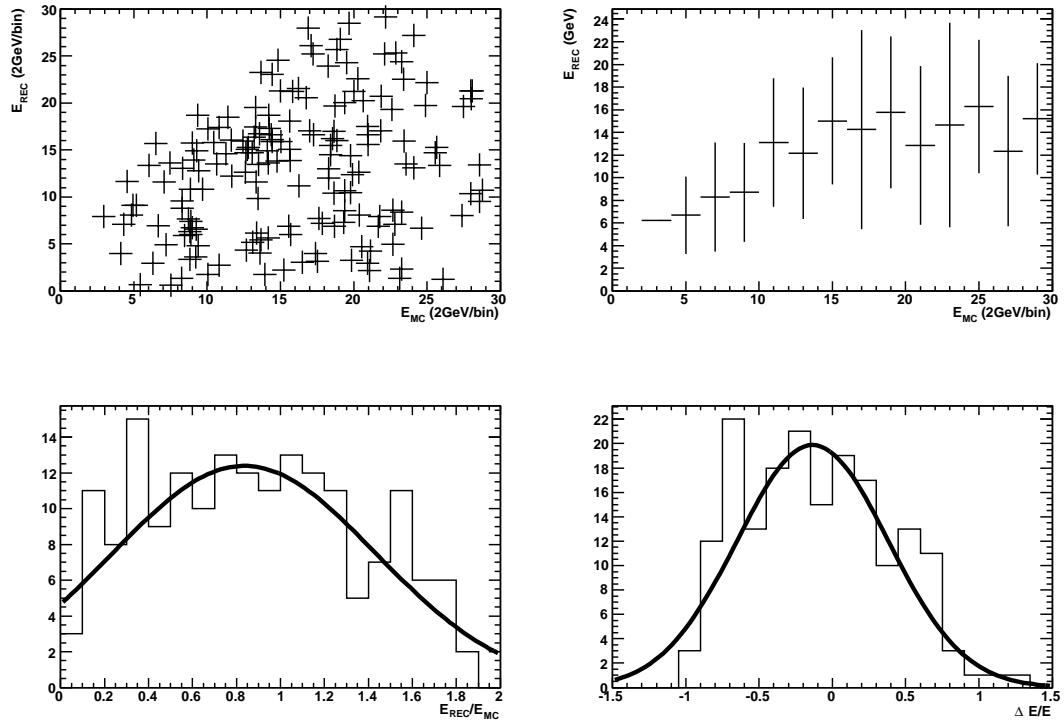
Figure 4.26: *Idem* with the **corrected energy** in the full volume.
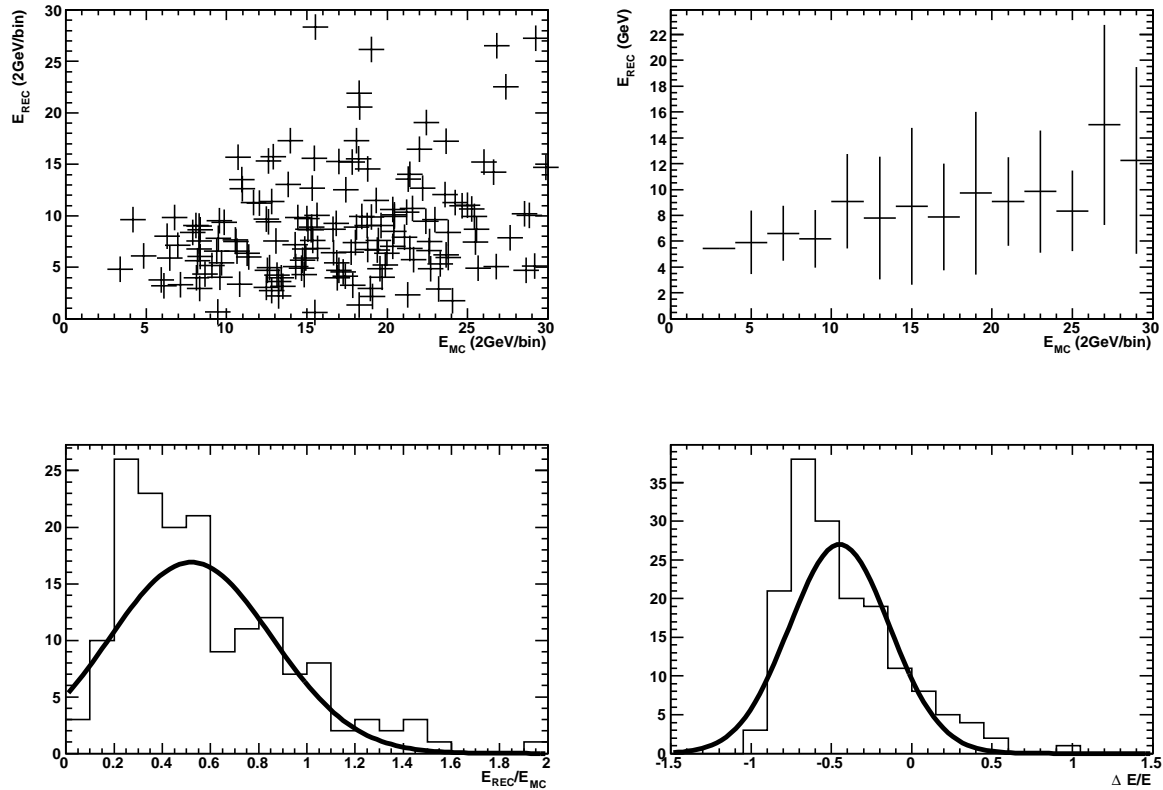
Figure 4.27: *Idem* with the **corrected energy** in the OPERA standard volume.

By comparing figure 4.25 with figure 4.24, the effect of the increased size of the analysis volume to reconstruct a shower is clear : the bias on the energy is improved while the resolution is kept under control. On the other hand, by comparing figure 4.25 with figure 4.26, the parametrization on the energy corrects the bias almost completely and degrades the resolution as it has been already shown with the MC study in section 4.4.3.1 with pure electrons. Both the full volume and the energy correction are necessary to estimate the energy of the electromagnetic showers unbiased.

Both figure 4.28 and figure 4.29 are obtained from the MC simulation of the oscillation process $\nu_\mu \rightarrow \nu_\tau$ with the τ lepton reconstructed into its electron decay channel. Similarly to the previous process, figure 4.28 shows a scatter plot of the MC true energy as a function of the reconstructed energy, below which the distributions of Reconstructed Energy over MC true energy ratio and of the reconstructed energy residuals (residual $= \frac{E_{REC} - E_{MC}}{E_{MC}}$) are presented. Here (figure 4.28), the showers are reconstructed over the full volume available for the event. The same plots and distributions have been computed considering the OPERA standard volume and are shown in figure 4.29.
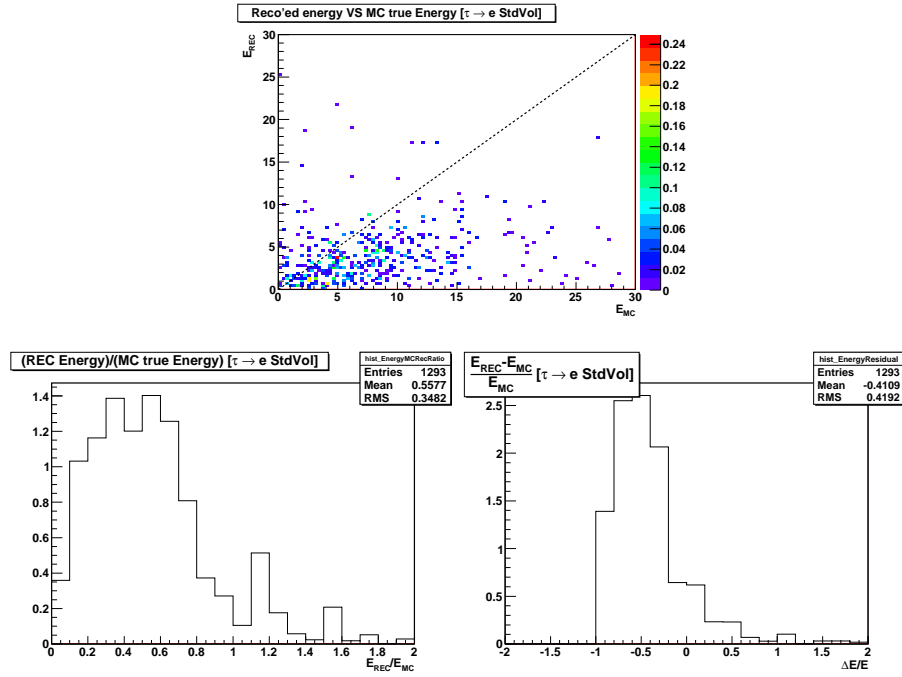
Figure 4.28: A scatter plot of the MC true energy as a function of the reconstructed energy is shown in the top plot, below which the ratio energy distribution and on the bottom, the distribution of the reconstructed energy residuals are presented for the MC simulation of the oscillation process $\nu_\mu \to \nu_\tau(\tau \to e)$. The showers are reconstructed over the full volume.
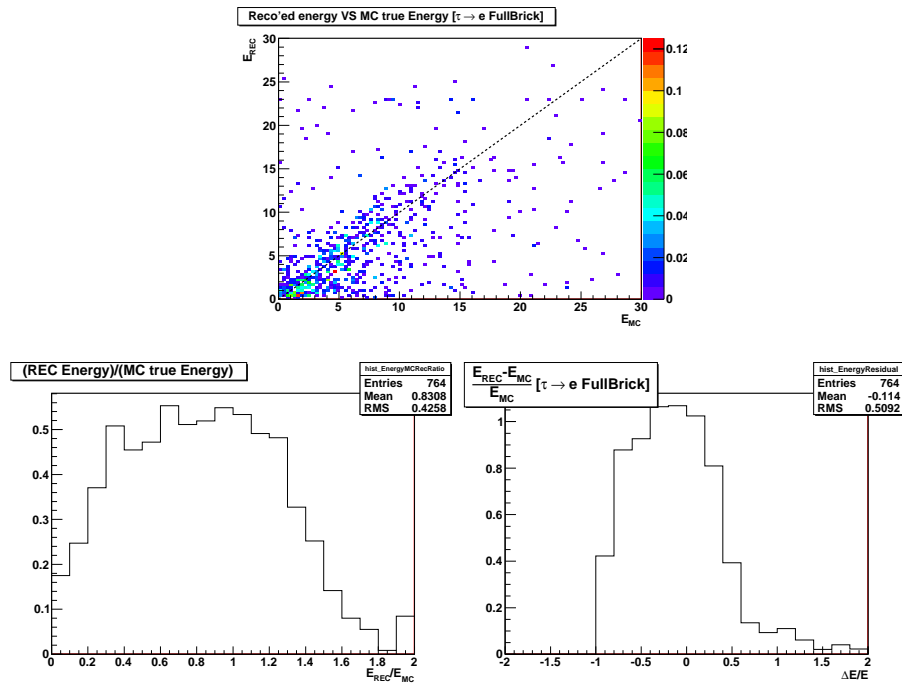
Figure 4.29: *Idem* with showers reconstructed over the full volume.

The importance to use all the emulsion films available for an event to estimate the energy of the electron showers is once more stressed by comparing figures 4.29 and 4.28.

In conclusion, the OPERA standard volume is shown not to be sufficient for the energy estimation. The latter is nevertheless correctly performed when the shower reconstruction is considered with the full available volume in the brick. Moreover the corrected energy is much closer to the MC truth but the resolution is clearly degraded.

4.5   Improvements   of   the   Shower   Reconstruction Algorithm

4.5.1   Electromagnetic shower reconstruction within two OPERA bricks

The standard analysis to estimate the energy of electromagnetic showers is performed by using 20 films for ν_e candidates and by using an entire brick for τ candidates. However, according to the electromagnetic shower model described in section 4.1, an electron can produce a shower with a transverse extension parametrized by the well known Moliere radius and a longitudinal extension parametrized by a complex function described by equation 4.5. From equation 4.6, the Moliere radius is about 1.7 cm in our ECC which is of the order of magnitude of a brick dimension. In addition, from a parametrization described in [21], the longitudinal spread of a 4 GeV electron shower is about 23 cm. Such an electron shower can hence spread over more than one brick. Moreover, our search and detection of ν_τ^{CC} interaction favours the downstream part of the brick as quoted in section 3.2, where the number of plates available to the interaction is smaller and thus the energy estimation could be biased for such events. The aim of this study is to estimate the number of candidates with a significant biased estimation of the energy, the error on the energy by using the standard procedure and to define a strategy to estimate the energy of electromagnetic showers within two bricks. The MC samples used in this study are $MC\_\nu_e\_1k\_march2011$ and $MC\_\tau \to e\_1k\_march2011$ and are described in section 3.1.5.

4.5.1.1   Motivation of reconstructing showers over two bricks

The natural approach to achieve the energy estimation for showers which spread over two bricks would be the use of the ANN trained in these conditions ; but such approach is a heavy procedure. Therefore, I just aimed to estimate the fraction of events concerned by the second brick, their topology, and the relevance of this estimation in terms of energy resolution of the OPERA calorimeter. Thus, a first approach has been to find a criterion to determine if an electromagnetic shower has a significant fraction inside the second brick. Regarding the large number of low energy BaseTracks (BTs), it has been decided that only the primary electron track extension is relevant to estimate this population. The electromagnetic shower reconstruction has shown a non-linear behaviour as a function of the BT multiplicity for the showers with energies lower than 1 Gev and greater than 14 GeV as shown on figure 4.30. Then, the algorithm can achieve a best resolution with a certain number of plates and area in the transverse plane, collecting more information does not necessary mean improve the energy estimation.

Considering the ν_τ ($\tau \to e$) sample, I estimated the fraction of events where a significant part of the electron shower decaying from the tau goes into the second brick in terms of extension of the electron secondary track. Then I estimated the fraction of events where a significant part of the electron shower outgoing from a ν_e^{CC} interaction goes into the second brick in terms of extension of the electron primary track. The results

are respectively 26% for the $\tau \to e$ channel and 44% for the ν_e channel as shown in figure 4.31, it remains to quantify the error on the estimation of the energy on these events.
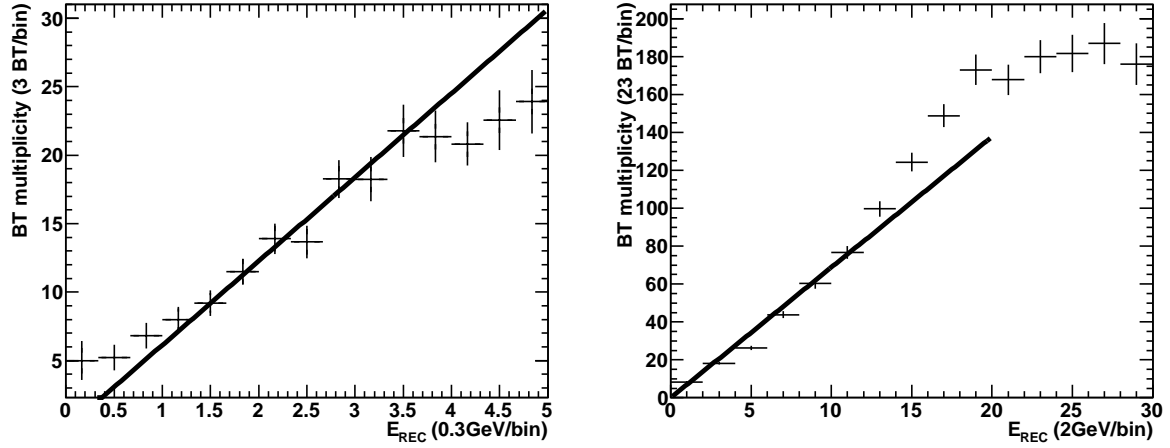
Figure 4.30: On the RHS, the BT multiplicity in the shower as a function of the reconstructed electron energy. On the LHS, a zoomed version of the plot on the RHS for energies between 0 and 5 GeV.
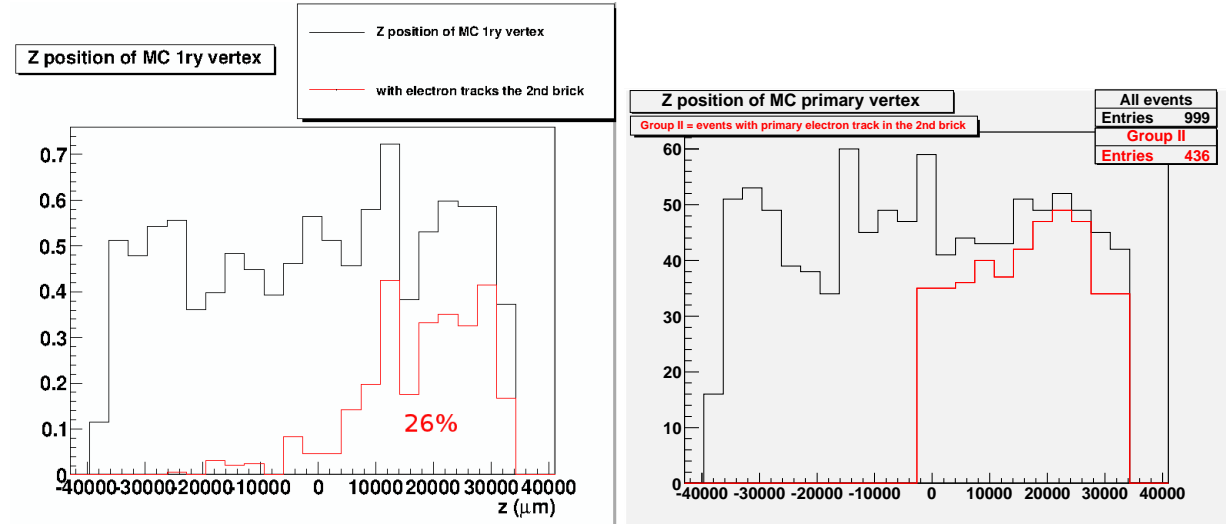
Figure 4.31: MC true vertex Z position of all events (black) and with the secondary electron in the next downstream brick (red) for a sample of 1 000 ν_τ^{CC} interactions with primary τ which decays into an electron on the LHS.The same plot for a sample of 1 000 ν_e^{CC} interactions of the beam on the RHS.

As a second step in this analysis, I looked at the fraction of MicroTracks (MTs) in the second brick with respect to the total number of MTs in the event for the two samples. This second idea seems more simple and able to deliver a more quantitative information than the first one based on the span of the primary electron track. The result is shown in figure 4.32.
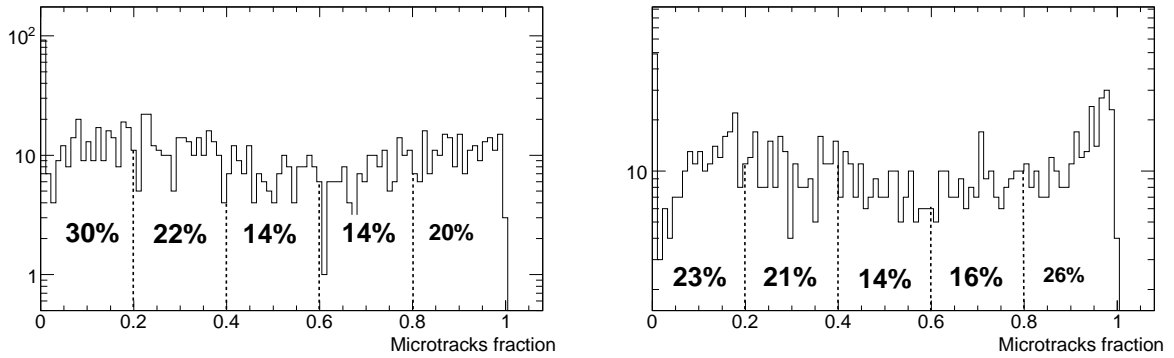
Figure 4.32: Fraction of MTs in the second brick with respect to the total number of MTs in the first and second bricks for the $\tau \to e$ sample on the left and for the ν_e sample on the right. The percentages indicates the fraction of events considered by the MT fraction delimited by the histogram.

Analysing the plot on the RHS of figure 4.32, we can say that about 50% of the ν_e correspond to events with more than 50% of the BTs in the second brick. The former estimation was actually fine. Concerning the $\tau \to e$ case, the former estimation of 26% seems underestimated since the plot on the LHS of figure 4.32 shows a MT fraction of 40% for 50% of events. Nevertheless, at this level of the study, the MTs correspond to MC true information without any detector efficiency. The reality is much probably between these two estimations of 26% and 40%. We expect a smaller fraction of $\tau \to e$ events going to the second brick because of a lower energy spectrum than in the ν_e case. The point of a reconstruction within two bricks is to be able to estimate the most accurate energy estimation of an electron shower as possible for the $\tau \to e$ candidates in OPERA knowing that only a few are expected as mentioned in section 5.2.3.

4.5.1.2   Determination of the missing part of the energy in the second brick for the $\tau \to$ e and ν_e channels

The strategy to determine this missing part of the energy is to create two subsamples of events, the one with the shower spreading over the second brick and another one with showers completely contained in the first brick. In addition, we impose a certain extension, i.e. 29 plates, of the shower to make matching longitudinal profiles with the showers of the first group as you can see in figure 4.33. Note that on the plot, the black profile is shifted by 28 plates to superimpose the two profiles.

The point of creating these two groups is to use the energy estimation on this second group reconstructing showers with a full profile and then, with a profile truncated in the same way as the profile of the first group is. A comparison between these two energy estimations gives a mean error of 20% which is done on the energy estimation of the events with a significant part of the electromagnetic shower in the second brick.
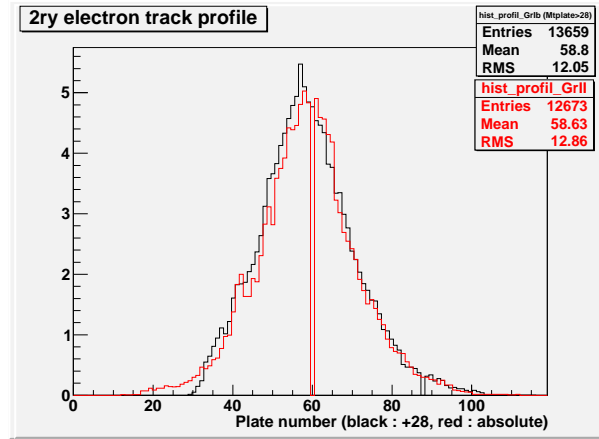
Figure 4.33: Electron track longitudinal profile over two consecutive bricks for 1 000 events with respect to that selection : Group Ib which are events with the ν_τ interaction in the first half-brick and within MTs beyond plate 29, Group II which are events which go up to the second brick and with the interaction in the second half-brick.

In conclusion of this chapter, for the purpose of the analysis of the OPERA electron neutrino events, from the oscillation process $\nu_\mu \to \nu_e$ as well as the OPERA tau neutrino events, from the oscillation process $\nu_\mu \to \nu_\tau$ with the τ lepton reconstructed into its electron decay channel, we have elaborated, and validated the reconstruction procedure of the electromagnetic showers using a MC simulation in the ANN approach within the OPERA emulsion computing framework, OpEmuRec.

The electron identification performance of the electromagnetic showers with the shower reconstruction tool of the OPERA collaboration has been assessed with MC simulations on single electrons as well as physics channels ($\nu_\mu \to \nu_e$ and $\nu_\mu \to \nu_\tau(\tau \to e)$). The systematic uncertainty of the identification process of about 20% has been also evaluated by using the MC true information on the physics channels. A comparison with testbeam data of this electron identification has been also performed. We conclude that the OPERA standard volume of 10 emulsion scanned films is well suited for the electron identification.

The performance of OPERA as an electromagnetic calorimeter has been then assessed. In one OPERA brick, the expected resolution on a electron shower is about 50% in a realistic case. Some improvements on this resolution could be done by correcting the reconstructed energy with a multivariate study (shower extension, vertex depth) in addition of the presented correction with the shower axis angle. The energy of electron showers have been also checked on the physics channels and a comparison of the MC simulation with data from the testbeam have shown a compatibility between the two estimations. We conclude that the full available volume and at least 3 to 4 radiation length (about 20 lead plates) are necessary for better results when the energy estimation is aimed.

Chapter 5

Analysis Of Electron Channels : Electron Neutrino And $\tau \to e$

The $\nu_\mu \to \nu_e$ oscillation study consists in the search of electron neutrino in the muon neutrino beam. This appearance will be explored in the CC interactions and DIS processes. The expected rates for the signal and all background channels will be evaluated with MC simulations. Then, based on the MC study, a signal will be searched in analysed data and the sensitivity of the OPERA experiment to the $\nu_\mu \to \nu_e$ oscillation will be presented. A signal of the $\nu_\mu \to \nu_\tau$ oscillation in the electronic decay of the tau with the OPERA detector is performed and its results are reported in this chapter.

5.1 Outline Of The Analysis

The OPERA sensitivity to the $\nu_\mu \to \nu_e$ oscillation is limited by the presence of ν_e in the CNGS beam, i.e. 0.87% of the ν_μ flux. These electron neutrinos are an irreducible background called in the following sections *prompt ν_e*. However, the energy spectra are different for prompt ν_e and for oscillated ν_e as shown in figure 2.22. Indeed, the energy distribution of oscillated ν_e's has its maximum below 20 GeV and is negligible above 30 GeV while prompt ν_e energy distribution has a long tail above 30 GeV : the (oscillated ν_e)/(prompt ν_e) ratio will be maximal below 20 GeV. Looking for the oscillation signal will depend on the energy of the electron shower. The neutrino energy is not easily calculated from electronic detectors since the electromagnetic component of the neutrino interaction is not well measured in the Target Tracker (TT) ; however, it would be possible to use the TT information to assess the electromagnetic energy leakage outside the brick. That is why the performance in energy evaluation of electron showers in the ECC has been studied carefully in section 4.4 giving an energy resolution of 50% for the OPERA calorimeter. The search for the $\nu_\mu \to \nu_e$ oscillation signal will be improved by applying other kinematical selections to reduce the other background sources described in section 2.6. The analysis presented in this chapter requires :

- A ν_e search procedure to select electron neutrino interactions in the data and apply in a similar way the procedure to the MC samples.
- The estimation of the beam components, the neutrino interaction cross sections and

the different efficiencies of the selections to weigh each channel properly.

– The estimation of the expected neutrino rates for each channel after selections to see if a significant excess in the ν_e events can be extracted and the statistics needed to reach this result if not. The constraints to the mixing angle θ_{13} and to the squared mass difference Δm^2 given by the OPERA result will be also evaluated.

The electron detection tools and the knowledge of the $\nu_\mu \to \nu_e$ oscillation study allow to perform also the research of the $\tau \to e$ events as an oscillation signal in the $\nu_\mu \to \nu_\tau$ channel.

The MNSP matrix parameters used in the analysis detailed in this chapter come from the global analysis of G.L. Fogli *et al.*[27] and are summarized in table 5.1.

Parameter	Best fit $\pm 1\sigma$ error
$\delta m^2 / 10^{-5} \, \text{eV}^2$ (NH or IH)	$7.54^{+0.26}_{-0.22}$
$sin^2\theta_{12}$ (NH or IH)	$0.307^{+0.018}_{-0.016}$
$\Delta m^2 / 10^{-3} \, \text{eV}^2$ (NH) $\Delta m^2 / 10^{-3} \, \text{eV}^2$ (IH)	$2.43^{+0.06}_{-0.10}$ $2.42^{+0.07}_{-0.11}$
$sin^2\theta_{13} / 10^{-2}$ (NH) $sin^2\theta_{13} / 10^{-2}$ (IH)	2.41 ± 0.25 $2.44^{+0.23}_{-0.25}$
$sin^2\theta_{23}$ (NH) $sin^2\theta_{23}$ (IH)	$0.386^{+0.024}_{-0.021}$ $0.392^{+0.039}_{-0.022}$
δ/π (NH) δ/π (IH)	$1.08^{+0.28}_{-0.31}$ $1.09^{+0.38}_{-0.26}$

Table 5.1: Result of the global 3ν oscillation analysis for the 3ν mass-mixing parameters in the NH or IH picture.

5.1.1   Event rates

The expected neutrino rates in the OPERA detector will be calculated for signal and background at generation level and after reconstruction. The signal event rate S is the convolution of the ν_μ flux $\Phi_{\nu_\mu}(E)$, the neutrino interaction cross section $\sigma_\nu^{\text{CC}}(E)$, the $\nu_\mu \to \nu_e$ oscillation probability $P_{\nu_\mu \to \nu_e}(E)$ and the signal efficiency $\varepsilon_{\text{signal}}$ where A is a normalisation factor to take into account the target mass :

$$S = A \int \Phi_{\nu_\mu}(E) \times \sigma_\nu^{\text{CC}}(E) \times P_{\nu_\mu \to \nu_e}(E) \times \varepsilon_{\text{signal}} \, dE \qquad (5.1)$$

The background event rate B is the sum of each different background channel event rate B_{prompt}, $B_{\tau \to e}$, $B_{\nu_\mu \text{NC}}$ and $B_{\nu_\mu \text{CC} \to \nu_\mu \text{NC}}$.

$$B_{\text{prompt}} = A \int \Phi_{\nu_e}(E) \times \sigma_\nu^{\text{CC}}(E) \times P_{\nu_e \to \nu_e}(E) \times \varepsilon_{\text{prompt}} \, dE \tag{5.2}$$

where $P_{\nu_e \to \nu_e}$ is the ν_e disappearance probability.

$$B_{\tau \to e} = A \int \Phi_{\nu_\mu}(E) \times \sigma_\nu^{\text{CC}}(E) \times P_{\nu_\mu \to \nu_\tau}(E) \times \text{BR}(\tau \to e) \times \varepsilon_{\tau \to e} \, dE \tag{5.3}$$

where $\text{BR}(\tau \to e)$ is the branching ratio of the electronic mode of the tau decay.

$$B_{\nu_\mu \text{NC}} = A \int \Phi_{\nu_\mu}(E) \times R_{\sigma_\nu}(\text{NC/CC}) \times \sigma_\nu^{\text{CC}}(E) \times P_{\nu_\mu \to \nu_\mu}(E) \times \varepsilon_{\nu_\mu \text{NC}} \, dE \tag{5.4}$$

where $R_{\sigma_\nu}(\text{NC/CC}) \approx 3$ is an experimental value of the NC/CC neutrino cross section ratio as presented in section 2.5.1.

$$B_{\nu_\mu \text{CC} \to \nu_\mu \text{NC}} = A \int \Phi_{\nu_\mu}(E) \times \sigma_\nu^{\text{CC}}(E) \times (1 - \varepsilon_\mu) \times P_{\nu_\mu \to \nu_\mu}(E) \times \varepsilon_{\nu_\mu \text{CC} \to \nu_\mu \text{NC}} \, dE \tag{5.5}$$

where ε_μ is the efficiency of identifying a muon in the electronic detectors and will be evaluated on MC ν_μ CC sample named *MC_ numucc_ 3k* and described in section 3.1.5.1.

All the ε_x efficiencies will include all event location efficiencies as well as electron identification efficiencies quoted in sections 3.2 and 4.3, respectively.

5.1.2   Estimation of minor backgrounds

Some other channels than those described above will participate, positively or negatively, to the electron search. However, all of them are expected to have a low contribution. An estimation of their rates is thus presented hereafter to motivate whether we should proceed further than event location process with a precise evaluation. These channels are :

- QE and RES interactions : ν_e and $\tau \to e$ represent additional signal and background with different event location efficiency, which are quoted in section 2.5.2, and kinematical selection strategy which will be described later in section 5.1.3.Otherwise, the rates for these interactions are given in section 3.2.
- charm $\to e$: charm particles D^+, D_S^+, D^0 and Λ_c^+ produced in DIS interactions have electronic decay modes. The expected charm to electron rate N_c is given by equation :

$$N_c = N_{\nu_\mu} \times \sigma_{\nu_\mu \text{CC charm}} \times f_c \times \text{BR}(\text{Charm particle} \to e^+ \text{semileptonic}) \tag{5.6}$$

where N_{ν_μ} is the expected number of ν_μ CC interactions in the detector per 10^{19} p.o.t., $\sigma_{\nu_\mu \text{CC charm}}$ is the charm cross section and, at OPERA energies, is equal to $4.38 \pm 0.26\%$ of the ν_μ CC one, according to the work of N. Agafonova $et\ al.$[59]. f_c represents the charm fractions given by the thesis of M. Besnier [39] and BR, the branching ratios of inclusive electronic modes for each charm particle, taken from [70], both are summarized in table 5.2.

Charm particle	f_c	BR(Charm particle $\to e^+$semileptonic)
Λ_c^+	0.253 ± 0.049	0.045 ± 0.017
D_s^+	0.092 ± 0.038	0.065 ± 0.004
D^+	0.217 ± 0.034	0.161 ± 0.003
D^0	0.438 ± 0.030	0.065 ± 0.0011

Table 5.2: Charm to electron fractions produced in ν_μ CC interactions in the OPERA experiment.

After computation, the number of charm events N_c per 10^{19} p.o.t. giving an electron in the final state is :

$$N_c = 2.2 \pm 0.4 \quad (10^{19}\text{p.o.t.})^{-1} \tag{5.7}$$

For these two contributions, QE+RES interactions and charm $\to e$, location efficiency given by section 3.2 will be applied and to the charm channel, the efficiency of misidentifying a muon track as well. Table 5.3 reports these rates at the event location level for charm $\to e$, ν_e for QE+RES and for DIS and $\tau \to e$ for QE+RES and for DIS and, finally, also for oscillated ν_e for the sake of comparison.

These rates are to be compared at the $\tau \to e$ channel ones. ν_μ^{NC} and $\nu_\mu^{\text{CC}} \xrightarrow{\text{mis}} \nu_\mu^{\text{NC}}$ channels are not in the table, indeed their high rate expected in the detector is not a good reference since they contribute poorly to background after selection because of good discriminating capability of the electron energy of these two background sources.

The $\tau \to e$ channel represents the less contributing background source in terms of expected rate before selection which makes it a good reference to estimate the importance of the minor background sources studied here. According to the results of table 5.3, the following contributions to the signal of background sources will be neglected :

– charm $\to e$ is at 21% level of the $\tau \to e$ background, the smallest background channel.

– $\tau \to e$ QE+RES represents about 12% of the $\tau \to e$ events and in 2008 and 2009 data (5.3×10^{19}p.o.t.) where 1.5 ± 0.2 located $\tau \to e$ events are expected.

– oscillated ν_e QE+RES : 12.6 ± 1.2 oscillated ν_e events are expected for 22.5×10^{19}p.o.t. and QE+RES events correspond to 21% of those. This additional signal will not be processed.

	charm $\rightarrow e$	prompt ν_e QE+RES	prompt ν_e	$\tau \rightarrow e$ QE+RES	$\tau \rightarrow e$	oscillated ν_e QE+RES	oscillated ν_e
Rate $(\nu.(10^{19}\text{p.o.t.})^{-1})$	2.2 ± 0.40	0.39 ± 0.10	5.95 ± 0.45	0.093 ± 0.009	0.55 ± 0.06	0.18 ± 0.01	0.87 ± 0.07
μ misidentification	0.052 ± 0.007	-	-	-	-	-	-
Event location	0.524 ± 0.026	0.730 ± 0.037	0.636 ± 0.032	0.374 ± 0.019	0.524 ± 0.026	0.691 ± 0.035	0.642 ± 0.032
Expected located rate $(\nu.(10^{19}\text{p.o.t.})^{-1})$	0.060 ± 0.011	0.28 ± 0.07	3.78 ± 0.34	0.034 ± 0.004	0.288 ± 0.035	0.12 ± 0.01	0.559 ± 0.053

Table 5.3: QE+RES interactions and charm $\rightarrow e$ channel rates with their associated systematic uncertainties in the OPERA detector at the event location level.

In general, QE and RES interaction rates at the vertexing level are small because of the small vertex reconstruction efficiency due to the absence of hadronic tracks. Moreover, the oscillated ν_e QE+RES simulation is absent from the official MC production.

Nevertheless, 1.5 ± 0.4 prompt ν_e QE+RES are expected in 2008-2009 data and are therefore interesting to take into account.

5.1.3   Kinematical variables

In 2009, I carried out a simplified analysis at the generation level with the following kinematical variables : the electron energy, the neutrino energy, the transverse momentum of the electron and the missing transverse momentum at the interaction vertex. A Gaussian smearing of these variables has been applied according to a 20% resolution of the momentum and a 40% resolution of the energy as quoted in the thesis of M. Besnier [39]. A significance analysis has been performed and a set of optimal cuts listed in table 5.4 has been obtained.

Variables	Values of the cut
Electron energy	$E_e < 20\,\text{GeV}$
Neutrino energy	$E_\nu < 25\,\text{GeV}$
Electron transverse momentum	$p_\text{T}^e < 1.8\,\text{GeV/c}$
Missing transverse momentum at interaction vertex	$p_\text{T}^\text{mis} < 1.6\,\text{GeV/c}$

Table 5.4: Set of cuts defined by a significance study on MC samples of each channel.

This analysis, and another one based on a likelihood ratio selection giving similar results and described in the work of F. Brunet [101] defined the following neutrino rates in the OPERA experiment summarized in table 5.5.

	signal	$\tau \to e$	ν_μ^NC	ν_e^CCbeam
ξ	0.53	0.53	0.48	0.53
ε	0.75	0.68	7×10^{-4}	0.30
$\varepsilon \times \xi$	0.40	0.36	3.4×10^{-4}	0.16
$\text{N}_\text{evt}^{5\,\text{ans}}$	10.3	4.3	2.3	26.2

Table 5.5: Efficiencies and neutrino rates expected in the OPERA experiment for five nominal years, i.e. 22.5×10^{19}p.o.t. ξ efficiency included BF, vertex finding and ED trigger efficiencies and a fiducial volume cut quoted in the work of M. Komatsu *et al.* [102]. ε efficiency corresponded to the cuts on the kinematical variables mentioned above. The MNSP parameters value was extracted from the global analysis of G.L. Fogli *et al.* [31]. Since the ν_μ^NC MC sample had not been processed at that time, result for this channel had been taken from the work of M. Komatsu *et al.* [102].

This analysis carried out in 2009 has been performed with different input rates as the ones used in this thesis work which explains that the numbers in table 5.5 are slightly different from those given in the next sections.

As expected the number of prompt ν_e is higher than the signal by a factor 2.5. The two background sources were equivalent but all these numbers were overestimated because of a rough treatment of the detection efficiencies. Another difference with the new study coming in the next sections is the oscillation probability since the measurement of the mixing angles have recently changed according to the results presented in section 1.3. Finally, the analysis at the generation level has been a good opportunity to test the discriminating capability of the variables and define them for the final analysis.

To optimize the appearance of oscillated ν_e in our analysis, all background sources have to be kept as low as possible. A set of kinematical cuts will be applied and has to be defined by a MultiVariate Analysis (MVA), method described in appendix E.2, on relevant variables listed in the following :

- *Electron energy E_e*
  As mentioned above, an electron energy upper cut is necessary. In addition a lower cut would be useful to suppress the NC background producing photon showers at lower energies than electrons of the signal. The performance of the electron energy estimation tool has been completely described in chapter 4 which explained the agreement between data and MC, and the calculation of the systematic errors which are used in this study.
- *TT visible energy $E_{\mathrm{TT}}^{\mathrm{vis}}$*
  The neutrino energy is not easily deduced from the electronic response of the detector since the latter contributes to only 2-3% of the total energy [87]. However, the output of the TT will give a useful information about the visible energy which can be included in the MVA. A brief description of this measurement is given in section 3.1.3.
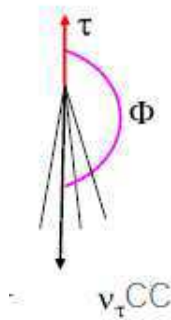
Figure 5.1: Sketch showing the definition of the Φ_{had} angle.

- *Event topology $p_{\mathrm{T}}^{\mathrm{mis}}$ and Φ_{had}*
  The position resolution of nuclear emulsions can also be used to measure the angle of each charged track with an accuracy of about 1 mrad. This allows momentum measurement by using the MCS with a resolution of about 20% and the reconstruction of kinematical variables characterising the event, i.e. the missing

transverse momentum at the interaction vertex and the transverse momentum of a track with respect to hadronic shower direction called Φ_{had} angle as shown in figure 5.1. These variables are built with the momentum measured of each charged track. Unfortunately, the MCS algorithm [43] has not been yet implemented in the new OpEmuRec framework. A parametrisation as a function of $1/p$ and depending on the number plates used has been computed and will be applied on the MC true value of the momentum. Note that these variables are useless for ν_e QE interactions since there is no hadronic shower.

– *Rejected variables* Σ_{trk}, p_{T}^e and θ_{PM}
These variables, i.e. the track multiplicity at primary vertex Σ_{trk}, the electron transverse momentum p_{T}^e and the angle between a primary track and its mother θ_{PM} have been included in this study and showed a low discriminating power which can cause overtraining effects of the MVA method if they would be included as explained in appendix E.2.

A new study to evaluate the oscillated ν_e and its associated background sources rates can be carried out taking into account all detector efficiencies and resolutions. The oscillation study at the generation level has selected relevant kinematical variables and the electron reconstruction tool allows to estimate the electron showers energy. It is also used to take into account the electron identification efficiency. Finally, the TT visible energy estimation and the track reconstruction with the MCS algorithm reconstruct the remaining kinematical variables.

5.2   Oscillated ν_e Rate Calculation And Measurement

The aim of this study is to estimate with MC simulations the number of events expected for the oscillation signal and all background channels described in section 2.6. The MC samples used for this study represent each channel and have been processed in the OpEmuRec framework from the generation up to the event location, the reconstruction of the electromagnetic shower and their identification. These samples are described in section 3.1.5.1 and listed below.

– *MC_ nue_ 1k* : ν_e from the beam contamination.
– *MC_ nueqe_ 1k* : ν_e QE+RES interactions from the beam contamination.
– *MC_ oscillated_ nue_ 1k* : oscillated ν_e.
– *MC_ oscillated_ nue_ 3k* : oscillated ν_e generated with ν_μ energy spectrum.
– *MC_ taue_ 3k* : oscillated ν_τ with τ decay in electronic mode.
– *MC_ numunc_ 3k* : ν_μ NC interactions.
– *MC_ numucc_ 3k* : ν_μ CC interactions.

5.2.1   Input variables

Relevant variables for this study are defined in section 5.1.3 at the generation level, applying a Gaussian smearing. To go further, this study will use reconstructed variables with the reconstruction process which is applied through the OpRelease software. The

discriminating power of these inputs for any background sources has thus to be checked. Figure 5.2 shows their distributions for the signal and each background source.
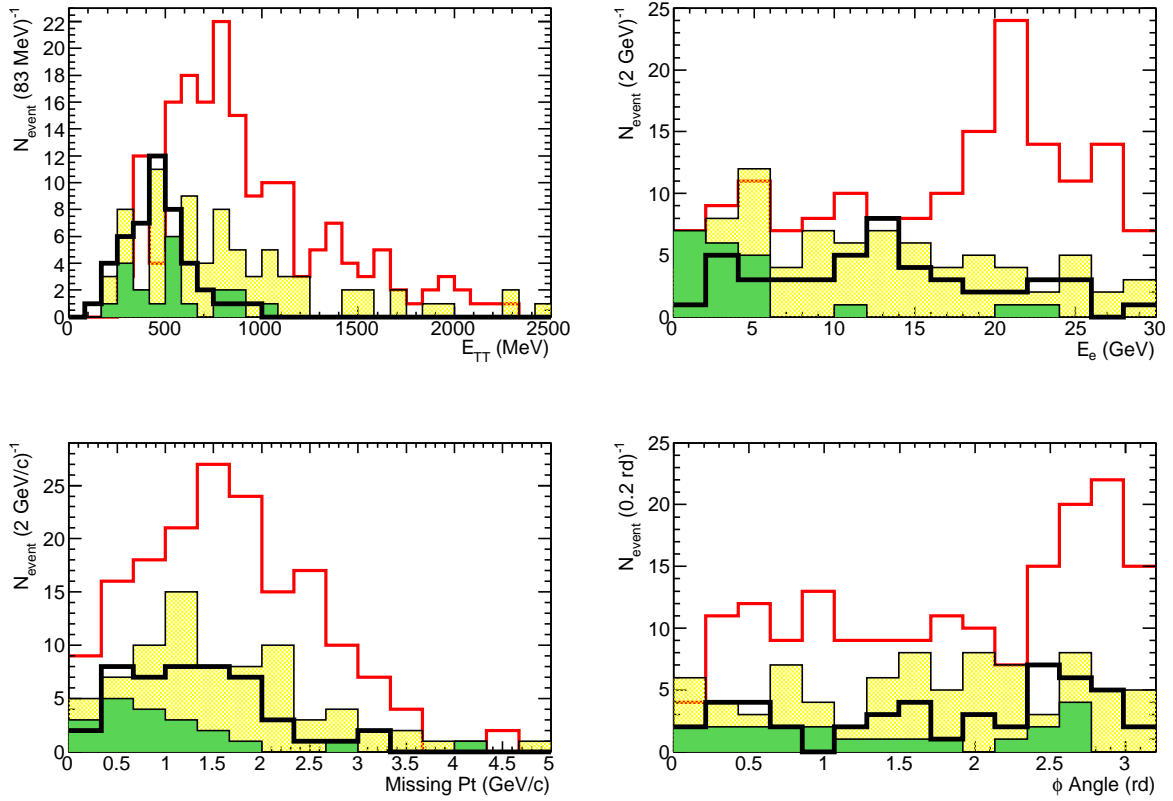
Figure 5.2: Distribution of the input variables of the MVA : the visible energy $E_{\mathrm{TT}}^{\mathrm{vis}}$, the electron energy E_e, the missing transverse momentum at primary vertex $p_{\mathrm{T}}^{\mathrm{mis}}$ and the phi angle Φ_{had} for the signal and each MC background channel superimposed. The black thick line represent the signal, i.e. the $\nu_\mu \to \nu_e(e)$ oscillation channel. The red, yellow and green histograms correspond to the prompt ν_e, the $\nu_\mu \to \nu_\tau(\tau \to e)$ and the ν_μ NC channels, respectively.

The mean value of each of these variables for each background source has been computed and is summarized in table 5.6.

	ν_e	Prompt ν_e	$\tau \to e$	ν_μNC
$\langle E_{\mathrm{TT}}^{\mathrm{vis}} \rangle$ (MeV)	462	943	850	635
$\langle E_e \rangle$ (GeV)	8.7	12.9	8.5	3.4
$\langle \Phi_{\mathrm{had}} \rangle$ (rad)	1.8	1.8	1.7	1.4
$\langle p_{\mathrm{T}}^{\mathrm{mis}} \rangle$ (GeV/c)	1.3	1.9	1.9	1.7

Table 5.6: Mean value of the input variables for each background and for the signal.

$E_{\mathrm{TT}}^{\mathrm{vis}}$ has a discriminating power for prompt ν_e events since their energy distribution has a long tail above $1\ 000\,\mathrm{MeV}$ whereas oscillated ν_e do not exceed this value. E_e presents also a discrepancy between prompt and oscillated ν_e but also with $\nu_\mu \mathrm{NC}$ because of the lower energy spectra of the photons in these processes. $p_{\mathrm{T}}^{\mathrm{mis}}$ for ν_μ NC and $\tau \to e$ channels peak to a lower value than the signal because of the presence of missed π^0 in NC events and because of the two escaping neutrinos in the electronic decay of the tau lepton in the $\tau \to e$ channel. The prompt ν_e channel presents a $p_{\mathrm{T}}^{\mathrm{mis}}$ of the same shape as the signal. For the same reason, $p_{\mathrm{T}}^{\mathrm{mis}}$ should be a good discriminating variable for the $\tau \to e$ background and ν_μ NC. However, the Decay Search Procedure (DSP) is not yet implemented in the MC simulation, implying that the topology is not completely described in the $\tau \to e$ channel. The vertexing simulation used in this study presents a poor efficiency and some systematic effect in the attachment of tracks to the reconstructed vertex. That is why the rate of the events used in this MVA, method described in section E.2, is low with respect to the number of located events especially for the NC channel.

The input variables distributions show that the $\tau \to e$ background is the most difficult to discriminate from the signal. Given the micrometric spatial resolution of the OPERA detector, one can use the kink topology of these events to reject them. Later in section 5.5.1, a detailed explanation is given to justify the use the Impact Parameter (IP), defined as the minimal distance of approach of the electron track to the vertex, as an additional input to the MVA ; figure 5.3 shows its distribution for signal and each background source.
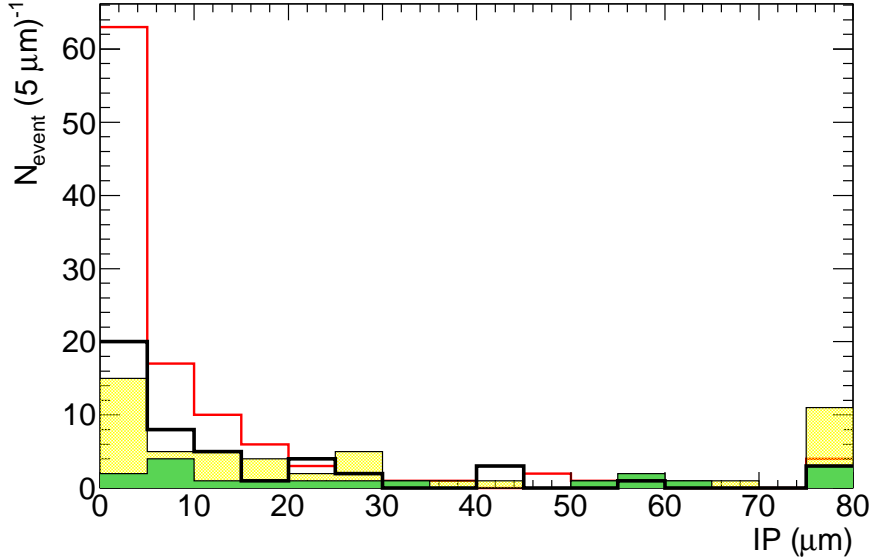
Figure 5.3: Distribution of the IP for the signal and each MC background source superimposed. The black thick line represent the signal, i.e. the $\nu_\mu \to \nu_e(e)$ oscillation channel. The red, yellow and green histograms correspond to the prompt ν_e, the $\nu_\mu \to \nu_\tau(\tau \to e)$ and the ν_μ NC channels, respectively. The last bin shows the overflow of each distribution.

Figure 5.2 shows that a pre-selection can be performed on the visible energy in the Electronic Detectors $E_{\mathrm{TT}}^{\mathrm{vis}}$ as well as the missing transverse momentum at the primary vertex $p_{\mathrm{T}}^{\mathrm{mis}}$ to reduce the background contribution while the signal efficiency is kept at 100% ; these cuts are summarized in table 5.7 and the effects of these cuts on the signal and the background sources are detailed in table 5.8. Then, the kinematical variables feed the MVA to optimize the background rejection where signal/background separation is less obvious.

	Cut value
$E_{\mathrm{TT}}^{\mathrm{vis}}$ (MeV)	1000
$p_{\mathrm{T}}^{\mathrm{mis}}$ (GeV/c)	3.4

Table 5.7: Pre-selection set of cuts to discriminate the signal from the background sources

	signal	prompt ν_e	$\tau \to e$	ν_μ^{NC}	$\nu_\mu^{\mathrm{CC}} \xrightarrow{\mathrm{mis}} \nu_\mu^{\mathrm{NC}}$
Efficiency of the cut $E_{\mathrm{TT}}^{\mathrm{vis}} < 1\,000$ MeV (%)	100	65.3	71.6	90.5	90.5
Efficiency of the cut $p_{\mathrm{T}}^{\mathrm{mis}} < 3.4$ GeV/c (%)	100	93.2	90.1	90.5	90.5
Efficiency of the two cuts combined (%)	100	63.1	66.7	85.7	85.7

Table 5.8: Efficiencies of the pre-selection cuts on the signal and the various background sources.

The cut efficiencies are not taken into account in the following MVA ; they will be added to the MVA result afterwards to calculate the final expected rates in table 5.11.

5.2.2 Discrimination of the ν_e signal with respect to background channels

Location efficiency as well as electron identification efficiency have been estimated with their statistical and systematic uncertainties in section 3.2 and 4.3. A set of discriminating variables is also described in section 5.1.3 and their contribution to each channel has been studied in section 5.2.1. Typical method to optimize cuts on variables to maximize the ν_e signal appearance while the background is minimized is the use of MVA and, especially, the computation of Fisher's coefficients or the use of ANN to compute a classifier separating the ν_e signal from the background. Both of these techniques are formally described in section 3.3 and the significance as defined in equation 5.8 will be looked at to estimate the performance of these methods.

$$S = \frac{N_S}{\sqrt{N_S + N_B}} \tag{5.8}$$

where N_S and N_B are the number of signal and background events respectively.

Figure 5.4 shows the distribution of classifiers computed in the two analysis methods and their separation capability is illustrated in table 5.9.
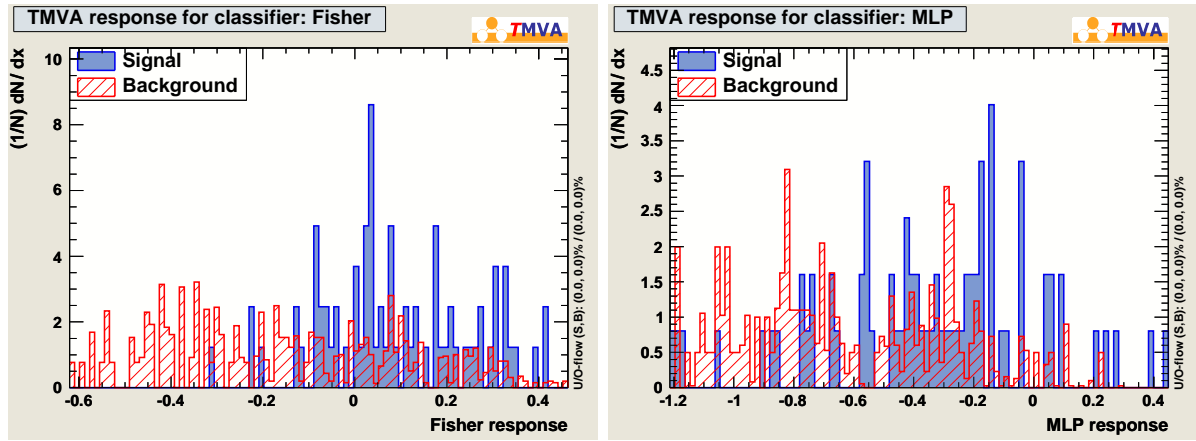
Figure 5.4: Distribution of classifiers for the Fisher method on the LHS and for the ANN method on the RHS for the ν_e signal and for all background combined.

Classifier	Optimal cut	Significance	ν_e Signal efficiency	Background efficiency
Fisher	-0.1336	25.4	0.947	0.448
ANN	-0.7803	23.3	0.907	0.604

Table 5.9: Optimal cut on classifiers and their associated significance, ν_e signal and background efficiencies.

MVA method	ν_e Signal efficiency with background at 10%	ν_e Signal efficiency with background at 30%
Fisher	0.239	0.731
ANN	0.369	0.555

Table 5.10: Signal efficiencies for both methods Fisher and MLP for different values of the background contamination.

These two methods have been preliminary selected for their best performance in classification. They gave similar optimization of the classification on the MC true study shown in section 5.1.3. Here, as it is shown on figure 5.4 and in table 5.9, the MultiLayer Perceptron (MLP) method is less efficient to separate signal from background sources because of the limited statistics to train properly the ANN. Fortunately, the Fisher's

method is able to optimize the cut on the classifier to deliver a 95% efficiency on signal with respect to 45% background contamination.

In general, more statistics would be helpful for both methods to improve the Signal-to-Noise Ratio (SNR) ; for the MLP method to ensure the consistency between the training and the test samples, for the Fisher's method to obtain reliable Probability Density Function (PDF) of the distributions of the input variables.

The ν_e signal efficiency versus the purity is plotted and shown in figure 5.5 and a summary of the ν_e signal efficiency as a function of the background rejection is given in table 5.10.
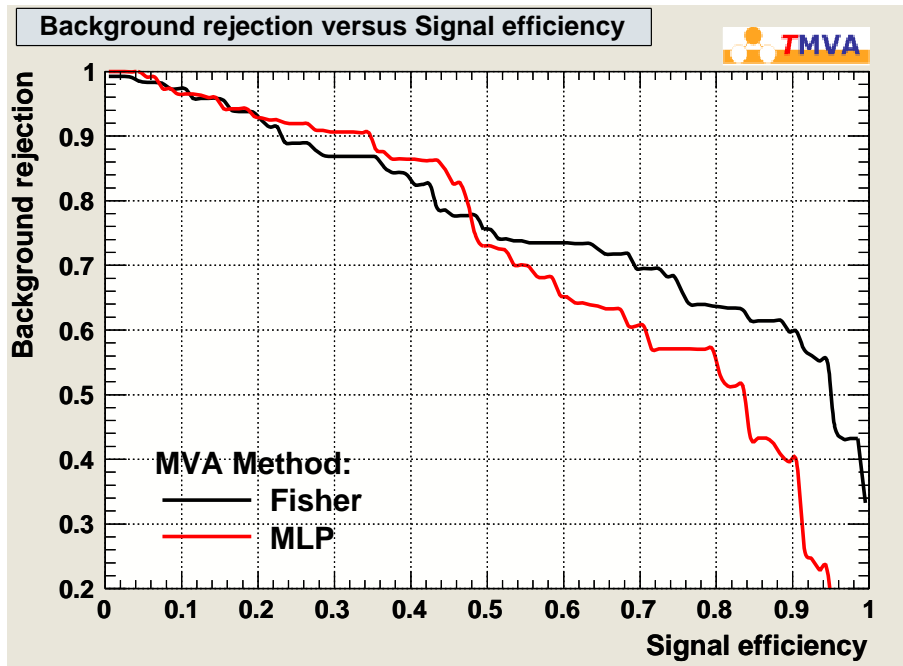
Figure 5.5: Efficiency versus purity for the ν_e signal with respect to the background sources for the two methods Fisher and ANN.

The prompt ν_e channel is an irreducible background below 30 GeV and definitely the most important in terms of rate which means the signal efficiency has to be taken as higher as possible to detect an excess of events. If we want to achieve a low background at 10% level for instance, the signal efficiency will drop to 25-35%. The Fisher's method will be used to evaluate the expected rates in the following.

5.2.3 Expected event rates

Selection efficiency has been obtained from section 5.2.2, including event location and electron identification. One can compute the final optimized expected number of events in the OPERA experiment as in table 5.11. The uncertainties on the rates are systematic and are computed with the quadratic sum of the systematic uncertainties on the fluxes quoted in table 2.5, on the event location quoted in table 3.6 and on the

electron identification quoted in section 4.3.3. In fact, those uncertainties are considered as uncorrelated since we simply count event numbers to estimate these rates without cutting on a influence parameter of this study, for instance the energy of electrons.

	signal	prompt ν_e	$\tau \to e$	ν_μ^{NC}	$\nu_\mu^{\mathrm{CC}} \xrightarrow{\mathrm{mis}} \nu_\mu^{\mathrm{NC}}$
Expected neutrino events in 2008-2009	4.6±0.3	31.5±2.4	2.9±0.3	1180±120	3530±360
Event location + electron identification efficiency	0.323±0.023	0.51±0.04	0.21±0.02	(5.0 ± 0.3) $\times10^{-3}$	(7.7 ± 0.6) $\times10^{-4}$
N_{evt} expected in 2008-2009	1.49 ± 0.15	16.1 ± 1.7	0.61 ± 0.09	5.9 ± 0.7	2.7 ± 0.3
N_{evt} expected @ 22.5×10^{19}p.o.t.	6.3 ± 0.6	68 ± 7	2.6 ± 0.4	25 ± 3	11.5 ± 1.3
N_{evt} expected in 2008-2009 after MVA	1.41 ± 0.15	4.6 ± 0.5	0.28 ± 0.04	1.1 ± 0.1	0.5 ± 0.1
N_{evt} expected @ 22.5×10^{19}p.o.t. after MVA	6.0 ± 0.6	20 ± 2	1.2 ± 0.2	4.7 ± 0.4	2.2 ± 0.4

Table 5.11: Neutrino rates expected in the OPERA experiment for 2008-2009 data (5.3×10^{19} p.o.t.) and five nominal years, i.e. 22.5×10^{19} p.o.t.. The MNSP parameters value was extracted from the global analysis of G.L. Fogli *et al.*[27].

The prompt ν_e channel being an irreducible background, the number of events is greater than the signal one ; however, the significance has been improved thanks to the MVA analysis. The SNR of the signal with respect to all background sources before MVA is 0.059. The SNR of the signal with respect to all background sources after MVA is 0.22. The other background sources which were higher or equivalent to the oscillated ν_e have been drastically reduced. The significance of the signal with respect to all background sources is in 2008-2009 : $0.5\,\sigma$ and with a luminosity of 22.5×10^{19}p.o.t. : $1.0\,\sigma$. These significances are inferred from 6.0 signal events divided by the square root of (6+20+1.2+4.7+2.2) background events. The main limits to that study are the contamination of the beam, the poor location efficiency at low energy where the SNR is maximal, as shown in figure 3.6 and the π_0 contamination represented by the ν_μ^{NC} and the $\nu_\mu^{\mathrm{CC}} \xrightarrow{\mathrm{mis}} \nu_\mu^{\mathrm{NC}}$ channels which could be reduced with a specific photon/electron separation algorithm as already discussed in section 4.3.2.

This study has defined the expectations in terms of event rates on MC sample with a full detector simulation.

5.3 OPERA Data Analysis

OPERA is an on going experiment still analysing data. This means that a data sample has to be determined to be used in this analysis. Data taking starts with "simple" events, which are published earlier in the year, the "complicated" ones which need several scanning and reconstruction procedure to quote a result arrive later. That is why, I only analysed data of a whole year.

5.3.1 Data selection

The analysis chain, described in section 2.4, represents a strong workload implying at least one year delay between the real-time data taking and the publication of the reconstructed event in the database. The fully analysed sample available for this thesis work is 2008 and 2009 data. The 2010 year data has been completely scanned but the decay search and ν_e search procedures are not finished yet. 2008-2009 data summary is given in table 5.12.

	2008		2009	
	0μ	1μ	0μ	1μ
Events found by the ED	406	1292	1097	2460
Events located in ECC	169	834	360	1490
Events analysed for ν_e search	505			

Table 5.12: Summary of the event location in 2008 and 2009 data. 1μ numbers are quoted as a reference sample. 0μ represents the sample in which we look for electrons [58].

In the 0μ data collection, a specific procedure has been applied in order to find electrons described hereafter.

5.3.2 Electron channels search procedure

This ν_e search process has been systematically applied on the localized events summarized in table 5.12 and it consists of a strategy based on two algorithms : the CS shower hint described in OPERA study [103] and the electromagnetic shower reconstruction and identification thoroughly studied in section 4.3.

- *CS shower hint* : first an algorithm looks for clusters of tracks in the CS corresponding to a shower. An electron hint is validated if the cluster is formed of at least three tracks or more and if the position difference and angular difference between the cluster and the other CS tracks are strictly less than 2 mm and 150 mrad respectively.
- *Electron identification* : it is applied on a standard 10 plates volume if the former CS shower hint did not recognize the event as an electron and on the entire brick if

the CS shower hint algorithm did validate the event as an electron candidate. The result of the shower identification algorithm finally distinguishes events containing an electron from those without an electron.

The interest of the CS shower hint algorithm is to trigger events in the inefficiency of the electron identification algorithm in a 10 plates volume which can be recovered with a larger number of plates. If the vertex of the event is located downstream the brick, less than 10 plates could be available for analysis which represents a difficulty not only to identify electrons but also to estimate their energy and to measure the momentum of other tracks. In this case, a two-bricks analysis can be discussed as it is done in section 4.5.1.

Moreover, additional pattern recognition algorithms are used to improve the electron identification efficiency. Those are CS to vertex hint, SB shower hint and gamma hint, they are described in the work of U. Kose[103].

5.3.3   Selected electron events

Vertex plate number	Corrected Electron energy (GeV)	$E_{\mathrm{TT}}^{\mathrm{vis}}$ (MeV)	$p_{\mathrm{T}}^{\mathrm{mis}}$ (GeV/c)	Φ_{had} (°)	IP (μm)
43	9.1	1032.34	0.6	150	2.4
12	18.7	332.415	1.4	102	0.1
45	3.4	1106.35	1.4	140	0.4
28	27.8	668.387	1.5	159	1.6
53	3.0	487.298	0.2	-	-
35	4.0	339.42	0.7	65	0.6
49	2.5	387.681	0.4	111	3.0
4	23.3	855.084	1.6	153	3.5
37	6.5	1137.96	0.9	170	0.3
35	16.4	1131.8	0.7	134	0.9
43	11.1	406.227	0.2	174	1.0
47	5.4	413.25	0.3	153	1.1
31	25.1	950.462	0.9	62	0.2
41	13.6	2107.54	0.5	128	1.6
32	10.8	513.544	0.7	72	2.3
15	15.6	2108.2	1.1	130	3.6
46	8.3	1967.98	1.7	9	0.9
45	5.1	1821.45	2.6	153	0.4
31	24.7	1967.5	1.0	123	0.3

Table 5.13:   2008 and 2009 electron data summary with their associated kinematical variables needed by the analysis.

CS shower hint have triggered 86 events out of 505 events of the 2008-2009 data campaign and the electron identification algorithm has confirmed 19 of these. These

former ν_e events constitute the data collection given in table 5.13. For each event, the electron shower energy estimation has been processed to measure the electron energy. Other kinematical variables measurements have been also carried out : visible energy in the TT $E_{\mathrm{TT}}^{\mathrm{vis}}$, the missing transverse momentum at primary vertex $p_{\mathrm{T}}^{\mathrm{mis}}$ and the transverse momentum of a track with respect to hadronic shower direction Φ_{had}.

5.4 OPERA Performance On $\nu_\mu \to \nu_e$ Oscillation

Table 5.13 gives all the information needed by the analysis procedure defined in section 5.2.2 to optimize the SNR for a search of a ν_e oscillation signal in this dataset. First, one has to check if these data are compatible with the MC simulations used in the previous analysis.

5.4.1 Comparison of MC simulations with data

Figures 5.6 and 5.7 show plots of the input variables of the MC simulations superimposed with the distribution of these variables from the dataset.
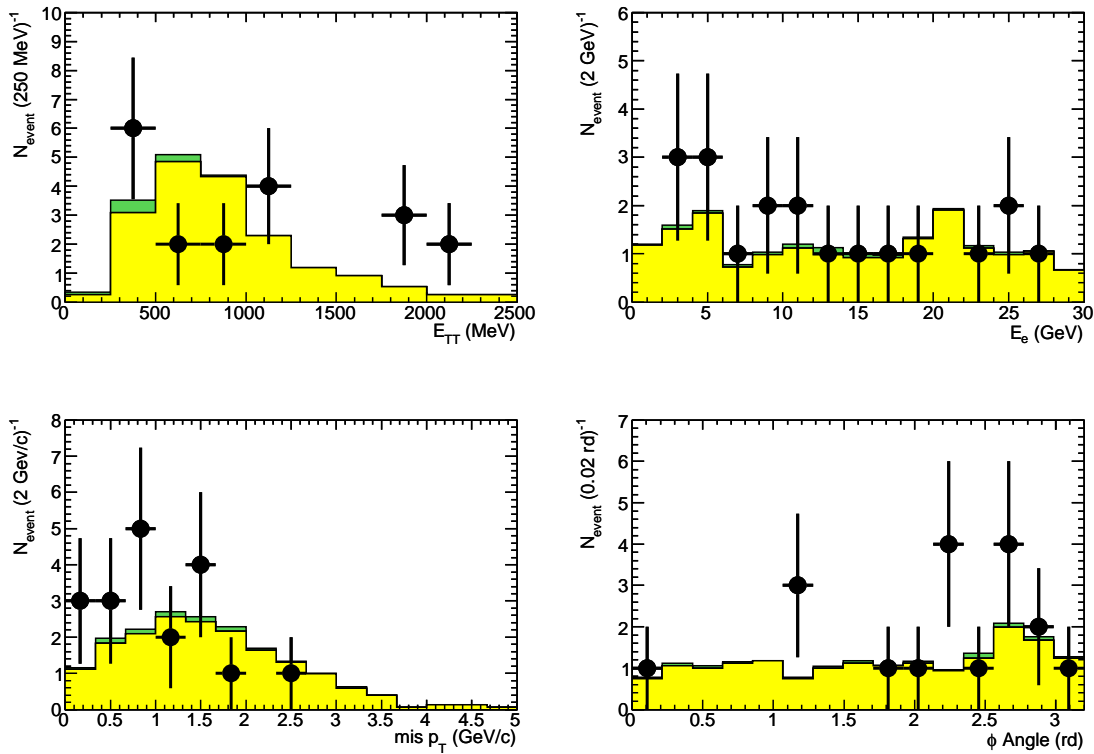
Figure 5.6: Comparison of the MC with data distributions of variables defined as inputs of the discriminating analysis : : $E_{\mathrm{TT}}^{\mathrm{vis}}$, E_e, $p_{\mathrm{T}}^{\mathrm{mis}}$ and Φ_{had}. Black dots represent the data. Yellow and green histograms correspond respectively to MC simulation of all background sources and the signal normalised to data.
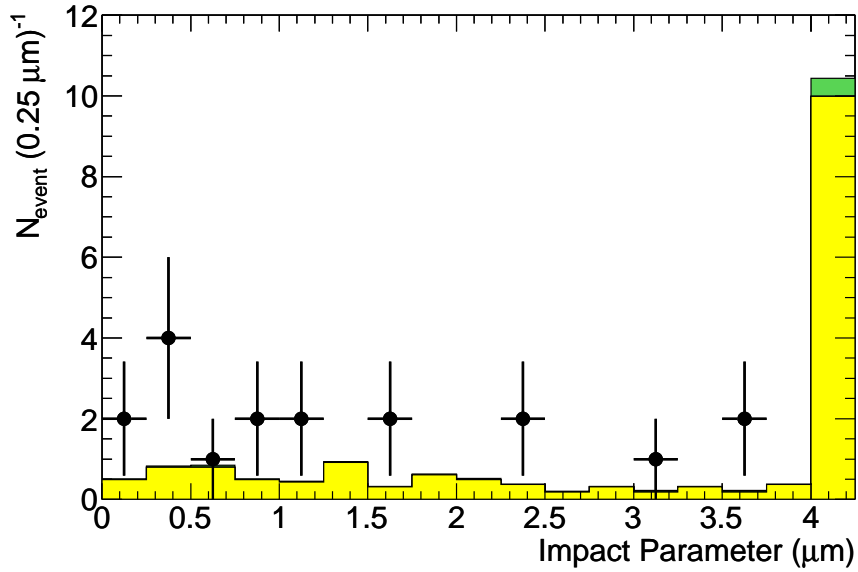
Figure 5.7: Comparison of the MC with data distributions of the IP defined as an input of the discriminating analysis. Black dots represent the data. Yellow and green histograms correspond respectively to MC simulation of all background sources and the signal normalised to data. The last bin shows the overflow of each distribution.

First, these MC distributions have been normalised to data since this comparison studies the reliability of the OPERA simulation to separate the signal from the background channels. In deed, the absolute normalisation of the MC does not contribute to the separation power of the kinematical variables.

The IP distribution of the MC simulation has a long tail beyond $3.5\,\mu$m which is not compatible with data. On the one hand, the IP contribution in the signal efficiency with respect to the background rejection in the discrimination study presented in section 5.2.2 is small (few percent). On the other hand, the vertexing algorithm used in this study is basic and introduces some systematic effects on the IP computation. In fact, the use of this vertexing algorithm is not straightforward with the data. The IP as an input variable to the MVA will be consequently removed from the following analysis. Note that the DSP properly applied will provide a uniform algorithm for MC simulations and data in the future.

The agreement between MC and data is good for all other variables and especially for the electron energy E_e. For the visible energy in the TT E_{TT}^{vis}, discrepancies are observed but we know that electromagnetic component of the neutrino interaction is poor in the EDs. If the agreement on the electron energy is good, one can not forget that, as it has been presented in chapter 4, the systematic uncertainty on the energy of the electron showers is important especially in the downstream half-brick where information leakage becomes significant : indeed our data are mainly localized in this part. The energy estimation within two bricks reported in section 4.5.1 would improve this situation.

The phi angle Φ_{had} and the missing transverse momentum at the primary vertex $p_{\mathrm{T}}^{\mathrm{mis}}$ would be also affected since they use the electron energy to determine the momentum of the electron track.

These distributions, showed in figure 5.6, are given as inputs to the MVA for the ν_e search analysis which classifies the data as signal or background with a cut on the Fisher classifier defined in section 5.2.2. In addition, from table 5.11, the MC expectations in terms of event rates in the signal and in the background regions can be computed with their associated systematic uncertainties. The resulting numbers are given in table 5.14.

MC expectations Signal	7.9 ± 2.7
MC expectations Backgrounds	18.9 ± 4.8
Data selected as signal	6 ± 2
Data selected as background	13 ± 4

Table 5.14: Signal and background MC expectations versus data. MC expectations uncertainties are systematic. Data uncertainties are statistical.

Note that 9 events in the data have been classified as background by the preliminary cuts on the visible energy in the TT $E_{\mathrm{TT}}^{\mathrm{vis}}$ and on the missing transverse momentum at the primary vertex $p_{\mathrm{T}}^{\mathrm{mis}}$.

Table 5.14 shows clearly an agreement between MC expectations and the data processed in the MVA taking into account the uncertainties.

5.5 $\quad \tau \to e$ Search

On the same principle as the ν_e search analysis, the performance of OPERA in $\tau \to e$ detection can be studied based on the knowledge of the electron detection given in chapter 4 and of the event location given by section 3.2. A specific procedure to search for τ-decay topology called Decay Search Procedure (DSP) is first presented as well as its implementation in this study. Then, the analysis presented in section 5.2 is started over searching for $\tau \to e$ detection.

5.5.1 The DSP

After a neutrino interaction is localized in a scanning laboratory, the DSP, described in detail in the thesis of T. Strauss [56] has to be performed to find possible decays downstream the primary vertex, as explained in section 3.1.4. The DSP was implemented in the FEDRA framework and was hence applied to the MC generated events. With studies done in Bern, the need of a common procedure for event analysis was shown and the DSP was optimized using these results, especially taking into account a higher number of emulsion films to be scanned to recover efficiency losses of reconstructed tracks due to bad emulsion quality. However, this procedure has not been yet fully implemented in the OpEmuRec framework which delays its use for the $\tau \to e$ search study.

The working group in charge of the development of the DSP algorithm has nevertheless computed efficiencies, summarized in table 5.15, for the $\tau \to e$ channel. But they cannot be used further in this work since the DSP efficiency of misidentifying background channels as a decay topology is unknown. The kinematical and topological selections will be applied in the exact same way as for the ν_e search and, as a first approach to the DSP effect on the event rates, the most discriminant criterion of the DSP, the IP cut - IP $< 10 \, \mu$m - will be applied.

$\tau \to e$ DIS		$\tau \to e$ QE
Long decays	Short decays	Long decays
58.4 ± 2.2 %	54.8 ± 2.2 %	22.1 ± 1.7 %

Table 5.15: The DSP efficiencies for different topologies long and short decay for $\tau \to e$ channels QE and DIS processes [104].

5.5.2 Discrimination of the $\tau \to e$ signal with respect to background channels

The location efficiency as well as the electron identification efficiency have been estimated with their statistical and systematic uncertainties in section 3.2 and 4.3. A set of discriminating variables is also described in section 5.1.3 and their contribution to each channel has been studied in section 5.2.1. Figure 5.2 shows that none preliminary cut can be performed before the MVA in order to reduce the background contribution without affecting the signal efficiency. The same statistical tools as those described in section 5.2.2 will be used. The significance as defined in equation 5.8 will be looked at to estimate the performance of these analyses.

Figure 5.8 shows the distribution of classifiers computed in the two analysis methods and their separation capability is illustrated in table 5.9.
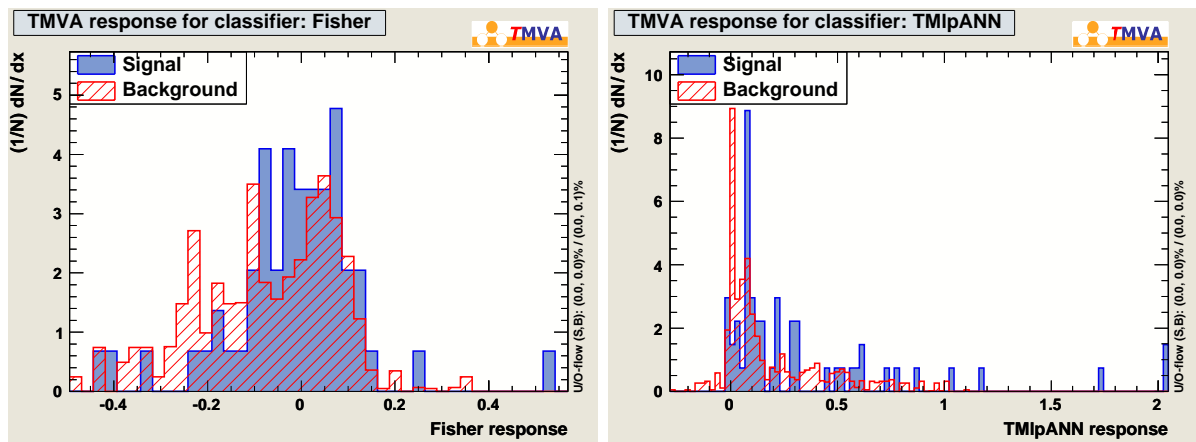
Figure 5.8: Distribution of classifiers for the Fisher method on the LHS and the ANN one on the RHS for the $\nu_\mu \to \nu_\tau (\tau \to e)$ signal and for all background combined.

Figure 5.8 shows that the classifiers distributions for signal and background are superimposed. It is thus difficult to set a cut to separate them efficiently.

Classifier	Optimal cut	Significance	Signal efficiency	Background efficiency
Fisher	0.53	22.4	1	1
ANN	-0.011	22.6	1	0.95

Table 5.16: Optimal cut on classifiers and their associated significance, signal $\tau \to e$ and background efficiencies.

The $\tau \to e$ signal efficiency versus the purity is plotted and shown in figure 5.9 and a summary of the $\tau \to e$ signal efficiency as a function of the background rejection is given in table 5.17.
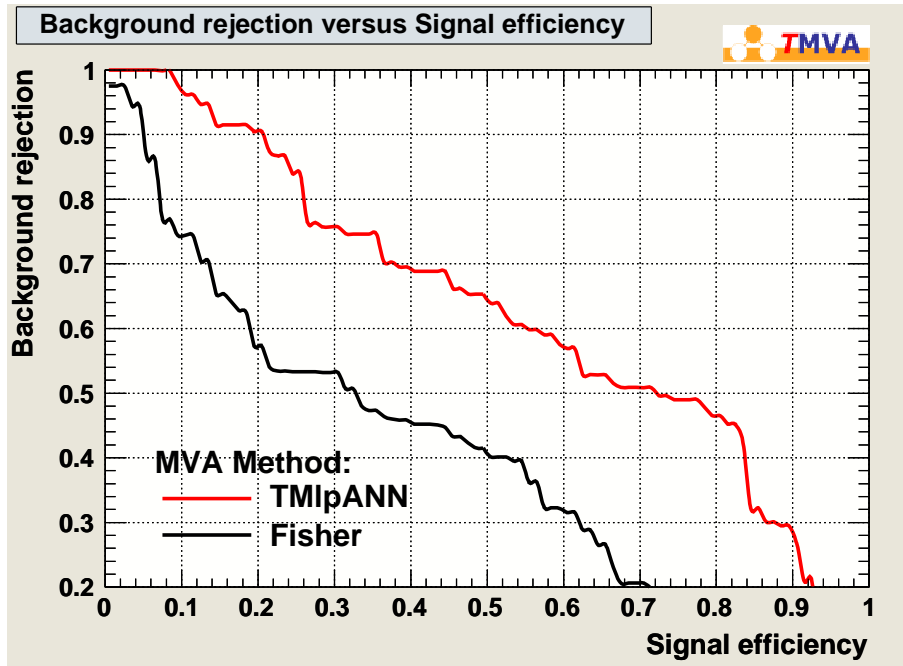
Figure 5.9: Efficiency versus purity for the $\tau \to e$ signal with respect to the background sources for the two methods Fisher and ANN.

MVA method	$\tau \to e$ Signal efficiency with background at 10%	$\tau \to e$ Signal efficiency with background at 30%
Fisher	0.05	0.14
ANN	0.21	0.45

Table 5.17: Signal efficiencies for both methods Fisher and MLP for different values of the background contamination.

The conclusion to this study is that is too difficult to separate the $\tau \to e$ signal from the background sources, especially from the ν_e without taking into account properly the kink topology using the DSP procedure.

5.5.3 Expected event rates

Selection efficiencies have been obtained from the MVA reported in section 5.5.2, including event location and electron identification, one can compute the final optimized expected number of events in the OPERA experiment in table 5.18. The uncertainties on the rates are systematic and are computed with the quadratic sum of the systematic uncertainties on the fluxes quoted in table 2.5, on the event location quoted in table 3.6 and on the electron identification quoted in section 4.3.3. In fact, those uncertainties are considered as uncorrelated since we simply count event numbers to estimate these rates without cutting on a influence parameter of this study, for instance the energy of electrons.

	$\tau \to e$ signal	oscillated ν_e	prompt ν_e	ν_μ^{NC}	$\nu_\mu^{\mathrm{CC}} \xrightarrow{\text{mis}} \nu_\mu^{\mathrm{NC}}$
Expected neutrino events in 2008-2009	2.9±0.3	4.6±0.3	31.5±2.4	1180±120	3530±360
Event location + electron identification efficiency	0.21±0.02	0.323±0.023	0.51±0.04	(5.0 ± 0.3) $\times10^{-3}$	(7.7 ± 0.6) $\times10^{-4}$
N_{evt} expected in 2008-2009	0.61±0.09	1.49±0.15	16.1±1.7	5.9±0.7	2.7±0.3
N_{evt} expected @ 22.5×10^{19} p.o.t.	2.6±0.4	6.3±0.6	68±7	25±3	11.5±1.3
N_{evt} expected @ 22.5×10^{19} p.o.t. after MVA	2.6±0.4	5.3±0.5	62±6	24±3	10.9±1.2

Table 5.18: Neutrino rates expected in the OPERA experiment for five nominal years, i.e. 22.5×10^{19} p.o.t.. The MNSP parameters value was extracted from the global analysis of G.L. Fogli *et al.*[27].

The expected number of $\tau \to e$ events in 2008-2009 is compatible with our data since there is still no such event. Here, the MVA gives poor results because of the absence of a proper estimation of the event topology. The observation of a $\nu_\mu \to \nu_\tau (\tau \to e)$ oscillation signal is possible with a significance of 0.3σ inferred from 2.6 signal events divided by the square root of (2.6+5.3+62+24+10.9) background events.

With an IP cut, the observation would be somehow not too limited by various background sources thanks to the good rejection capability of this future study as a global analysis which would be run on OPERA data sample to see if a $\tau \to e$ candidate could emerge.

In conclusion, this chapter has shown a calculation of the event rates expected in the OPERA experiment based on a full MC simulation of the detector for the $\nu_\mu \to \nu_e$ oscillation study. A MVA has been set and has shown a good capability to reject ll the background sources to let an oscillation signal emerge with a significance of $1.0\,\sigma$ computed with MC simulations for the nominal luminosity.

A MC/data comparison has been given for this analysis and has shown a good agreement. It also stressed that a dedicated study of the π^0 background conducted on both MC simulations and OPERA data is crucial as well as a dedicated photon/electron separation algorithm.

Finally, another oscillation study in the $\nu_\mu \to \nu_\tau (\tau \to e)$ channel has been carried out and has shown a limited potential without a proper DSP. Nevertheless, the systematic study performed for the $\nu_\mu \to \nu_e$ oscillation study will be useful for the study of the $\tau \to e$ mode.

Conclusion

The OPERA experiment is designed to measure the $\nu_\mu \to \nu_\tau$ oscillation in appearance mode in the muon neutrino CNGS beam. The signature of this signal is searched with the tau detection through its decay channels, among them the electronic one. Thanks to a sensitivity to electrons, OPERA can also investigate the oscillation in the $\nu_\mu \to \nu_e$ channel through the detection of electrons escaping the electron neutrino interactions. This thesis work has allowed to develop analysis tools to optimize and estimate the OPERA capability in measuring the $\nu_\mu \to \nu_e$ oscillation and eventually, setting a constrain on the mixing angle θ_{13}. It also gives the performance in the $\nu_\mu \to \nu_\tau$ oscillation detection in the electronic decay of the tau lepton.

We present a calculation of the neutrino expected rates and their associated uncertainties in the OPERA detector based on the present knowledge of the beam composition, neutrino cross sections and status of the OPERA detector. In the 2008-2009 data sample, without taking into account any detector and selection efficiencies, 4.6±0.3 oscillated ν_e events are expected in the detector while all associated background sources contributes to 2.9±0.3 events for the $\tau \to e$ channel, 1180±120 events for the ν_μ NC channel, 31.5±2.4 events for the prompt ν_e channel, 2.1±0.5 for the prompt ν_e QE+RES channel and 138±14 for the $\nu_\mu \text{CC} \xrightarrow{\text{mis}} \nu_\mu \text{NC}$ channel ; for the nominal luminosity accumulated for the total duration of the experiment, a multiplication factor of 4.25 is applied. These rates are not only necessary to estimate the OPERA sensitivity to the $\nu_\mu \to \nu_e$ oscillation but are also used as inputs in the MC simulation of the detector. The result of the analysis of this simulation and its comparison to data in terms of event location is also reported. It gives event location efficiencies of $(64 \pm 5)\%$ for the oscillated ν_e channel and $(52 \pm 6)\%$ for the $\nu_\mu \to \nu_\tau(\tau \to e)$ channel.

The purpose of this thesis work, using the electron detection, the reconstruction and analysis of electromagnetic showers is crucial. The identification of electron shower and its energy estimation are based on the use of an Artificial Neural Network tool in the ROOT framework. The performance of the electron identification and the energy estimation are assessed with MC simulations. The electron identification requires the standard volume of 10 plates $(1.8X_0)$ to achieve efficiencies of $(80\pm17)\%$ for the $\nu_\mu \to \nu_e(e)$ channel and $(87\pm26)\%$ for the $\nu_\mu \to \nu_\tau(\tau \to e)$ channel. The energy estimation has to be used with at least 20 plates $(3.5X_0)$ to reach the best performance. A correction has been defined to the energy of electrons as a function of the shower axis angle to come to a calorimetric resolution of $\frac{\sigma_E}{E} = 50\%$.

Finally, the results of this study are combined to search for the oscillation signals in the two studied channels. A MultiVariate Analysis (MVA) in the TMVA software is run

with MC simulations in order to determine the capability of our experiment to isolate the oscillation signals among all background sources. The relevant kinematical variables to separate the different contributions are the visible energy in the Electronic Detectors, the electron energy, the missing transverse momentum at the primary vertex and the angle between the electron and the transverse momentum of the hadronic shower. A dedicated procedure to search for ν_e events in data has been processed on the 2008-2009 data sample and implemented in the simulation. The comparison between the MC expectations and the 2008-2009 data gives a good agreement. For the nominal luminosity accumulated for the total duration of the experiment, the result of the MVA analysis shows a possibility to measure the $\nu_\mu \to \nu_e$ oscillation in the OPERA experiment with a significance of 1.0σ. The $\nu_\mu \to \nu_\tau(\tau \to e)$ oscillation signal is expected to be measured with a significance of 0.3σ.

Nowadays, nuclear reactor experiments have measured θ_{13} and confirmed the 3ν oscillation picture. These latest results lead the present neutrino experiments to investigate the remaining undetermined parameter : the CP violation phase δ. In addition the first or second octant value of the atmospheric mixing angle θ_{23} is still to determine.

Acronyms

Appendix A

Neutrinos And The Standard Model

A.1   The Standard Model

The Standard Model (SM) describes the strong, electromagnetic and weak interactions of the known elementary particles where interactions are represented by the exchange of mediator elementary particles.

The strong interaction is the force responsible of the binding between protons and neutrons in an atom nucleus and also of the cohesion of quarks composing these particles. This interaction is very peculiar since its coupling constant increases as a function of the distance between the two interacting particles but shows an asymptotic freedom when the distance is of the order of the atom radius. The mediator of the strong interaction is coloured, i.e. charged with respect to the strong interaction, and therefore can interact with itself. This self coupling of the mediator is responsible of the increasing coupling constant with the distance.

The electromagnetic interaction is the force responsible of the binding of electrons to the nucleus in an atom. It corresponds to the exchange of photons between charged particles.

All particles are sensitive to the weak interaction but its coupling constant is small compared to the previous forces because its mediators are massive implying a short range interaction.

The SM is a renormalizable gauge theory based on the quantum field theory that merges the quantum mechanic and the special relativity. The symmetry group that describes the interactions is $SU(3)_C \times SU(2)_L \times U(1)_Y$ with U stands for a unitary matrix, S means that the determinant of the matrix is equal to 1, the number N between brackets is the dimension of the matrix $N \times N$. The indices rely each group on an interaction : C means color and stands for the strong charge, L means left-handed and stands for the weak interaction since it violates parity and Y means weak hypercharge, together with the isospin I_3, the weak charge, it gives the electric charge through the Gell-Mann-Nishijima relation: $Q = I_3 + \frac{Y}{2}$. The $SU(3)_C$ term is the gauge group of the strong interaction mediated by 8 massless gluons (g). The theory behind is called Quantum ChromoDynamics (QCD) and it can be decoupled from the other interactions.

The $SU(2)_L$ and $U(1)_Y$ terms correspond to the weak and electromagnetic interactions respectively. The unification of these two interactions leads to the electroweak interaction mediated by bosons, particles with spin 1 : three massive ones for the weak force ($W^\pm$, Z^0) and a massless one (the photon γ) for the electromagnetic force.

The elementary particles are divided into two categories fermions, particles with spin $\frac{1}{2}$, and bosons, particles with spin 0 or 1. On the one hand, fermions are separated into quarks and leptons. Quarks are sensitive to all interactions unlike leptons that are sensitive only to the electroweak interaction. Among the leptons, it should be remarked that neutrinos are neutral and thereby only subject to the weak force resulting in a small cross-section responsible of their elusive nature. Their interactions are through charge current with the exchange of a charged weak boson $W^\pm$ or through neutral current and the exchange of the weak neutral boson Z^0. There are three generations where the two last generations are replica of the first one with a higher mass. In the case of neutrinos, it is the electron neutrino ν_e associated to the electron (e^-), muon neutrino ν_μ associated to the muon (μ^-) and tau neutrino ν_τ associated to the tau (τ^-). Table A.1 summarizes the particles of the SM and their properties.

Generation	First	Second	Third
Leptons spin=$\frac{1}{2}$	ν_e $Q=0$ mass$< 2 \times 10^{-6}$ MeV	ν_μ $Q=0$ mass< 0.19 MeV	ν_τ $Q=0$ mass< 18.2 MeV
	e $Q=-1$ mass$= 0.511$ MeV	μ $Q=-1$ mass$= 105.7$ MeV	τ $Q=-1$ mass$= 1.777$ GeV
Quarks spin=$\frac{1}{2}$	u $Q=\frac{2}{3}$ mass$= 1.7 - 3.3$ MeV	c $Q=\frac{2}{3}$ mass$= 1.27$ GeV	t $Q=\frac{2}{3}$ mass$= 171.2$ GeV
	d $Q=-\frac{2}{3}$ mass$= 4.1 - 5.8$ MeV	s $Q=-\frac{2}{3}$ mass$= 101$ MeV	b $Q=-\frac{2}{3}$ mass$= 4.2$ GeV
Interaction	Electromagnetic	Weak	Strong
Bosons spin=1	γ $Q=0$ mass$= 0$ MeV	$W^\pm$ $Q=\pm 1$ mass$= 80.399$ MeV Z^0 $Q=0$ mass$= 91.1876$ MeV	g $Q=0$ mass$= 0$ MeV

Table A.1: Summary of the elementary particles of the SM, the interaction mediators. Mass and charge of each component are given. Quarks do not exist as free particles, the indicated masses are the input parameters of the QCD. The neutrino masses are derived from weak decays kinematics. The corresponding elementary antiparticles of the elementary particles have the same mass and opposite charge. Note that the Higgs boson, mediator of the mass generation, is absent of this table.[21]

This panorama has to be completed by the Higgs boson of spin 0 that gives rise to mass terms for the elementary particles and massive bosons through the Higgs mechanism. The discovery of this particle is one of the main purpose of the experiments taking place at the Large Hadron Collider (LHC) at CERN in Geneva (Switzerland). At M. Goldhaber *et al.* experiment's time [9], neutrinos were thought massless until neutrino oscillation was discovered. The SM describes accurately the experimental observations but it is nevertheless believed to be an effective theory at low energy since the strong and electroweak interactions are not yet merged and the gravitation is not accounted for. For now, tests have been performed to look for new physics unsuccessfully.

Appendix B

Neutrino Properties

B.1   The Discovery Of Neutrinos

The neutrino[1] was first postulated by W. Pauli in 1930 in an attempt to save the principle of energy conservation. β-decay was believed to be a 2-body decay corresponding to discrete values of the energy for the emitted electron but the β-decay spectrum of the tritium $^3H \to\, ^3He^+ + e^- + \overline{\nu_e}$ was found to be continuous what matched a situation with another particle in the final state. When E. Fermi developed his theory of weak interaction [1] including the β-decay as a 3-body process, he decided to call the famous Pauli neutral particle "neutrino" ; it was in 1934. On the same year, H. Bethe and R. Peierls showed the peculiar nature of the neutrino because they calculated its cross section [2] and predicted the neutrinos were not easy to be detected. However the inverse β-decay : $\overline{\nu} + p \to n + e^+$ reaction was used by F. Reines and C.L. Cowan in 1956 to detect neutrinos for the first time. They used 2 tanks of 200 litres of a mixture of water and cadmium chloride each as a fiducial target and 3 tanks of 1400 litres of liquid scintillator each as detectors of charged particles placed in the vicinity of the Savannah River nuclear power plant in South Carolina (USA) and found an event rate compatible with 3 per hour. By measuring this low rate with respect to the huge number of neutrinos produced in a reactor core, they confirmed the elusive character of the neutrino. In addition, precise measurements of the energy spectrum of the β-decay process [4] gave hints of the smallness of the neutrino mass implying a massless neutrino in most of theoretical calculations including the SM.

Later, in 1962, L. Lederman *et al.* [5] observed neutrinos in the pion decay which mainly produced muons when interacting. This neutrino was identified to be of muon type ν_μ.

---

[1]The neutrino was first called neutron but was renamed in 1933 to neutrino by E. Fermi after the discovery of the neutron in 1932 by J. Chadwick.

B.2 Parity Non-Conservation

In 1956, T.D. Lee and C.N. Yang made a review of the latest experimental results and showed that there was no evidence for parity conservation in the weak interaction [105]. To check if parity is conserved, in 1957, C.S. Wu and her colleagues decided to look at the β-decay of polarized ^{60}Co nuclei [106]. A ^{60}Co sample was cooled (0.003 K) and placed in a solenoid (2.3 T) so that the ^{60}Co total angular momentum is aligned with the magnetic field direction. The parity operator reverses the particles momenta while leaving the spin unchanged. Thus, if parity is conserved, electrons should be emitted isotropically in the ^{60}Co sample rest frame. A detector was placed above the ^{60}Co sample to detect electrons. As can be seen on figure B.1, it was found that the electrons were preferentially emitted in the opposite direction of the magnetic field, even when it was reversed. It was a strong indication that parity is violated by the weak interaction leading to the V-A structure of the weak interaction where V stands for vector and A for axial vector, with A remaining unaffected under the parity operator on the contrary of the V part.
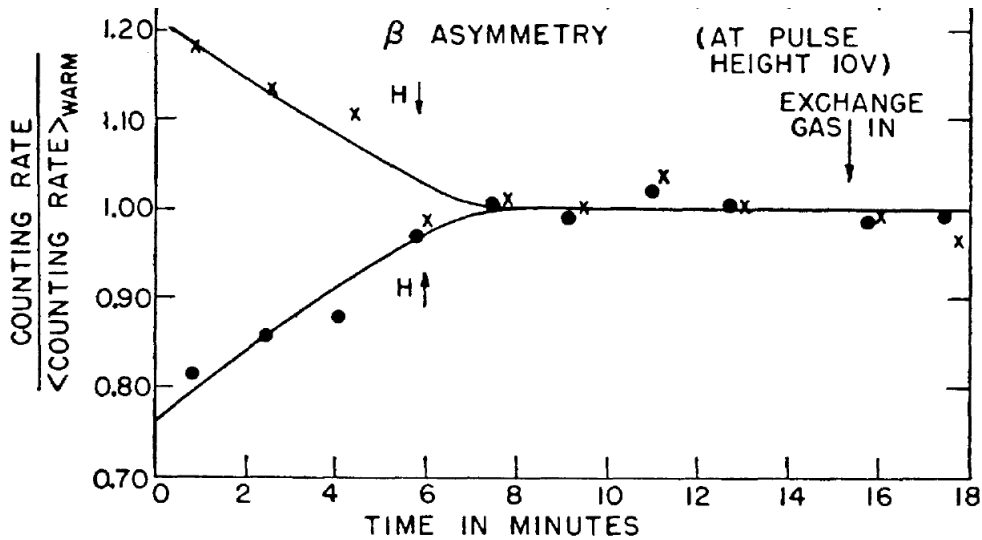
Figure B.1: Counting rate over counting rate mean value when the ^{60}Co sample is warm as a function of time. One can see that electrons are preferentially emitted in the opposite direction of the magnetic field indicating parity violation [106].

C.S. Wu *et al.* later confirmed these observations on β^+ emitters and even more beautifully demonstrated by M. Goldhaber *et al.* in 1958 that moreover determined the neutrino helicity. The helicity being defined as the projection of the angular momentum $\vec{S}$ on the momentum $\vec{P}$:

$$h = \frac{\vec{S} \cdot \vec{P}}{|\vec{S}|\,|\vec{P}|} \tag{B.1}$$

The parity operator reverses the momentum but not the angular momentum and thus the sign of the helicity should change under the application of the parity operator.

B.3 Measurement Of The Neutrino Helicity

The Goldhaber experiment proved that neutrinos have negative helicity and that the parity is maximally violated by the weak interaction. M. Goldhaber *et al.*[9] used ^{152}Eu that, after capturing an orbital electron, decays into a neutrino and ^{152}Sm* which subsequently decays to ^{152}Sm and a γ :

$$e^- + {}^{152}\text{Eu } (J = 0) \longrightarrow {}^{152}\text{Sm}^* \ (J = 1) + \nu_e \qquad \text{(B.2)}$$
$${}^{152}\text{Sm}^* \ (J = 1) \longrightarrow {}^{152}\text{Sm } (J = 0) + \gamma$$
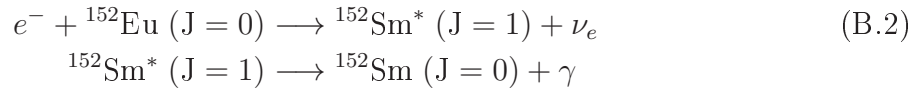
Since ^{152}Eu has an angular momentum (J) equal to zero, the neutrino spin and the ^{152}Sm* angular momentum should have opposite orientations following the electron spin orientation. Furthermore, the ^{152}Sm* decays into ^{152}Sm that has J=0 and a γ that should thus have a spin aligned with the angular momentum of ^{152}Sm*. The helicity of the γ is the same as the ^{152}Sm* that should then be the same as the neutrino since they have both opposite momenta and angular momenta. Hence measuring the γ helicity gives the neutrino helicity. As shown in equation B.1, to measure the helicity, one has to determine the particle momentum and its polarization. It was respectively achieved through resonance and the use of a magnet. The resonance is achieved when the emitted γ can be reabsorbed on ^{152}Sm*. However, some energy is lost in the recoil during the decay and in the possible re-absorption process. The Doppler shift can recover this energy loss only if the neutrino is emitted in a precise direction allowing the neutrino momentum determination [107]. It has been found that the neutrino has only a negative helicity leading to a neutrino mass set to zero in the SM. A similar experiment for antineutrinos has been carried out involving the emission of a photon following the positron decay of the ^{203}Hg nucleus. The polarization is consistent with the earlier statement that only right-handed antineutrinos take part in weak interactions.

B.4 The Second Generation Of Neutrinos

In the 1960's, two leptons, the electron and the muon, were known and only one neutrino without knowing if it should be associated to one lepton or to both of them. In 1962, L. Lederman, M. Schwartz and J. Steinberger found that neutrinos from pion decays are related to muons showing the existence of two generations: (e, ν_e) and (μ, ν_μ). Pions were accelerated towards a detector at Brookhaven National Laboratory (USA) made of spark chambers. From the pion decay in flight arose a muon and a neutrino with the muon being stopped by a beam dump before decay. Measurements of charged current neutrino interactions in coincidence with the beam yielded 29 muons and 6 electrons with the 6 electrons being compatible with the background expectations [5]. It was therefore the discovery of the ν_μ.

B.5   Discovery And Study Of Electroweak Currents At CERN

From the observations, theorists attempted to build a satisfactory theory of the weak interaction. Several problems arose and were solved leading around 1973 to a viable renormalizable gauge theory predicting, in addition to the mediators of charged current, the charged bosons W, the existence of neutral current mediated by a massive boson called Z. The Gargamelle experiment was a large bubble chamber cylinder operated under a 2 T magnetic field located at CERN in Geneva (Switzerland). Alternatively, neutrinos and antineutrinos were produced using the SPS to be detected through interactions either on electrons or nuclei. In the case of neutral current, the signature would be a unique scattered electron or hadrons respectively. The excitement for neutral current began with the observation of an isolated scattered electron in an antineutrino run. In 1973, the experiment claimed the observation of 102 neutral current events. In 1974, it was shown that they have a flat spatial distribution compared to the background one giving strong confidence in the result and thereby in the recently elaborated theory of the weak interaction [108]. In addition, the W and Z bosons were discovered in 1983 by UA1 (and subsequently UA2) experiment [109, 110] at the SPS accelerator, a protons-antiprotons collider at CERN. In the 1990's, the Large Electron Positron (LEP) collider studied the properties of Z and W with high statistic positron-electron collisions allowing precise knowledge of the energy in the center of mass. The W resonance was first found in the neutrino channel thanks to the missing energy and the Z resonance allowed the determination of the number of neutrino generations.

B.6   Number Of Neutrino Generations

The neutral Z boson decays into a fermion and the associated antifermion. Hadrons and leptons are detected while neutrinos are not. However, they contribute to the total Z boson width. The number of neutrino species N_ν is inferred through [8] :

$$N_\nu = \frac{\Gamma_{\mathrm{inv}}}{\Gamma_{\mathrm{l}}} \left(\frac{\Gamma_{\mathrm{l}}}{\Gamma_\nu} \right)_{\mathrm{SM}} = 2.9840 \pm 0.0082 \tag{B.3}$$

where Γ_{inv} is determined from the measurements of the decay widths to all visible final states and the total width, Γ_{l} is a lepton flavour contribution to the width and Γ_ν is the theoretical contribution of one neutrino flavour. The ratio $\frac{\Gamma_{\mathrm{l}}}{\Gamma_\nu}$ is used to reduce the uncertainty.

As can be observed on figure B.2, the Z width was found to be best fitted by three neutrino flavours. It has however to be noticed that it is a proof of the existence of only three species that are active with a mass lower than 45.5 GeV corresponding to the Z mass divided by two. There is a possibility of sterile neutrinos that do not couple to the Z boson from some oscillation experiments [111].
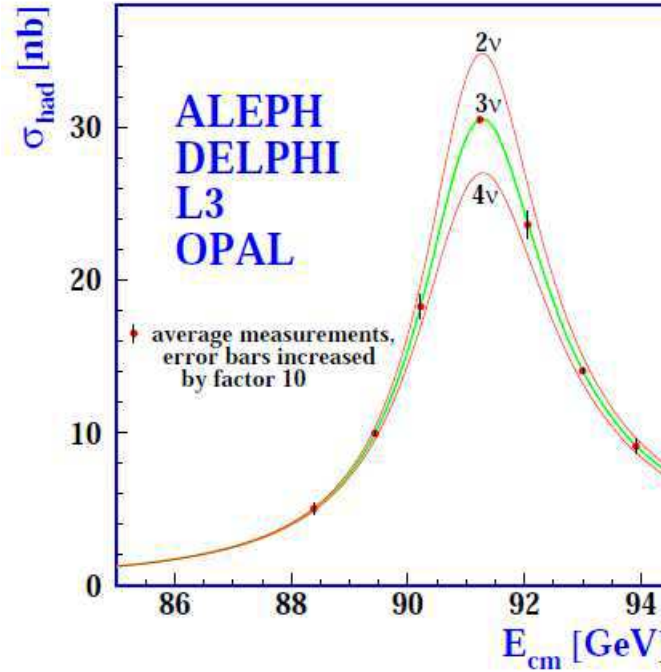
Figure B.2: Measurements of the hadron production cross-section around the Z^0 resonance. It is best fitted by the existence of three neutrino species [8]

B.7 The ν_τ Discovery

The τ lepton was discovered at SLAC in the USA in 1975 leading to the hypothesis of the ν_τ existence. The τ lepton was found to be heavy with 1.8 GeV/c^2, implying a travel distance of a few mm before its decay. It was therefore very difficult to reveal a ν_τ CC interaction. The first confirmation of its existence came from the Z width at LEP and its direct detection was brought only in 2000 by the DONUT experiment at FermiLAB (Chicago, USA) [7]. This experiment was using emulsions for a satisfactory spatial resolution and an accurate determination of the kink pattern of τ decays that is due to the high mass difference between the τ and its daughter particles.

Appendix C

Addendum To Neutrino Properties

C.1 A Left-Handed Neutrino ?

First, if one assumes a fermion, i.e. a neutrino, it can be described by the Dirac equation :

$$\mathrm{H}\psi = (\vec{\alpha} \cdot \vec{p} + \beta m)\psi \tag{C.1}$$

Considering neutrino has a zero mass, it gives two decoupled equations for two-component spinors $\chi(p)$ and $\Phi(p)$:

$$\mathrm{E}\chi = -\vec{\sigma} \cdot \vec{p}\,\chi \tag{C.2}$$
$$\mathrm{E}\Phi = +\vec{\sigma} \cdot \vec{p}\,\Phi$$

where σ are 2x2 Pauli matrices.

Then, each of these equations has respectively a solution which describes a particle with a positive energy and a negative helicity $\lambda = -\frac{1}{2}$ for the first one : a left-handed neutrino ν_L and an antiparticle with a negative energy and a positive helicity $\lambda = +\frac{1}{2}$ for the second one : a right-handed antineutrino $\overline{\nu_R}$. At this point, a useful reminder about weak interactions is needed : the weak current J^μ for an electron and its neutrino is defined by :

$$\mathrm{J}^\mu = \overline{\psi_e}\gamma^\mu \frac{1}{2}(1 - \gamma^5)\psi_\nu \tag{C.3}$$

where this form is called the V-A form and $\overline{\psi_e}$ stands for the electron wave-function, ψ_ν stands for the neutrino wave-function and γ^μ and γ^5 stand for Dirac operators. The $\frac{1}{2}(1 - \gamma^5)$ term ensure the V-A form and that parity will be maximally violated through :

$$\frac{1}{2}(1 - \gamma^5)u_\nu = \begin{pmatrix} \mathrm{I} & 0 \\ 0 & 0 \end{pmatrix} \begin{pmatrix} \chi \\ \Phi \end{pmatrix} = \begin{pmatrix} \chi \\ 0 \end{pmatrix} \tag{C.4}$$

As far as the neutrino interacts only by the weak current, it becomes straightforward from equation C.4 that only a left-handed neutrino and a right-handed antineutrino, respectively can exist. Of course, this statement can only be made if the neutrino mass is strictly zero. Otherwise, the development is the same as for a standard massive lepton which can have both negative or positive helicities.

C.2   See-saw Mechanism

Since different experiments bring the evidence of a massive neutrino, especially about neutrino oscillation as shown in section 1.1, it is needed to look beyond a model where the neutrino is massless and find the theoretical origin of the neutrino mass. The mechanisms of neutrino mass generation are not really understood ; in fact, mechanisms of the electron mass generation is not yet understood as well, but several possible explanations can be discussed. Neutrino mass should be considered in the general context of all fermion masses. Two topics can be distinguished : origins of the smallness of neutrino mass compared to masses of charged leptons and quarks and origins of the difference of mixing pattern between leptons and quarks. Both of them are discussed in the lecture of A. Smirnov[18].

Section 1.2.2 set the different mass terms, nevertheless section 1.2.2.2 explained that m_{L} cannot break the electroweak symmetry which leads to exclude this term from the mass matrix since the mass generation occurs through coupling to a Higgs doublet. Consequently, the mass matrix turns to :

$$M = \begin{pmatrix} 0 & m_{\mathrm{D}} \\ m_{\mathrm{D}}^{\mathrm{T}} & M_{\mathrm{R}} \end{pmatrix} \tag{C.5}$$

After diagonalisation of that matrix, the mass eigenstates are :

$$|m_{\pm}| = \frac{1}{2}(M_{\mathrm{R}} \pm \sqrt{M_{\mathrm{R}}^2 + 4m_{\mathrm{D}}m_{\mathrm{D}}^{\mathrm{T}}}) \tag{C.6}$$

The See-saw limit assumption is $M_{\mathrm{R}} \gg m_{\mathrm{D}}$ which allows to distinguish two neutrinos with two masses at different order : $m_{\mathrm{heavy}} \propto M_{\mathrm{R}}$ and $m_{\mathrm{light}} \propto \frac{m_{\mathrm{D}}m_{\mathrm{D}}^{\mathrm{T}}}{M_{\mathrm{R}}}$. The word see-saw becomes meaningful since the product $m_{\mathrm{heavy}}m_{\mathrm{light}} = m_{\mathrm{D}}m_{\mathrm{D}}^{\mathrm{T}}$ having to be constant. If M_{R} tends to be large, m_{light} will be small while m_{heavy} will be large. Typically, M_{R} could converge to the M_{GUT} scale which means a large value and a window opened on the new physics.

The mass eigenstates according to the See-saw mechanism are :

$$\nu_{\text{light}}^{\text{L}} = \nu_{\text{L}} + \sqrt{\frac{m_{\text{light}}}{m_{\text{heavy}}}}\nu_{\text{R}}^{\text{C}} \tag{C.7}$$

$$\nu_{\text{heavy}}^{\text{L}} = \nu_{\text{R}} + \sqrt{\frac{m_{\text{light}}}{m_{\text{heavy}}}}\nu_{\text{L}}^{\text{C}}$$

$$\nu_{\text{light}}^{\text{R}} = \nu_{\text{L}}^{\text{C}} + \sqrt{\frac{m_{\text{light}}}{m_{\text{heavy}}}}\nu_{\text{R}}$$

$$\nu_{\text{heavy}}^{\text{R}} = \nu_{\text{R}}^{\text{C}} + \sqrt{\frac{m_{\text{light}}}{m_{\text{heavy}}}}\nu_{\text{L}}$$

Finally, the left-handed neutrino described in the weak interaction is a mixture of the left-handed light neutrino and the right-handed heavy neutrino.

C.3 β-Decay Experiments

β-decay is a three body decay with the emission of an electron and a $\overline{\nu_e}$:

$$^{\text{A}}_{\text{Z}}\text{Y} \rightarrow ^{\text{A}}_{\text{Z+1}}\text{X} + e^- + \overline{\nu_e} \tag{C.8}$$

The mass difference between the initial and final states gives the excess energy Q (end point) that is shared between the $\overline{\nu_e}$ and the e^- by neglecting the X atom recoil. Hence, if the neutrino is massive, it affects the Q value but also the differential decay rate $\frac{d\text{N}}{d\text{T}}$ given by :

$$\frac{d\text{N}}{d\text{T}} \propto (\text{Q} - \text{T})\sqrt{(\text{Q} - \text{T})^2 - m_{\nu_e}^2} \tag{C.9}$$

where T is the electron kinetic energy and m_{ν_e} the neutrino mass.

One can see on figure C.1 and from equation C.9 that the effect of the neutrino mass is the most pronounced close to the end point. Consequently, the β-decaying isotope has to be chosen in order to have as much decays as possible in this region. This is achieved with an atom showing a small Q-value (18.57 keV) and a short half-life time (12.3 years) as tritium (^{3}H). Experimentally, electrons of the Q-value region are selected thanks to the combination of magnetic and electric fields. The past experiments Mainz [112] and Troitzk [113] measured respectively at 95% C.L.:

$$m_{\overline{\nu_e}} < 2.3\,\text{eV} \tag{C.10}$$

$$m_{\overline{\nu_e}} < 2.5\,\text{eV}$$
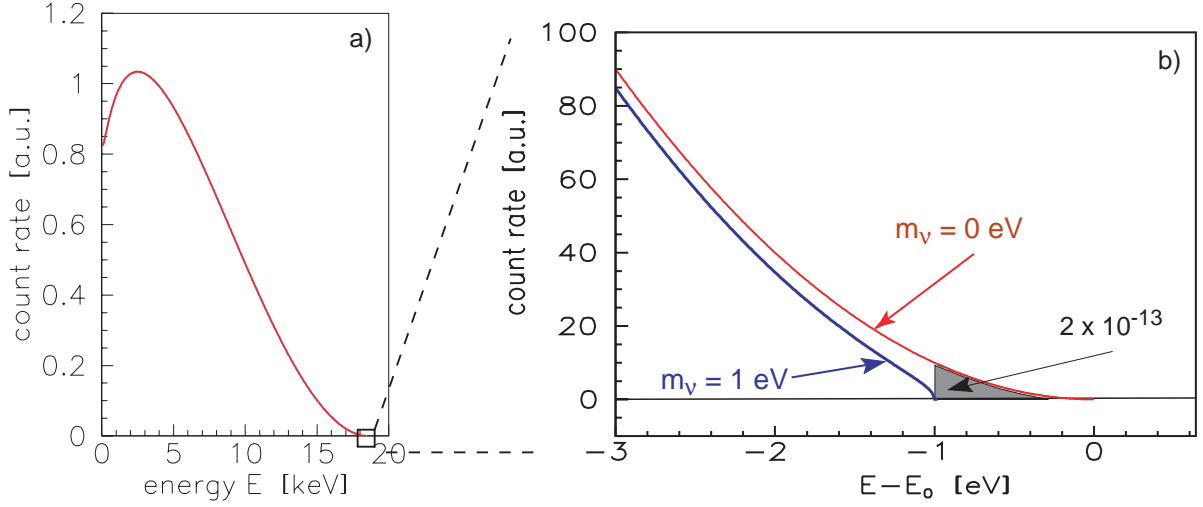
Figure C.1: The electron energy spectrum of tritium β-decay: the complete spectrum on the LHS and the narrow region around the end point E on the RHS. The β-spectrum is shown for neutrino masses of 0 and 1 eV [114].

The two collaborations have merged in an experiment with an improved sensitivity called KArlsruhe TRItium Neutrino experiment (KATRIN) that will soon start and try to lower the sensitivity down to 0.2 eV [29].

C.4 Neutrinoless Double β-Decay Experiments

In the SM, the double β-decay is a second order electroweak transition overwhelmed by the classical β-decay unless the latter is forbidden. This happens for instance to the ^{76}Ge where the β-decay daughter nucleus ^{76}As has a higher energy level on the contrary of ^{76}Se allowing the double β-decay to be viewed through the spectrum of the two electrons. An interesting case is the possibility to see the neutrino emitted at the first β-decay vertex being reabsorbed at the second β-decay vertex : the neutrinoless double β-decay as illustrated on figure C.2. Let us take for instance the case of $2e2\overline{\nu_e}$. The antineutrino emitted at the first vertex has positive helicity while to be absorbed at the second vertex, it should be a neutrino of negative helicity. Thereby, this reaction is uniquely possible for massive Majorana neutrinos. Note that a Dirac particle has the two helicities only if it is massive. Furthermore, only Majorana neutrino exhibits the equality particle-antiparticle. The neutrinoless double β-decay half-life of a nucleus N , $T_{\frac{1}{2}}(N)$ is given by :

$$T_{\frac{1}{2}}^{-1}(N) = F(Q_{\beta\beta}, Z)|M^2|\langle m_\nu \rangle \qquad (C.11)$$

where M^2 and $F(Q_{\beta\beta}, Z)$ are the nuclear matrix element and the phase space factor, respectively, and m_ν is the effective Majorana mass.
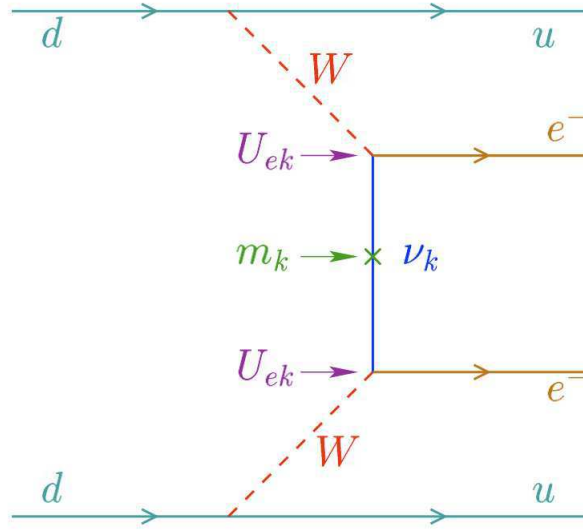
Figure C.2: Feynman diagram of the neutrinoless double β-decay [115]

One should look for the highest phase space factor element corresponding to the highest end point nucleus out of the 35 double β-decay emitters in the periodic table. Several experiments have been carried out with different techniques (germanium crystals, bolometers, tracking detectors) and different nuclei (germanium, tellure dioxide, molybdene, selenium, xenon) reaching a sensitivity for instance for one of them, Nemo3, of $\langle m_\nu \rangle < 0.3-1.3\,\text{eV}$. No signal has been yet observed but future generations of experiment are in development increasing the mass of double β-decay emitter and will expect a sensitivity of $\langle m_\nu \rangle < 0.04 - 0.4\,\text{eV}$ depending on the techniques employed.

Appendix D

Phenomenology Of Electromagnetic Showers

D.1 Passage Of Charged Particles Through Matter

Charged particles, like pions, muons, kaons or protons, having an energy lower than $100\,\mathrm{GeV}$, loose energy in matter primarily by ionization and atomic excitation. Nuclear diffusion are, usually, negligible in the calculation of the energy loss. The mean rate of energy loss (or stopping power) is given by the Bethe-Bloch equation D.1 :

$$-\frac{d\mathrm{E}}{dx} = \mathrm{K}z^2\,\frac{\mathrm{Z}}{\mathrm{A}}\,\frac{1}{\beta^2}\,\left[\frac{1}{2}\,ln\,\frac{2m_ec^2\beta^2\gamma^2\mathrm{T_{max}}}{\mathrm{I}^2} - \beta^2 - \frac{\delta}{2}\right] \tag{D.1}$$

where z is the charge of the incident particle, Z and A are the atomic number and the atomic mass of the absorber respectively, $\mathrm{T_{max}}$ is the maximum kinetic energy which can be imparted to a free electron in a single collision, I is the mean excitation energy measured in eV and $\mathrm{K} = 4\pi\mathrm{N}_A r_e^2 m_e c^2$ measured in $\mathrm{MeV.mol^{-1}.cm^2}$. The average energy loss has a very characteristic dependence on the velocity of the incident particles as shown for a muon going through copper on figure D.1. The function is characterized by a broad minimum which position drops from $\beta\gamma = 3.5$ to 3.0 as Z goes from 7 to 100. In this energy region, the incident particle are called Minimum Ionizing Particle (mip) and, expressing the absorber thickness in unit of $x = \rho*\mathrm{d}$, where ρ is the density of the absorber $(\mathrm{g.cm^{-3}})$ and d is the thickness (cm), it is found that for a mip the average energy loss varies from a value of $2\,\mathrm{MeV.g^{-1}.cm^2}$ for low-Z materials to $1.1\,\mathrm{MeV.g^{-1}.cm^2}$ for high-Z materials, such as lead. For lower $\beta\gamma$-values than in the mip region energy loss increase as $1/\beta^2$ while for greater $\beta\gamma$-values, as in electron showers energy range in OPERA, energy loss increases approximately logarithmically.
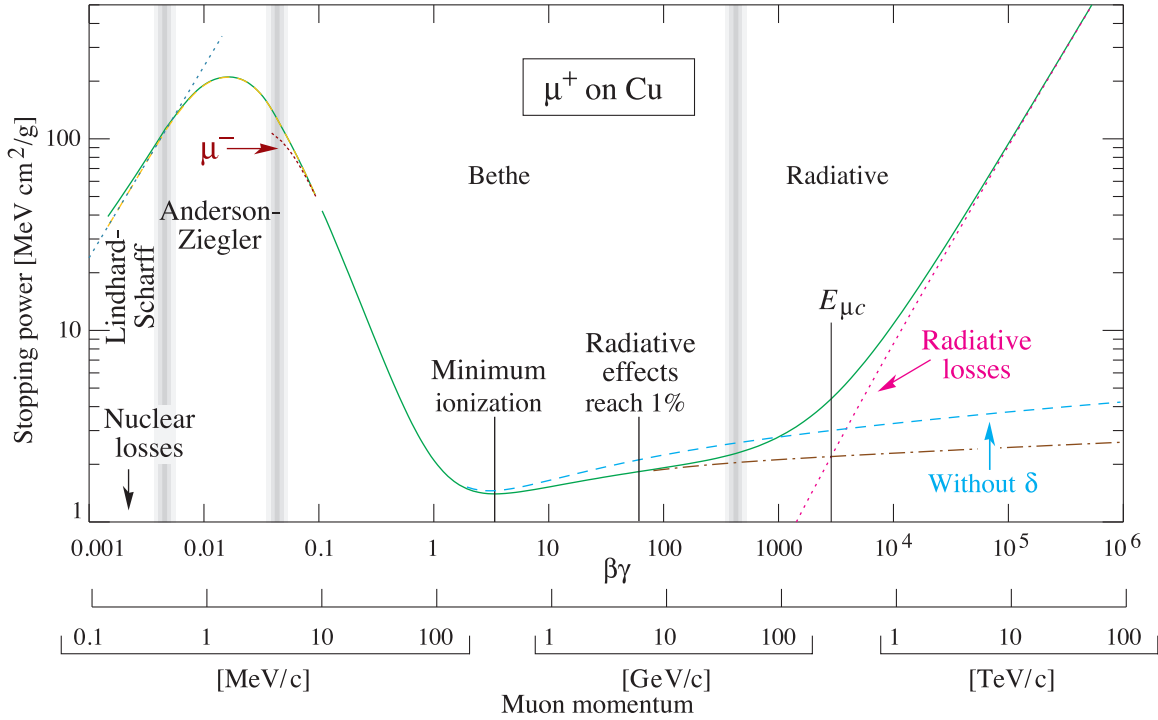
Figure D.1: Stopping power ($= \langle -dE/dx \rangle$) for positive muons in copper as a function of $\beta\gamma = p/Mc$ [70].

D.2   Multiple Coulomb Scattering

A charged particle traversing a medium is deflected by many small angle scatterings. Most of these deflections are due to Coulomb scattering from nuclei, and hence the effect is called Multiple Coulomb Scattering (MCS). For hadronic projectiles, the strong interactions also contribute to multiple scattering. The Coulomb scattering distribution is well described by the theory of Moliere. It is roughly Gaussian for small deflection angles, but at larger angles, greater than a few θ_0 defined in D.2, it behaves like Rutherford scattering, having larger tails than does a Gaussian distribution. It is sufficient for many applications to use a Gaussian approximation for the central 98% of the projected angular distribution, with a width given by D.2.

$$\theta_0 = \frac{13.6 \text{ MeV}}{\beta c p} \, z \, \sqrt{\frac{x}{X_0}} \left[1 + 0.038 \, ln \left(\frac{x}{X_0} \right) \right] \tag{D.2}$$

where p, βc and z are the momentum, the velocity and the charge of the incoming particle, respectively and $\frac{x}{X_0}$ is the absorber thickness in term of radiation length expressed in 4.1.

Since this formula is depending on the momentum of the passing through particle, it can be used for particle identification.

Appendix E

Statistical Methods

E.1   Linear Method : The Fisher Discriminant

The Fisher discriminant has been introduced by the geneticist Sir Ronald Fisher in 1936 [116] in order to classify iris according to their physical properties. This method combines linearly the input variables to create an output variable optimized to separate two populations. The coefficients of that linear combination are called Fisher's coefficients. This output variable determines an axis in the input variables space where classes projections (signal and background) are well separated keeping populations of each class as confined as possible.

Let us consider a sample exclusively composed by events to classify in two categories signal and background and a vector X of n variables $X = (x_1, x_2, \ldots, x_n)$. X^s and X^b are the vectors corresponding to signal and background respectively. The mean distributions vectors are defined as $\langle X^s \rangle = (\langle x_1^s \rangle, \langle x_2^s \rangle, \ldots, \langle x_n^s \rangle)$ and $\langle X^b \rangle = (\langle x_1^b \rangle, \langle x_2^b \rangle, \ldots, \langle x_n^b \rangle)$. The event classification of the two populations will depend on :

- the mean value of the distributions for each sample, signal and background merged
- the mean value of the distributions for each sample and for each variable, signal and background separated
- the covariance matrix C given by the relation $C = B + W$ where B and W are two covariance matrices describing the spread with respect to the mean value of the whole sample for B (Between) and with respect to the mean value of the proper class W (Within).

The Fisher's coefficients F_k are given by [117] :

$$F_k = \frac{\sqrt{N_s N_b}}{N_s + N_b} \sum_{l=1}^{n} W_{kl}^{-1} (\overline{x}_l^s - \overline{x}_l^b) \qquad (E.1)$$

where N_s and N_b are the number of signal and background events respectively.

The Fisher's discriminant for event i is then given by the relation :

$$\mathrm{F}(i) = \mathrm{F}_0 + \sum_{k=1}^{n} \mathrm{F}_k x_k(i) \tag{E.2}$$

where F_0 is the offset which centres the discriminant value about 0 for all the classes of the sample. An example of a Fisher's discriminant distribution is shown below in figure E.1, details of the analysis which inferred this plot is given in the section 5.2.
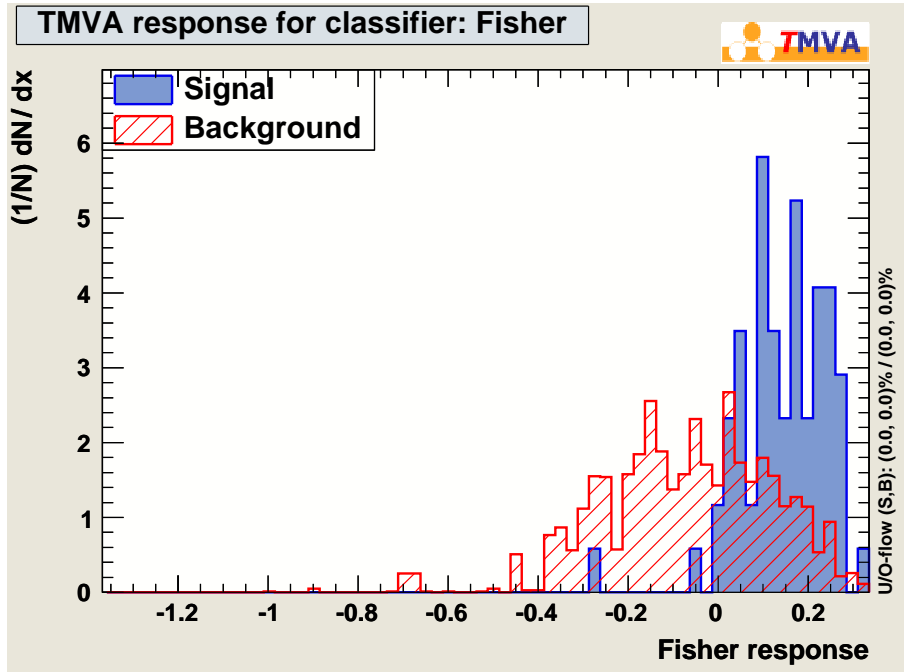
Figure E.1: Example of a Fisher's discriminant distribution. The signal is in blue and the background in red.

E.2 Non-Linear Method : The Artificial Neural Network

An Artificial Neural Network (ANN) is an analysis tool which the principle derives from the biological neural network. A neuron is formally a non-linear parametrized function of several variables called inputs which can give one or several output variables. A neural network is thus a combination of parametrized functions which can be simplified with respect to a biological neural network by only allowing one-way connexions from a layer to another one, i.e. neurons of a layer n are fed with inputs coming from neurons of the layer n−1 and feed neurons of the layer n+1. Note that there is no connexion between neurons belonging to the same layer. This kind of network is known as a MultiLayer Perceptron (MLP) composed at least of one input layer of neurons and one output layer of neurons, then hidden layers can be inserted in between as shown on figure E.2.
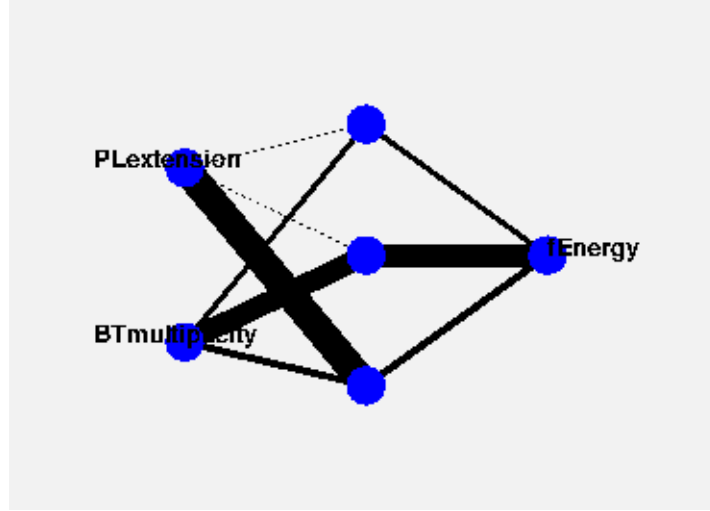
Figure E.2: Example of a simple neural net structure.

A weight is associated to a connexion between two neurons meaning that the output of a neuron is multiplied and then given as an input for the following neuron. If there are multiple inputs for one neuron, they are linearly combined to feed this neuron. The typical response of a neuron is a non-linear function combining all inputs. This function is usually a sigmoid which is a realistic binary response :

$$f(x) = \frac{1}{1 + e^{-\text{k}x}} \tag{E.3}$$

The architecture of the ANN, number of layers and number of neurons per layer, is chosen empirically according to the performance of the analysis. Nevertheless, the Weierstrass theorem which, if applied to neural nets, tells that for a MLP, a single hidden layer is sufficient to approximate a given continuous correlation function to any precision, as far as the number of neurons is sufficient. One usually chooses more than one hidden layer to keep the number of neurons relatively low, the robustness and the training time are thus significantly better.

Once the ANN structure is determined, the ANN has to be trained. This phase aims to modify the network to teach it the desired behaviour. In other words, the training adjusts the weights to get the expected output value. We commonly use MC samples to train the ANN. For each event of the sample, the output is compared to the expected value and weights are adjusted iteratively to minimize the error function E :

$$\text{E} = \frac{1}{2} \left(\sum_{a=1}^{N} \text{y}_a - \hat{\text{y}}_a \right) \tag{E.4}$$

This method prevents that the net response is a differential function of the weights. The error function values are going back from a layer to the previous one : the back-propagation training method. Due to the fundamental properties of the ANN, this analysis tool takes into account linear and non-linear correlations. However, the neural nets are sensitive to overtraining effects if low discriminating variables are given as inputs.

The output of an ANN goes to -1 for the background events and +1 for the signal events ; in between we can find background events which look like signal and vice and versa. Figure E.3 shows an example of a neural net output.
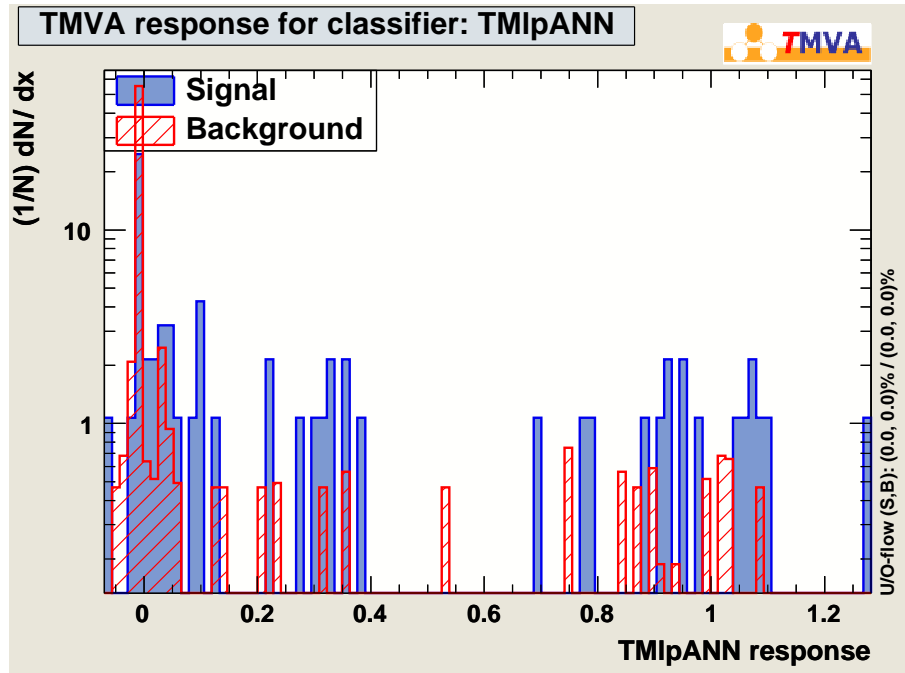
Figure E.3: Example of a neural net output distribution. The signal is in blue and the background in red.

A probability to look like signal is assigned to each event.

Appendix F

Event Location Efficiency Assessment
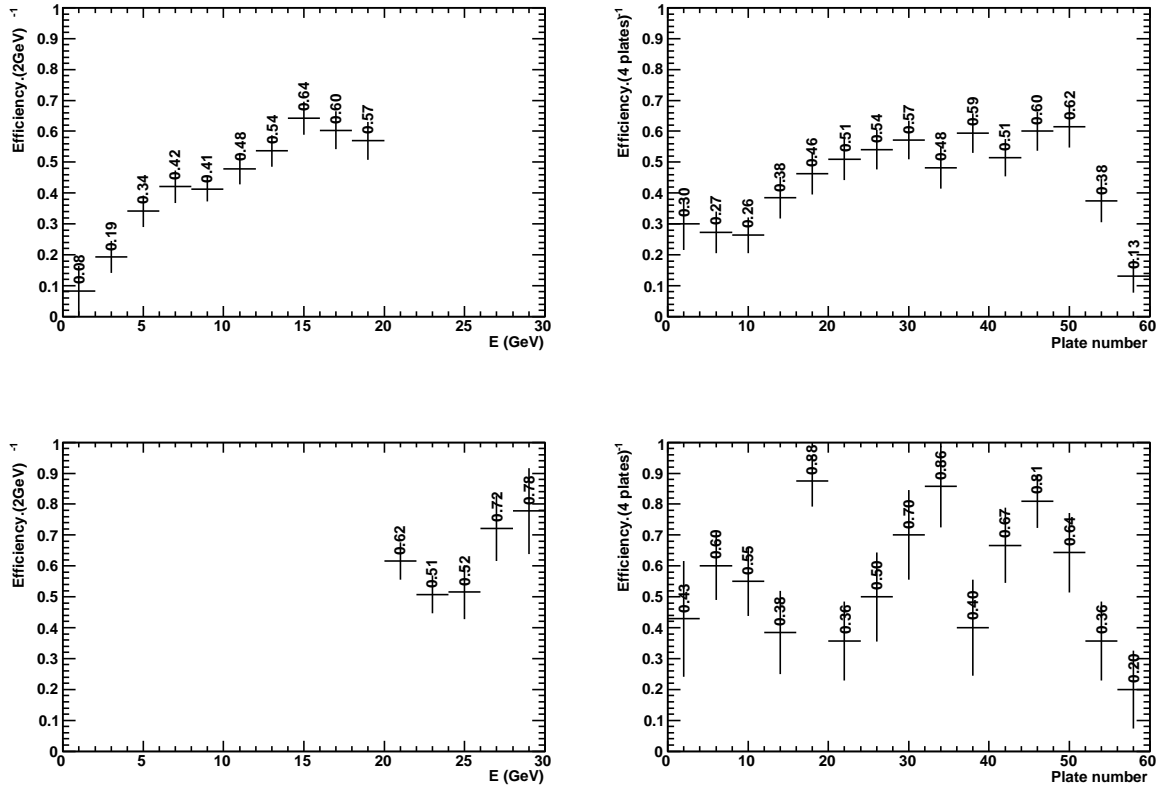
Figure F.1: Location efficiency as a function of the MC true vertex depth in the brick on the RHS and as a function of the MC true neutrino energy on the LHS. The neutrino events with energy less or equal to 20 GeV on the top panels and the neutrino events with energy greater than 20 GeV on the bottom panels. All these plots have been obtained with MC simulation of the $\nu_\mu \to \nu_e$ oscillation channel.
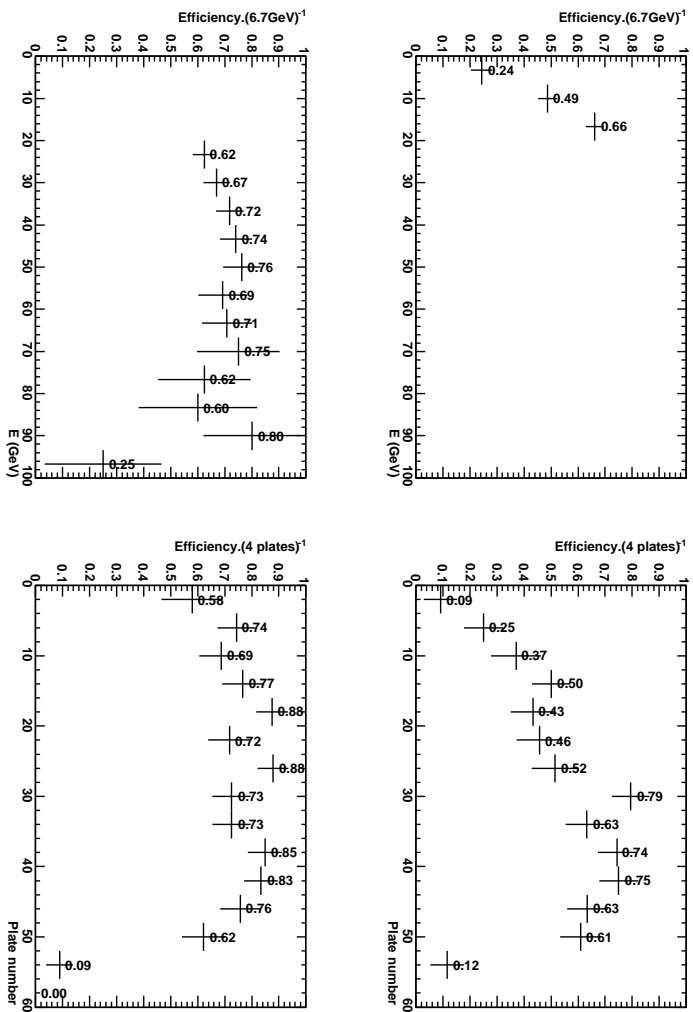
Figure F.2: *Idem* with MC simulation of the prompt ν_e QE+RES channel.
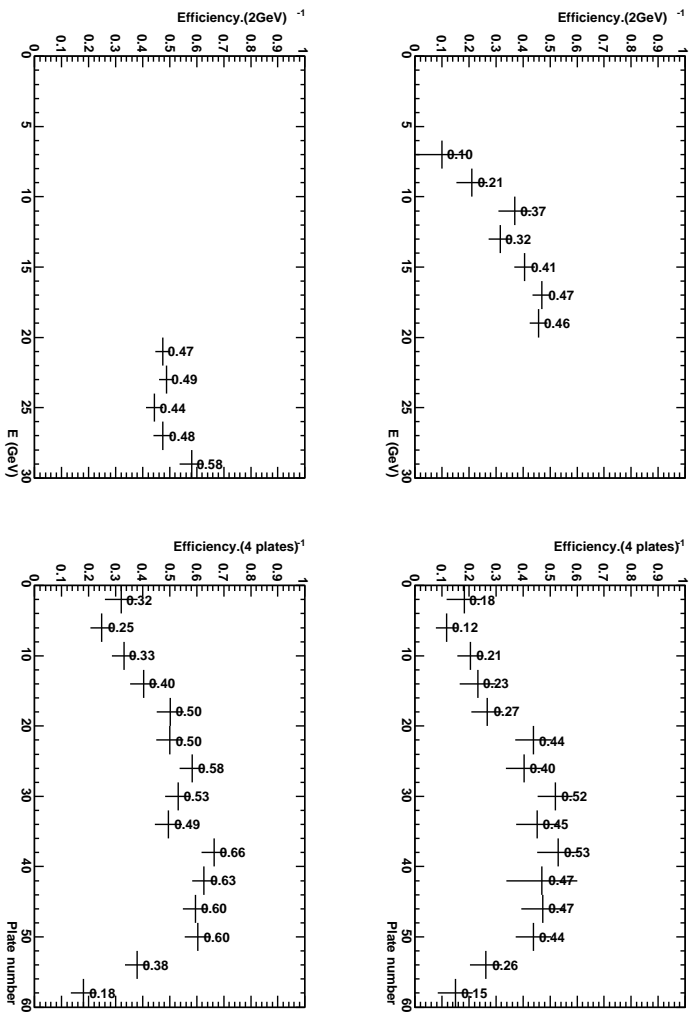
Figure F.3: *Idem* with MC simulation of the $\nu_\mu \to \nu_\tau(\tau \to e)$.

Efficiency.(2GeV)$^{-1}$

E (GeV)

Efficiency.(2GeV)$^{-1}$

E (GeV)

Efficiency.(4 plates)$^{-1}$

Plate number

Efficiency.(4 plates)$^{-1}$

Plate number

Figure F.5: *Idem* with MC simulation of the $\nu_\mu^{CC} \xrightarrow{mis} \nu_\mu^{NC}$ channel.

Efficiency.(2GeV)$^{-1}$

E (GeV)

Efficiency.(2GeV)$^{-1}$

E (GeV)

Efficiency.(4 plates)$^{-1}$

Plate number

Efficiency.(4 plates)$^{-1}$

Plate number
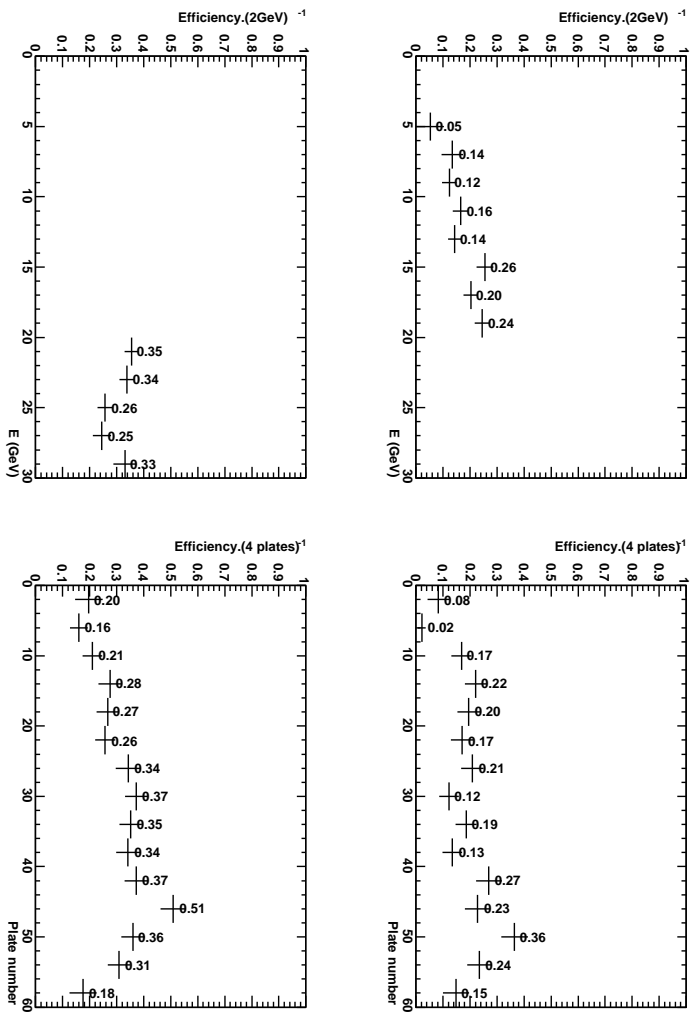
Figure F.4: *Idem* with MC simulation of the ν_μ NC channel.
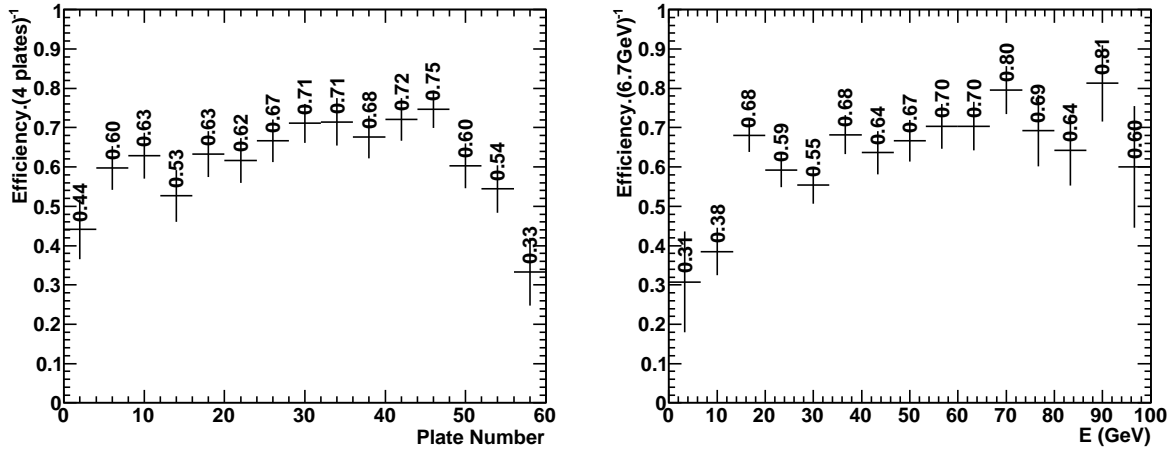
Figure F.6: In the top panel, location efficiency as a function of the MC true vertex depth in the brick. In the bottom panel, location efficiency as a function of the MC true neutrino energy. Both of these plots have been obtained with MC simulation of the prompt ν_e channel by using only the OpCarac "CONTAINED" or "BORDERSOFTNC" classification.
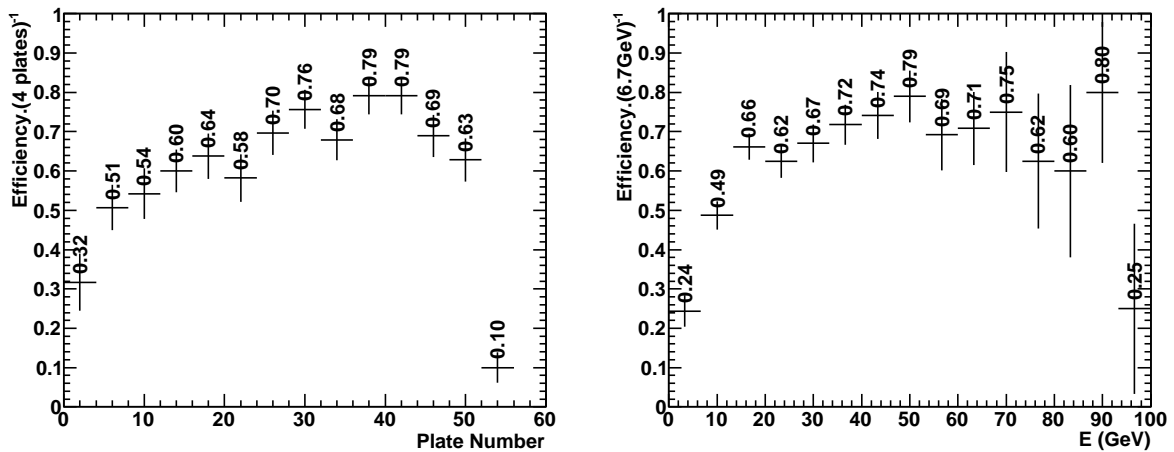
Figure F.7: In the top panel, location efficiency as a function of the MC true vertex depth in the brick. In the bottom panel, location efficiency as a function of the MC true neutrino energy. Both of these plots have been obtained with MC simulation of the prompt ν_e QE+RES channel by using only the OpCarac "CONTAINED" or "BORDERSOFTNC" classification.
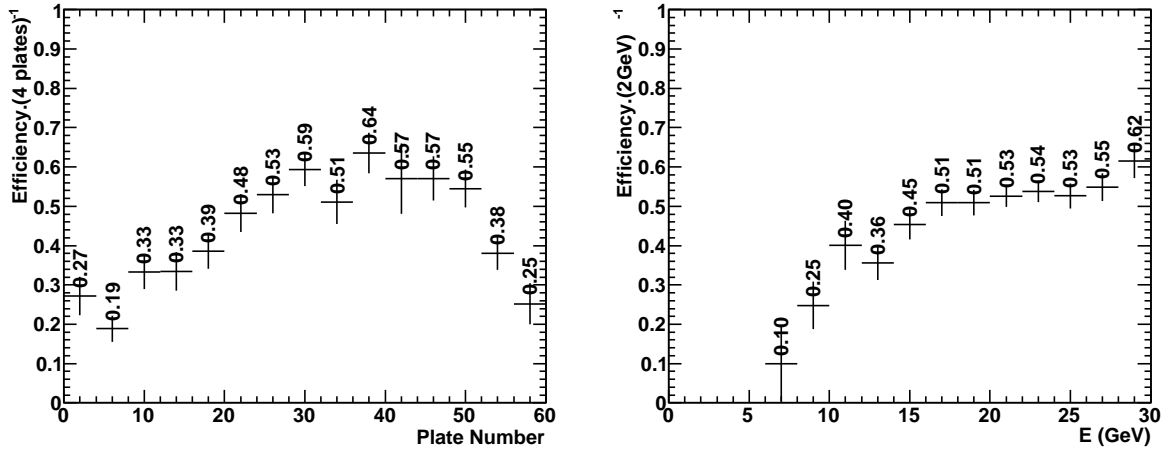
Figure F.8: In the top panel, location efficiency as a function of the MC true vertex depth in the brick. In the bottom panel, location efficiency as a function of the MC true neutrino energy. Both of these plots have been obtained with MC simulation of the $\nu_\mu \to \nu_\tau$ with the τ lepton into its electron decay channel by using only the OpCarac "CONTAINED" or "BORDERSOFTNC" classification.
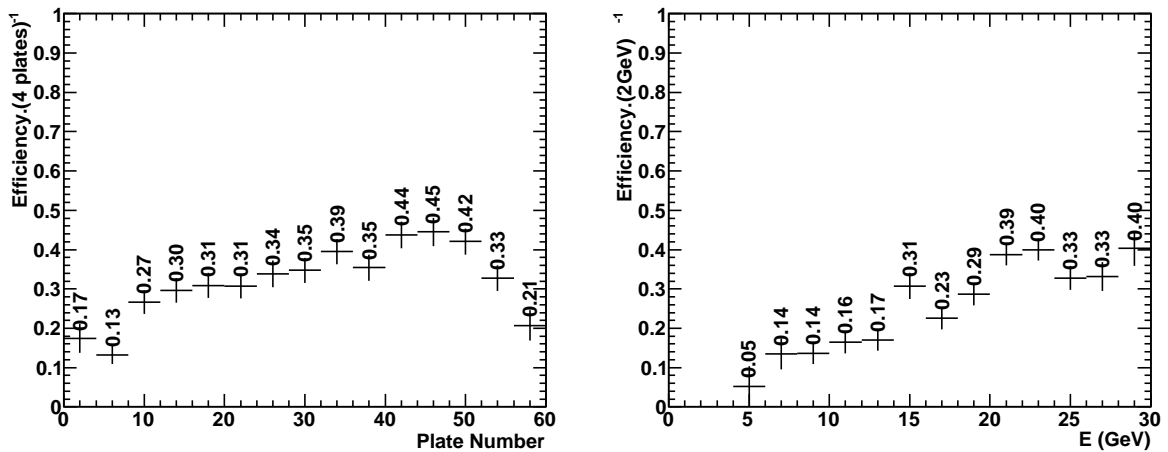
Figure F.9: In the top panel, location efficiency as a function of the MC true vertex depth in the brick. In the bottom panel, location efficiency as a function of the MC true neutrino energy. Both of these plots have been obtained with MC simulation of the ν_μ NC channel by using only the OpCarac "CONTAINED" or "BORDERSOFTNC" classification.
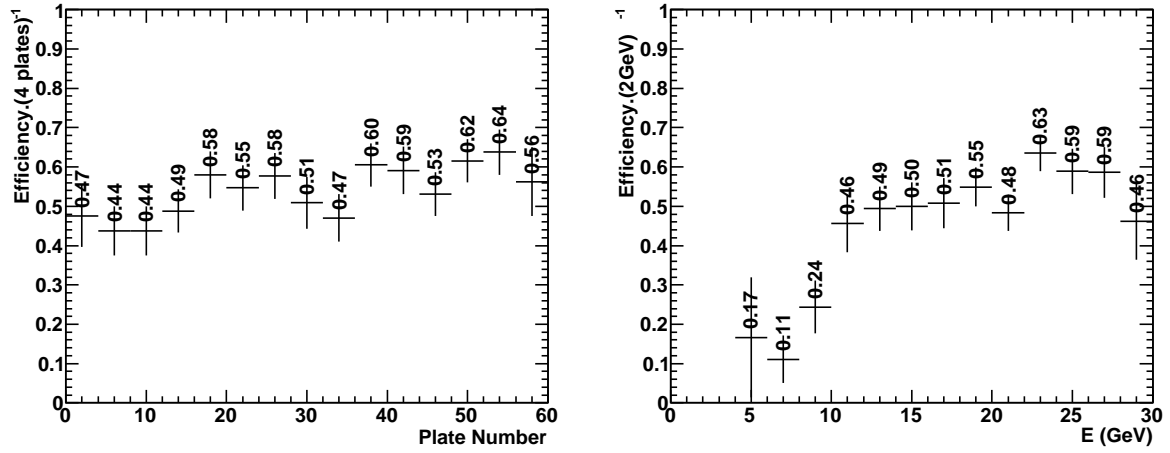
Figure F.10: In the top panel, location efficiency as a function of the MC true vertex depth in the brick. In the bottom panel, location efficiency as a function of the MC true neutrino energy. Both of these plots have been obtained with MC simulation of the $\nu_\mu^{CC} \xrightarrow{mis} \nu_\mu^{NC}$ channel by using only the OpCarac "CONTAINED" or "BORDERSOFTNC" classification.

List of Figures

List of Tables

Bibliography

[1] E. Fermi. An attempt of a theory of beta radiation. 1. *Z.Phys.*, 88:161–177, 1934. 1, 145

[2] H. Bethe *et al.* The 'neutrino'. *Nature*, 133:532, 1934. 1, 145

[3] F. Reines *et al.* Detection of the free anti-neutrino. *Phys.Rev.*, 117:159–173, 1960. 1

[4] L.M. Langer *et al.* The Beta-Spectrum of Tritium and the Mass of the Neutrino. *Phys. Rev.*, 88:689–694, Nov 1952. 1, 145

[5] G. Danby *et al.* Observation of High-Energy Neutrino Reactions and the Existence of Two Kinds of Neutrinos. *Phys.Rev.Lett.*, 9:36–44, 1962. 1, 145, 147

[6] M.L. Perl *et al.* Evidence for Anomalous Lepton Production in e+ - e- Annihilation. *Phys.Rev.Lett.*, 35:1489–1492, 1975. 1

[7] K. Kodama *et al.* Observation of tau neutrino interactions. *Phys.Lett.*, B504:218–224, 2001. 1, 149

[8] Precision electroweak measurements on the Z resonance. *Phys.Rept.*, 427:257–454, 2006. 1, 148, 149

[9] M. Goldhaber *et al.* Helicity of neutrinos. *Phys.Rev.*, 109:1015–1017, 1958. 1, 143, 147

[10] B. Pontecorvo. Mesonium and anti-mesonium. *Sov.Phys.JETP*, 6:429, 1957. 2, 5

[11] Z. Maki *et al.* Remarks on the unified model of elementary particles. *Prog.Theor.Phys.*, 28:870–880, 1962. 2, 5

[12] R. Davis. A review of the Homestake solar neutrino experiment. *Prog.Part.Nucl.Phys.*, 32:13–32, 1994. 2

[13] J.N. Abdurashitov *et al.* Solar neutrino flux measurements by the Soviet-American Gallium Experiment (SAGE) for half the 22 year solar cycle. *J.Exp.Theor.Phys.*, 95:181–193, 2002. 2

[14] M. Altmann *et al.* Complete results for five years of GNO solar neutrino observations. *Phys.Lett.*, B616:174–190, 2005. 2

[15] Y. Fukuda *et al.* Evidence for oscillation of atmospheric neutrinos. *Phys. Rev. Lett.*, 81:1562–1567, 1998. 2, 23

[16] Q.R. Ahmad *et al.* Measurement of the rate of nu/e + d –> p + p + e-interactions produced by B-8 solar neutrinos at the Sudbury Neutrino Observatory. *Phys.Rev.Lett.*, 87:071301, 2001. 2

[17] M. Apollonio *et al.* Limits on neutrino oscillations from the CHOOZ experiment. *Phys.Lett.*, B466:415–430, 1999. 2, 16

[18] A. Smirnov. Origins of neutrino mass. In *Ecole de GIF*, 2011. 5, 12, 152

[19] C. Sutton. *Spaceship neutrino.* Cambridge University Press, 1992. 5

[20] C. Giunti *et al.* Neutrino mixing. 2003. 6

[21] C. Amsler *et al.* Review of Particle Physics. *Phys.Lett.*, B667:1–1340, 2008. 9, 73, 74, 104, 142

[22] L. Wolfenstein. Neutrino Oscillations in Matter. *Phys.Rev.*, D17:2369–2374, 1978. 10

[23] S. Pascoli. Theory and phenomenology of neutrino oscillations. In *Ecole de GIF*, 2011. 10

[24] S. Mikheyev *et al.* Resonant amplification of ν oscillations in matter and solar-neutrino spectroscopy. *Il Nuovo Cimento C*, 9:17–26, 1986. 10.1007/BF02508049. 10

[25] J. Bouchez. La physique du neutrino auprès des réacteurs nucléaires. In *Ecole de GIF*, 1992. 11

[26] M. Kaplinghat. Absolute Neutrino Mass from Cosmology. In *TAUP03*, 2003. 14

[27] G.L. Fogli *et al.* Global analysis of neutrino masses, mixings and phases: entering the era of leptonic CP violation searches. *Phys.Rev.*, D86:013012, 2012. 15, 17, 19, 20, 21, 48, 110, 122, 130, i, xiii, xiv

[28] F. Piquemal. Mesure de la masse du neutrino. In *Ecole de GIF*, 2011. 15, i

[29] J. Wilkerson. A review of direct neutrino mass experiments. In *Neutrino 2012*, 2012. 15, 154

[30] A. Chapon. SuperNEMO status. *AIP Conf.Proc.*, 1417:18–22, 2011. 15

[31] G.L. Fogli *et al.* Observables sensitive to absolute neutrino masses. *Phys.Rev.*, D78:033010, 2008. 16, 17, 63, 114, xiii

[32] F.P. An *et al.* Observation of electron-antineutrino disappearance at Daya Bay. *Phys.Rev.Lett.*, 108:171803, 2012. 17

[33] J.K. Ahn *et al.* Observation of Reactor Electron Antineutrino Disappearance in the RENO Experiment. *Phys.Rev.Lett.*, 108:191802, 2012. 17

[34] T. Matsubara *et al.* First result from the Double Chooz reactor-neutrino experiment. 2012. 17

[35] T. Nakaya. Results from T2K. In *Neutrino 2012*, 2012. 17

[36] M. Guler *et al.* OPERA: An appearance experiment to search for nu/mu <-> nu/tau oscillations in the CNGS beam. Experimental proposal. 2000. CERN-SPSC-2000-028. 23, 25, 30, 44, xi

[37] R. Acquafredda *et al.* First events from the CNGS neutrino beam detected in the OPERA experiment. *New J.Phys.*, 8:303, 2006. 23

[38] CNGS. The CNGS website. `http://proj-cngs.web.cern.ch/proj-cngs/`. 24, 25, 44, i

[39] M. Besnier. *Reconstruction et analyse d'interactions de neutrinos dans les blocs-cibles-émulsions d'OPERA et discrimination du fond charmé dans le canal $\tau \to 3h$*. PhD thesis, Université de Savoie, 2008. 25, 54, 112, 114

[40] A. Anokhina *et al.* Emulsion sheet doublets as interface trackers for the OPERA experiment. *JINST*, 3:P07005, 2008. 26, 27, 32, 37

[41] T. Nakamura *et al.* The OPERA film: New nuclear emulsion for large-scale, high-precision experiments. *Nucl.Instrum.Meth.*, A556:80–86, 2006. 26, 27, i

[42] A. Anokhina *et al.* Study of the effects induced by lead on the emulsion films of the OPERA experiment. *JINST*, 3:P07002, 2008. 27

[43] N. Agafonova *et al.* Momentum measurement by the Multiple Coulomb Scattering method in the OPERA lead emulsion target. *New J.Phys.*, 14:013026, 2012. 27, 59, 116

[44] T. Adam *et al.* The OPERA experiment target tracker. *Nucl.Instrum.Meth.*, A577:523–539, 2007. 29, i

[45] R. Acquafredda *et al.* The OPERA experiment in the CERN to Gran Sasso neutrino beam. *JINST*, 4:P04018, 2009. 29

[46] N. Agafonova *et al.* Measurement of the atmospheric muon charge ratio with the OPERA detector. *Eur.Phys.J.*, C67:25–37, 2010. 30

[47] J. Janicskó-Csáthy. *Study of ν interactions and background estimation in the OPERA Emulsion Film Detector*. PhD thesis, University of Neuchâtel, 2006. 31, 75, ii

[48] K. Morishima *et al.* Development of a new automatic nuclear emulsion scanning system, S-UTS, with continuous 3D tomographic image read-out. *JINST*, 5:P04011, 2010. 31

[49] T. Fukuda *et al.* The analysis of interface emulsion detector for the OPERA experiment in JAPAN scanning facility. *JINST*, 5:P04009, 2010. 31

[50] C. Pistillo. *An automatic scanning system for nuclear emulsion analysis in the OPERA experiment*. PhD thesis, Università degli studi di Napoli Federico II, 2004. 32, 49, iii

[51] N. Armenise *et al.* High-speed particle tracking in nuclear emulsion by last-generation automatic microscopes. *Nucl.Instrum.Meth.*, A551:261–270, 2005. 32, 33, 57

[52] L. Arrabito *et al.* Hardware performance of a scanning system for high speed analysis of nuclear emulsions. *Nucl.Instrum.Meth.*, A568:578–587, 2006. 32, 34

[53] L. Arrabito *et al.* Track reconstruction in the emulsion-lead target of the OPERA experiment using the ESS microscope. *JINST*, 2:P05004, 2007. 32, 33, ii

[54] R. Acquafredda and the OPERA collaboration. The opera experiment in the cern to gran sasso neutrino beam. *Journal of Instrumentation*, 4(04):P04018, 2009. 36

[55] C. Jollet *et al.* Comparison of the kinematical variables between Monte-Carlo and data on 2008 and 2009 runs. *OPERA internal note 114*, 2010. 36

[56] T. Strauss. *Charm production in the OPERA experiment and the study of a high temperature superconducting solenoid for a liquid argon time projection chamber.* PhD thesis, ETH Zurich, 2010. 36, 54, 59, 60, 127, ii, iii

[57] A. Ariga. *Development and realization of a super-low-background interface detector using emulsions for the OPERA experiment.* PhD thesis, Nagoya University, 2008. 36, 59, 60, iii

[58] G. DeLellis. Analysis of 2010 and 2011 runs : towards Neutrino 2012. In *Collaboration Meeting*, 2012. 37, 69, 123, xi, xii, xiii

[59] N. Agafonova and The OPERA Collaboration. Search for nu/mu —> nu/tau oscillation with the OPERA experiment in the CNGS beam. *New Journal of Physics*, 14(3):033017, 2012. 37, 49, 50, 112, xi

[60] N.T. Tran. *Recherche des oscillations de neutrinos par apparition du nu-tau avec désintégration muonique du tau dans l'expérience OPERA*. PhD thesis, Université Claude Bernard Lyon I, 2010. 38, ii

[61] E. Barbuto *et al.* Atmospheric muon flux measurements at the external site of the Gran Sasso Lab. *Nucl.Instrum.Meth.*, A525:485–495, 2004. 38

[62] Samoil M. Bilenky *et al.* Glashow-Weinberg-Salam theory of electroweak interactions and the neutral currents. *Phys.Rept.*, 90:73–157, 1982. 40

[63] K. Nakamura and Particle Data Group. Review of Particle Physics. *Journal of Physics G: Nuclear and Particle Physics*, 37(7A):075021, 2010. 41, ii

[64] S. Zeller. Neutrino cross sections. In *PANIC 2011*, 2011. 42, ii

[65] C. Borer. Determination of the numu-spectrum of the CNGS neutrino beam by studying muon events in the OPERA experiment. Master's thesis, University of Bern, 2008. 42

[66] KLiN. The KLiN project website. `http://hep.fi.infn.it/PAMELA/naumov/Eng/KLiN/index.ht` 43

[67] M. Nakamura. Results from OPERA. In *Neutrino 2012*, 2012. 44, xi

[68] A. Meregaglia. OPERA oscillation results. In *NNN11*, 2011. 44, xi

[69] A. Ferrari *et al.* CNGS neutrino beam systematics for theta(13). *Nucl.Phys.Proc.Suppl.*, 145:93–97, 2005. 48

[70] PDG. The PDG website. `http://pdglive.lbl.gov`. 48, 112, 158, viii

[71] E. Barbuto *et al.* Vertex Reconstruction in SySal.NET : the "global vertexing" algorithm. *OPERA internal note 78*, 2006. 49, 61

[72] Y. Caffari. *Caractérisation des électrons dans l'expérience OPERA*. PhD thesis, Université Claude Bernard Lyon 1, 2006. 53, 75

[73] F. Juget *et al.* Electromagnetic shower reconstruction and energy measurement in the opera brick. *internal note 99*, 2009. 53, 82

[74] D. Autiero. The OPERA event generator and the data tuning of nuclear re-interactions. *Nucl.Phys.Proc.Suppl.*, 139:253–259, 2005. 54

[75] Geant. The Geant website. `http://geant4.cern.ch/`. 54

[76] Fluka. The Fluka website. `http://www.fluka.org/fluka.php`. 54

[77] CERNLIB. The CERNLIB website. `http://cernlib.web.cern.ch/cernlib/`. 54

[78] CLHEP. The CLHEP website. `http://proj-clhep.web.cern.ch/proj-clhep/`. 54

[79] ROOT. The ROOT website. `http://root.cern.ch/`. 54

[80] Pythia. The Pythia website. `http://home.thep.lu.se/~torbjorn/Pythia.html`. 54

[81] ROOT VMC. The ROOT VMC website. `http://root.cern.ch/drupal/content/vmc`. 54, 55

[82] ORACLE. The ORACLE website. `http://www.oracle.com/technetwork/database/features/` 54

[83] L. Chaussard. OpGeom : Software model of the OPERA detector. *OPERA internal note 69*, 2005. 55, iii

[84] A. Bertolin *et al.* OpCarac : an algorithm for the classification of the neutrino interactions recorded by the OPERA experiment. *OPERA internal note 100*, 2009. 56

[85] A. Bertolin. Analysis of the OPERA events recorded since 2008 using the Electronic Detectors data. *OPERA internal note 142*, 2012. 56

[86] N. Agafonova *et al.* Study of neutrino interactions with the electronic detectors of the OPERA experiment. *New J.Phys.*, 13:053051, 2011. 56

[87] C. Jollet *et al.* Energy Reconstruction. *OPERA internal note 112*, 2010. 56, 115

[88] V. Tioukov *et al.* The FEDRA Framework for emulsion data reconstruction and analysis in the OPERA experiment. *Nucl.Instrum.Meth.*, A559:103–105, 2006. 57, 61

[89] S. Dusini. Introduction to OpEmuRec. Private Communication. 58, iii

[90] Kalman filter. Th. Glebe Hera-B Note 00-175, 2000. 61

[91] L. Durieu *et al.* Optics Studies for the T9 Beam Line in the CERN PS East Area Secondary Beam Facility. *Conf.Proc.*, C0106181:1547–1549, 2001. 62

[92] K. Abe *et al.* Indication of Electron Neutrino Appearance from an Accelerator-produced Off-axis Muon Neutrino Beam. *Phys.Rev.Lett.*, 107:041801, 2011. 63

[93] TMVA. Toolkit for Multivariate Data Analysis with ROOT. http://tmva.sourceforge.net/. 72

[94] O.I. Dahl. Private communication cited in the PDG. 74

[95] E. Longo *et al.* Monte Carlo calculation of photon-initiated electromagnetic showers in lead glass. *Nuclear Instruments and Methods*, 128(2):283 – 307, 1975. 74

[96] W.R. Nelson *et al.* Electron induced cascade showers in copper and lead at 1-GeV. *Phys.Rev.*, 149:201–208, 1966. 74

[97] G. Bathow *et al.* Measurements of the longitudinal and lateral development of electromagnetic cascades in lead, copper and aluminum at 6 gev. *Nucl.Phys.*, B20:592–602, 1970. 74

[98] C.W. Fabjan *et al.* Calorimetry in high-energy physics. *Ann.Rev.Nucl.Part.Sci.*, 32:335–389, 1982. 77

[99] A. Ariga. Private communication. 79, iv

[100] L. Arrabito *et al.* Electron/pion separation with an emulsion cloud chamber by using a neural network. *JINST*, 2:P02001, 2007. 82

[101] F. Brunet. Simulation des oscillations des neutrinos muon vers les neutrinos électrons dans le détecteur OPERA au Gran Sasso (ITALIE). Master's thesis, Université Claude Bernard Lyon 1, 2009. 114

[102] M. Komatsu *et al.* Sensitivity to Theta(13) of the CERN to Gran Sasso neutrino beam. *J. Phys.*, G29:443, 2003. 114, xiii

[103] U. Kose. MC Study of CS Shower Hint and Vertex to CS Shower Search. *OPERA internal note 141*, 2011. 123, 124

[104] A. Pastore *et al.* Tau decay search efficiencies. In *Collaboration Meeting*, 2012. 128, xiii

[105] T.D. Lee *et al.* Question of Parity Conservation in Weak Interactions. *Phys.Rev.*, 104:254–258, 1956. 146

[106] C.S. Wu *et al.* Experimental test of parity conservation in beta decay. *Phys.Rev.*, 105:1413–1414, 1957. 146, viii

[107] L. Grodzins. Measuring the helicity of the neutrino. In *XXIV International Conference on Neutrino Physics and Astrophysics*, 2010. 147

[108] F.J. Hasert *et al.* Observation of Neutrino Like Interactions Without Muon Or Electron in the Gargamelle Neutrino Experiment. *Phys.Lett.*, B46:138–140, 1973. 148

[109] G. Arnison *et al.* Experimental Observation of Isolated Large Transverse Energy Electrons with Associated Missing Energy at s**(1/2) = 540-GeV. *Phys.Lett.*, B122:103–116, 1983. 148

[110] G. Arnison *et al.* Experimental Observation of Lepton Pairs of Invariant Mass Around 95-GeV/c**2 at the CERN SPS Collider. *Phys.Lett.*, B126:398–410, 1983. 148

[111] G. Karagiorgi. Toward solution of the miniboone-lsnd anomalies. *Nuclear Physics B - Proceedings Supplements*, 229âĂŞ232(0):50 – 54, 2012. 148

[112] Ch. Kraus *et al.* Final results from phase II of the Mainz neutrino mass search in tritium beta decay. *Eur.Phys.J.*, C40:447–468, 2005. 153

[113] V.M. Lobashev *et al.* Direct search for neutrino mass and anomaly in the tritium beta-spectrum: Status of 'Troitsk neutrino mass' experiment. *Nucl.Phys.Proc.Suppl.*, 91:280–286, 2001. 153

[114] A. Osipowicz et al. KATRIN: A Next generation tritium beta decay experiment with sub-eV sensitivity for the electron neutrino mass. Letter of intent. 2001. 154, viii

[115] T. Akiri. *Test des Flash-ADCs, optimisation de la conception du détecteur et développement d'un nouveau concept de reconstruction spatiale dans l'expérience d'oscillation de neutrinos Double Chooz*. PhD thesis, Université Paris Diderot - Paris 7, 2010. 155, viii

[116] R.A. Fisher. The Use of multiple measurements in taxonomic problems. *Annals of Human Genetics*, 7:179–188, 1936. 10.1111/j.1469-1809.1936.tb02137.x. 159

[117] A. Hocker *et al.* TMVA - Toolkit for Multivariate Data Analysis. *PoS*, ACAT:040, 2007. 159

Résumé : Un vaste programme international est en cours pour déterminer les paramètres du phénomène d'oscillation des neutrinos et approfondir la connaissance de la matrice de mélange des neutrinos (MNSP). Le détecteur OPERA, qui est installé dans le laboratoire souterrain du Gran Sasso en Italie, a pour but principal de mettre en évidence l'apparition de neutrinos de type tau dans un faisceau de neutrinos initialement de type muon, produit au CERN (CNGS) 730 km en amont. Il est aussi en mesure de détecter les oscillations des neutrinos muon en neutrinos électron, donnant accès au paramètre de mélange $sin(2\theta_{13})^2$, où θ_{13} est le dernier angle de la matrice MNSP finalement déterminé en 2012 conjointement par Daya Bay, RENO et Double Chooz. Pour déterminer la présence des ν_τ dans le faisceau, le détecteur OPERA est composé de cibles calorimétriques utilisant une alternance de plaques de plomb et de films d'émulsion. Ceux-ci permettront de reconstruire les traces des particules chargées résultant des interactions neutrino avec une précision inégalable (de l'ordre du micron). La recherche des événements de signal d'oscillation $\nu_\mu \rightarrow \nu_e$ sera basée sur l'aptitude à identifier les électrons, à rejeter les événements de fond où un π^0 est produit et à soustraire le fond dominant intrinsèque provenant du faisceau. Ce travail de thèse a pour objectif l'élaboration de méthodes d'analyse pour améliorer les performances du détecteur OPERA dans la recherche d'oscillations $\nu_\mu \rightarrow \nu_e$.

Mots-Clefs : neutrino, oscillation, angle de mélange, gerbe électromagnétique, simulation Monte-Carlo, OPERA.

Abstract : An international program is ongoing to measure the neutrino oscillation phenomenon and to determine the neutrino mixing matrix (MNSP) parameters. OPERA is a long-baseline neutrino experiment located at the Gran Sasso Laboratory in Italy, 730 km from CERN, downstream in the CNGS neutrino beam. The OPERA experiment is designed and optimised for a direct appearance search of $\nu_\mu \rightarrow \nu_\tau$ oscillations. It can also detect the $\nu_\mu \rightarrow \nu_e$ oscillation driven by $sin(2\theta_{13})^2$, where θ_{13} is the last mixing angle finally measured by the Daya Bay, RENO, and Double Chooz experiments in 2012. To observe the presence of ν_τ interactions in the beam, the OPERA detector is composed of calorimetric targets made of a modular structure called the "brick": a sandwich of lead plates interspaced with emulsion layers. The latter allows reconstructing tracks of charged particles produced in the neutrino interactions with a micrometric resolution. The search for the $\nu_\mu \rightarrow \nu_e$ oscillation signal is based on the capability of identifying the electrons, rejecting background events where neutral pions are produced and keeping under control the intrinsic and dominant background source from the beam contamination. This work aims to elaborate analysis methods to improve the OPERA detector performance in the $\nu_\mu \rightarrow \nu_e$ oscillation search.

Keywords : neutrino, oscillation, mixing angle, electromagnetic shower, Monte-Carlo simulation, OPERA.